



Universiteit
Leiden
The Netherlands

Chemical genetic approaches for target validation

Wel, T. van der

Citation

Wel, T. van der. (2020, January 22). *Chemical genetic approaches for target validation*. Retrieved from <https://hdl.handle.net/1887/83257>

Version: Publisher's Version

License: [Licence agreement concerning inclusion of doctoral thesis in the Institutional Repository of the University of Leiden](#)

Downloaded from: <https://hdl.handle.net/1887/83257>

Note: To cite this publication please use the final published version (if applicable).

Cover Page



Universiteit Leiden



The handle <http://hdl.handle.net/1887/83257> holds various files of this Leiden University dissertation.

Author: Wel, T. van der

Title: Chemical genetic approaches for target validation

Issue Date: 2020-01-22

Chemical genetic approaches for target validation

PROEFSCHRIFT

ter verkrijging van
de graad van Doctor aan de Universiteit Leiden
op gezag van Rector Magnificus prof. mr. C.J.J.M. Stolker,
volgens besluit van het College voor Promoties
te verdedigen op woensdag 22 januari 2020
klokke 11:15 uur

door

Tom van der Wel

geboren te Delft op 6 mei 1991

Promotiecommissie

Promotoren:	Prof. dr. M. van der Stelt	<i>Leiden University</i>
	Prof. dr. H.S. Overkleeft	<i>Leiden University</i>
Copromotor:	Dr. T. Barf	<i>Covalution BioSciences</i>
Overige leden:	Prof. dr. J. Brouwer	<i>Leiden University</i>
	Prof. dr. J.M.F.G. Aerts	<i>Leiden University</i>
	Prof. dr. A.H. Meijer	<i>Leiden University</i>
	Prof. dr. J.J.C. Neefjes	<i>Leiden University Medical Center</i>
	Prof. dr. E.W. Tate	<i>Imperial College London, United Kingdom</i>
	Prof. dr. D. Rauh	<i>TU Dortmund University, Germany</i>

ISBN: 978-94-028-1875-8
Printed by: Ipskamp Printing
Quote page 3: Quotation from Francis Crick.
"What Mad Pursuit: A Personal View of Scientific Discovery
(1988)"

All rights reserved. No parts of this thesis may be reproduced in any matter or any means without prior written permission from the author.

“Almost all aspects of life are engineered at the molecular level, and without understanding molecules we can only have a very sketchy understanding of life itself.”

— Francis Crick

Table of contents

Chapter 1	7
General introduction	
Chapter 2	19
A chemical genetic strategy for visualization of engineered kinases and their target engagement by covalent complementary probes	
Chapter 3	61
Precise gene editing allows visualization of endogenous FES kinase engagement during myeloid differentiation	
Chapter 4	81
Covalent complementary probes reveal the role of FES tyrosine kinase in neutrophil phagocytosis via SYK activation	
Chapter 5	97
Towards a chemical genetic strategy for subtype-selective inhibition of diacylglycerol lipase alpha	
Chapter 6	121
A natural substrate activity assay for high-throughput screening on monoacylglycerol lipase	
Chapter 7	141
Summary & Future prospects	
Samenvatting	161
List of publications	168
Curriculum vitae	171
Nawoord	172

1

General introduction

The drug discovery process

In the last decades, the field of drug discovery and development has advanced tremendously. Improvements in synthetic chemistry, DNA sequencing, protein crystallography, high-throughput screening and computational drug design, among others, have contributed to a faster and more efficient drug discovery process.¹ Despite these efforts, it still takes 10-12 years for a drug candidate to reach the market and less than 10% of the drugs that enter clinical trials actually make it to the patient.^{2,3}

Drug development is a time- and resource-consuming process and consists of multiple stages (Figure 1.1).⁴ The search for a new drug usually starts at the discovery and validation of a (protein) target that contributes to the pathogenesis or progression of a disease.⁵ After this, an assay that reports on the functional activity of the target protein has to be set up. The process of hit identification is then initiated, which aims to identify molecules that modulate the target's function, *e.g.* its catalytic activity in case of an enzyme. Nowadays, hit identification usually involves high-throughput screening campaigns in which large libraries of small molecules are screened against the target of interest in an automated setup.⁶ Identified 'hit compounds' typically have low affinity, insufficient functional efficacy, and/or a poor selectivity profile and should be optimized in a hit-to-lead optimization program.⁷ The most promising candidate, the 'lead compound', then enters the stage of lead optimization, where its pharmacokinetic and pharmacodynamic properties and toxicological profile are assessed, usually in multiple animal models. If a compound successfully passes this stage, it can enter clinical trials. At this point, it is first tested in healthy human subjects to investigate the drug's pharmacokinetic and safety profile. Next, the drug is administered to a small group of patients to evaluate its efficacious dose. The final phase of clinical trials aims to assess efficacy and safety of the compound on a larger patient group. If the experimental drug passes these stages and is approved by authorities, it can enter the market.¹

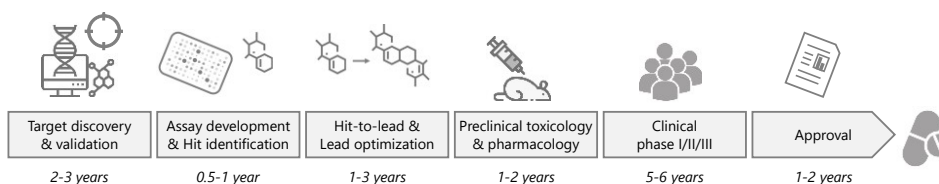


Figure 1.1 – Overview of the different stages of drug discovery and development. Estimated duration is indicated for each stage.^{3,5}

Chemical tools for target discovery and validation

The discovery and development of most new drugs starts with the target discovery. Nowadays, novel targets are generally identified using genetic methods, such as RNA interference (RNAi) or CRISPR/Cas9-based library screens that abrogate the expression of proteins, in combination with a functional assay that reports on a disease-relevant phenotypic response.^{8,9} The identification of novel therapeutic targets can be a challenging endeavor in itself and greatly depends on the predictive value of the employed phenotypic assay.^{10,11} Genetic knockdown or knockout of a target does not always match the effects of its acute pharmacological modulation.¹² Long-term genetic disruption may have different effects on cellular physiology in comparison to acute and dynamic modulation by small molecules. In addition, genetic models may be hampered by potential compensatory mechanisms that obscure the role of the target protein.¹³

It is thus essential to validate that pharmacological modulation (*e.g.* inhibition) of the target leads to the desired phenotype, a process which is collectively referred to as target validation.¹⁴ Target validation heavily relies on the availability of suitable chemical tools to study engagement of the compound to the intended biological target, and the ability to connect these molecular interactions with proximal biomarkers or phenotypic effects.^{15,16} These chemical tools, or 'probes', can guide in selecting the best compound from a panel of drug candidates and can help to determine the dose required for complete target occupancy without inducing off-target effects.^{17,18} Depending on their application, probes can be diverse in chemical structure and characteristics, and include radioligands¹⁹, fluorescent or biotinylated small molecules²⁰, positron emission tomography (PET) tracers²¹, photoaffinity-based probes²², and activity-based probes.^{23,24}

Structurally, chemical probes typically consist of a binding element with affinity for the intended target, a reactive group that covalently links the probe to the target, and a reporter moiety that enables visualization (*e.g.* fluorescent group) or identification (*e.g.* biotin) of the probe-bound targets (Figure 1.2A).²⁵ A covalent mode of action renders these probes exceptionally useful for target engagement and target validation studies, since they can irreversibly react with one or multiple target proteins in a complex proteome mixture.^{26,27} Fluorescent reporter groups can be used for visualization of these probe-bound targets using sodium dodecyl sulfate polyacrylamide gel electrophoresis (SDS-PAGE) followed by in-gel fluorescence scanning. On the other hand, biotinylated probes allow streptavidin-based enrichment of probe-bound targets, followed by tryptic digestion and liquid chromatography coupled to mass spectrometry (LC-MS) analysis of target peptides.¹⁶ Generally, the large size of a reporter group is a limiting factor, since it reduces probe solubility and cell-permeability. This limitation can be addressed by the use of 'two-step probes', which typically possess bioorthogonal ligation handles that enable conjugation of reporter groups in a later experimental stage.^{28–30} Including an inhibitor

Chapter 1

pre-incubation step allows a competitive experimental setup to profile a compound's proteome-wide target engagement (Figure 1.2B).

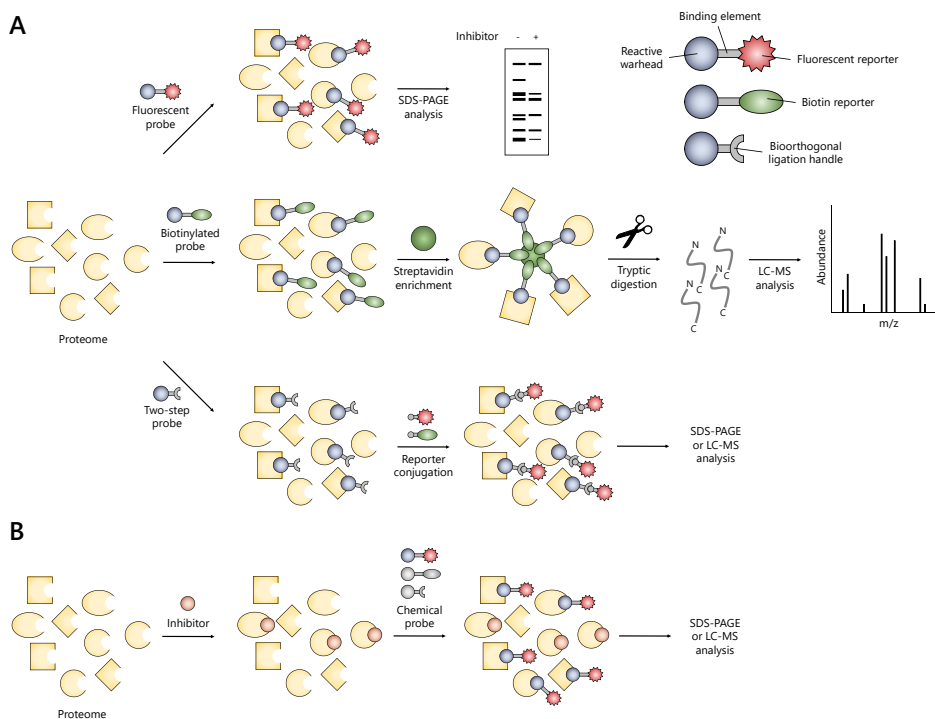


Figure 1.2 – Chemical probes as tools to study target engagement and target validation. (A) Chemical probes have an irreversible, covalent mode of action and can be used to label one or multiple proteins in a complex proteome sample. Fluorescent reporter groups can be used for visualization of probe-bound targets using SDS-PAGE and in-gel fluorescence scanning. Biotinylated probes enable streptavidin-based enrichment of probe-bound targets, followed by tryptic digestion and LC-MS analysis of target peptides. Two-step probes are versatile tools harboring bioorthogonal ligation handles, which enable conjugation to reporter tags in a later experimental stage. (B) Competitive experiment to study target engagement of inhibitors using chemical probes. The proteome is pre-incubated with inhibitor and subsequently labeled with a chemical probe of choice. Figures are modified from literature.¹⁷

A variety of chemical probes has been developed for many protein classes, in particular enzymes, including kinases³¹, phosphatases³², serine hydrolases^{23,33}, proteases^{34,35}, and glycosidases.³⁶ On the one hand, non-selective probes that bind to a broad spectrum of protein targets can serve as valuable tools for target discovery^{37,38} or to investigate a compound's selectivity profile using chemical proteomics techniques.^{23,31,39,40} On the other hand, selective probes are exceptionally suited for cellular target engagement studies⁴¹ or for molecular imaging of the protein target.^{35,42,43}

Chemical genetics

The development of a selective chemical probe that specifically targets a particular protein can be challenging to achieve due to the off-target activity towards structurally and/or functionally related homologs, *e.g.* other members within the same protein class. Selectivity can be improved in an iterative process of design, synthesis, testing, and refining the original scaffold, but this is a time-consuming and tedious effort. To overcome such limitations, various chemical genetic methods and technologies have been developed that allow for selective modulation of specific targets using small molecules (Figure 1.3).

Chemical genetics combines the specificity of genetics with benefits of acute, pharmacological modulation by a small molecule. It generally uses engineered, mutant proteins that can accommodate unnatural substrates or modified ligands that do not affect other, native proteins in the cellular environment. The most prominent example is the 'bump-hole' technology that has been successfully applied to a wide range of protein families, including kinases⁴⁴, GTPases⁴⁵, proteases⁴⁶, phosphatases⁴⁷, receptors⁴⁸ and various types of transferases.⁴⁹ This strategy is based on mutagenesis of bulky amino acid residues into smaller residues, creating an additional pocket ('hole') in the target protein's active site (Figure 1.3A). This engineered, mutant protein can accommodate bulkier ligands than its wild-type counterpart, making these ligands mutant-specific.⁵⁰⁻⁵² Since off-targets of the original ligand maintain their native active site structure, these proteins are typically not targeted by these bulky analogues.⁵³ An alternative to this steric complementation approach is the use of charge complementation, where active site residues are mutated to induce electronic repulsion to the original ligand while establishing novel electrostatic interactions (*e.g.* hydrogen bonds) with a modified ligand (Figure 1.3B).⁵⁴

Although these concepts allow one to selectively modulate a target protein and study its function, the lack of a covalent binding mode limits the opportunities for use in target engagement studies. Covalent, irreversible ligands can have additional advantages over reversible ligands, such as sustained target occupancy, lower susceptibility to competition with high intracellular substrate concentrations and a pharmacodynamic profile that is dependent on the target's *de novo* protein synthesis rate. Most importantly, ligands with a covalent binding mode are powerful tools by serving as chemical probes. Shokat and co-workers introduced the chemical genetic strategy of 'covalent complementarity', which involves mutagenesis of active site residues into cysteines (Figure 1.3C).^{55,56} The thiol group of cysteine can function as a nucleophile to covalently react with electrophilic ligands.^{37,57} Although conceptually promising, mutant proteins may suffer from distorted protein folding, reduced catalytic activity or otherwise impeded protein function.⁵⁵ Another general limitation of all described chemical genetic strategies remains that they rely on overexpression of the mutant protein of interest, which in itself may

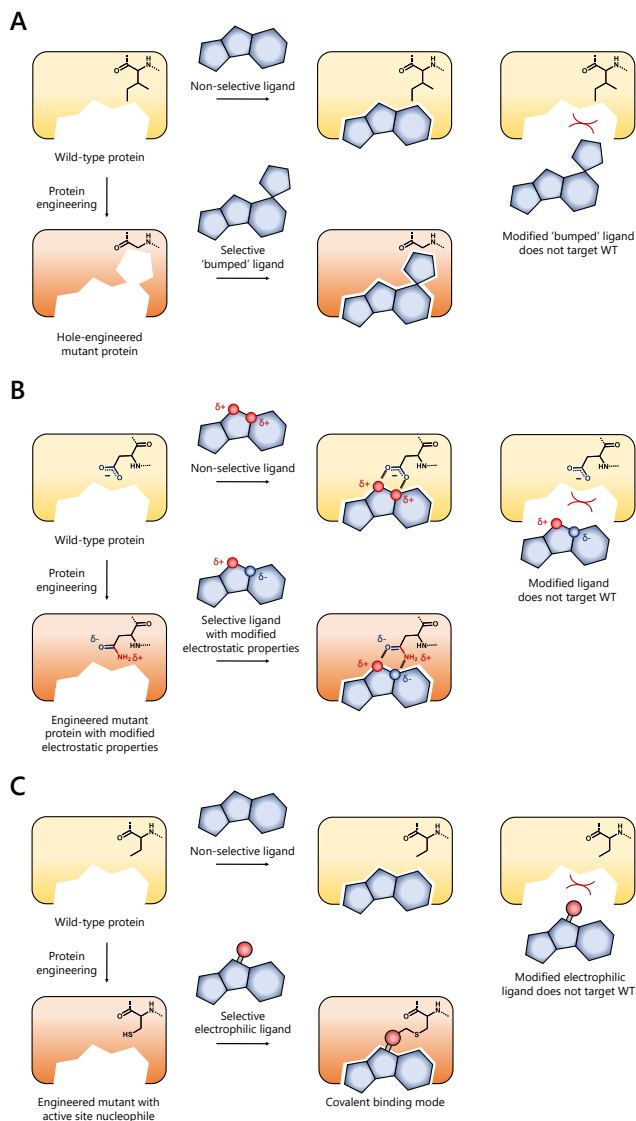


Figure 1.3 – Chemical genetic approaches to establish selective modulation of specific protein targets by small molecules. (A) Steric complementation or 'bump-hole' strategy. The target protein is engineered by mutation of a bulky amino acid residue in the active site into a smaller residue ('hole'). A non-selective ligand is modified by incorporation of a bulky substituent ('bump') to fill the mutant's pocket. This modified bumped ligand does not target the wild-type protein due to steric clash. (B) Charge complementation strategy. The target protein is engineered based on electrostatic interactions in the active site, e.g. by modification of hydrogen bonding patterns. A non-selective ligand is modified by changing its electronic properties to complement the mutated residue in the engineered protein pocket. This modified ligand does not target the wild-type protein due to electrostatic repulsion and/or loss of affinity. (C) Covalent binding mode strategy. The target protein is engineered by mutating an active site residue into a nucleophilic residue, e.g. cysteine. A non-selective ligand is modified by incorporation of an electrophile that covalently reacts with the nucleophilic residue. This modified electrophilic ligand does not target the wild-type protein due to a lack of nearby nucleophilic residues. Figures modified from literature.^{58,59}

induce artefacts and disturbs normal cellular physiology.⁶⁰ Further improvements are thus required to facilitate the application of chemical genetics-based probes in target engagement and target validation studies on endogenously expressed proteins.

Aim and outline

The aim of the research described in this thesis is to develop a chemical genetic strategy that can be used for target engagement and target validation studies.

Chapter 2 describes the development of a chemical genetic toolbox for visualization of engineered kinases and their target engagement. Using the tyrosine kinase FES as exemplary target, various cysteine point mutants are generated and expressed, followed by comprehensive biochemical profiling. After identification of a suitable mutant, structure-based design is employed to synthesize mutant-specific probes that covalently react with the introduced cysteine. Next, the selectivity and covalent mode of action of the compounds are characterized in more detail. Cellular target engagement studies are performed to investigate the *in situ* potency. Lastly, broader application of the generated tools is examined on a panel of wild-type and cysteine mutant kinases.

Chapter 3 applies the tools developed in chapter 2 to investigate the role of FES activity in myeloid differentiation. The use of CRISPR/Cas9 gene editing allows the visualization of an endogenous mutant FES kinase in a relevant model system. Gel-based labeling experiments reveal the cellular target engagement profile of the probe, and chemical proteomics is used to study its proteome-wide selectivity. This chapter also demonstrates the power of the chemical genetic strategy to dissect on-target from off-target effects using mutant and wild-type cells, respectively.

Chapter 4 reports on the application of the chemical genetic tools from chapter 2 and the generated mutant cell line from chapter 3 to study the role of FES activity in neutrophil phagocytosis. A flow cytometry assay is used to measure phagocytic uptake of fluorescent *E. coli* by neutrophils, which reveals that FES plays a role in this process. Guided by a substrate profiling experiment, a novel FES substrate is identified and validated *in situ*. Phospho-specific immunoblot experiments are used to gain insight in the underlying molecular mechanism, which results in a model proposing a novel role of FES in neutrophil phagocytosis.

Chapter 5 extends the chemical genetic strategy described in chapter 2 to diacylglycerol lipase α (DAGL α), an enzyme belonging to the family of serine hydrolases. This chapter describes the first steps towards a strategy to subtype-selectively inhibit DAGL α without affecting its structurally related homolog DAGL β . To this end, DAGL α cysteine mutants are designed based on a homology model, followed by biochemical profiling using activity-based protein profiling (ABPP) and substrate hydrolysis assays. The design and synthesis of mutant-selective inhibitors of DAGL α are described, followed by characterization of its irreversible, covalent binding mode. Competitive ABPP is used to

Chapter 1

investigate the ability of the compounds to subtype-selectively target DAGL α in presence of DAGL β .

Chapter 6 discusses the development and miniaturization of a biochemical activity assay for monoacylglycerol lipase (MAGL), a serine hydrolase that is currently considered as a therapeutic target for various diseases. Currently, nearly all MAGL inhibitors have an irreversible mode of action and the number of reversible compounds is limited. To identify novel reversible MAGL inhibitors, the assay was used in a high-throughput screening campaign on 233,820 unique compounds. Hit validation using orthogonal ABPP experiments results in a qualified list of hit compounds that constitute starting points for the development of novel, reversible MAGL inhibitors as well as chemical probes for use in chemical genetic strategies.

Chapter 7 provides a summary of the work described in this thesis and discusses future directions.

References

1. Scannell, J. W., Blanckley, A., Boldon, H. & Warrington, B. Diagnosing the decline in pharmaceutical R&D efficiency. *Nature Reviews Drug Discovery* **11**, 191–200 (2012).
2. Paul, S. M. *et al.* How to improve RD productivity: The pharmaceutical industry's grand challenge. *Nature Reviews Drug Discovery* **9**, 203–214 (2010).
3. Waring, M. J. *et al.* An analysis of the attrition of drug candidates from four major pharmaceutical companies. *Nature Reviews Drug Discovery* **14**, 475–486 (2015).
4. DiMasi, J. A., Grabowski, H. G. & Hansen, R. W. Innovation in the pharmaceutical industry: New estimates of R&D costs. *J. Health Econ.* **47**, 20–33 (2016).
5. Hughes, J. P., Rees, S. S., Kalindjian, S. B. & Philpott, K. L. Principles of early drug discovery. *British Journal of Pharmacology* **162**, 1239–1249 (2011).
6. Copeland, R. A. *Evaluation of Enzyme Inhibitors in Drug Discovery: A Guide for Medicinal Chemists and Pharmacologists: Second Edition.* (Wiley, 2013).
7. Keseru, G. M. & Makara, G. M. Hit discovery and hit-to-lead approaches. *Drug Discovery Today* **11**, 741–748 (2006).
8. Tiedemann, R. E. *et al.* Kinome-wide RNAi studies in human multiple myeloma identify vulnerable kinase targets, including a lymphoid-restricted kinase, GRK6. *Blood* **115**, 1594–1604 (2010).
9. Schuster, A. *et al.* RNAi/CRISPR Screens: from a Pool to a Valid Hit. *Trends in Biotechnology* **37**, 38–55 (2019).
10. Moffat, J. G., Rudolph, J. & Bailey, D. Phenotypic screening in cancer drug discovery-past, present and future. *Nat. Rev. Drug Discov.* **13**, 588–602 (2014).
11. Vincent, F. *et al.* Developing predictive assays: The phenotypic screening 'rule of 3'. *Sci. Transl. Med.* **7**, 293ps15 (2015).
12. Weiss, W. A., Taylor, S. S. & Shokat, K. M. Recognizing and exploiting differences between RNAi and small-molecule inhibitors. *Nat. Chem. Biol.* **3**, 739–744 (2007).
13. Knight, Z. A. & Shokat, K. M. Chemical Genetics: Where Genetics and Pharmacology Meet. *Cell* **128**, 425–430 (2007).
14. Nicolaou, K. C. The chemistry-biology-medicine continuum and the drug discovery and development process in academia. *Chemistry and Biology* **21**, 1039–1045 (2014).
15. Bunnage, M. E., Chekler, E. L. P. & Jones, L. H. Target validation using chemical probes. *Nat. Chem. Biol.* **9**, 195–199 (2013).
16. Drewes, G. & Knapp, S. Chemoproteomics and Chemical Probes for Target Discovery. *Trends in Biotechnology* **36**, 1275–1286 (2018).
17. Nomura, D. K., Dix, M. M. & Cravatt, B. F. Activity-based protein profiling for biochemical pathway discovery in cancer. *Nat. Rev. Cancer* **10**, 630–638 (2010).
18. Simon, G. M., Niphakis, M. J. & Cravatt, B. F. Determining target engagement in living systems. *Nat. Chem. Biol.* **9**, 200–205 (2013).
19. Maguire, J. J., Kuc, R. E. & Davenport, A. P. Radioligand binding assays and their analysis. *Methods Mol. Biol.* **897**, 31–77 (2012).
20. Dittus, L., Werner, T., Muelbaier, M. & Bantscheff, M. Differential Kinobeads Profiling for Target Identification of Irreversible Kinase Inhibitors. *ACS Chem. Biol.* **12**, 2515–2521 (2017).
21. Sharma, R. & Aboagye, E. Development of radiotracers for oncology - The interface with pharmacology. *British Journal of Pharmacology* **163**, 1565–1585 (2011).
22. Soethoudt, M. *et al.* Selective Photoaffinity Probe That Enables Assessment of Cannabinoid CB 2 Receptor Expression and Ligand Engagement in Human Cells. *J. Am. Chem. Soc.* **140**, 6067–6075 (2018).
23. Baggelaar, M. P. *et al.* Development of an activity-based probe and in silico design reveal highly selective inhibitors for diacylglycerol lipase- α in brain. *Angew. Chemie - Int. Ed.* **52**, 12081–12085 (2013).
24. Ogasawara, D. *et al.* Rapid and profound rewiring of brain lipid signaling networks by acute diacylglycerol lipase inhibition. *Proc. Natl. Acad. Sci.* **113**, 26–33 (2016).
25. Niphakis, M. J. & Cravatt, B. F. Enzyme Inhibitor Discovery by Activity-Based Protein Profiling. *Annu. Rev. Biochem.* **83**, 341–377 (2014).
26. Schenone, M., Dančik, V., Wagner, B. K. & Clemons, P. A. Target identification and mechanism of action in chemical biology and drug discovery. *Nature Chemical Biology* **9**, 232–240 (2013).
27. Arrowsmith, C. H. *et al.* The promise and peril of chemical probes. *Nat. Chem. Biol.* **11**, 536–541 (2015).
28. Rostovtsev, V. V., Green, L. G., Fokin, V. V. & Sharpless, K. B. A stepwise huisgen cycloaddition process: Copper(I)-catalyzed regioselective 'ligation' of azides and terminal alkynes. *Angew. Chemie - Int. Ed.* **41**, 2596–2599 (2002).
29. Van Rooden, E. J. *et al.* Mapping in vivo target interaction profiles of covalent inhibitors using chemical proteomics with label-free quantification. *Nat. Protoc.* **13**, 752–767 (2018).

Chapter 1

30. van Rooden, E. J., Bakker, A. T., Overkleef, H. S. & van der Stelt, M. Activity-Based Protein Profiling. in *eLS* 1–9 (John Wiley & Sons, Ltd, 2018).
31. Zhao, Q. *et al.* Broad-spectrum kinase profiling in live cells with lysine-targeted sulfonyl fluoride probes. *J. Am. Chem. Soc.* **139**, 680–685 (2017).
32. Kawaguchi, M., Hanaoka, K., Komatsu, T., Terai, T. & Nagano, T. Development of a highly selective fluorescence probe for alkaline phosphatase. *Bioorganic Med. Chem. Lett.* **21**, 5088–5091 (2011).
33. Liu, Y., Patricelli, M. P. & Cravatt, B. F. Activity-based protein profiling: The serine hydrolases. *Proc. Natl. Acad. Sci.* **96**, 14694–14699 (1999).
34. Sexton, K. B., Witte, M. D., Blum, G. & Bogoy, M. Design of cell-permeable, fluorescent activity-based probes for the lysosomal cysteine protease asparaginyl endopeptidase (AEP)/legumain. *Bioorganic Med. Chem. Lett.* **17**, 649–653 (2007).
35. de Bruin, G. *et al.* A Set of Activity-Based Probes to Visualize Human (Immuno)proteasome Activities. *Angew. Chemie - Int. Ed.* **55**, 4199–4203 (2016).
36. Kallemeijn, W. W. *et al.* Investigations on therapeutic glucocerebrosidases through paired detection with fluorescent activity-based probes. *PLoS One* **12**, e0170268 (2017).
37. Backus, K. M. *et al.* Proteome-wide covalent ligand discovery in native biological systems. *Nature* **534**, 570–574 (2016).
38. Hacker, S. M. *et al.* Global profiling of lysine reactivity and ligandability in the human proteome. *Nat. Chem.* **9**, 1181–1190 (2017).
39. Lanning, B. R. *et al.* A road map to evaluate the proteome-wide selectivity of covalent kinase inhibitors. *Nat. Chem. Biol.* **10**, 760–767 (2014).
40. van Esbroeck, A. C. M. *et al.* Activity-based protein profiling reveals off-target proteins of the FAAH inhibitor BIA 10-2474. *Science* **356**, 1084–1087 (2017).
41. Dubach, J. M. *et al.* Quantitating drug-Target engagement in single cells in vitro and in vivo. *Nat. Chem. Biol.* **13**, 168–173 (2017).
42. Oresic Bender, K. *et al.* Design of a Highly Selective Quenched Activity-Based Probe and Its Application in Dual Color Imaging Studies of Cathepsin S Activity Localization. *J. Am. Chem. Soc.* **137**, 4771–4777 (2015).
43. Kallemeijn, W. W. *et al.* Endo- β -Glucosidase Tag Allows Dual Detection of Fusion Proteins by Fluorescent Mechanism-Based Probes and Activity Measurement. *ChemBioChem* **17**, 1698–1704 (2016).
44. Bishop, A. C. *et al.* A chemical switch for inhibitor-sensitive alleles of any protein kinase. *Nature* **407**, 395–401 (2000).
45. Hwang, Y.-W. & Miller, D. L. A Mutation That Alters the Nucleotide Specificity of Elongation Factor Tu, a GTP Regulatory Protein. *J. Biol. Chem.* **262**, 13081–13085 (1987).
46. Morell, M. *et al.* Coupling protein engineering with probe design to inhibit and image matrix metalloproteinases with controlled specificity. *J. Am. Chem. Soc.* **135**, 9139–9148 (2013).
47. Hoffman, H. E., Blair, E. R., Johndrow, J. E. & Bishop, A. C. Allele-specific inhibitors of protein tyrosine phosphatases. *J. Am. Chem. Soc.* **127**, 2824–2825 (2005).
48. Tedesco, R., Thomas, J. A., Katzenellenbogen, B. S. & Katzenellenbogen, J. A. The estrogen receptor: A structure-based approach to the design of new specific hormone-receptor combinations. *Chem. Biol.* **8**, 277–287 (2001).
49. Luo, M. Current chemical biology approaches to interrogate protein methyltransferases. *ACS Chemical Biology* **7**, 443–463 (2012).
50. Belshaw, P. J., Schoepfer, J. G., Liu, K.-Q., Morrison, K. L. & Schreiber, S. L. Rational Design of Orthogonal Receptor–Ligand Combinations. *Angew. Chemie Int. Ed. English* **34**, 2129–2132 (1995).
51. Au-Yeung, B. B. *et al.* A genetically selective inhibitor demonstrates a function for the kinase Zap70 in regulatory T cells independent of its catalytic activity. *Nat. Immunol.* **11**, 1085–1092 (2010).
52. Carter-O’Connell, I. *et al.* Combining Chemical Genetics with Proximity-Dependent Labeling Reveals Cellular Targets of Poly(ADP-ribose) Polymerase 14 (PARP14). *ACS Chem. Biol.* **13**, 2841–2848 (2018).
53. Koh, J. T. Engineering selectivity and discrimination into ligand-receptor interfaces. *Chemistry and Biology* **9**, 17–23 (2002).
54. Tairis, N., Gabriel, J. L., Soprano, K. J. & Soprano, D. R. Alteration in the retinoid specificity of retinoic acid receptor- β by site-directed mutagenesis of Arg269 and Lys220. *J. Biol. Chem.* **270**, 18380–18387 (1995).
55. Garske, A. L., Peters, U., Cortesi, A. T., Perez, J. L. & Shokat, K. M. Chemical genetic strategy for targeting protein kinases based on covalent complementarity. *Proc. Natl. Acad. Sci. U. S. A.* **108**, 15046–15052 (2011).
56. Xiao, J. *et al.* A coupled protein and probe engineering approach for selective inhibition and activity-based probe labeling of the caspases. *J. Am. Chem. Soc.* **135**, 9130–9138 (2013).
57. Barf, T. & Kaptein, A. Irreversible protein kinase inhibitors: Balancing the benefits and risks. *J. Med. Chem.* **55**, 6243–6262 (2012).
58. Islam, K. Allele-specific chemical genetics: Concept, strategies, and applications. *ACS Chem. Biol.* **10**, 343–363 (2015).

59. Islam, K. The Bump-and-Hole Tactic: Expanding the Scope of Chemical Genetics. *Cell Chem. Biol.* **25**, 1171–1184 (2018).
60. Prelich, G. Gene overexpression: Uses, mechanisms, and interpretation. *Genetics* **190**, 841–854 (2012).

2

A chemical genetic strategy
for visualization of engineered kinases
and their target engagement
by covalent complementary probes

Introduction

Protein kinases comprise a 518-membered family of enzymes that play an essential role in intracellular signaling processes. They transfer a phosphate group from ATP to specific amino acid residues in proteins, thereby modulating protein activity, localization and protein-protein interactions.^{1,2} Protein kinases are involved in many cellular functions, including proliferation, differentiation, migration and host-pathogen interactions. Kinases are also an important class of drug targets for the treatment of cancer.³ However, current FDA-approved kinase inhibitors intend to target only <5% of the entire kinome⁴ and therapeutic indications outside oncology are vastly underrepresented.^{5,6} These so-far untargeted kinases thus offer great opportunities for the development of novel molecular therapies for various diseases. The non-receptor tyrosine kinase feline sarcoma oncogene (FES), subject of this study, is a potential therapeutic target for cancer and immune disorders.⁷⁻⁹

FES has a restricted expression pattern and is primarily found in hematopoietic, neuronal, endothelial and epithelial cells.¹⁰ FES, together with FES-related kinase (FER), constitutes a distinct subgroup within the family of tyrosine kinases, defined by their unique structural organization (Figure 2.1A). FES is able to interact via its F-Bin-Amphiphysin-Rvs (F-BAR) domain, either with itself or other F-BAR-containing proteins.¹¹ These interactions are proposed to maintain an inactive conformation in absence of activating stimuli.¹² The FES F-BAR domain binds to phosphoinositide-containing lipids, such as phosphatidylinositol 4,5-bisphosphate (PIP₂). In addition, phosphatidic acid binding via the F-BAR extension (FX) domain can increase kinase activity, although the exact mechanism remains poorly understood.¹³ FES also possesses a Src Homology 2 (SH2) domain that binds phosphorylated tyrosine residues and thereby functions as protein interaction domain. Moreover, electrostatic interactions between the SH2 domain and adjacent kinase domain of FES are essential to adopt an active conformation required for catalysis and disruption of this SH2-kinase domain interface severely impairs kinase activity.¹⁴ The kinase domain that performs the transfer of phosphate groups from ATP to protein substrates is located on the C-terminal end of FES. Phosphorylation of Y713 in the activation loop of FES is a prerequisite for its kinase activity¹⁵ and can occur either via autophosphorylation¹⁶ or phosphorylation by Src family kinases.¹⁷ Upon activating stimuli, FES translocates to the membrane to form oligomers, followed by autophosphorylation at Y713, after which FES adopts an active conformation suitable for catalysis (Figure 2.1B).¹⁸

The successful development of new drugs targeting kinases strongly depends on the understanding of their underlying molecular and cellular mechanism of action, *i.e.* the preclinical target validation.¹⁹ The physiological function of many kinases remains, however, poorly characterized and their direct protein substrates are often unknown.

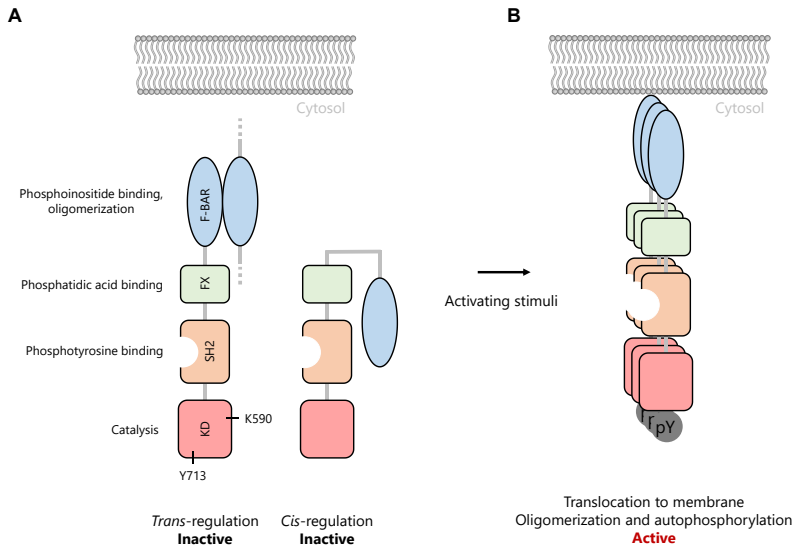


Figure 2.1 – Structural domains of FES and regulation of FES activity. (A) FES has a unique structural organization consisting of an F-Bin-Amphiphysin-Rvs (F-BAR), F-BAR extension (FX), Src Homology 2 (SH2) and kinase domain (KD). FES is present in an inactive conformation in absence of activation stimuli. K590 is the catalytic lysine residue that forms a salt bridge with E607 to adopt an active conformation. Y713 in the activation loop of FES is an autophosphorylation site that increases kinase activity. (B) Upon activation stimuli, FES translocates to the membrane, resulting in oligomerization via its F-BAR domain. FES is then activated by autophosphorylation of its Y713 residue.

Genetic models (congenital deletion or expression of kinase-dead variants) may be used to study these questions (Figure 2.2A). However, the interpretation of results from long-term, constitutive genetic disruption may sometimes be hampered by potential compensatory mechanisms. In addition, these models are poorly suited to dissect rapid and dynamic catalytic processes from the scaffolding function of kinases.^{20,21} A complementary approach is the use of small molecule inhibitors to modulate kinase activity in an acute and temporal fashion. This approach more closely resembles therapeutic intervention, but the available pharmacological tools, especially for non-validated kinases, often suffer from a lack of selectivity.^{20,22} Currently, there are no suitable FES inhibitors available for target validation studies, because they either lack potency or selectivity and all cross-react with FER.^{7,23}

Another important aspect of drug discovery is to obtain proof of target engagement, which correlates the exposure at the site of action to a pharmacological or phenotypic readout.²⁴ Information about kinase engagement is essential for determining the dose required for full target occupancy without inducing undesired off-target activity.²⁵ Activity- and affinity-based protein profiling is a chemical biology technique that is ideally suited to study target engagement.²⁴ Chemical probes make use of a covalent, irreversible mode of action, combined with reporter tags such as fluorophores to enable target visualization or biotin to enable target enrichment and identification. In the field of kinases,

reported chemical probes either target a conserved active site lysine residue in a non-selective fashion²⁶ or non-catalytic cysteine residues in the ATP binding pocket.^{27,28} The first class of kinase ABPs lacks the selectivity required for cellular target engagement studies. On the other hand, the majority of kinases, including FES, do not possess targetable cysteine residues in the catalytic pocket²⁹. Garske *et al.* previously introduced the elegant concept of covalent complementarity: the use of an engineered kinase in which the gatekeeper amino acid residue is mutated into a cysteine, combined with electrophilic ATP analogs to study target engagement.³⁰ Other positions in the kinase active site have also been investigated^{31,32}, but secondary mutations were required to improve cysteine reactivity or compound selectivity and potency.

Inspired by these established and emerging concepts, in this study, a chemical genetic strategy was developed to visualize target engagement of kinases and aid in their validation as potential therapeutic targets.

Results

General strategy: an engineered kinase in combination with complementary probes

The key feature of the strategy is the combination of an engineered, mutant kinase with the design and application of complementary, covalent inhibitors (Figure 2.2B). The ATP-binding pocket of the kinase of interest is sensitized towards pharmacological inactivation using complementary probes by replacing an amino acid for a cysteine residue. Candidate mutants are rationally designed *in silico* using existing structural data, taking into account residue accessibility and avoiding mutagenesis of residues essential for catalysis (Figure 2.2C, step 1). The mutant is biochemically characterized to verify that the cysteine point mutation minimally affects kinase function (Figure 2.2C, step 2). Subsequently, complementary electrophilic inhibitors are designed to covalently react with this cysteine (Figure 2.2C, step 3). Covalent, irreversible inhibitors can have several advantages over reversible compounds, such as sustained target occupancy, lower susceptibility to competition by high intracellular ATP concentrations and a pharmacodynamic profile that is dependent on the target's *de novo* protein synthesis rate^{33,34}. The inhibitor will have far lower potency on the wild-type kinase, which does not possess a nucleophilic residue in its active site, thereby making the inhibitor mutant-specific. Transient overexpression of the mutant kinase allows *in situ* target engagement profiling in live cells, while the wild-type kinase serves as a negative control (Figure 2.2C, step 4). Importantly, the covalent binding mode of the inhibitor enables target engagement profiling by acting as a chemical probe and its ligation handle can be further functionalized with reporter tags for visualization by SDS-PAGE (fluorophore) or identification of the bound targets by mass spectrometry (biotin) (Figure 2.2C, step 5).

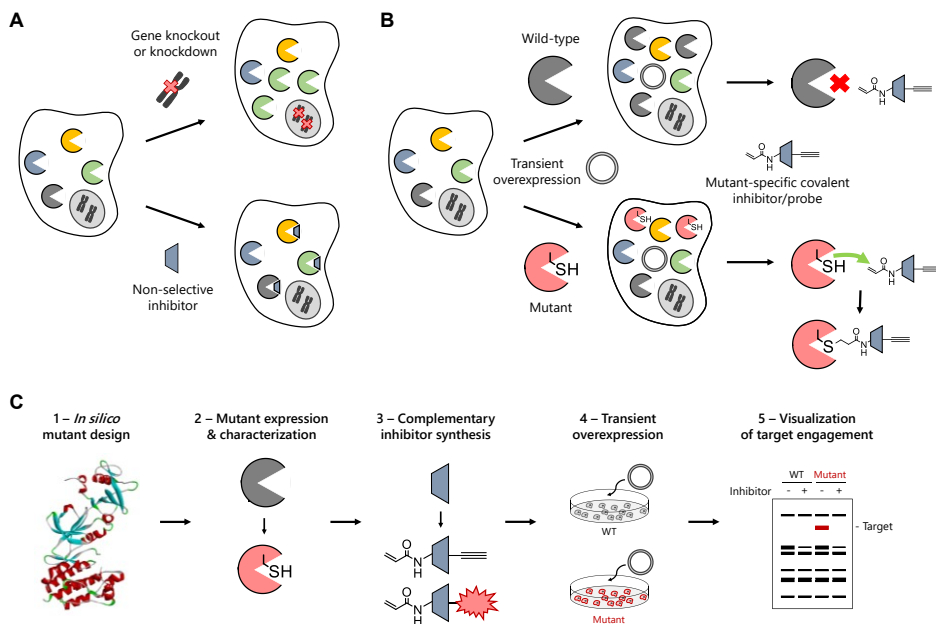


Figure 2.2 – Chemical genetic strategy for visualization of kinase target engagement. (A) Gene knockout or knockdown approaches suffer from a lack of temporal control, possibly inducing compensatory mechanisms such as upregulation of other kinases. On the other hand, many kinase inhibitors suffer from selectivity issues, leading to inactivation of multiple kinases and thereby resulting in a complex phenotype. (B) Chemical genetic strategy involving mutagenesis of a kinase active site residue into a nucleophilic cysteine accompanied by mutant-specific covalent inhibitor design. A non-selective, reversible inhibitor is modified with an acrylamide electrophile to covalently react with the introduced cysteine, along with an alkyne ligation handle for conjugation to reporter tags using click chemistry. (C) Schematic workflow encompassing mutant design, expression and characterization, the design and synthesis of complementary inhibitors, transient expression of the wild-type or mutant kinase and visualization of target engagement by inhibitors using fluorescent probes.

Biochemical characterization of engineered FES kinases

To introduce a cysteine residue at an appropriate position in the ATP-binding pocket of FES, a previously reported crystal structure of FES with reversible inhibitor TAE684 (compound **1**) (PDB: 4e93) was inspected.²³ Nine active site residues situated in proximity of the bound ligand were selected (Figure 2.3A) and the respective cysteine point mutants were generated by site-directed mutagenesis on truncated human FES fused to an N-terminal His-tag. The wild-type protein and the mutants were recombinantly expressed in *Escherichia coli* (*E. coli*), purified using Ni²⁺-affinity chromatography and tested for catalytic activity using a time-resolved fluorescence resonance energy transfer (TR-FRET) assay (Figure 2.3B).^{35,36} Four of the nine tested mutants did not display any catalytic activity, including G570C (located on P-loop) and G642C (hinge region). Three mutants near the kinase hydrophobic backpocket (I567C, V575C and L638C) retained partial activity, whereas only two mutants (T646C and S700C) displayed catalytic activity similar to wild-type FES.

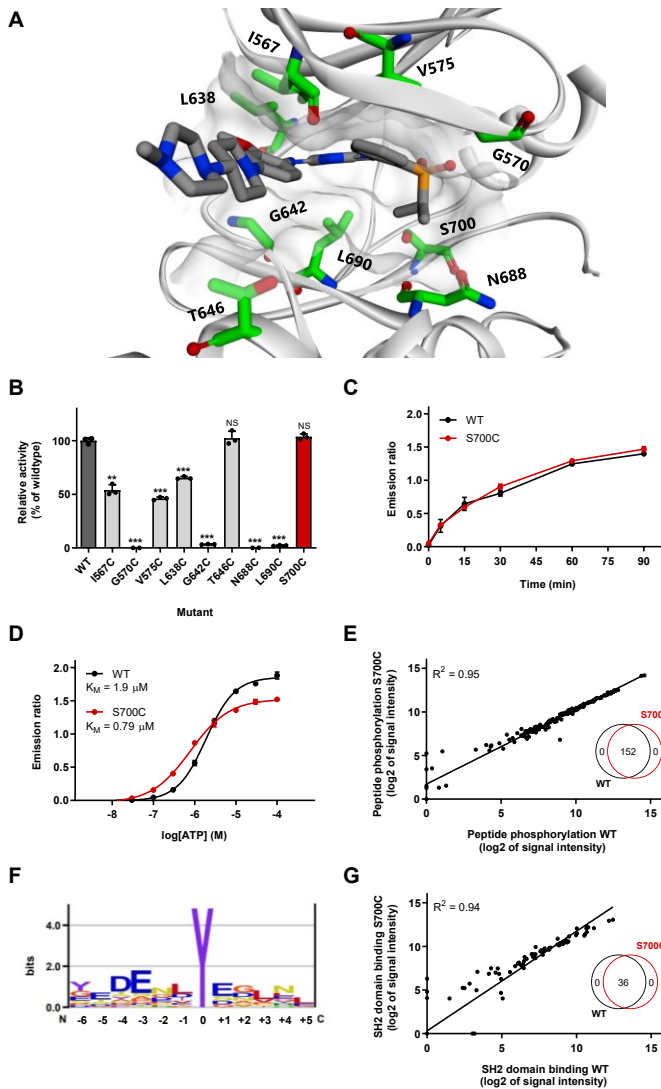


Figure 2.3 - Design and characterization of FES cysteine point mutants. (A) Location of mutated active site residues in FES crystal structure with bound reversible inhibitor TAE684 (PDB code: 4e93). (B) Activity of recombinantly expressed FES mutants compared to wild-type, determined as relative amount of phosphorylated peptide substrate after 60 min incubation using TR-FRET assay. (C) Reaction progress curve for FES^{WT} and FES^{S700C}. (D) Determination of ATP K_M for FES^{WT} and FES^{S700C}. Enzyme reactions in TR-FRET assays were performed with *ULight*-TK peptide (50 nM) and ATP (B, C: 100 μ M, D: variable) and quenched (B, D: after 60 min, C: variable). (E) Peptide substrate profile for FES^{WT} and FES^{S700C} as determined in PamChip® microarray. Peptides were filtered for those with ATP-dependent signal and \log_2 of signal intensity >3. The peptide substrates were identical for FES^{WT} and FES^{S700C} (Venn diagram, inset). (F) Preferred substrate consensus sequence based on FES^{WT} substrate profile. Illustration was rendered using Enologos (<http://www.benoslab.pitt.edu>). (G) SH2 domain binding profile for FES^{WT} and FES^{S700C} as determined in PamChip® microarray. Samples with non-specific antibody binding were excluded. The peptide-SH2 binding partners were identical for FES^{WT} and FES^{S700C} (Venn diagram, inset). Data represent means \pm SEM (N = 3). Statistical analysis was performed using ANOVA with Holm-Sidak's multiple comparisons correction: *** $P < 0.001$; NS if $P > 0.05$.

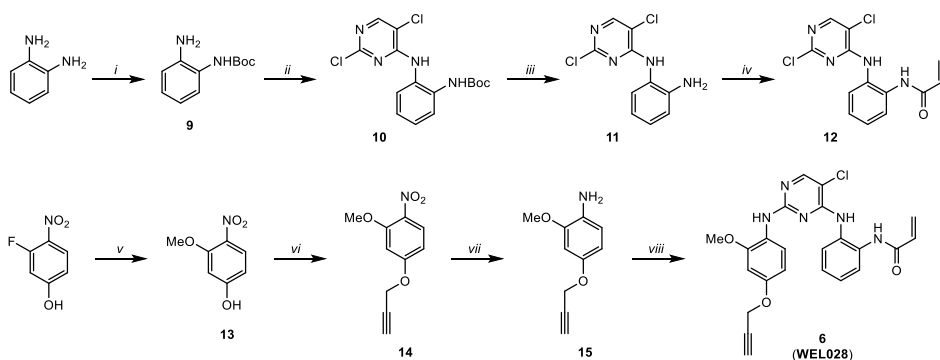
The attention was particularly drawn to the S700C mutant, which involves the residue adjacent to the highly conserved DFG motif (DFG-1). Since several other kinases (e.g. MAPK1/3³⁷, RSK1-4³⁸ and TAK1³⁹) express an endogenous cysteine at DFG-1 that can be targeted by electrophilic traps, FES^{S700C} was selected for more detailed biochemical profiling. The engineered kinase displayed identical reaction progress kinetics (Figure 2.3C) and similar affinity for ATP ($K_M = 1.9 \mu\text{M}$ for FES^{WT} and $K_M = 0.79 \mu\text{M}$ for FES^{S700C}; Figure 2.3D and Supplementary Figure 2.1A).

To assess whether the introduced mutation affected substrate recognition, a comparative substrate profiling assay was performed using the PamChip® microarray technology. This assay is based on the phosphorylation of immobilized peptides by purified FES and detection using a fluorescent phosphotyrosine antibody. Strikingly, the substrate profiles of FES^{WT} and FES^{S700C} were completely identical (Figure 2.3E, inset; Supplementary Table 2.1), indicating that the S700C mutation did not affect substrate recognition. Moreover, the absolute peptide phosphorylation levels showed a strong correlation ($R^2 = 0.95$). Sequence analysis of the top 30 of highest signal peptides revealed that FES prefers negatively charged substrates with hydrophobic residues at positions -1 and +3 and acidic residues at position -4, -3 and +1 relative to the tyrosine phosphorylation site (Figure 2.3F). These results are in line with a previous study that reported on FES substrate recognition.¹⁴ Lastly, a modified PamChip array to measure phosphopeptide binding to the Src homology 2 (SH2) domain of FES^{WT} and FES^{S700C} showed that the introduced mutation did not affect the SH2 binding profile (Figure 2.3G and Supplementary Table 2.2). In short, the DFG-1 residue (S700) in the ATP-binding pocket of FES was identified as an excellent position to mutate into a nucleophilic cysteine, without affecting FES kinase activity, kinetics, substrate recognition and SH2 binding profile.

Design, synthesis and characterization of complementary probes for FES^{S700C}

The reversible ligand TAE684 was used as a starting point to develop a complementary probe for FES^{S700C}. To assess whether the FES^{S700C} was still sensitive to inhibition by TAE684, the protein was incubated with various concentrations of TAE684 and its half maximum inhibitory concentration (expressed as pIC₅₀) was determined. This revealed that TAE684 was a potent inhibitor both on FES^{WT} and FES^{S700C} with pIC₅₀ values of 8.1 ± 0.04 and 9.0 ± 0.02 , respectively (Table 2.1). According to the co-crystal structure of FES^{WT} with TAE684 (PDB: 4e93) the isopropyl sulfone moiety is in the close proximity of the S700 residue at the DFG-1 position. Therefore, several derivatives of TAE684 were synthesized, in which the R₂-phenyl ring was substituted with an acrylamide group as electrophilic warhead (Scheme 2.1 and Supplementary Scheme 2.1-2.4).

The acrylamide is hypothesized to covalently interact with the engineered cysteine, but not with the serine of the wild-type protein. Since the strategy aims at exclusively inhibiting mutant but not wild-type FES, the piperidine-piperazine group was



Scheme 2.1 - Synthesis of WEL028. Reagents and conditions: i) Boc_2O , THF, rt, 58%. ii) 2,4,5-trichloropyrimidine, DIPEA, EtOH, reflux, 92%. iii) TFA, DCM, rt, 85%. iv) acryloyl chloride, DIPEA, DCM, 0 °C, 85%. v) NaOMe, MeOH, 50 °C, 94%. vi) propargyl bromide, K_2CO_3 , DMF, 60 °C to rt, 88%. vii) SnCl_2 , HCl, 1,4-dioxane, rt, 77%. viii) compound **12**, *p*-TSA, isopropanol, reflux, 36%.

removed as it is known to form water-mediated hydrogen bonds with hinge region residues and contribute to ligand affinity.²³ The pIC_{50} values of compound **2-6** are listed in Table 2.1 (dose-response curves in Supplementary Figure 2.1B-F). Removal of the piperidine-piperazine group (compound **2**) resulted in a modest reduction in potency on FES^{WT} and $\text{FES}^{\text{S700C}}$. Introduction of an acrylamide at the *meta*-position of the phenyl ring (compound **3**) further decreased affinity for FES^{WT} , but also led to significant loss in activity on the $\text{FES}^{\text{S700C}}$ mutant. Moving the acrylamide to the *ortho*-position resulted in compound **4**, which exhibited excellent potency on $\text{FES}^{\text{S700C}}$ ($\text{pIC}_{50} = 8.4 \pm 0.03$), whereas a major reduction in potency on FES^{WT} ($\text{pIC}_{50} = 5.7 \pm 0.21$) was found, resulting in an apparent selectivity window of 238-fold. The acrylamide was substituted for a propionamide (compound **5**) to confirm its important role in binding to $\text{FES}^{\text{S700C}}$. In line with the proposed mode of action, compound **5** displayed low inhibitory potency on $\text{FES}^{\text{S700C}}$.

Next, a docking study was performed with compound **4** in $\text{FES}^{\text{S700C}}$ (Figure 2.4A). The binding mode of **4** resembled the original binding pose of TAE684 and could explain the observed structure-activity relationships. Catalytic lysine residue 590 interacts with the amide carbonyl, ideally positioning the warhead on the *ortho*-position, but not on the *meta*-position, to undergo a Michael addition with the engineered cysteine. The binding pose also revealed a suitable position to install an alkyne moiety on the scaffold of compound **4** to develop a two-step chemical probe for target engagement studies. This led to the synthesis of compound **6** (hereafter referred to as WEL028) with an *ortho*-acrylamide and alkyne ligation handle (Scheme 2.1), which displayed a similar potency profile as **4** with strong inhibition of $\text{FES}^{\text{S700C}}$ ($\text{pIC}_{50} = 8.4 \pm 0.03$) but not FES^{WT} ($\text{pIC}_{50} = 5.0 \pm 0.37$) (Figure 2.4B and Table 2.1). The mutant-specific inhibition profile was additionally verified using the orthogonal PamChip® microarray assay (Figure 2.4C).

Table 2.1 - Inhibitory potency of synthesized TAE684 derivatives against FES^{WT} and FES^{S700C}. Half maximal inhibitory concentrations (expressed as pIC₅₀) determined on recombinantly expressed FES^{WT} and FES^{S700C} in a TR-FRET assay. Apparent fold selectivity was calculated as IC₅₀ on FES^{WT} divided by IC₅₀ on FES^{S700C}. Data represent means ± SD (N = 3). ND: not determined. Dose-response curves can be found in Figure 2.4B and Supplementary Figure 2.1).

Compound	R ₁	R ₂	pIC ₅₀		Apparent fold selectivity
			FES ^{WT}	FES ^{S700C}	
1 (TAE684)			8.1 ± 0.04	9.0 ± 0.02	8.6
2	H		7.3 ± 0.06	7.8 ± 0.04	2.5
3	H		6.5 ± 0.06	6.3 ± 0.06	0.65
4	H		5.7 ± 0.21	8.4 ± 0.03	238
5	H		ND	5.2 ± 0.08	ND
6 (WEL028)			5.0 ± 0.37	8.4 ± 0.03	232

To confirm that WEL028 undergoes a Michael addition to cysteine 700, recombinant FES^{S700C} was incubated with WEL028, digested to peptide fragments with trypsin and subsequently analyzed by LC-MS/MS (Figure 2.4D and Supplementary Figure 2.2). The mass of the expected FES peptide covalently bound to WEL028 was identified, whereas this mass was not present in a vehicle-treated control sample. The parent ion was further analyzed by collision-induced dissociation and the corresponding MS/MS fragmentation pattern showed clear ladders of predicted b and y ions, which confirmed covalent addition of WEL028 to Cys700.

Cys700 is located directly adjacent to the DFG motif, which is highly conserved among kinases and plays an essential role in binding Mg²⁺ ions that coordinate to the phosphates of ATP.⁴⁰ A substantial number of kinases also harbors a native cysteine at this

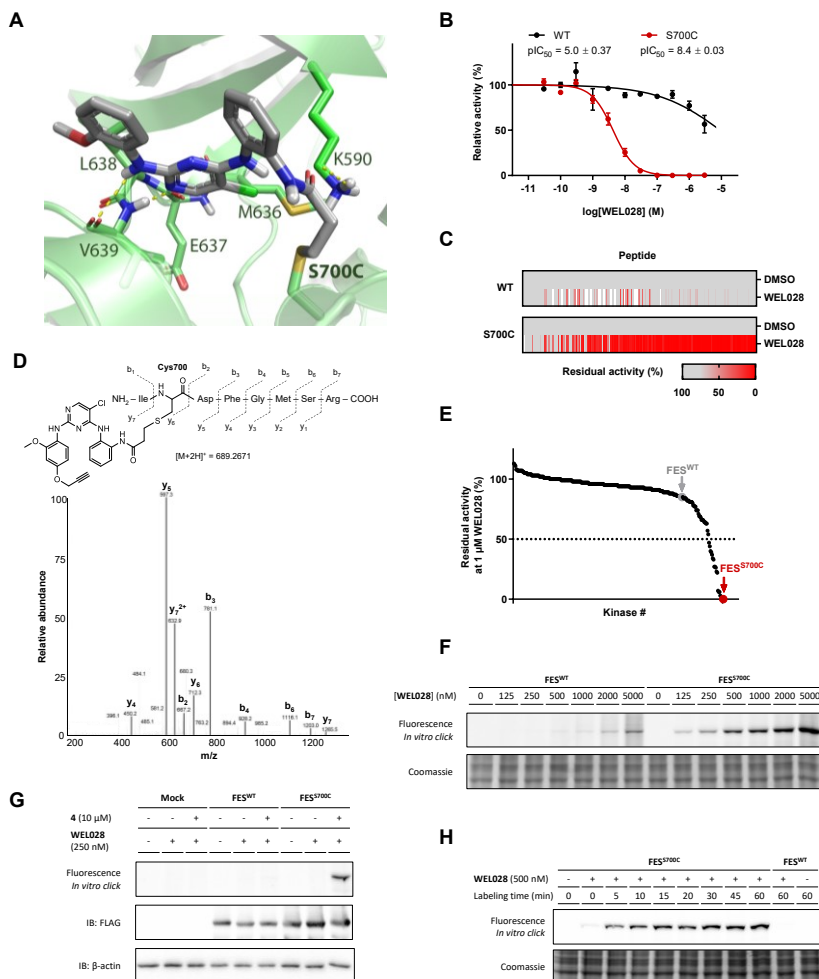


Figure 2.4 – WEL028 is a mutant-specific inhibitor of FES^{S700C} that covalently binds to Cys700. (A) Proposed covalent binding mode of compound **4** to Cys700 in crystal structure of FES (PDB code: 4e93). (B) *In vitro* inhibition profile of FES^{WT} and FES^{S700C} by WEL028. Data was obtained using time-resolved FRET assay. (C) Inhibition profile of WEL028 (100 nM) on FES^{WT} and FES^{S700C} on individual peptide substrates determined in PamChip® microarray. Signal intensity was normalized to vehicle-treated control. (D) MS/MS-based identification of WEL028 covalently bound to Cys700. The precursor ion (m/z $[M+2H]^{2+} = 689.2671$) was fragmented and signature ions of the WEL028-bound peptide are shown. The precursor ion was not observed in a vehicle-treated control sample. (E) Selectivity profile of WEL028 (1 μM, 1 h pre-incubation) on 279 kinases including all kinases with native active site cysteines, visualized as waterfall plot (each data point is an individual kinase). Kinases with <50% inhibition at 1 μM were further profiled in dose-response experiments. Data represent means (N = 2) and were obtained from SelectScreen™ selectivity profiling service except for FES^{S700C}, which was determined in-house. (F) Visualization of dose-dependent labeling of full-length FES^{S700C} but not FES^{WT} in HEK293T cell lysate using click chemistry. Lysates were incubated with WEL028 (indicated concentration, 30 min, rt), followed by addition of click mix containing Cy5-azide (2 eq., 30 min, rt). (G) Two-step labeling by WEL028 is specific and exclusive for FES^{S700C}. Lysate was incubated with vehicle or compound **4** (10 μM, 30 min, rt), followed by WEL028 (250 nM, 30 min, rt) and click mix containing Cy5-azide (2 eq., 30 min, rt). Protein expression was verified by immunoblot against a C-terminal FLAG-tag and β-actin as loading control. (H) Time-dependent labeling of FES^{S700C} by WEL028. Lysates were incubated with WEL028 (500 nM, indicated time, rt) and visualized by click chemistry as in F. Data represent means ± SEM (N = 3).

position, which might have implications for the kinome-wide selectivity of WEL028.³⁴ The selectivity profile was therefore assessed using the SelectScreen™ screening technology in a panel of 279 wild-type, mammalian kinases including all kinases with a native cysteine residue at any position in the active site. The assays were performed at a single dose of 1 μ M with 1 h of pre-incubation to identify the full spectrum of potential off-target kinases. Only 19 of the tested 279 kinases showed >50% inhibition under these conditions, meaning that WEL028 exhibited a >100-fold selectivity window against the residual 260 kinases (93% of tested kinases, Figure 2.4E and Supplementary Figure 2.3). Subsequently, dose-response experiments were performed for kinases showing >50% inhibition in the initial screen (Table 2.2 and Supplementary Figure 2.4). The only off-targets of WEL028 with a $pIC_{50} \leq 7$ were LRRK2 ($pIC_{50} = 7.3 \pm 0.05$) and MKNK2 ($pIC_{50} = 7.0 \pm 0.06$). Importantly, the potency of WEL028 on FES^{S700C} was unmatched by any of the tested kinases, with a minimal 10-fold apparent selectivity window in all cases.

Table 2.2 – Selectivity profile of WEL028. All data ($pIC_{50} \pm SD$, N = 2) were obtained from SelectScreen™ selectivity profiling service except for FES^{S700C}, which was determined in-house. Kinases exhibiting >50% inhibition at 1 μ M in an initial screen on 279 kinases (Supplementary Figure 2.3) were selected for dose-response experiments. Assays were performed with 1 h pre-incubation. Indicated molecular weight is based on UniProt database records. Location of native cysteine residues in the kinase active site is indicated if applicable, with nomenclature as previously described.²⁷ Apparent fold selectivity was calculated as IC_{50} on that kinase divided by IC_{50} on FES^{S700C}. Dose-response curves can be found in Supplementary Figure 2.4.

Kinase	Molecular weight (kDa)	Native cysteine	pIC_{50}	Apparent fold selectivity
AURKA	45.8	None	6.2 \pm 0.06	155
BRAF	84.4	Hinge2	7.0 \pm 0.06	25
CLK4	57.5	None	5.9 \pm 1.3	272
FES^{S700C}	93.5	DFG-1	8.4 \pm 0.03	N/A
FLT3	112.9	DFG-1	5.5 \pm 0.10	718
FLT4 (VEGFR3)	152.8	DFG-1, Hinge2	6.7 \pm 0.07	50
KDR (VEGFR2)	151.5	DFG-1, Hinge2	6.2 \pm 0.06	153
LRRK2	286.1	None	7.3 \pm 0.05	12
MAP2K1 (MEK1)	43.4	DFG-1, GK-1	6.6 \pm 0.06	60
MAP2K2 (MEK2)	44.4	DFG-1, GK-1	6.6 \pm 0.06	54
MAP2K6 (MEK6)	37.5	DFG-1, GK-1	6.5 \pm 0.07	68
MAP3K8 (COT)	52.9	DFG+1	6.6 \pm 0.05	57
MAPKAPK5 (PRAK)	54.2	DFG-1	6.3 \pm 0.09	112
MKNK2 (MKN2)	51.9	DFG-1	7.0 \pm 0.06	23
PDGFRA	122.7	DFG-1, Hinge2	6.1 \pm 0.06	184
PTK2 (FAK)	119.2	Hinge2	6.4 \pm 0.06	89
ROS1	263.9	None	< 5	> 238
STK33	57.8	Hinge2	6.0 \pm 0.58	254
TNK2 (ACK)	114.6	None	6.5 \pm 0.26	76

To visualize covalent binding of FES^{S700C} by WEL028, full-length FES^{S700C} was overexpressed in HEK293T cells and cell lysates were incubated with different concentrations of WEL028, followed by *in vitro* conjugation to a Cy5 fluorophore using click chemistry. Dose-dependent labeling at the expected molecular weight of 93 kDa was observed for FES^{S700C} but not FES^{WT} (Figure 2.4F). Pre-incubation with compound **4** completely abolished labeling of FES^{S700C} (Figure 2.4G). Time course experiments revealed that complete labeling was achieved within 15 min incubation and that labeling was stable up to 60 min (Figure 2.4H). In summary, WEL028 was identified as a complementary two-step probe for engineered FES^{S700C} that does not label wild-type FES and is highly selective over other kinases.

Target engagement studies with complementary one-step probe WEL033

Next, a one-step fluorescent probe was synthesized to facilitate visualization of FES^{S700C}: a Cy5-conjugated analog of WEL028 termed WEL033 (Figure 2.5A and Supplementary Scheme 2.5). WEL033 dose-dependently labeled recombinantly expressed full-length FES^{S700C} but not FES^{WT} in HEK293T cell lysate (Figure 2.5B). Interestingly, introduction of a secondary K590E mutation, resulting in a kinase-dead FES mutant that is unable to acquire an active “DFG-in” conformation¹⁷, abolished labeling by WEL033 (Figure 2.5C). This indicates that the Lys590 residue is essential for covalent binding of WEL028 to the FES active site, either directly by coordination of Lys590 to position the acrylamide warhead to undergo covalent addition to Cys700 as predicted by the docking studies (Figure 2.4A), or indirectly by restricted access to the inactive “DFG-out” conformation of FES.

A competitive probe binding assay was then performed to visualize target engagement in lysates with overexpressed full-length FES^{S700C}. Two inhibitors, TAE684 and WEL028, were able to prevent the labeling of FES^{S700C} in a dose-dependent manner ($pIC_{50} = 7.6 \pm 0.06$ and $pIC_{50} = 7.9 \pm 0.06$, respectively; Figure 2.5D, E). A similar dose-dependent profile was observed for **4** and biotin-conjugate WEL034 (Supplementary Figure 2.5). This demonstrates that gel-based ABPP using lysates of cells expressing full-length engineered FES^{S700C} is a valuable orthogonal method to standard biochemical assays using purified, truncated proteins.

The mode of action of TAE684 and WEL028 was then evaluated using time-dependent displacement experiments with these inhibitors (Figure 2.5F, G). After inhibitor incubation at their respective IC_{80} concentrations, labeling of FES^{S700C} activity by WEL033 recovers for TAE684 but not for WEL028, indicating a reversible and irreversible mode of action for these compounds, respectively. In line with these results, inhibitor washout experiments using overnight dialysis also showed irreversible inhibition by WEL028 but not

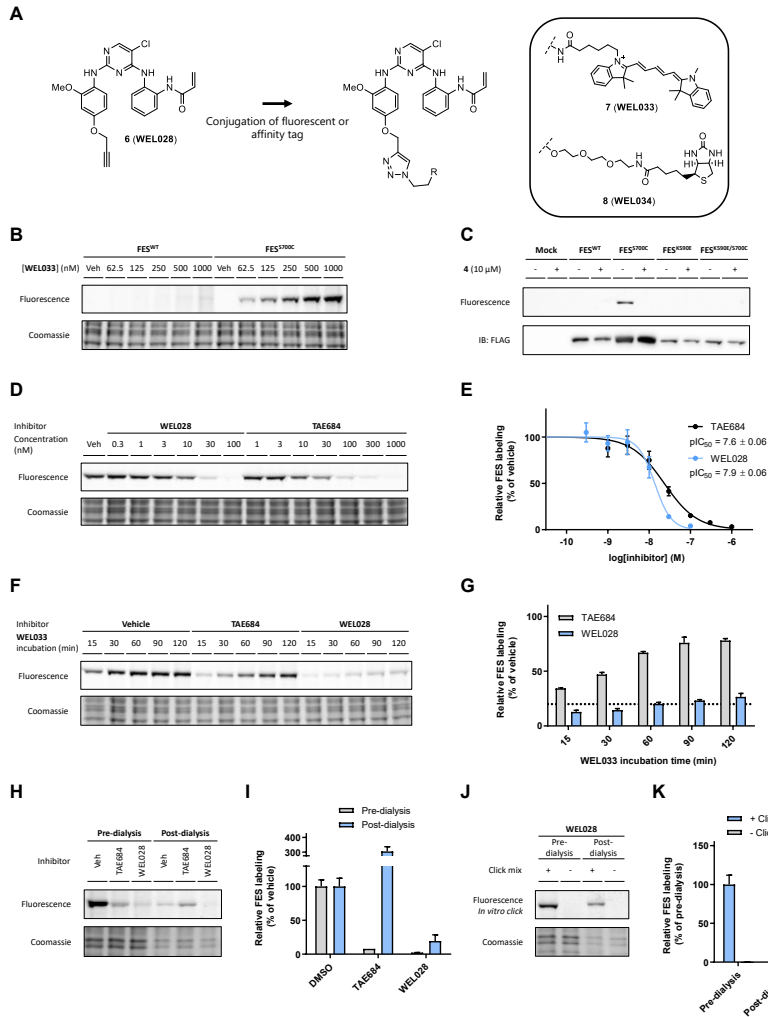


Figure 2.5 - Characterization of one-step probe WEL033 for visualization of FES^{S700C} target engagement.

(A) Design of one-step probes WEL033 (Cy5-conjugate) and WEL034 (biotin-conjugate) from two-step probe WEL028. (B) Dose-dependent labeling of full-length FES^{S700C} but not FES^{WT} by WEL033 (indicated concentration, 30 min, rt) in HEK293T lysate. (C) Labeling by WEL033 is specific, exclusive for FES^{S700C} and dependent on catalytic lysine 590. Lysates were incubated with vehicle or **4** (10 μM, 30 min, rt), followed by WEL033 (250 nM, 30 min, rt). Protein expression was verified by immunoblot against a C-terminal FLAG-tag. (D, E) Visualization of FES^{S700C} target engagement by WEL028 and TAE684. Lysate was pre-incubated with WEL028 or TAE684 (indicated concentration, 30 min, rt), followed by incubation with probe WEL033 (250 nM, 30 min, rt). Band intensities were normalized to vehicle-treated control. (F, G) WEL033 outcompetes TAE684 but not WEL028 binding over time. Lysate was incubated with vehicle, TAE684 or WEL028 at the respective IC₈₀-concentration (20% remaining activity; TAE684: 82 nM, WEL028: 27 nM; 30 min, rt), followed by incubation with WEL033 (1 μM, indicated time, rt). Band intensities were normalized to vehicle-treated control at same time point. (H, I) Sustained FES^{S700C} inhibition by WEL028 but not TAE684 after overnight dialysis. Lysates were treated with vehicle, TAE684 or WEL028 as in panel F. Pre-dialysis samples were directly flash-frozen after incubation and residual lysate was dialyzed overnight at 4 °C. Pre- and post-dialysis samples were then labeled by WEL033 (250 nM, 30 min, rt). Band intensities were normalized to vehicle-treated control. (J, K) Two-step labeling of WEL028-bound FES^{S700C} before and after dialysis. Samples were processed as in panel H, but conjugated to BODIPY-azide using click chemistry (2 eq., 30 min, rt). Band intensities were normalized to pre-dialysis control. Data represent means ± SEM (N = 3).

TAE684 (Figure 2.5H, I). Direct visualization of the covalent adduct using click chemistry confirmed sustained engagement of FES^{S700C} by WEL028 post-dialysis (Figure 2.5J, K). Of note, the labeling intensity of vehicle-treated control samples was decreased after dialysis, possibly due to protein degradation or aggregation. Interestingly, the labeling intensity TAE684-treated FES^{S700C} post-dialysis was higher than the vehicle-treated control, indicating that this reversible ligand may induce a conformational change that increases protein stability.

Subsequently, it was investigated whether WEL028 could also engage FES^{S700C} in living cells. To this end, HEK293T cells overexpressing FES^{WT} or FES^{S700C} were incubated with various concentrations of WEL028, after which cells were harvested and lysed. WEL028-labeled proteins were then visualized using click chemistry. Dose-dependent labeling of FES^{S700C} was observed (Figure 2.6A), which indicates that WEL028 is cell-permeable and can serve as a two-step probe in living cells. Interestingly, the potency of WEL028 *in situ* ($pIC_{50} = 7.6 \pm 0.05$, Figure 2.6B) is similar to its potency *in vitro* ($pIC_{50} = 7.9 \pm 0.06$, Figure 2.5E), which demonstrates the benefit of an irreversible binding mode with lower susceptibility to high intracellular ATP concentrations.

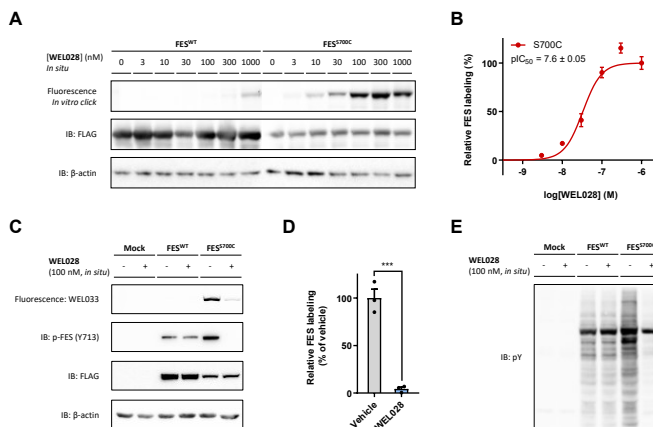


Figure 2.6 – WEL028 engages FES^{S700C} in live cells, blocks FES autophosphorylation and reduces downstream tyrosine phosphorylation. (A, B) WEL028 engages recombinantly expressed FES^{S700C} in live cells. HEK293T cells were transfected with FES^{WT} and FES^{S700C} and 48 h post-transfection, cells were treated with WEL028 (indicated concentration, 1 h, 37 °C). Cells were harvested, lysed and WEL028-labeled proteins were visualized by conjugation to Cy5-azide using click chemistry. Protein expression was verified by immunoblot against a C-terminal FLAG-tag and β -actin served as loading control. Band intensities were normalized to highest concentration. (C, D) WEL028 blocks FES^{S700C} but not FES^{WT} autophosphorylation *in situ*. U2OS cells were transfected as in panel A and treated with WEL028 (100 nM, 1 h, 37 °C). Lysates were incubated with WEL033 (250 nM, 30 min, rt) to post-label residual active FES. Autophosphorylation at Y713 was visualized by immunoblot. Band intensities were normalized to vehicle-treated control. (E) WEL028 reduces global tyrosine phosphorylation downstream of FES^{S700C} but not FES^{WT}. Samples were processed as in D and tyrosine phosphorylation was visualized by immunoblot using anti-phosphotyrosine antibody (4G10). Data represent means \pm SEM (N = 3). Statistical analysis was performed using two-tailed t-test: *** $P < 0.001$.

To determine whether WEL028 also blocked FES-mediated phosphorylation *in situ*, FES^{WT}- or FES^{S700C}-overexpressing cells were incubated with WEL028 (100 nM, 1 h), followed by lysis and visualization of residual FES activity by WEL033 (Figure 2.6C). Under these conditions, WEL028 showed >90% engagement of FES^{S700C} (Figure 2.6D). Autophosphorylation of Y713 on the activation loop of FES is a hallmark for its kinase activity.^{14,15,41} Consequently, immunoblot analysis using a phospho-specific antibody for pY713 revealed that WEL028 fully abolished autophosphorylation of FES^{S700C} but not FES^{WT}. Furthermore, a drastic increase in the global phosphotyrosine profile was observed upon overexpression of FES^{WT} or FES^{S700C} (Figure 2.6E), which was almost completely blocked by acute inactivation of FES^{S700C} by WEL028. This indicates that the target engagement as measured by gel-based ABPP assay correlates with the functional activity of FES^{S700C} as determined in the biochemical and immunoblot assays.

Applicability to other kinases

To investigate the broader applicability of this strategy, it was explored whether the complementary probes could also target other kinases than FES in a similar chemical genetic strategy. To this end, a cysteine residue was introduced at the DFG-1 position (S701) of the kinase FER, which together with FES forms a unique kinase subfamily with high structural and functional similarity.¹¹ FER^{WT} and FER^{S701C} were recombinantly expressed, purified and biochemically characterized and exhibited similar affinity for ATP ($K_M = 11 \mu\text{M}$ for FER^{WT} and $K_M = 3.5 \mu\text{M}$ for FER^{S701C}; Supplementary Figure 2.6A). Profiling the panel of synthesized compounds on FER^{WT} and FER^{S701C} (Supplementary Table 2.3 and Supplementary Figure 2.6B-F) revealed that WEL028 potently targeted mutant but not wild-type FER ($pIC_{50} = 6.3 \pm 0.36$ for FER^{WT}, $pIC_{50} = 8.2 \pm 0.06$ for FER^{S701C}). Moreover, incubation of cell lysates from HEK293T cells overexpressing FER^{S701C} with WEL033 resulted in dose-dependent labeling that was prevented by pre-incubation with inhibitor **4** (Figure 2.7A, B).

In addition, cysteine mutants were generated of two other tyrosine kinases with lower sequence similarity and different amino acids at the DFG-1 position: LYN and PTK2 (resulting in LYN^{A384C} and PTK2^{G536C}, respectively). Overexpression of these kinases and incubation with complementary probes exhibited dose-dependent, mutant-specific labeling (Figure 2.7C-F). Interestingly, no labeling was observed for LYN^{A384C} with one-step probe WEL033 (data not shown), which may indicate that the bulky Cy5 fluorophore prohibits active site binding in this particular case. Finally, it was investigated whether PAK4, a kinase belonging to the serine/threonine kinase subgroup, could also be sensitized to the complementary probes in a similar fashion. Strikingly, also this corresponding mutant PAK4^{S457C} but not PAK4^{WT} was dose-dependently labeled by WEL033 (Figure 2.7G, H). In conclusion, these results suggest that the here presented chemical genetic strategy is not exclusively applicable to tyrosine kinases closely related to FES, but can also be employed to visualize target engagement of kinases with lower structural and functional similarity.

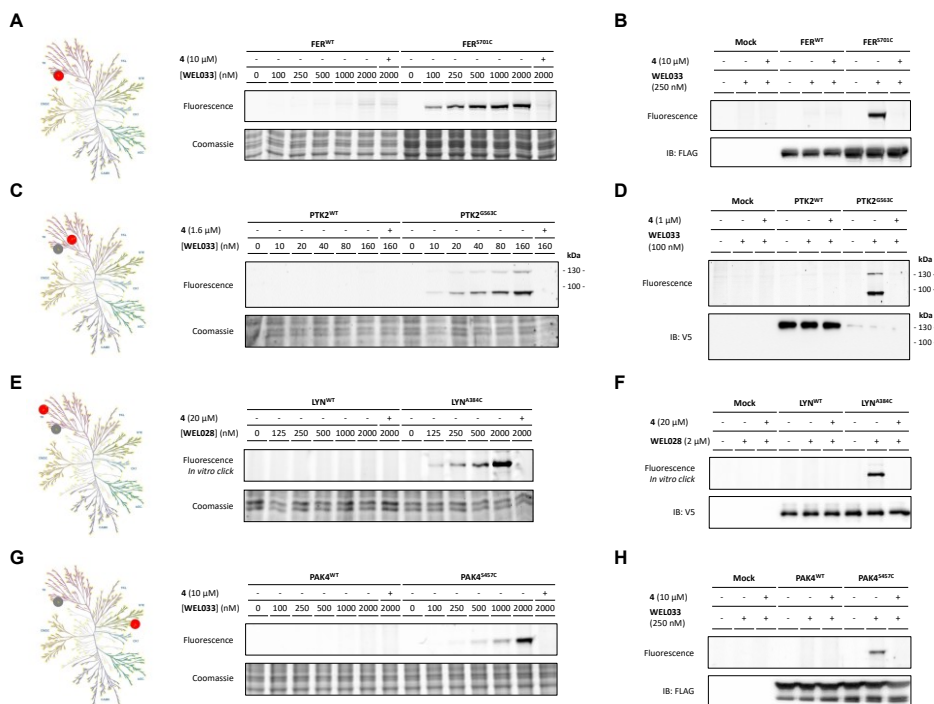


Figure 2.7 - Applicability of chemical genetic strategy on various kinases with DFG-1 residues mutated into cysteine. (A, C, E, G) Dose-dependent labeling of DFG-1 cysteine mutants but not wild-type kinases by complementary probes. Recombinantly expressed kinase (A: FER, C: PTK2, E: LYN, G: PAK4) in HEK293T cell lysate was pre-incubated with vehicle or **4** (indicated concentration, 30 min, rt), followed by incubation with probe (A, C, G: one-step probe WEL033, E: two-step probe WEL028; indicated concentrations, 30 min, rt). For E, samples were then conjugated to Cy5-azide using click chemistry. Homology-based similarity of corresponding kinase (red) to FES (gray) is visualized in kinome tree illustrations. **(B, D, F, H)** Labeling by complementary probes is specific and exclusive for DFG-1 cysteine mutants. Samples were treated as aforementioned, but at optimal probe concentration (indicated, 30 min, rt). Protein expression was verified by immunoblot against a C-terminal FLAG-tag or V5-tag. Of note, PTK2 migrated a two bands of which only the upper band was detected by immunoblot. Kinome illustrations were rendered using KinMap (www.kinhub.org/kinmap), reproduced courtesy of Cell Signaling Technology, Inc. (www.cellsignal.com).

Discussion and conclusion

In this chapter, a novel chemical genetic strategy is presented to study kinase target engagement, combining an engineered, mutant kinase with the design and application of complementary covalent probes. The field of chemical genetics has previously generated tools to aid in kinase target validation⁴², such as the “analog-sensitive” (AS) technology, where the gatekeeper residue is changed into a less bulky residue, enabling the kinase of interest to accommodate bulky ATP analogs in its active site.^{43,44} However, these analogs do not form covalent adducts with the kinase and therefore do not readily allow visualization of target engagement. Furthermore, mutagenesis of gatekeeper residues often results in impaired catalytic activity.⁴⁵ In addition, the disadvantageous pharmacokinetic properties of ATP analogs used in the AS technology, such as a short *in*

in vivo half-life, limit their applicability for target validation studies.⁴⁶ The concept of “covalent complementarity” is based on mutagenesis of the gatekeeper³⁰ or gatekeeper+6³² residue into a cysteine to function as nucleophile. Although this allows the development of covalent probes and thereby target engagement studies, a second mutation in the active site was required to improve gatekeeper cysteine reactivity or compound selectivity and potency.^{30,31} This is particularly challenging when moving to an endogenous model system, since it would involve CRISPR/Cas9 gene editing of two independent point mutations.

Importantly, the introduced nucleophilic cysteine needs to be functionally silent, *i.e.* it should not affect catalytic activity and substrate binding. Site-directed mutagenesis of the DFG-1 position into a cysteine fulfilled this criterion. FES^{S700C} retained full catalytic activity and exhibited an identical substrate and SH2 binding profile as FES^{WT}. FES^{S700C} showed a minor increase in ATP binding affinity, but this difference in K_M is unlikely to have any consequences at physiologically relevant ATP concentrations, which are typically in the millimolar range.³⁴ Although nearly 10% of all known kinases have a native DFG-1 cysteine residue, many kinases harboring a DFG-1 cysteine showed limited or no inhibition by WEL028 (Table 2.2, Supplementary Figure 2.3 and 2.4), suggesting that the choice of the chemical scaffold constitutes an additional selectivity filter. An acrylamide group was selected as the electrophile to react with the intended cysteine, since it exhibits sufficient reactivity towards cysteines only when appropriately positioned for a Michael addition reaction and has limited reactivity to other intracellular nucleophiles.⁴⁷ This may additionally prevent non-specific interactions with targets outside of the kinase cysteinome. Given the favorable selectivity profile and cellular permeability of WEL028, the diaminopyrimidine scaffold is a useful addition to the toolbox of covalent complementary probes applied in chemical genetic strategies, which previously consisted of mainly quinazolines and pyrazolopyrimidines.^{30,32}

The presented chemical genetic strategy is not limited to FES, but can be applied to other kinases, either structurally related (FER) or more distinct (LYN, PTK2 and PAK4). Complementary probes dose-dependently labeled the corresponding DFG-1 cysteine mutants (Figure 2.7), whereas the kinome selectivity screen (Supplementary Figure 2.3) indicated that wild-type FER, LYN, PTK2 and PAK4 are not potently targeted by WEL028 ($pIC_{50} < 6$ for FER, LYN and PAK4, $pIC_{50} = 6.4 \pm 0.06$ for PTK2). For follow-up target validation studies, however, more thorough biochemical profiling is necessary to establish the selectivity of WEL028 for the mutant over the wild-type kinase of interest, which was in this study only performed for FER (Supplementary Table 2.3). Nevertheless, the selectivity acquired by combining DFG-1 cysteine mutants and a complementary probe enables acute, pharmacological inhibition without the need for extensive hit optimization programs to identify compounds of adequate potency and selectivity for each kinase individually.

In conclusion, the DFG-1 residue in the kinase active site was identified as an excellent position for mutagenesis into a reactive cysteine without affecting kinase function. Complementary, covalent probes WEL028 and WEL033 allow for visualization of target engagement *in vitro* as well as in living cells. Additionally, this chemical genetic strategy can be applied to various kinases in different subfamilies. The favorable selectivity profile of WEL028 makes it a useful tool for acute inactivation of kinase activity *in situ*, especially in combination with functional assays to provide insight in kinase function. This could prove especially useful for kinases with poorly characterized substrates or for kinases with limited availability of selective ligands. It is thus envisioned that the presented methodology could provide powerful tools to visualize target engagement and to study poorly characterized kinases, thereby aiding in their validation as therapeutic target.

Acknowledgments

Riet Hilhorst, Tim van den Hooven and Rob Ruijtenbeek are kindly acknowledged for microarray measurements and helpful discussions, Nienke M. Prins, Jessica Schlachter and Joost. A. P. M. Wijnakker for cloning and expression of constructs, Bogdan I. Florea for mass spectrometry analysis, Eelke B. Lenselink for docking studies and Hans den Dulk for valuable general advice. The Cloning & Purification Facility (Geri F. Moolenaar and Nora Goosen) and Hans van den Elst are acknowledged for technical support.

Experimental procedures - Biochemistry

General

All chemicals were purchased at Sigma Aldrich, unless stated otherwise. DNA oligos were purchased at Sigma Aldrich or Integrated DNA Technologies and sequences can be found in Supplementary Table 2.1. Cloning reagents were from Thermo Fisher. TAE684 was purchased at Selleckchem. Cy5-azide and BODIPY-azide were previously synthesized in-house and characterized by NMR and LC-MS.⁴⁸ All cell culture disposables were from Sarstedt. Bacterial and mammalian protease inhibitor cocktails were obtained from Amresco.

Cloning

Full-length human cDNA encoding FES and PAK4 was obtained from Source Bioscience. pDONR223-constructs with full-length human cDNA of FER, LYN and PTK2 were a gift from William Hahn & David Root (Addgene Human Kinase ORF Collection). For bacterial expression constructs, human FES cDNA encoding residues 448-822 (protein MW = 45.8 kDa) or human FER cDNA encoding residues 448-820 (protein MW = 46.2 kDa) was amplified by PCR and cloned into expression vector pET1a in frame with an N-terminal His₆-tag and Tobacco Etch Virus (TEV) recognition site. Eukaryotic expression constructs of FES, FER and PAK4 were generated by PCR amplification and restriction/ligation cloning into a pcDNA3.1 vector, in frame with a C-terminal FLAG-tag. Eukaryotic expression constructs of LYN and PTK2 were generated using Gateway™ recombinational cloning into a pDest40 vector, in frame with a C-terminal V5-tag, according to recommended procedures (Thermo Fisher). Point mutations were introduced by site-directed mutagenesis and all plasmids were isolated from transformed XL10-Gold competent cells (prepared using *E. coli* transformation buffer set; Zymo Research) using plasmid isolation kits following the supplier's protocol (Qiagen). All sequences were verified by Sanger sequencing (Macrogen).

Supplementary Table 2.1 – List of oligonucleotide sequences.

ID	Name	Sequence	ID	Name	Sequence
P1	FES_SH2-KD_forw	AGGGCCCATGGGGATCCGGAGGTGCAAGAAGC	P16	FER_SH2-KD_forw	CGTCTCCCATGATCTCCATCAGTGAGAAGCCTT
P2	FES_SH2-KD_rev	CACCTCGAGCACCGGCGCTTACCAGTCCCGTTTCGGAT	P17	FER_SH2-KD_rev	CACCGCGCGCCTTATGTGAGTTTCTCTTGAT
P3	FES_I567C_forw	GTGTGGTGGAGCAGGTGGACGGGGAACTTT	P18	FER_S701C_forw	AATGTTCTGAAAATCTGTGACTTTGGAATG
P4	FES_G570C_forw	GAGCAGATGGACGGTGCACCTTTGGCGAAGTG	P19	FER_S701C_rev	ACATCCAAAGTCACAGATTTCCAGAATTT
P5	FES_V575C_forw	GGGAACCTTGGCGAATGCTCAGCGGACGCTG	P20	FER_forw	AGCCGTCTCGGTACCGCGCCACCATGGGTTGGGAGTGACC
P6	FES_L638C_forw	TACATCTGATGGAAGTGTGTGCAAGGGGGCGAC	P21	FER_rev	CATTCTAGATCACTCGAGACCGGTTGTGATTTCTCTGA
P7	FES_G642C_forw	GAGCTGTGCGAGGGGTGGCACTTCTGACCTTC	P22	LYN_A384C_forw	GTCACTCATGTGCAAGATCTGTGATTTGGCCCTGCT
P8	FES_T646C_forw	GGGGGGCGACTTCTGCTTCTCCGACCGGAG	P23	LYN_A384C_rev	AGCAAGGCCAAAATCACAGATTTCCACATGAGTGAC
P9	FES_N688C_forw	GACCTGGCTGCTGGTGTGCTGCTGGTGACAGAG	P24	PTK2_G563C_forw	GATTGTGTAATAATGATGGACTTTGGTCTCCCGATATATGGAA
P10	FES_L690C_forw	GCTGCTGGAACTGCTGCTGCTGACAGAGAAGAAT	P25	PTK2_G563C_rev	TTCCATATATCGGGGAGAGACCAAGTCGATAATTTACACAATC
P11	FES_S700C_forw	AATGCTCTGAAGATCTGTGACTTTGGGATGCTC	P26	PAK4_forw	CTTAAGCTTTGTACCGCGCCACCATGTTGGGAAGGAGGAACA
P12	FES_forw	CTTAAGCTTTGTACCGCGCCACCATGTTGGGCTTCTCTGAGC	P27	PAK4_rev	CATTCTAGATCACTCGAGACCGGTTCTGGTGGGTTCTGGCGCA
P13	FES_rev	CATTCTAGATCACTCGAGACCGTCCGATCCGCTTTCGGAT	P28	PAK4_S457C_forw	GGCAGGGTGAAGCTGTGTGACTTTGGTCTGCG
P14	FES_K590E_forw	ACCCCTGGCGGGTGGAGTCTGTGTGAGAGACG	P29	PAK4_S457C_rev	CGCAAGCCAAAAGTCCACAGCTTCCACCTGCG
P15	FES_K590E_rev	CGTCTCTGACAGACTCCACCGCCACCAAGGT			

Protein expression and purification

Bacterial expression constructs were transformed into *E. coli* BL21(DE3) co-transformed with a pCDFDuet-1 vector encoding *Yersinia* phosphatase YopH (kindly provided by prof. dr. Kuriyan).³⁵ Cells were grown in Luria Broth (LB) medium containing 50 µg/mL kanamycin and 50 µg/mL streptomycin at 37 °C to an OD₆₀₀ of 0.4. The cultures were cooled on ice and protein expression was induced by addition of isopropyl-β-D-thiogalactopyranoside (IPTG, 50 µM; 16 h, 18 °C, 180 rpm). Cultures (typically 10 mL per mutant) were centrifuged (1000 g, 10 min, 4 °C) and washed with 1 mL physiological salt solution (0.9% (w/v) NaCl). The pellet was then resuspended in 400 µL lysis buffer (100 mM NaH₂PO₄ pH 8.0, 500 mM NaCl, 10% glycerol, 0.5 mM tris(2-carboxyethyl)phosphine (TCEP), 20 mM imidazole, 1 x bacterial protease inhibitor cocktail) and cells were lysed by sonication on ice (15 cycles of 4" on, 9.9" off at 25% maximum amplitude; Vibra Cell (Sonics)). MgCl₂ and OmniCleave (Epitcentre) were added to final concentrations of 10 mM and 125 U/mL respectively, and lysates were

incubated for 10 min at rt. Meanwhile, 200 μ L Nickel Magnetic Beads (BiMake) were homogenized by vortexing and washed in lysis buffer (3 x 200 μ L) using a magnetic separator. Lysate was added to beads and incubated for 1 h at 4 °C with vigorous shaking. Beads were then washed with lysis buffer containing 75 mM imidazole (3 x 400 μ L), after which the beads were transferred to a clean Eppendorf tube. Protein was phosphorylated on beads by addition of autophosphorylation buffer (50 mM HEPES pH 7.5, 500 mM NaCl, 5% glycerol, 10 mM dithiothreitol (DTT), 10 mM Na_3VO_4 , 2 mM $(\text{NH}_4)_2\text{SO}_4$, 10 mM MgCl_2 , 5 mM MnCl_2 , 2 mM ATP) and vigorous shaking for 2 h at rt. Beads were subsequently washed with lysis buffer containing 20 mM imidazole (3 x 400 μ L), after which the protein was eluted in lysis buffer containing 250 mM imidazole (2 x 200 μ L). The elution fractions were combined, applied onto a 10 kDa cutoff centrifugal filter unit (Amicon) and centrifuged (14,000 g , 10 min, 4 °C). The retentate was reconstituted in 100 μ L protein storage buffer (10 mM HEPES pH 7.5, 500 mM NaCl, 5% glycerol, 10 mM DTT), aliquoted and stored at -80 °C. Protein concentration was measured using Qubit fluorometric quantitation (Thermo Fisher) and protein purity was monitored by SDS-PAGE and Coomassie staining.

***In vitro* TR-FRET kinase assay**

Assays were performed in white ProxiPlate-384 Plus™ 384-well microplates (Perkin Elmer). Incubation steps were performed at 21 °C in kinase reaction buffer (50 mM HEPES pH 7.5, 150 mM NaCl, 10 mM MgCl_2 , 1 mM EGTA, 2 mM DTT, 0.01% Tween-20). Purified proteins were diluted in kinase reaction buffer prior to use. All measurements were performed in triplicate.

Plates were read on a TECAN Infinite M1000 Pro plate reader, using fluorescence top reading settings ($\lambda_{\text{ex}} = 320/20$ nm, $\lambda_{\text{em,donor}} = 615/10$ nm, $\lambda_{\text{em,acceptor}} = 665/10$ nm, 100 μ s integration time, 50 μ s lag time). Emission ratios were calculated as fluorescence of acceptor / fluorescence of donor. Z' -factors were determined for each individual assay plate as $Z' = 1 - 3(\sigma_{\text{pc}} + \sigma_{\text{nc}})/(\mu_{\text{pc}} - \mu_{\text{nc}})$, with σ = standard deviation and μ = mean of measured replicates, wild-type or untreated samples as positive control (pc) and samples incubated with no ATP as negative control (nc). All plates met the requirement of $Z' > 0.7$. Emission ratios were corrected for background signal of samples incubated with no ATP. Corrected ratios were averaged and normalized to wild-type or untreated signal as 100% reference.

For relative activity determination of mutants, purified wild-type or mutant FES (12.5 ng per well) or FER (5 ng per well) was incubated with 50 nM *ULight*-TK peptide (Perkin Elmer) and 100 μ M ATP for 60 min at 21 °C in a total volume of 10 μ L. The reaction was quenched by addition of 10 μ L development solution (20 mM EDTA, 4 nM Europium-anti-phosphotyrosine antibody (PT66, Perkin Elmer) and incubated for 60 min before fluorescence was measured.

For K_M determinations, assay was performed as described above, but with variable ATP concentrations in a dilution series of 1 mM to 100 nM. For IC_{50} determinations, serial dilutions of inhibitor were prepared in DMSO, followed by further dilution in kinase reaction buffer. The inhibitors were premixed with peptide and ATP (5 μ M final concentration, unless indicated otherwise), after which wild-type or mutant kinase was added to initiate the reaction. The final DMSO concentration during the reaction was 1%. K_M and IC_{50} curves were fitted using GraphPad Prism® 7 (GraphPad Software Inc.).

PamChip® microarray assay

Kinase activity assay

Kinase activity profiles were determined using the PamChip® 12 protein tyrosine (PTK) peptide microarray system (PamGene International B.V.) according to the instructions of the manufacturer, essentially as described⁴⁹ with the exception that arrays were blocked with 2% BSA and the assay buffer contained EDTA instead of EGTA. Sample input was 0.25 ng purified FES (wild-type or S700C) per array and [ATP] = 400 μ M. For arrays with inhibitor, recombinant FES was pre-incubated in assay mix without ATP with vehicle or WEL028 (100 nM, 30 min, on ice, 2% final DMSO concentration).

SH2 domain binding assay

PamChip® protein tyrosine kinase (PTK) arrays were blocked by pumping a 2% BSA solution up and down through the array (30 μ L, 15 min, 2 cycles/min). After three washing steps, the arrays were pre-phosphorylated by incubation with 1.5 pmol of (His₆-tagged) JAK2 catalytic domain for 60 cycles in kinase assay buffer with 0.01% BSA. After 3 washing steps, the arrays were incubated with 0.75 μ g of FES (wild-type or S700C) in PBS/0.1% Tween-20 supplemented with 0.01% BSA. Incubations without FES served as negative control. After 3 washing steps, binding of FES was visualized by incubation with Alexa Fluor 488 labeled anti-penta-His antibody (Qiagen, #1019199), 1 μ L per array, in PBS/0.01% Tween-20. Peptide phosphorylation of JAK2 was detected with the same anti p-Tyr antibody as used in the PTK activity assay. After incubation for 30 min (2 cycles/min), arrays were washed, and images taken at different exposure times.

Data analysis and quality control

Data quantification of the images at all exposure times and reaction times and visualization of the data were performed using BioNavigator software (PamGene International B.V.). Post-wash signals (local background subtracted) were used. After signal quantification and integration of exposure times, signals were log₂-transformed for visualization. Peptides with no ATP-dependent signal were excluded from analysis. Identification of peptides that were significantly different between conditions was performed using a Mixed Model statistical analysis. Substrate consensus motif was generated using Enologos (<http://www.benoslab.pitt.edu>).

Selectivity profiling

Selectivity profiling assays were performed by the Invitrogen SelectScreen™ Services. A complete list of tested kinases can be found in Supplementary Figure 2.3, detailed assay procedures are described in SelectScreen Assay Conditions documents located at www.invitrogen.com/kinaseprofiling. All kinases were pre-incubated for 1 h at indicated concentrations of inhibitor. The concentration of ATP was selected to be equal to the K_M , unless indicated otherwise. An initial screen was performed on 279 kinases at single dose of 1 μ M. All available kinases with native cysteine residues in the active site were included in this panel. Kinases showing >50% inhibition at 1 μ M were further profiled in dose-response experiments in a 10-point dilution series of 10 μ M to 0.5 nM.

Docking studies

All structure-based modeling was performed in Schrödinger Suite 2017-2 (Schrödinger). The docking of compound **4** was based on the crystal structure of FES co-crystallized with TAE684 (PDB: 4e93)²³, which was prepared by the protein preparation wizard. Prior to docking, the Ser700 residue was manually changed into a cysteine. Subsequently, compound **4** was aligned to TAE684 on the basis of the diaminopyrimidine (both ligands share the same kinase/hinge binding moiety). This pose was optimized using an exhaustive hierarchical optimization procedure available in Prime.⁵⁰ The acrylamide warhead was found in proximity of Cys700 and the ligand was then covalently attached to this residue, followed by another round of hierarchical optimization.⁵⁰ Figures were rendered using PyMOL Molecular Graphics System (Schrödinger).

MS identification of covalent inhibitor-peptide adduct

Purified FES^{S700C} (1.2 μ g in 38 μ L) was treated with vehicle or WEL028 (2 μ L of 20x concentrated stock in DMSO, 1 μ M final concentration) for 30 min at rt. The reaction was quenched by addition of 3x Laemmli buffer (20 μ L), incubated for 5 min at 95 °C and sample (400 ng, 20 μ L) was resolved by SDS-PAGE on a 10% polyacrylamide gel (200 V, 60 min). Gel was stained using Coomassie Brilliant Blue R-250, bands were cut out of gel into small blocks and then destained in 500 μ L of 50% MeOH in 100 mM NH₄HCO₃ pH 8.0 for 10 min at rt. Acetonitrile (500 μ L) was added for gel blocks dehydration, after which gel blocks were digested with sequencing-grade trypsin (Promega) in 250 μ L trypsin buffer (100 mM Tris pH 7.5, 100 mM NaCl, 1 mM CaCl₂, 10% acetonitrile) overnight at 37 °C with vigorous shaking. The pH was adjusted with formic acid to pH 3, after which the sample was diluted in extraction solution

Chapter 2

(65% acetonitrile/35% MilliQ) and concentrated in a SpeedVac concentrator. Samples were subsequently desalted using stage tips with C₁₈ material and processed as previously described.⁵¹

Tryptic peptides were analyzed on a Surveyor nano-LC system (Thermo) hyphenated to a LTQ-Orbitrap mass spectrometer (Thermo) as previously described.⁵² General mass spectrometric conditions were: electrospray voltage of 1.8 kV, no sheath and auxiliary gas flow, ion transfer tube temperature 150 °C, capillary voltage 41 V, tube lens voltage 150 V. Internal mass calibration was performed with polydimethylcyclsiloxane ($m/z = 445.12002$) and dioctyl phthalate ions ($m/z = 391.28429$) as lock mass. Samples of 10 μ l were separated via a trap-elute setup at 250 nL/min flow and analyzed by data-dependent acquisition of one full scan/ top 3 method. For shotgun proteomics, fragmented precursor ions measured twice within 10 s were dynamically excluded for 60 s and ions with $z < 2$ or unassigned charges were not analyzed. Peptide ID was determined with the Mascot search engine. A parent ion list of the m/z ratios of the active-site peptides was compiled and used for LC-MS/MS analysis in a data-dependent protocol. The parent ion was electrostatically isolated in the ion trap of the LTQ and fragmented by MS/MS. Data from MS/MS experiments were validated manually.

Inhibitor washout by dialysis

FES^{S700C}-overexpressing HEK293T lysate (396 μ L, 1.43 mg/mL) was incubated with vehicle, TAE684 or WEL028 (4 μ L of 100x concentrated stock in DMSO) at final concentrations corresponding to their respective IC₅₀ values (TAE684: 225 nM, WEL028: 231 nM) for 30 min at rt. One fraction (200 μ L) of the sample was immediately flash-frozen and stored at -80 °C until use. The remaining sample was transferred to a dialysis cassette (Slide-A-Lyzer™ Dialysis Cassette, 7K MWCO, 0.5 mL; Thermo Fisher), followed by dialysis in 200 mL PBS overnight at 4 °C. Pre- and post-dialysis samples were then incubated with probe WEL033 or conjugated to BODIPY-N₃ by CuAAC as aforementioned.

Cell culture

General cell culture

Cell lines were purchased at ATCC and were tested on regular basis for mycoplasma contamination. Cultures were discarded after 2-3 months of use. HEK293T (human embryonic kidney) and U2OS (human osteosarcoma) cells were cultured at 37 °C under 7% CO₂ in DMEM containing phenol red, stable glutamine, 10% (v/v) heat-inactivated newborn calf serum (Seradigm), penicillin and streptomycin (200 μ g/mL each; Duchefa). Medium was refreshed every 2-3 days and cells were passaged two times a week at 80-90% confluence. Cell viability was assessed by Trypan Blue exclusion and quantification using a TC20™ Automated Cell Counter (Bio-Rad).

Transfection

One day prior to transfection, HEK293T or U2OS cells were transferred from confluent 10 cm dishes to 15 cm dishes. Before transfection, medium was refreshed (13 mL). A 3:1 (m/m) mixture of polyethyleneimine (PEI; 60 μ g/dish) and plasmid DNA (20 μ g/dish) was prepared in serum-free medium and incubated for 15 min at rt. The mixture was then dropwisely added to the cells, after which the cells were grown to confluence in 72 h. Cells were then harvested by suspension in PBS, followed by centrifugation for 5 min at 200 g . Cell pellets were flash-frozen in liquid nitrogen and stored at -80 °C until sample preparation.

Inhibitor treatment in live cells

The term *in situ* is used to designate experiments in which live cell cultures are treated with inhibitor, whereas the term *in vitro* refers to experiments in which the inhibitor is incubated with cell lysates. Compounds were diluted in growth medium from a 1000x concentrated stock solution in DMSO. For *in situ* assays on live transfected cells, cells were transfected prior to treatment as described above. After 48 h, cells were treated with compound for 1 h. Cells were collected by suspension in PBS and

centrifuged (1000 *g*, 5 min, rt). Pellets were flash-frozen in liquid nitrogen and stored at -80 °C until use.

Preparation of cell lysates

Pellets were thawed on ice and suspended in lysis buffer (50 mM HEPES pH 7.2, 150 mM NaCl, 1 mM MgCl₂, 0.1% (w/v) Triton X-100, 2 mM Na₃VO₄, 20 mM NaF, 1 x mammalian protease inhibitor cocktail, 25 U/mL benzonase). Cells were lysed by sonication on ice (15 cycles of 4" on, 9.9" off at 25% maximum amplitude). Protein concentration was determined using Quick Start™ Bradford Protein Assay (Bio-Rad) and diluted to appropriate concentration in dilution buffer (50 mM HEPES pH 7.2, 150 mM NaCl). Lysates were aliquoted, flash-frozen and stored at -80 °C until use.

Probe labeling experiments

One-step labeling

For *in vitro* inhibition experiments, cell lysate (14 μL) was pre-incubated with inhibitor (0.5 μL, 29x concentrated stock in DMSO, 30 min, rt), followed by incubation with WEL033 (0.5 μL, 30x concentrated stock in DMSO, 30 min, rt). For *in situ* inhibition experiments, treated cell lysate (14.5 μL) was directly incubated with WEL033 (0.5 μL, 30x concentrated stock in DMSO, 30 min, rt). Final concentrations of inhibitors and/or WEL033 are indicated in the main text and figure legends. Reactions were quenched with 4x Laemmli buffer (5 μL, final concentrations 60 mM Tris pH 6.8, 2% (w/v) SDS, 10% (v/v) glycerol, 5% (v/v) β-mercaptoethanol, 0.01% (v/v) bromophenol blue) and boiled for 5 min at 95 °C. Samples were resolved by SDS-PAGE on a 10% polyacrylamide gel (180 V, 75 min). Gels were scanned using Cy3 and Cy5 multichannel settings (605/50 and 695/55 filters, respectively; ChemiDoc™ MP System, Bio-Rad). Fluorescence intensity was corrected for protein loading determined by Coomassie Brilliant Blue R-250 staining and quantified with Image Lab (Bio-Rad). IC₅₀ curves were fitted with Graphpad Prism® 7 (Graphpad Software Inc.).

Two-step labeling

For *in vitro* experiments, cell lysate (12 μL) was pre-incubated with inhibitor (0.5 μL, 25x concentrated stock in DMSO, 30 min, rt), followed by incubation with WEL028 (0.5 μL, 26x concentrated stock in DMSO, 30 min, rt). Meanwhile, "click mix" was prepared freshly by combining CuSO₄ (1 μL of 15 mM stock), sodium ascorbate (0.6 μL of 150 mM stock), THPTA (0.2 μL of 15 mM stock) and fluorophore-azide (0.2 μL of 150x concentrated stock in DMSO, 2 eq.). Click mix was added to the reaction, followed by incubation for 30 min at rt, after which the reaction was quenched and further processed as described above. For *in situ* inhibition experiments, WEL028-treated cells were lysed and directly incubated with click mix.

Immunoblot

Samples were resolved by SDS-PAGE as described above, but transferred to 0.2 μm polyvinylidene difluoride membranes by Trans-Blot Turbo™ Transfer system (Bio-Rad) directly after fluorescence scanning. Membranes were washed with TBS (50 mM Tris pH 7.5, 150 mM NaCl) and blocked with 5% milk in TBS-T (50 mM Tris pH 7.5, 150 mM NaCl, 0.05% Tween-20) for 1 h at rt.

Membranes were then incubated with either primary antibody in 5% milk in TBS-T (FLAG, V5, β-actin; o/n at 4 °C) or washed three times with TBS-T and incubated with primary antibody in 5% BSA in TBS-T (other antibodies, o/n at 4 °C). Membranes were washed three times with TBS-T, incubated with matching secondary antibody in 5% milk in TBS-T (1 h at rt) and then washed three times with TBS-T and once with TBS. Luminol development solution (10 mL of 1.4 mM luminol in 100 mM Tris pH 8.8 + 100 μL of 6.7 mM *p*-coumaric acid in DMSO + 3 μL of 30% (v/v) H₂O₂) was added and chemiluminescence was detected on ChemiDoc™ MP System.

Primary antibodies: monoclonal mouse anti-FLAG M2 (1:5000, Sigma Aldrich, F3156), monoclonal mouse anti-β-actin (1:1000, Abcam, ab8227), monoclonal mouse anti-V5 (1:5000, Thermo Fisher,

Chapter 2

R960-25), streptavidin-HRP (1:2000, Thermo Fisher, N100), polyclonal rabbit anti-phospho-FES Tyr713 (1:1000, Thermo Fisher, PA5-64504), monoclonal mouse anti-phosphotyrosine (4G10, 1:1000, Merck Millipore, 05-321). Secondary antibodies: goat anti-mouse-HRP (1:5000, Santa Cruz, sc-2005), goat anti-rabbit-HRP (1:5000, Santa Cruz, sc-2030).

Statistical analysis

All statistical measures and methods are included in the respective figure or table captions. In brief: all replicates represent biological replicates and all data represent means \pm SEM, unless indicated otherwise. Statistical significance was determined using Student's *t*-tests (two-tailed, unpaired) or ANOVA with Holm-Sidak's multiple comparisons correction. *** $P < 0.001$; ** $P < 0.01$; * $P < 0.05$; NS if $P > 0.05$. All statistical analyses were conducted using GraphPad Prism® 7 or Microsoft Excel.

Experimental procedures - Chemistry

General information

All reactions were performed using oven- or flame-dried glassware and dry solvents. Reagents were purchased from Sigma-Aldrich, Acros, and Merck and used without further purification unless noted otherwise. All moisture sensitive reactions were performed under an argon atmosphere. ^1H and ^{13}C NMR spectra were recorded on a Bruker AV 400 MHz spectrometer at 400.2 (^1H) and 100.6 (^{13}C) MHz or on a Bruker DMX-600 spectrometer at 600 (^1H) and 151 (^{13}C) MHz using CDCl_3 , $\text{DMSO}-d_6$ or MeOD as solvent. Chemical shift values are reported in ppm with tetramethylsilane or solvent resonance as the internal standard (CDCl_3 : δ 7.26 for ^1H , δ 77.16 for ^{13}C ; $\text{DMSO}-d_6$, δ 2.50 for ^1H , δ 39.52 for ^{13}C ; MeOD: δ 3.31 for ^1H , δ 49.00 for ^{13}C). Data are reported as follows: chemical shifts (δ), multiplicity (s = singlet, d = doublet, dd = double doublet, td = triple doublet, t = triplet, q = quartet, br = broad, m = multiplet), coupling constants J (Hz), and integration. HPLC purification was performed on a preparative LC-MS system (Agilent 1200 serie) with an Agilent 6130 Quadruple MS detector. High-resolution mass spectra were recorded on a Thermo Scientific LTQ Orbitrap XL. Compound purity (> 95% unless stated otherwise) was determined by liquid chromatography on a Finnigan Surveyor LC-MS system, equipped with a C18 column. Flash chromatography was performed using SiliCycle silica gel type SiliaFlash P60 (230–400 mesh). TLC analysis was performed on Merck silica gel 60/Kieselguhr F254, 0.25 mm. Compounds were visualized using KMnO_4 stain (K_2CO_3 (40 g), KMnO_4 (6 g) in water (600 mL)) or ninhydrin stain (ninhydrin (1.5 g) in *n*-butanol (100 mL) and 3 mL acetic acid).

Synthesis of tert-butyl (2-aminophenyl)carbamate (9)

To a solution of *o*-phenylenediamine (2.19 g, 20.2 mmol) in THF (20 mL) was dropwisely added a solution of $(\text{Boc})_2\text{O}$ (4.45 g, 20.4 mmol) in THF (5 mL). The reaction mixture was stirred at rt for 16 h, after which the mixture was concentrated under reduced pressure and the residue was taken up in a cold mixture of EtOAc/Petroleum ether (1:4 ratio, 15 mL), causing the product to precipitate. The precipitate was collected by filtration and dried to yield the title compound (2.43 g, 11.7 mmol, 58%). ^1H NMR (400 MHz, CDCl_3): δ 7.28 (s, 1H), 7.00 (td, J = 7.6, 1.5 Hz, 1H), 6.82 – 6.74 (m, 2H), 6.28 (s, 1H), 3.55 (s, 2H), 1.51 (s, 9H). ^{13}C NMR (101 MHz, CDCl_3): δ 154.0, 140.0, 126.3, 124.9, 120.5, 119.7, 117.7, 117.0, 80.6, 28.5, 28.4. Spectroscopic data are in accordance with those reported in literature.⁵³

Synthesis of tert-butyl (2-((2,5-dichloropyrimidin-4-yl)amino)phenyl)carbamate (10)

2,4,5-Trichloropyrimidine (1.18 g, 6.43 mmol) and DIPEA (1.68 g, 13.0 mmol) were dissolved in EtOH (25 mL). To the stirring solution was added compound **9** (1.35 g, 6.48 mmol), after which the reaction mixture was heated at reflux for 16 h. After TLC indicated depletion of starting material, the mixture was allowed to cool to rt and subsequently triturated with cold H_2O (20 mL), causing precipitation of the product. The precipitate was collected by vacuum filtration and dried to yield the title compound (2.11 g, 5.94 mmol, 92%). ^1H NMR (400 MHz, CDCl_3): δ 8.64 (s, 1H), 8.16 (s, 1H), 7.78 (dd, J = 8.1, 1.2 Hz, 1H), 7.32–7.27 (m, 1H), 7.24 – 7.16 (m, 2H), 6.59 (s, 1H), 1.53 (s, 9H). ^{13}C NMR (101 MHz, CDCl_3): δ 158.3, 157.4, 154.8, 154.7, 130.9, 130.2, 126.6, 126.5, 126.4, 124.9, 114.4, 82.0, 28.4.

Synthesis of N^1 -(2,5-dichloropyrimidin-4-yl)benzene-1,2-diamine (11)

Compound **10** (323 mg, 0.91 mmol) was dissolved in DCM (10 mL), after which TFA (3 mL) was slowly added. The reaction mixture was stirred at rt for 16 h and subsequently evaporated to dryness. The residue was dissolved in water, neutralized with aqueous K_2CO_3 to pH 7–8 and the resulting precipitate was collected by filtration and dried to yield the title compound (197 mg, 0.77 mmol, 85%). ^1H NMR (400 MHz, DMSO): δ 9.01 (s, 1H), 8.14 (s, 1H), 7.03 (d, J = 7.8 Hz, 1H), 6.95 (s, 1H), 6.72 (d, J = 8.0 Hz, 1H), 6.54 (t, J = 7.5 Hz, 1H), 4.92 (s, 2H). ^{13}C NMR (101 MHz, DMSO): δ 158.7, 158.2, 157.3, 154.4, 144.9, 128.4, 127.8, 121.7, 115.8, 115.6.

Synthesis of N-(2-((2,5-dichloropyrimidin-4-yl)amino)phenyl)acrylamide (12)

Compound **11** (250 mg, 0.98 mmol) was dissolved in DCM (5 mL) and cooled to 0 °C. Subsequently, DIPEA (127 mg, 0.98 mmol) was added and the reaction mixture was stirred for 10 min. Acryloyl chloride (93 mg, 1.03 mmol) dissolved in DCM (1 mL) was dropwisely added to the mixture. After stirring for 1 h, the reaction was quenched by addition of water (50 mL). The mixture was extracted with DCM (50 mL), the organic extract was dried over MgSO₄ and concentrated. The crude residue was purified by flash column chromatography (20% → 40% EtOAc in pentane) to yield the title compound (259 mg, 0.84 mmol, 85%). ¹H NMR (400 MHz, CDCl₃): δ 8.72 (d, *J* = 18.0 Hz, 2H), 8.13 (s, 1H), 7.72 (dd, *J* = 8.2, 1.3 Hz, 1H), 7.26 (td, *J* = 7.8, 1.5 Hz, 1H), 7.08 (td, *J* = 7.7, 1.4 Hz, 1H), 6.95 (dd, *J* = 8.0, 1.5 Hz, 1H), 6.44 (dd, *J* = 16.9, 1.4 Hz, 1H), 6.30 (dd, *J* = 16.9, 10.1 Hz, 1H), 5.77 (dd, *J* = 10.1, 1.6 Hz, 1H). ¹³C NMR (101 MHz, CDCl₃): δ 165.2, 157.8, 157.2, 154.7, 131.1, 129.8, 129.8, 129.0, 127.0, 126.3, 125.8, 125.0, 114.6.

Synthesis of 3-methoxy-4-nitrophenol (13)

3-Fluoro-4-nitrophenol (1.00 g, 6.4 mmol) was added to a solution of NaOMe in MeOH (0.5M, 14 mL), which was then heated at 50 °C for 12 h. Additional NaOMe in MeOH (0.5M, 14 mL) was added and the mixture was stirred at 50 °C until TLC indicated complete depletion of starting material. The mixture was diluted with H₂O (100 mL), neutralized with 3M HCl and the product was extracted with EtOAc (3 x 100 mL). The combined organic layers were washed with brine (100 mL), dried over MgSO₄ and evaporated to yield the title compound (1.01 g, 6.0 mmol, 94%). ¹H NMR (400 MHz, DMSO): δ 10.90 (s, 1H), 7.89 (d, *J* = 9.0 Hz, 1H), 6.60 (d, *J* = 2.4 Hz, 1H), 6.47 (dd, *J* = 9.0, 2.4 Hz, 1H), 3.86 (s, 3H). ¹³C NMR (101 MHz, DMSO): δ 164.4, 156.1, 131.2, 128.8, 108.0, 100.8, 56.8. Spectroscopic data are in accordance with those reported in literature.⁵⁴

Synthesis of 2-methoxy-1-nitro-4-(prop-2-yn-1-yloxy)benzene (14)

Compound **13** (600 mg, 3.6 mmol) and K₂CO₃ (1.47 g, 10.6 mmol) were taken up in DMF (10 mL) and heated at 60 °C for 30 min. The reaction mixture was cooled to rt, after which propargyl bromide (1.34 g, 9.0 mmol as 80% (w/w) solution in toluene) was added. The mixture was stirred at rt for 16 h, after which it was poured into ice water (200 mL) with stirring for 10 min. The formed precipitate was collected by filtration and dried under vacuum to yield the title compound (648 mg, 3.1 mmol, 88%), which was directly used in the next reaction.

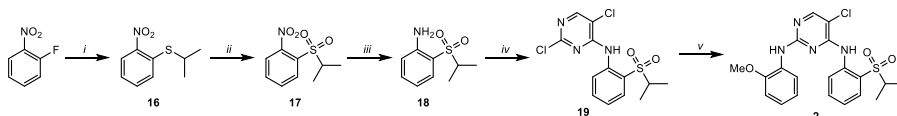
Synthesis of 2-methoxy-4-(prop-2-yn-1-yloxy)aniline (15)

Compound **14** (600 mg, 2.9 mmol) was dissolved in 1,4-dioxane (10 mL) and cooled to 0 °C. Cooled (0 °C) stannous chloride dihydrate (3.28 g, 14.5 mmol) in concentrated HCl (10 mL) was dropwisely added to the reaction mixture. After stirring for 16 h at rt, the mixture was basified to pH >9 by addition of NaOH pellets and extracted with DCM (4 x 10 mL). The organic layer was washed with brine (10 mL), dried over MgSO₄ and concentrated to dryness. The crude product was then purified by flash column chromatography (0% → 25% EtOAc in pentane) to yield the title compound (395 mg, 2.23 mmol, 77%). ¹H NMR (400 MHz, CDCl₃): δ 6.62 (d, *J* = 8.4 Hz, 1H), 6.52 (d, *J* = 2.6 Hz, 1H), 6.42 (dd, *J* = 8.5, 2.6 Hz, 1H), 4.61 (d, *J* = 2.4 Hz, 2H), 3.81 (s, 3H), 3.49 (s, 2H), 2.51 (t, *J* = 2.4 Hz, 1H). ¹³C NMR (101 MHz, CDCl₃): δ 151.0, 148.3, 130.8, 115.0, 105.9, 100.7, 79.3, 75.3, 56.8, 55.6.

Synthesis of N-(2-((5-chloro-2-((2-methoxy-4-(prop-2-yn-1-yloxy)phenyl)amino)pyrimidin-4-yl)amino)-phenyl)acrylamide (6, WEL028)

Compound **12** (46 mg, 0.15 mmol) and compound **15** (26 mg, 0.15 mmol) were taken up in isopropanol (5 mL), followed by the addition of *p*-TSA (28 mg, 0.15 mmol). The reaction mixture was heated under reflux for 16 h, after which it was concentrated under reduced pressure. The residue was taken up in saturated aqueous NaHCO₃ (20 mL) and the product was extracted with EtOAc (20 mL). The organic layer was dried over MgSO₄ and concentrated to dryness. The crude residue was purified by flash column chromatography (10% → 35% EtOAc in pentane) to yield the title compound (24 mg, 0.05 mmol, 36%). HRMS (ESI+) *m/z*: calculated for C₂₃H₂₀ClN₅O₃ ([M+H]): 450.13274; found: 450.13231.

^1H NMR (400 MHz, CDCl_3): δ 8.04 (d, J = 17.6 Hz, 2H), 7.87 (d, J = 8.9 Hz, 1H), 7.67 (s, 1H), 7.59 (t, J = 4.8 Hz, 2H), 7.38 (s, 1H), 7.29 (dd, J = 6.0, 3.5 Hz, 2H), 6.52 (d, J = 2.7 Hz, 1H), 6.40–6.31 (m, 2H), 6.16 (dd, J = 16.9, 10.3 Hz, 1H), 5.72 (d, J = 10.2 Hz, 1H), 4.65 (d, J = 2.4 Hz, 2H), 3.81 (s, 3H), 2.54 (t, J = 2.4 Hz, 1H). ^{13}C NMR (101 MHz, CDCl_3): δ 164.6, 157.8, 156.9, 153.5, 149.6, 131.6, 131.1, 130.8, 128.4, 127.2, 126.8, 126.4, 125.1, 123.2, 120.1, 105.1, 99.8, 78.9, 75.7, 56.5, 55.9.



Supplementary Scheme 2.1 – Synthesis of compound 2. Reagents and conditions: *i*) 2-propanethiol, K_2CO_3 , DMF, 100 °C, 98%. *ii*) *m*-CPBA, DCM, rt, 98%. *iii*) Pd/C, H_2 , MeOH, rt, quant. *iv*) 2,4,5-trichloropyrimidine, NaH, DMF/DMSO (9:1), 0 °C to rt, 37%. *v*) *o*-anisidine, Xantphos, Pd(OAc) $_2$, Cs_2CO_3 , 1,4-dioxane, 100 °C, 15%.

Synthesis of isopropyl(2-nitrophenyl)-sulfane (16)

1-Fluoro-2-nitrobenzene (9.88 g, 70 mmol) was dissolved in DMF (100 mL), followed by the addition of 2-propanethiol (5.47 g, 70 mmol) and K_2CO_3 (24.19 g, 175 mmol). The reaction mixture was heated at 100 °C for 16 h and subsequently cooled to rt. The mixture was diluted with H_2O (200 mL) and the product was extracted with EtOAc (3 x 200 mL). The organic layers were combined, dried over Na_2SO_4 and concentrated to yield the title compound (13.5 g, 68 mmol, 98%). ^1H NMR (400 MHz, CDCl_3): δ 8.12 (dd, J = 8.3, 1.5 Hz, 1H), 7.54 (ddd, J = 8.4, 7.1, 1.4 Hz, 1H), 7.48 (dd, J = 8.1, 1.4 Hz, 1H), 7.25 (ddd, J = 8.4, 7.1, 1.5 Hz, 1H), 3.58 (p, J = 6.6 Hz, 1H), 1.40 (d, J = 6.6 Hz, 6H). ^{13}C NMR (101 MHz, CDCl_3): δ 147.2, 136.5, 133.3, 128.3, 125.9, 124.9, 35.8, 22.4.

Synthesis of 1-(isopropylsulfonyl)-2-nitrobenzene (17)

Compound **16** (12.2 g, 61.3 mmol) was dissolved in DCM (120 mL), followed by portion wise addition of 3-chloroperbenzoic acid (31.6 g, 143 mmol). The reaction mixture was stirred at rt for 16 h. The mixture was diluted with 10% Na_2SO_3 (120 mL) and stirred for 10 min, after which layers were separated and the aqueous layer was extracted with DCM (3 x 120 mL). The organic layers were combined, washed with sat. NaHCO_3 (2 x 200 mL), brine (1 x 250 mL), dried over MgSO_4 and concentrated to yield the title compound (13.9 g, 60.7 mmol, 98%). ^1H NMR (400 MHz, CDCl_3): δ 8.15–8.07 (m, 1H), 7.86–7.72 (m, 3H), 4.04–3.95 (m, 1H), 1.41 (d, J = 6.8 Hz, 6H). ^{13}C NMR (101 MHz, CDCl_3): δ 134.8, 133.1, 132.2, 125.1, 56.0, 15.5.

Synthesis of 2-(isopropylsulfonyl)aniline (18)

Compound **17** (2.03 g, 8.85 mmol) was dissolved in MeOH (25 mL), followed by addition of Pd/C (93 mg, 0.87 mmol). The mixture was stirred under H_2 atmosphere for 16 h at rt, after which it was filtered over celite and concentrated to yield the title compound (1.76 g, 8.85 mmol, quant.). ^1H NMR (400 MHz, CDCl_3): δ 7.64 (dd, J = 8.0, 1.5 Hz, 1H), 7.40–7.30 (m, 1H), 6.80 (m, 1H), 6.74 (d, J = 8.2 Hz, 1H), 4.49 (s, 2H), 3.34 (m, 1H), 1.31 (d, J = 6.7 Hz, 6H). ^{13}C NMR (101 MHz, CDCl_3): δ 147.2, 135.2, 131.4, 118.3, 117.7, 117.7, 54.3, 15.4.

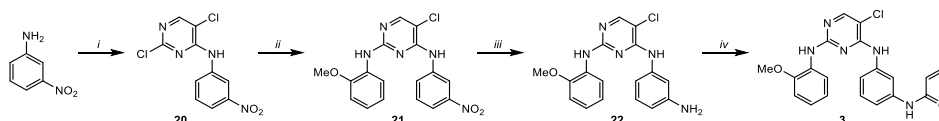
Synthesis of 2,5-dichloro-N-(2-(isopropylsulfonyl)phenyl)pyrimidin-4-amine (19)

A mixture of DMF/DMSO (9:1 ratio, 10 mL) was cooled to 0 °C, after which NaH (354 mg, 14.8 mmol) was added. Compound **18** (1.15 g, 5.77 mmol) was dissolved in DMF/DMSO (5 mL) and added to the reaction mixture. The suspension was stirred at 0 °C for 30 min, followed by the addition of 2,4,5-trichloropyrimidine (1.94 g, 10.6 mmol) diluted in DMF/DMSO (5 mL). The mixture was allowed to warm to rt and was then stirred for 16 h. The reaction mixture was diluted with H_2O (150 mL) and extracted with EtOAc (50 mL). The organic layer was washed with H_2O (5 x 50 mL), 5% LiCl (50 mL) and brine (50 mL), dried over MgSO_4 and subsequently concentrated. The crude residue was purified by flash column chromatography (0% → 20% EtOAc in pentane) to yield the title compound (777 mg, 2.24 mmol, 37%). ^1H NMR (400 MHz, CDCl_3): δ 10.06 (s, 1H), 8.62 (dd, J = 8.5, 1.2 Hz, 1H), 8.30 (s, 1H),

7.92 (dd, $J = 8.0, 1.7$ Hz, 1H), 7.75-7.71 (m, 1H), 7.37-7.27 (m, 1H), 3.26-3.16 (m, 1H), 1.31 (d, $J = 6.8$ Hz, 6H). ^{13}C NMR (101 MHz, CDCl_3): δ 157.9, 156.4, 155.7, 137.5, 135.3, 131.6, 124.7, 124.3, 122.8, 115.4, 56.2, 15.5.

Synthesis of 5-chloro- N^4 -(2-(isopropylsulfonyl)phenyl)- N^2 -(2-methoxyphenyl)pyrimidine-2,4-diamine (**2**)

Compound **19** (399 mg, 1.15 mmol), *o*-anisidine (142 mg, 1.15 mmol), XantPhos (67 mg, 0.12 mmol), $\text{Pd}(\text{OAc})_2$ (14 mg, 0.06 mmol) and Cs_2CO_3 (756 mg, 2.30 mmol) were dissolved in 1,4-dioxane (15 mL) and the resulting mixture was heated at 100 °C for 16 h. The reaction mixture was diluted with EtOAc (50 mL), filtered over celite and subsequently concentrated. The crude residue was purified by flash column chromatography (0% \rightarrow 30% EtOAc in pentane) to yield the title compound (77 mg, 0.18 mmol, 15%). HRMS (ESI+) m/z : calculated for $\text{C}_{20}\text{H}_{21}\text{ClN}_4\text{O}_3\text{S}$ ([M+H]): 433.10957; found: 433.10837. ^1H NMR (400 MHz, DMSO): δ 9.53 (s, 1H), 8.53 (d, $J = 8.4$ Hz, 1H), 8.37 (s, 1H), 8.25 (s, 1H), 7.82 (dd, $J = 8.0, 1.6$ Hz, 1H), 7.72 (dd, $J = 7.9, 1.5$ Hz, 1H), 7.66-7.62 (m, 1H), 7.38-7.29 (m, 1H), 7.14-7.02 (m, 2H), 6.92-6.88 (m, 1H), 3.79 (s, 3H), 3.47-3.40 (m, 1H), 1.15 (d, $J = 6.8$ Hz, 6H). ^{13}C NMR (101 MHz, DMSO): δ 158.6, 155.8, 155.3, 151.3, 138.5, 135.3, 131.4, 128.5, 124.6, 124.5, 124.0, 123.9, 123.5, 120.6, 111.6, 105.1, 56.0, 55.3, 15.3.



Supplementary Scheme 2.2 – Synthesis of compound 3. Reagents and conditions: *i*) 2,4,5-trichloropyrimidine, DIPEA, DMF, 70 °C, 99%. *ii*) *o*-anisidine, *p*-TSA, isopropanol, reflux, 36%. *iii*) PtO_2 , H_2 , THF, rt, 97%. *iv*) acryloyl chloride, DIPEA, DCM, 0 °C, 68%.

Synthesis of 2,5-dichloro- N -(3-nitrophenyl)pyrimidin-4-amine (**20**)

2,4,5-Trichloropyrimidine (1.42 g, 7.74 mmol) and DIPEA (2.00 g, 15.5 mmol) were dissolved in DMF (4 mL). To the stirring solution was added 3-nitroaniline (1.07 g, 7.74 mmol), after which the reaction mixture was heated at 70 °C for 16 h. The mixture was allowed to cool down to rt and subsequently diluted with EtOAc (75 mL) and washed with H_2O (3 x 50 mL). The organic layer was dried over MgSO_4 and concentrated to dryness to yield the title compound (2.18 g, 7.66 mmol, 99%). ^1H NMR (400 MHz, DMSO): δ 9.96 (s, 1H), 8.63 (t, $J = 2.2$ Hz, 1H), 8.49 (s, 1H), 8.17 – 8.09 (m, 1H), 8.01 (ddd, $J = 8.3, 2.3, 0.9$ Hz, 1H), 7.68 (t, $J = 8.2$ Hz, 1H). ^{13}C NMR (101 MHz, DMSO): δ 157.0, 156.2, 147.8, 139.0, 129.9, 129.0, 122.5, 119.1, 117.2, 114.2.

Synthesis of 5-chloro- N^2 -(2-methoxyphenyl)- N^4 -(3-nitrophenyl)pyrimidine-2,4-diamine (**21**)

Compound **20** (600 mg, 2.10 mmol) and *o*-anisidine (259 mg, 2.10 mmol) were taken up in isopropanol (20 mL), followed by the addition of *p*-TSA (400 mg, 2.10 mmol). The reaction mixture was heated under reflux for 16 h, after which it was concentrated under reduced pressure. The residue was taken up in saturated aqueous NaHCO_3 (20 mL) and the product was extracted with EtOAc (20 mL). The organic layer was concentrated under reduced pressure and the crude residue was purified by flash column chromatography (10% \rightarrow 30% EtOAc in pentane) to yield the title compound (284 mg, 0.38 mmol, 36%). ^1H NMR (400 MHz, DMSO): δ 9.31 (s, 1H), 8.51 (t, $J = 2.2$ Hz, 1H), 8.23 – 8.15 (m, 2H), 8.09 (s, 1H), 7.92 (ddd, $J = 8.2, 2.3, 0.9$ Hz, 1H), 7.81 – 7.74 (m, 1H), 7.55 (t, $J = 8.2$ Hz, 1H), 7.04 – 6.98 (m, 2H), 6.80 – 6.74 (m, 1H), 3.80 (s, 3H). ^{13}C NMR (101 MHz, DMSO): δ 157.8, 155.6, 155.5, 150.0, 147.7, 140.0, 129.5, 128.5, 128.1, 123.5, 121.8, 120.0, 117.8, 116.8, 110.9, 104.3, 55.6.

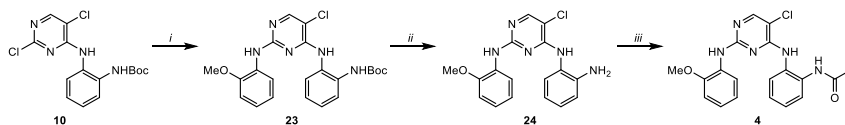
Synthesis of N^4 -(3-aminophenyl)-5-chloro- N^2 -(2-methoxyphenyl)pyrimidine-2,4-diamine (**22**)

Compound **21** (200 mg, 0.54 mmol) was dissolved in THF (10 mL), followed by addition of PtO_2 (21 mg, 0.09 mmol). The mixture was stirred under H_2 atmosphere at rt for 72 h, after which it was diluted

in MeOH, filtered over celite and concentrated to yield the title compound (179 mg, 0.54 mmol, 97%), which was directly used in the next step.

Synthesis of N-(3-((5-chloro-2-((2-methoxyphenyl)amino)pyrimidin-4-yl)amino)phenyl)acrylamide (3)

Compound **22** (77 mg, 0.23 mmol) was taken up in DCM (2 mL) and cooled to 0 °C. Subsequently, DIPEA (29 mg, 0.23 mmol) was added and the reaction mixture was stirred for 10 min. Acryloyl chloride (20 mg, 0.23 mmol) dissolved in DCM (1 mL) was dropwisely added to the mixture. After stirring for 30 min, the reaction was quenched by addition of water (5 mL). The product was extracted from the reaction mixture with DCM (3 x 25 mL) and the organic layer was dried over MgSO₄ and concentrated to dryness. The crude residue was purified by flash column chromatography (10% → 40% EtOAc in pentane) to yield the title compound (61 mg, 0.15 mmol, 68%). HRMS (ESI+) *m/z*: calculated for C₂₀H₁₈ClN₅O₂ ([M+H]): 396.12218; found: 396.12156. ¹H NMR (400 MHz, CDCl₃): δ 8.21 (dd, *J* = 7.9, 1.6 Hz, 1H), 8.04 (d, *J* = 12.2 Hz, 2H), 7.70 (s, 1H), 7.58 (d, *J* = 7.9 Hz, 1H), 7.41 (s, 1H), 7.33 (t, *J* = 8.0 Hz, 1H), 7.26 (d, *J* = 8.5 Hz, 1H), 7.16 (s, 1H), 7.04 – 6.95 (m, 1H), 6.94 – 6.83 (m, 2H), 6.45 (dd, *J* = 16.9, 1.3 Hz, 1H), 6.23 (dd, *J* = 16.8, 10.2 Hz, 1H), 5.79 (dd, *J* = 10.2, 1.3 Hz, 1H), 3.88 (s, 3H). ¹³C NMR (101 MHz, CDCl₃): δ 155.7, 148.8, 138.6, 138.5, 131.2, 129.6, 128.8, 128.2, 122.6, 120.5, 120.1, 117.3, 116.5, 115.7, 112.8, 110.3, 105.1, 55.8.



Supplementary Scheme 2.3 – Synthesis of compound 4. Reagents and conditions: *i*) *o*-anisidine, Xantphos, Pd(OAc)₂, Cs₂CO₃, 1,4-dioxane, 100 °C, 6%. *ii*) TFA, DCM, rt. *iii*) acryloyl chloride, DIPEA, DCM, 0 °C, 45% over 2 steps.

Synthesis of tert-butyl(2-((5-chloro-2-((2-methoxyphenyl)amino)pyrimidin-4-yl)amino)phenyl)carbamate (23)

Compound **10** (600 mg, 1.69 mmol), *o*-anisidine (208 mg, 1.69 mmol), Xantphos (98 mg, 0.17 mmol), Pd(OAc)₂ (19 mg, 0.084 mmol) and cesium carbonate (1.10 g, 3.38 mmol) were dissolved in 20 mL 1,4-dioxane. The reaction mixture was purged with argon and subsequently heated at 100 °C for 16 h. Subsequently, the mixture was diluted with EtOAc and filtered over Celite®, after which the filtrate was concentrated. The crude residue was purified by flash column chromatography (0% → 20% EtOAc in pentane) to yield the title compound (48 mg, 0.11 mmol, 6%). ¹H NMR (400 MHz, CDCl₃): δ 8.12 – 8.03 (m, 2H), 7.79 (s, 1H), 7.72 – 7.66 (m, 1H), 7.63 (s, 1H), 7.49 – 7.41 (m, 1H), 7.29 – 7.22 (m, 2H), 6.89 (m, 1H), 6.82 (dd, *J* = 8.1, 1.5 Hz, 1H), 6.78 – 6.70 (m, 1H), 6.66 (s, 1H), 3.85 (s, 3H), 1.50 (s, 9H). ¹³C NMR (101 MHz, CDCl₃): δ 157.0, 154.1, 147.8, 131.9, 130.9, 129.2, 128.9, 127.6, 126.5, 125.4, 123.9, 121.6, 120.8, 118.7, 114.2, 109.8, 105.2, 81.5, 55.8, 28.4.

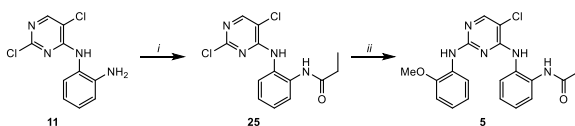
Synthesis of N⁴-(2-aminophenyl)-5-chloro-N²-(2-methoxyphenyl)pyrimidine-2,4-diamine (24)

Compound **23** (50 mg, 0.11 mmol) was dissolved in DCM (3 mL), after which TFA (3 mL) was slowly added. The reaction mixture was stirred at rt for 16 h and subsequently evaporated to dryness to yield the title compound, which was directly used in the next reaction.

Synthesis of N-(2-((5-chloro-2-((2-methoxyphenyl)amino)pyrimidin-4-yl)amino)phenyl)acrylamide (4)

Compound **24** (84 mg, 0.18 mmol) was taken up in DCM (2 mL) and cooled to 0 °C. Subsequently, DIPEA (24 mg, 0.18 mmol) was added and the reaction mixture was stirred for 10 min. Acryloyl chloride (17 mg, 0.18 mmol) dissolved in DCM (1 mL) was dropwisely added to the mixture. After stirring for 15 min, the reaction was quenched by addition of water (5 mL). The product was extracted from the reaction mixture with DCM (50 mL) and the organic layer was dried over MgSO₄ and concentrated to

dryness. The crude residue was purified by flash column chromatography (10% → 40% EtOAc in pentane) to yield the title compound (20 mg, 0.05 mmol, 45% over two steps). HRMS (ESI+) *m/z*: calculated for C₂₀H₁₈ClN₅O₂ ([M+H]): 396.12218; found: 396.12156. ¹H NMR (400 MHz, MeOD): δ 8.04 (s, 1H), 7.81 (dd, *J* = 8.1, 1.6 Hz, 1H), 7.76 – 7.69 (m, 1H), 7.51 – 7.44 (m, 1H), 7.41 – 7.33 (m, 2H), 7.03 – 6.95 (m, 2H), 6.73 (ddd, *J* = 8.6, 7.1, 1.8 Hz, 1H), 6.48 (dd, *J* = 17.0, 9.5 Hz, 1H), 6.40 (dd, *J* = 16.9, 2.4 Hz, 1H), 5.81 (dd, *J* = 9.4, 2.4 Hz, 1H), 3.87 (s, 3H). ¹³C NMR (101 MHz, MeOD): δ 166.9, 158.8, 149.9, 132.9, 132.5, 131.4, 129.9, 129.2, 128.9, 128.2, 127.9, 127.4, 126.0, 125.5, 125.0, 122.0, 121.6, 111.5, 106.5, 56.3.



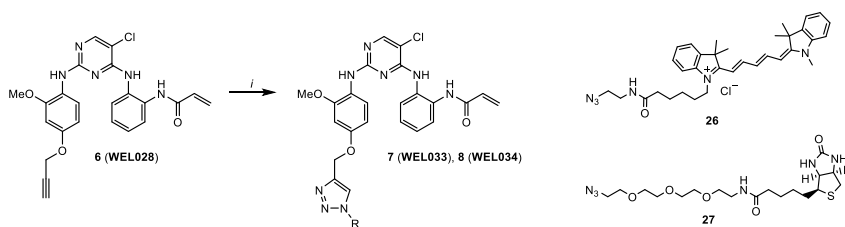
Supplementary Scheme 2.4 – Synthesis of compound 5. Reagents and conditions: *i*) propionyl chloride, DIPEA, DCM, 0 °C, 52%. *ii*) *o*-anisidine, *p*-TSA, isopropanol, reflux, 56%.

Synthesis of N-(2-((2,5-dichloropyrimidin-4-yl)amino)phenyl)propionamide (25)

Compound **11** (171 mg, 0.67 mmol) was dissolved in DCM (5 mL) and cooled to 0 °C. Subsequently, DIPEA (85 mg, 0.67 mmol) was added and the reaction mixture was stirred for 10 min. Propionyl chloride (64 mg, 0.67 mmol) dissolved in DCM (3 mL) was dropwisely added. After stirring for 2 h, the reaction mixture was diluted with DCM (50 mL) and washed with H₂O (2 x 50 mL). The organic extract was dried over MgSO₄ and concentrated to dryness. The crude residue was purified by flash column chromatography (20% → 30% EtOAc in pentane) to yield the title compound (109 mg, 0.35 mmol, 52%). ¹H NMR (400 MHz, CDCl₃): δ 8.67 (s, 1H), 8.16 (s, 1H), 8.07 (s, 1H), 7.73 (dd, *J* = 8.2, 1.3 Hz, 1H), 7.32 – 7.23 (m, 1H), 7.14 – 7.05 (m, 1H), 6.87 (dd, *J* = 7.9, 1.5 Hz, 1H), 2.38 (q, *J* = 7.6 Hz, 2H), 1.20 (t, *J* = 7.6 Hz, 3H). ¹³C NMR (101 MHz, CDCl₃): δ 174.4, 158.1, 157.4, 155.0, 131.4, 130.2, 127.0, 126.5, 126.1, 125.0, 114.7, 30.0, 10.2.

Synthesis of N-(2-((5-chloro-2-((2-methoxyphenyl)amino)pyrimidin-4-yl)amino)phenyl)propionamide (5)

Compound **25** (59 mg, 0.19 mmol) and *o*-anisidine (23 mg, 0.19 mmol) were taken up in isopropanol (10 mL), followed by the addition of *p*-TSA (37 mg, 0.19 mmol). The reaction mixture was heated under reflux for 16 h, after which it was concentrated under reduced pressure. The residue was taken up in saturated aqueous NaHCO₃ (20 mL) and the product was extracted with EtOAc (20 mL). The organic layer was dried over MgSO₄ and concentrated. The crude residue was purified by flash column chromatography (10% → 40% EtOAc in pentane), affording a mixture of compound **25** and **5** that was further purified by HPLC to yield the title compound (42 mg, 0.10 mmol, 56%). HRMS (ESI+) *m/z*: calculated for C₂₀H₂₀ClN₅O₂ ([M+H]): 398.13783; found: 398.13722. ¹H NMR (400 MHz, CDCl₃): δ 10.04 (s, 1H), 9.24 (s, 1H), 7.85 (s, 1H), 7.68 – 7.60 (m, 2H), 7.58 (dd, *J* = 8.0, 1.6 Hz, 1H), 7.26 (s, 3H), 7.16 (dd, *J* = 7.5, 2.0 Hz, 1H), 7.06 (ddd, *J* = 8.3, 7.6, 1.6 Hz, 1H), 6.84 (dd, *J* = 8.3, 1.4 Hz, 1H), 6.70 (td, *J* = 7.8, 1.3 Hz, 1H), 3.80 (s, 3H), 2.46 (q, *J* = 7.5 Hz, 2H), 1.26 (t, *J* = 7.6 Hz, 3H). ¹³C NMR (101 MHz, CDCl₃): δ 174.3, 157.7, 153.3, 152.8, 151.2, 130.6, 127.8, 127.6, 126.9, 126.1, 125.8, 124.9, 123.1, 120.3, 111.0, 105.4, 56.0, 30.3, 10.2.



Supplementary Scheme 2.5 – Synthesis of one-step probes 7 and 8. *i*) 26 or 27, CuSO₄, sodium ascorbate, H₂O/DCM (1:1), rt, 5% (7) or 17% (8) after HPLC purification.

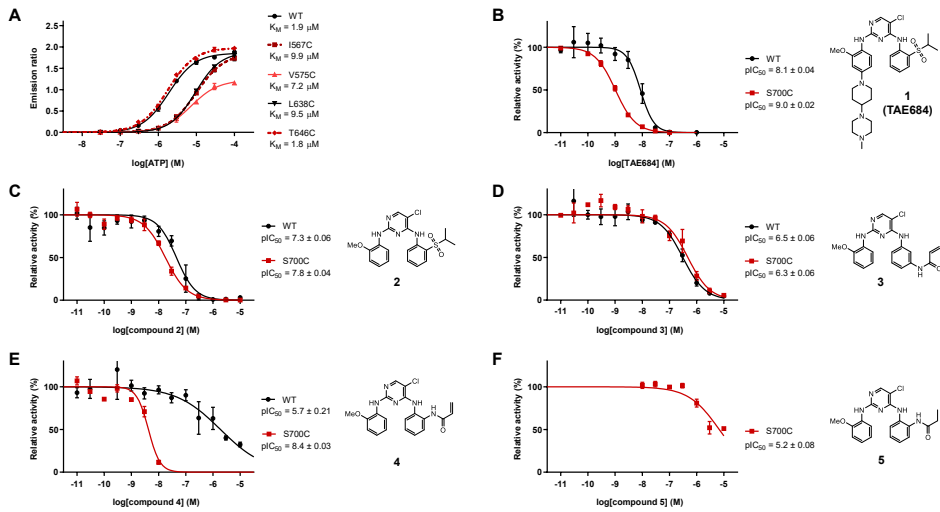
Synthesis of 1-(6-((2-(4-((4-((2-acrylamidophenyl)amino)-5-chloropyrimidin-2-yl)amino)-3-methoxy-phenoxy)methyl)-1H-1,2,3-triazol-1-yl)ethyl)amino)-6-oxohexyl)-3,3-dimethyl-2-((1E,3E)-5-((E)-1,3,3-trimethylindolin-2-ylidene)penta-1,3-dien-1-yl)-3H-indol-1-ium (7, WEL033)

Compound **6** (30 mg, 0.07 mmol) and Cy5-azide **26** (77 mg, 0.14 mmol) were dissolved in degassed DCM (3 mL). CuSO₄ (8 mg, 0.01 mmol) and sodium ascorbate (16 mg, 0.03 mmol) were separately dissolved in degassed H₂O (3 mL) and added to the reaction mixture. The reaction mixture was vigorously stirred for 16 h at rt and subsequently evaporated to dryness. The crude residue was purified by flash column chromatography (DCM → 2% MeOH in DCM), followed by further HPLC purification to yield the title compound (3.2 mg, 3 μmol, 5%). HRMS (ESI⁺) *m/z*: calculated for [C₅₇H₆₃ClN₁₁O₄]⁺: 1000.47475; found: 1000.47462. ¹H NMR (600 MHz, MeOD): δ 8.20 (td, *J* = 13.1, 3.2 Hz, 2H), 8.07 (s, 1H), 7.97 (s, 1H), 7.66 (dd, *J* = 7.8, 1.7 Hz, 1H), 7.52 – 7.45 (m, 4H), 7.39 (m, 2H), 7.35 – 7.30 (m, 2H), 7.29 (d, *J* = 7.1 Hz, 1H), 7.27 – 7.22 (m, 4H), 6.66 (d, *J* = 2.6 Hz, 1H), 6.57 (t, *J* = 12.4 Hz, 1H), 6.51 – 6.42 (m, 2H), 6.40 (dd, *J* = 16.9, 1.9 Hz, 1H), 6.27 (d, *J* = 13.7 Hz, 1H), 6.19 (d, *J* = 13.7 Hz, 1H), 5.82 (dd, *J* = 9.9, 1.9 Hz, 1H), 5.17 (s, 2H), 4.57 – 4.53 (m, 2H), 4.04 (t, *J* = 7.7 Hz, 2H), 3.77 (s, 3H), 3.69 – 3.65 (m, 2H), 3.56 (s, 3H), 2.66 (s, 3H), 2.15 (t, *J* = 7.2 Hz, 2H), 1.79 – 1.58 (m, 18H), 1.40 – 1.31 (m, 2H). ¹³C NMR (151 MHz, MeOD): δ 176.2, 175.3, 174.6, 166.9, 155.4, 145.1, 144.2, 143.5, 142.6, 142.5, 133.0, 131.4, 129.8, 129.7, 129.0, 128.7, 128.1, 127.4, 126.6, 126.2, 126.2, 126.0, 125.6, 123.4, 123.2, 112.0, 111.8, 106.8, 104.3, 104.2, 100.7, 62.8, 56.4, 49.8, 44.8, 40.3, 36.5, 28.1, 27.9, 27.9, 27.8, 27.1, 26.4.

Synthesis of N-(2-(2-(2-(2-(4-((4-((2-acrylamidophenyl)amino)-5-chloropyrimidin-2-yl)amino)-3-methoxy-phenoxy)methyl)-1H-1,2,3-triazol-1-yl)ethoxy)ethoxy)ethoxy)ethyl)-5-((3aS,4S,6aR)-2-oxohexahydro-1H-thieno[3,4-d]imidazol-4-yl)pentanamide (8, WEL034)

Compound **6** (8.7 mg, 0.02 mmol) and biotin-PEG₃-azide **27** (9.1 mg, 0.02 mmol) were dissolved in degassed DCM (2 mL). CuSO₄ (2.3 mg, 0.01 mmol) and sodium ascorbate (4.4 mg, 0.02 mmol) were separately dissolved in degassed H₂O (2 mL) and added to the reaction mixture. The reaction mixture was vigorously stirred for 16 h at rt and subsequently evaporated to dryness. The crude residue was purified by HPLC to yield the title compound (3.0 mg, 3 μmol, 17%). HRMS (ESI⁺) *m/z*: calculated for C₄₁H₅₂ClN₁₁O₈S [M+H]⁺: 894.34823; found: 894.34883. ¹H NMR (600 MHz, MeOD): δ 8.14 (s, 1H), 8.00 (d, *J* = 19.0 Hz, 1H), 7.69 (dd, *J* = 7.9, 1.6 Hz, 1H), 7.49 (dd, *J* = 7.9, 1.5 Hz, 1H), 7.43 (s, 1H), 7.38 (td, *J* = 7.7, 1.6 Hz, 1H), 7.34 (td, *J* = 7.6, 1.5 Hz, 1H), 6.73 (d, *J* = 2.5 Hz, 1H), 6.49 (dd, *J* = 17.0, 9.9 Hz, 2H), 6.42 (dd, *J* = 17.0, 2.0 Hz, 1H), 5.84 (dd, *J* = 9.9, 2.0 Hz, 1H), 5.18 (s, 2H), 4.62 (dd, *J* = 5.5, 4.4 Hz, 2H), 4.46 (ddd, *J* = 7.9, 5.0, 0.9 Hz, 1H), 4.26 (dd, *J* = 7.9, 4.5 Hz, 1H), 3.90 (dd, *J* = 5.6, 4.4 Hz, 2H), 3.84 (s, 3H), 3.64 – 3.54 (m, 10H), 3.48 (t, *J* = 5.5 Hz, 2H), 3.16 (ddd, *J* = 9.0, 5.8, 4.5 Hz, 1H), 2.93 – 2.86 (m, 1H), 2.72 – 2.63 (m, 2H), 2.20 – 2.12 (m, 2H), 2.04 (s, 1H), 1.76 – 1.49 (m, 5H), 1.43 – 1.34 (m, 2H). ¹³C NMR (151 MHz, MeOD): δ 176.1, 167.0, 166.1, 159.3, 154.9, 144.7, 133.2, 131.6, 131.4, 129.1, 128.9, 128.5, 127.5, 126.3, 126.0, 107.0, 100.9, 71.5, 71.4, 71.4, 71.2, 70.6, 70.3, 63.3, 62.7, 61.6, 57.0, 56.5, 51.5, 49.8, 49.6, 41.0, 40.3, 36.7, 29.8, 29.5, 26.8.

Supplementary Data



Supplementary Figure 2.1 - Determination of ATP K_M for other active FES mutants and concentration-response curves of inhibitors against FES^{WT} and FES^{S700C}. (A) Determination of ATP K_M for FES^{WT} and other FES mutants with >50% relative activity as determined in Figure 2.3B. (B-F) Concentration-response curves of inhibitors against FES^{WT} and FES^{S700C} as determined in TR-FRET assay. Compound code and structure is depicted right of the corresponding curve. Data represent means \pm SEM (N = 3).

A chemical genetic strategy for visualization of engineered kinases

Supplementary Table 2.2 – Substrate identification using PamChip® activity assay. Top 30 of peptides with highest signal intensity are shown. Numbers behind substrate names indicate the amino acid residue numbers within the corresponding protein sequence. Predicted phosphorylated tyrosine residues are indicated in bold red.

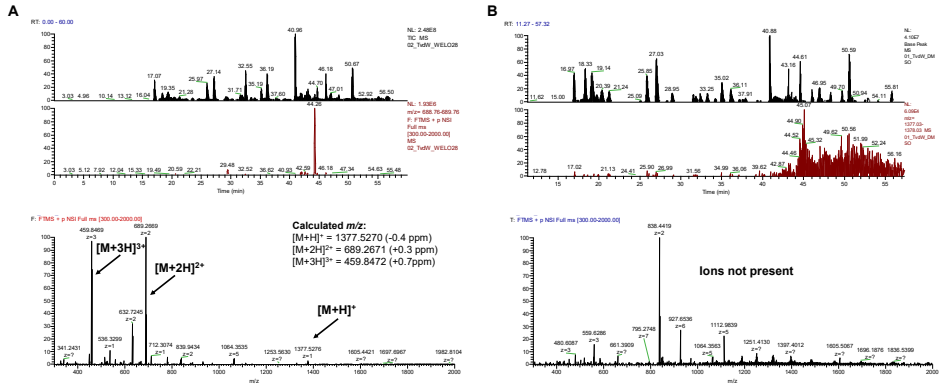
Substrate	Peptide	log ₂ of signal intensity	
		FES ^{WT}	FES ^{S700C}
CD79A_181_193	EYEDENL Y EGLNL	14.59	14.18
ENOG_37_49	SGASTGI Y EALEL	14.39	14.13
ZAP70_313_325	SVYESP Y SDPEEL	12.83	12.51
EFS_246_258	GGTDEGI Y DVPLL	12.68	12.43
PLCG1_764_776	IGTAEPD Y GALYE	12.56	12.48
RET_1022_1034	TPSDSLI Y DDGLS	12.53	12.29
IRS2_626_638	HPYPED Y GDIEIG	12.38	12.20
EPHA1_774_786	LDDFDGT Y ETQGG	12.35	12.24
PGFRB_572_584	VSSDGHE Y IYVDP	12.33	12.09
P85A_600_612	NENTEDQ Y SLVED	12.27	12.19
LAT_249_261	EEGAPD Y ENLQEL	12.14	12.23
PLCG2_1191_1203_C1200S	ESEEEEL Y SSSRQL	12.14	12.04
PDPK1_2_14	ARTTSQL Y DAVPI	12.10	11.97
FRK_380_392	KVDNED Y ESRHE	11.99	11.88
PTN11_57_67	QNTGD Y YDLYG	11.89	11.89
PTN11_580_590	SARV Y ENVGLM	11.71	11.71
KIT_930_942_C942S	ESTNHI Y SNLANS	11.68	11.59
PDPK1_369_381	DEDCYGN Y DNLLS	11.55	11.57
EGFR_1165_1177	ISLDNPD Y QQDFF	11.40	11.59
PECA1_708_718	DTETV Y SEVRK	11.36	11.53
PGFRB_709_721	RPPSAEL Y SNALP	11.35	11.53
EPHA7_607_619	TYIDPET Y EDPNR	11.30	11.43
VGFR2_989_1001	EEAPEDL Y KDFLT	11.26	11.38
PGFRB_1002_1014	LDTSSVL Y TAVQP	11.25	11.33
PTN6_558_570	KHKEDV Y ENLHTK	11.18	11.16
EPHA2_765_777	EDDPEAT Y TTSGG	11.16	11.32
PTN6_531_541	GQESE Y GNITY	11.15	11.29
FES_706_718	REEADGV Y AASGG	11.07	11.21
FER_707_719	RQEDGGV Y SSSGL	10.98	11.13
IRS1_890_902	PKSPGE Y VNIEFG	10.93	11.11

Chapter 2

Supplementary Table 2.3 - SH2 binding partner identification using PamChip® binding assay. Top 30 of peptides with highest signal intensity are shown. Numbers behind substrate names indicate the amino acid residue numbers within the corresponding protein sequence.

Binding partner	Peptide	log ₂ of signal intensity	
		FES ^{WT}	FES ^{S700C}
PGFRB_572_584	VSSDGHEYIYVDP	12.44	13.06
PGFRB_1014_1028	PNEGDNNDYIIPDP	12.17	12.94
LAT_249_261	EEGAPDYENLQEL	10.79	12.19
VGFR2_1168_1180	AQQDGKDYIVLPI	10.69	11.64
ENOG_37_49	SGASTGIYEALEL	10.67	12.29
PTN11_57_67	QNTGDYDYLYG	10.66	12.05
CD3E_182_194	PVPNPDYPIRKG	10.03	11.48
CD79A_181_193	EYEDENLYEGLNL	10.02	12.05
IRS1_890_902	PKSPGEYVNIIEFG	9.97	11.28
LAT_194_206	MESIDDYVNVPEP	9.51	11.14
MAPK3_198_210_C203S	ALQTPSYTPYYVA	9.32	10.68
MK12_180_189_M182B	SEBTGYVVTR	9.16	10.58
PTN6_558_570	KHKEDVYENLHTK	8.74	10.88
FGFR2_762_774	TLTTNEEYLDLSQ	8.26	9.86
TYK2_1048_1060	VPEGHEYRVRED	7.88	9.60
JAK3_974_986	LPLDKDYVVREP	7.87	9.77
RON_1346_1358	SALLGDHYVQLPA	7.75	9.04
FGFR3_753_765	TVTSTDEYLDLSA	7.66	9.57
MET_1227_1239	RDMYDKEYYSVHN	7.59	9.42
PTN11_580_590	SARVYENVGLM	7.27	9.94
EGFR_1190_1202	STAENAEYLRVAP	7.12	9.01
MK14_173_185	RHTDDEMTGYVAT	7.08	9.11
FAK2_572_584	RYIEDEDYYKASV	7.00	9.11
JAK1_1027_1039	AIETDKEYYTVKD	6.53	8.78
MK03_199_208	GFLTEYVATR	6.49	8.31
EPOR_419_431	ASAASFYETILD	6.42	7.97
MK12_178_190	ADSEMTGYVVTRW	6.15	8.13
41_654_666	LDGENIYIRHSNL	6.08	8.02
MK07_212_224	AEHQYFMTEYVAT	4.96	6.25
HAVR2_257_267	GIRSEENIYTI	4.95	4.67

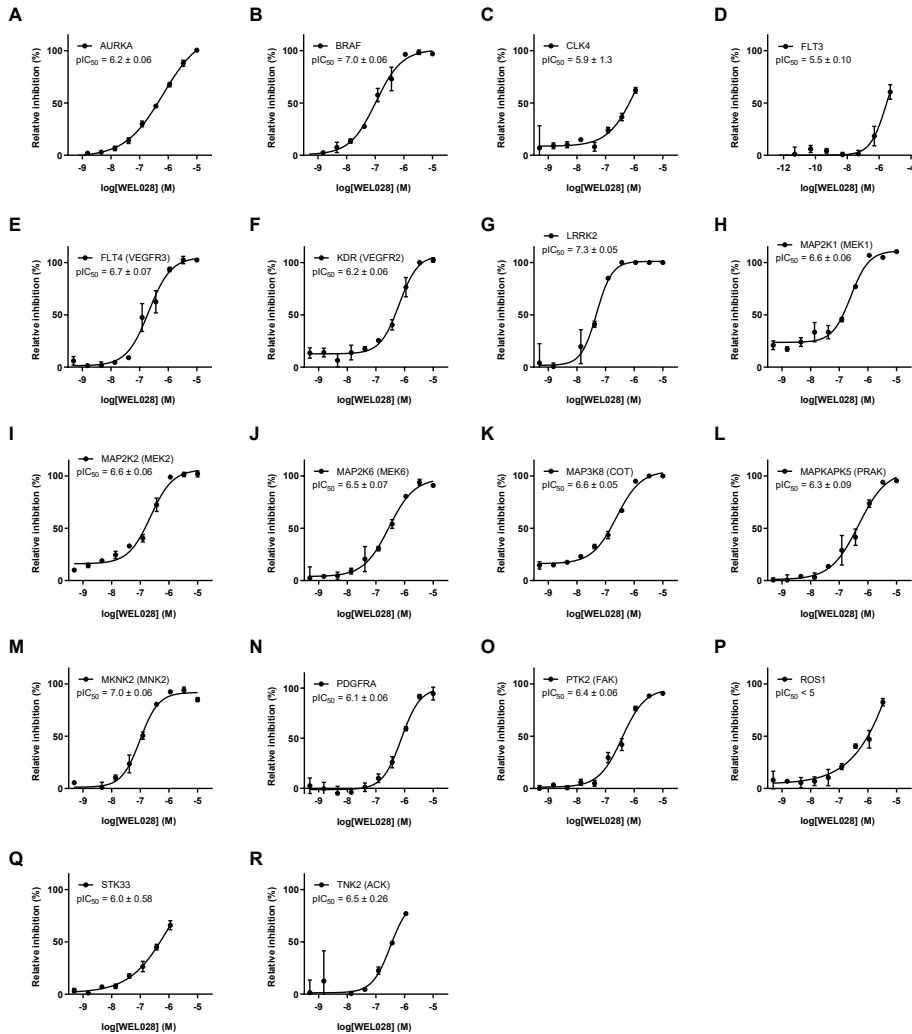
A chemical genetic strategy for visualization of engineered kinases



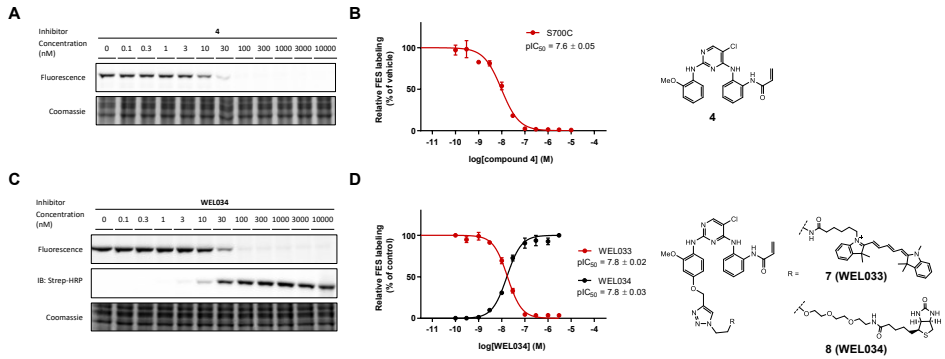
Supplementary Figure 2.2 - LC-MS elution profiles of FES^{5700C} incubated with WEL028 (A) or vehicle (B). Expected precursor ions and corresponding calculated m/z values are indicated. Ions were not present in vehicle-treated control sample.

ABL1	-3	CSNK1D (CK1 delta)	18	GSG2 (Haspin)	6	MAPK3 (ERK1)	19	PIK3C3 (mP334)	11	SRMS (Srm)	7
ABL1 (A9)	4	CSNK1E (CK1 epsilon)	9	GSG3A (GSG3 alpha)	6	MAPK3 (JNK1)	16	PIK3CA/PIK3R1	14	SRPK1	7
ACVR1 (ALK2)	2	CSNK1G1 (CK1 gamma1)	4	GSG3B (GSG3 beta)	4	MAPK3 (JNK2)	2	PIK3CD/PIK3R1 (p110delta)	8	SRPK2	-1
ACVR1B (ALK4)	1	CSNK1G2 (CK1 gamma2)	4	HCK	6	MAPKAPK2	2	PIK3CG (p110 gamma)	13	STK16 (PKL12)	32
ACVR2B	9	CSNK1G3 (CK1 gamma3)	0	HIPK1 (Myak)	-4	MAPKAPK3	9	PIK3I	8	STK17A (DRAK1)	9
ADRBK1 (GRK2)	4	CSNK2A1 (CK2 alpha 1)	4	HIPK2	2	MAPKAPK5 (PRAK)	66	PIK1	8	STK22B (TSBK2)	18
ADRBK2 (GRK3)	7	CSNK2A2 (CK2 alpha 2)	6	HIPK3 (YAK1)	-3	MAR1 (MAR1)	3	PKM1 (PRK1)	7	STK22Z (TSBK1)	19
AKT1 (PKB alpha)	-3	DAPK1	12	HIPK4	14	MAR2	8	PKL1	12	STK3 (MSSK1)	-1
AKT2 (PKB beta)	-1	DAPK3 (ZPK)	4	IGF1R	15	MAR3	6	PKL2	12	STK24 (MST3)	12
AKT3 (PKB gamma)	-1	DDR1	-2	IKBKB (IKK beta)	1	MAR4	8	PKL3	-1	STK25 (YSK1)	5
AMPK A1/B1/G1	13	DDR2	3	IKBKE (IKK epsilon)	2	MATK (HTL)	8	PRKACA (PKA)	2	STK3 (MST2)	5
AMPK A2/B1/G1	4	DMPK	3	INSR	11	MELK	-2	PRKCA (PKC alpha)	14	STK33	66
AURKA (Aurora A)	24	DNA-PK	6	INSRR (IRN)	9	MERTK (MER)	4	PRKCB1 (PKC beta 1)	19	STK4 (MST1)	3
AURKB (Aurora B)	37	DYRK1A	1	IRAK1	26	MET (cMet)	-4	PRKCB2 (PKC beta 2)	0	SYK	3
AURKC (Aurora C)	37	DYRK1B	0	IRAK4	4	MINK1	20	PRKCD (PKC delta)	14	TAOK2 (TAO1)	4
BLK	0	DYRK3	2	ITK	-7	MKNK1 (MNK1)	13	PRKCE (PKC epsilon)	-13	TAOK3 (JIK)	1
BLM	0	DYRK4	0	JAK1	-3	MKNK2 (MNK2)	29	PRKCG (PKC gamma)	1	TBK1	7
BMPRIA (ALKO)	-2	EEF2K	9	JAK2	0	MLOK (BLOC)	9	PRKCH (PKC eta)	4	TEC	5
BMX	16	EGFR (ErbB1)	6	JAK3	14	MST1R (RON)	5	PRKI (PKC iota)	0	TEK (Tae2)	6
BRAF	24	EPIA1	5	KDR (VEGFR2)	67	MST4	19	PRKKN (PKC theta)	31	TGFBRI (ALK5)	6
BRSK1 (SAD1)	2	EPIA2	7	KIT	18	MUSK	26	PRKCO (PKC theta)	8	TNKC (ACK)	79
BTK	11	EPIA3	9	LCK	5	MYLK (MLCK)	15	PRKCC (PKC zeta)	-1	TKK	7
CAMK1 (CAMKI)	6	EPIA4	5	LIMK1	14	MELK2 (sMLCK)	-3	PRKD1 (PKC mu)	11	TYK2	-1
CAMK1D (CAMKI delta)	6	EPIA5	0	LIMK2	-2	NEK1	6	PRKD2 (PKC nu)	3	TYRO3 (RSE)	5
CAMK2A (CaMKII alpha)	-6	EPIA7	4	LRRK2 FL	26	NEK2	12	PRKGI	-3	WEE1	-5
CAMK2B (CaMKII beta)	0	EPIA8	-7	LRRK2	21	NEK6	9	PRKG2 (PKG2)	4	WNK2	5
CAMK2D (CaMKII delta)	8	EPIH1	0	LTK (TYK1)	23	NEK7	-3	PRKK	-3	YES1	8
CAMK2E (CaMKII epsilon)	-5	EPIH2	4	LYN A	5	NEK9	-8	PTK2 (PAK)	78	ZAK	4
CAMKK1 (CaMKKA)	22	EPIH3	4	LYN B	1	NLK	3	PTK2B (FAK2)	2	ZAP70	2
CAMKK2 (CaMKK beta)	23	EPIH4	1	MAP2K1 (MEK1)	30	NTRK1 (TRKA)	17	PTK6 (Btk)	31		
CDC42 BPA (MRCKA)	-7	ERBB2 (HER2)	2	MAP2K2 (MEK2)	30	NTRK2 (TRKB)	5	RET	7		
CDC42 BPB (MRCKB)	6	ERBB4 (HER4)	8	MAP2K3 (MEK3)	26	NTRK3 (TRKC)	4	RIPK2	1		
CDK1/cyclin B	1	FER	23	MAP2K6 (MKK6)	78	NUAK1 (ARK5)	35	ROCK1	-3		
CDK2/cyclin A	-3	FES (FRS)	15	MAP3K10 (MLK2)	4	PAK1	9	ROCK2	0		
CDK2/p25	2	FGFR1	3	MAP3K11 (MLK3)	7	PAK2 (PAK6)	29	RON	59		
CDK3/p35	-4	FGFR2	7	MAP3K14 (NIK)	3	PAK3	7	RPS8K1 (RSK1)	5		
CDK7/cyclin H/M/N/T1	6	FGFR3	8	MAP3K2 (MEK2)	3	PAK4	-4	RPS8K2 (RSK3)	19		
CDK8/cyclin C	0	FGFR4	6	MAP3K3 (MEK3)	7	PAK6	7	RPS8K4 (RSK2)	13		
CDK9/cyclin K	5	FGFR4	34	MAP3K4 (SKN1)	6	PAK7 (KIAA1254)	12	RPS8K6 (MSK2)	1		
CDK9/cyclin T1	16	FRG	10	MAP3K6 (COT)	77	PASK	2	RPS8K8 (MSK1)	7		
CHEK1 (CHK1)	0	FLT1 (VEGFR1)	38	MAP3K8 (MLK1)	-11	PDGFRFA (PDGFR alpha)	63	RPS8K8 (RSK4)	5		
CHEK2 (CHK2)	4	FLT3	67	MAP4K2 (GCK)	-12	PDGFRFB (PDGFR beta)	22	RPS8K9 (p70S6K)	4		
CHUK (IKK alpha)	7	FLT4 (VEGFR3)	11	MAP4K4 (HGK)	7	PKD1 Direct	5	SGK (SGK1)	10		
CLK1	5	FRAP1 (mTOR)	7	MAP4K6 (RIS1)	5	PKD1	36	SGK2	2		
CLK2	1	FRK (PTKS)	7	MAPK1 (ERK2)	26	PHK01	-2	SGKL (SGK3)	7		
CLK3	1	FYN	4	MAPK10 (JNK3)	-7	PHK02	0	SLK	4		
CLK4	53	GRK4	-1	MAPK11 (p38 beta)	6	PH4KA (PH4K alpha)	7	SNF1LK2	-6		
CSFR1 (FMS)	11	GRK5	4	MAPK12 (p38 gamma)	10	PH4KB (PH4K beta)	34	SPHK1	2		
CSK	5	GRK6	0	MAPK13 (p38 delta)	5	PIK3C2A (PIK-C2 alpha)	5	SPHK2	2		
CSNK1A1 (CK1 alpha 1)	9	GRK7	11	MAPK14 (p38 alpha)	7	PIK3C2B (PIK-C2 beta)	-1	SRC	6		

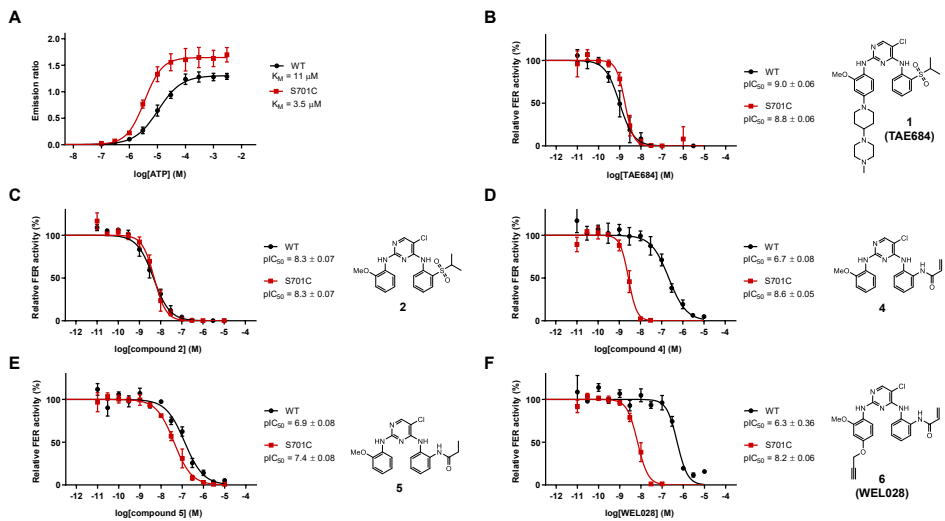
Supplementary Figure 2.3 - Single-point selectivity screen of WEL028 on a panel of 279 kinases. All data were obtained from SelectScreen™ selectivity profiling service. Assays were performed at 1 μM WEL028 with 1 h pre-incubation. The ATP concentration was equal to the kinase K_M, except for those indicated († = LanthaScreen technology, no ATP; * = 100 μM ATP; ** = 10 μM ATP). Values represent mean percentage inhibition compared to vehicle-treated control (N = 2).



Supplementary Figure 2.4 - Concentration-response curves of WEL028 against kinases with >50% inhibition at 1 μ M in initial single-dose screen. Data (means \pm SD, N = 2) were obtained from SelectScreen™ selectivity profiling service. Assays were performed with 1 h pre-incubation and concentration of ATP was selected to be equal to the K_M, unless indicated otherwise in Supplementary Figure 2.3.

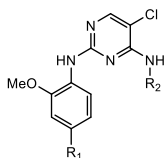


Supplementary Figure 2.5 - Competition of WEL033 labeling by compound 4 and biotin-conjugate 8 (WEL034). (A, B) Recombinantly expressed FER^{S700C} in HEK293T cell lysate was incubated with compound 4 (indicated concentrations, 30 min, rt), followed by two-step probe WEL028 (250 nM, 30 min, rt) and click mix containing Cy5-azide (2 eq., 30 min, rt). Samples were resolved by SDS-PAGE, followed by in-gel fluorescence scanning. Band intensities were normalized to vehicle-treated control. (C, D) Dose-dependent competition by WEL034. Samples were processed as described in A, but labeled with one-step probe WEL033 (250 nM, 30 min, rt). After in-gel fluorescence scanning, proteins were transferred to a PVDF membrane and immunoblotted against streptavidin-HRP. Band intensities (red: WEL033, black: WEL034) were normalized to vehicle-treated control (WEL033) or highest concentration (WEL034). Compound codes and structures are depicted right of the corresponding curves. Data represent means \pm SEM (N = 3).



Supplementary Figure 2.6 - Determination of ATP K_M for FER^{WT} and FER^{S701C} and concentration-response curves of inhibitors against FER^{WT} and FER^{S701C}. (A) Determination of ATP K_M for FER^{WT} and FER^{S701C}. (B-F) Concentration-response curves of inhibitors against FER^{WT} and FER^{S701C} as determined in TR-FRET assay. Compound code and structure is depicted right of the corresponding curve. Data represent means \pm SEM (N = 3).

Supplementary Table 2.4 - Inhibitory potency of synthesized TAE684 derivatives against FER^{WT} and FER^{S701C}. Half maximal inhibitory concentrations (expressed as pIC₅₀) were determined using recombinantly expressed FER^{WT} and FER^{S701C} in a TR-FRET assay. Final ATP concentration was 12 μM and 1 μM for FER^{WT} and FER^{S701C}, respectively. Apparent fold selectivity was calculated as IC₅₀ on FER^{WT} divided by IC₅₀ on FER^{S701C}. Data represent means ± SEM (N = 3). ND: not determined. Dose-response curves can be found in Supplementary Figure 2.6.



Compound	R ₁	R ₂	pIC ₅₀		Apparent fold selectivity
			FER ^{WT}	FER ^{S701C}	
1 (TAE684)			9.0 ± 0.06	8.8 ± 0.06	0.54
2	H		8.3 ± 0.07	8.3 ± 0.07	0.92
4	H		6.7 ± 0.08	8.6 ± 0.05	81
5	H		6.9 ± 0.08	7.4 ± 0.08	3.2
6 (WEL028)			6.3 ± 0.06	8.2 ± 0.06	74

References

1. Ubersax, J. A. & Ferrell, J. E. Mechanisms of specificity in protein phosphorylation. *Nature Reviews Molecular Cell Biology* **8**, 530–541 (2007).
2. Manning, G., Whyte, D. B., Martinez, R., Hunter, T. & Sudarsanam, S. The protein kinase complement of the human genome. *Science* **298**, 1912–1934 (2002).
3. Zhang, J., Yang, P. & Gray, N. Targeting cancer with small molecule kinase inhibitors. *Nat. Rev. Cancer* **9**, 28–39 (2009).
4. Fedorov, O., Müller, S. & Knapp, S. The (un)targeted cancer kinome. *Nat. Chem. Biol.* **6**, 166–169 (2010).
5. Grimminger, F., Schermuly, R. T. & Ghofrani, H. A. Targeting non-malignant disorders with tyrosine kinase inhibitors. *Nature Reviews Drug Discovery* **9**, 956–970 (2010).
6. Roskoski, R. Properties of FDA-approved small molecule protein kinase inhibitors. *Pharmacological Research* **144**, 19–50 (2019).
7. Weir, M. C. *et al.* Dual inhibition of Fes and Flt3 tyrosine kinases potently inhibits Flt3-ITD+ AML cell growth. *PLoS One* **12**, e0181178 (2017).
8. Miyata, Y. *et al.* Pathological significance and predictive value for biochemical recurrence of c-Fes expression in prostate cancer. *Prostate* **72**, 201–208 (2012).
9. Asai, A. *et al.* Pathological significance and prognostic significance of FES expression in bladder cancer vary according to tumor grade. *J Cancer Res Clin Oncol* **1**, 1–11 (2017).
10. Haigh, J., McVeigh, J. & Greer, P. The fps/fes tyrosine kinase is expressed in myeloid, vascular endothelial, epithelial, and neuronal cells and is localized in the trans-golgi network. *Cell growth Differ.* **7**, 931–44 (1996).
11. Greer, P. Closing in on the biological functions of Fps/Fes and Fer. *Nat. Rev. Mol. Cell Biol.* **3**, 278–89 (2002).
12. Cheng, H. Y., Schiavone, A. P. & Smithgall, T. E. A Point Mutation in the N-Terminal Coiled-Coil Domain Releases c-Fes Tyrosine Kinase Activity and Survival Signaling in Myeloid Leukemia Cells. *Mol. Cell. Biol.* **21**, 6170–6180 (2001).
13. Di Fulvio, M. *et al.* Phospholipase D2 (PLD2) shortens the time required for myeloid leukemic cell differentiation: Mechanism of action. *J. Biol. Chem.* **287**, 393–407 (2012).
14. Filippakopoulos, P. *et al.* Structural Coupling of SH2-Kinase Domains Links Fes and Abl Substrate Recognition and Kinase Activation. *Cell* **134**, 793–803 (2008).
15. Takashima, Y., Delfino, F. J., Engen, J. R., Superti-Furga, G. & Smithgall, T. E. Regulation of c-Fes tyrosine kinase activity by coiled-coil and SH2 domains: Analysis with *Saccharomyces cerevisiae*. *Biochemistry* **42**, 3567–3574 (2003).
16. Rogers, J. A., Read, R. D., Li, J., Peters, K. L. & Smithgall, T. E. Autophosphorylation of the Fes tyrosine kinase. Evidence for an intermolecular mechanism involving two kinase domain tyrosine residues. *J. Biol. Chem.* **271**, 17519–17525 (1996).
17. Laurent, C. E., Delfino, F. J., Cheng, H. Y. & Smithgall, T. E. The human c-Fes tyrosine kinase binds tubulin and microtubules through separate domains and promotes microtubule assembly. *Mol. Cell. Biol.* **24**, 9351–9358 (2004).
18. Condorelli, F. *et al.* Role of the Non-Receptor Tyrosine Kinase Fes in Cancer. *Curr. Med. Chem.* **18**, 2913–2920 (2011).
19. Nomura, D. K., Dix, M. M. & Cravatt, B. F. Activity-based protein profiling for biochemical pathway discovery in cancer. *Nat. Rev. Cancer* **10**, 630–638 (2010).
20. Knight, Z. A. & Shokat, K. M. Chemical Genetics: Where Genetics and Pharmacology Meet. *Cell* **128**, 425–430 (2007).
21. Weiss, W. A., Taylor, S. S. & Shokat, K. M. Recognizing and exploiting differences between RNAi and small-molecule inhibitors. *Nat. Chem. Biol.* **3**, 739–744 (2007).
22. Karaman, M. W. *et al.* A quantitative analysis of kinase inhibitor selectivity. *Nat. Biotechnol.* **26**, 127–132 (2008).
23. Hellwig, S. *et al.* Small-molecule inhibitors of the c-Fes protein-tyrosine kinase. *Chem. Biol.* **19**, 529–540 (2012).
24. Bunnage, M. E., Chekler, E. L. P. & Jones, L. H. Target validation using chemical probes. *Nat. Chem. Biol.* **9**, 195–199 (2013).
25. Simon, G. M., Niphakis, M. J. & Cravatt, B. F. Determining target engagement in living systems. *Nat. Chem. Biol.* **9**, 200–205 (2013).
26. Zhao, Q. *et al.* Broad-spectrum kinase profiling in live cells with lysine-targeted sulfonyl fluoride probes. *J. Am. Chem. Soc.* **139**, 680–685 (2017).
27. Liu, Q. *et al.* Developing irreversible inhibitors of the protein kinase cysteinome. *Chem. Biol.* **20**, 146–159 (2013).
28. Lanning, B. R. *et al.* A road map to evaluate the proteome-wide selectivity of covalent kinase inhibitors. *Nat. Chem. Biol.* **10**, 760–767 (2014).
29. Zhao, Z., Liu, Q., Bliven, S., Xie, L. & Bourne, P. E. Determining Cysteines Available for Covalent Inhibition

- Across the Human Kinome. *J. Med. Chem.* **60**, 2879–2889 (2017).
30. Garske, A. L., Peters, U., Cortesi, A. T., Perez, J. L. & Shokat, K. M. Chemical genetic strategy for targeting protein kinases based on covalent complementarity. *Proc. Natl. Acad. Sci. U. S. A.* **108**, 15046–15052 (2011).
 31. Koch, A., Rode, H. B., Richters, A., Rauh, D. & Hauf, S. A chemical genetic approach for covalent inhibition of analogue-sensitive Aurora kinase. *ACS Chem. Biol.* **7**, 723–731 (2012).
 32. Kung, A. *et al.* A Chemical–Genetic Approach to Generate Selective Covalent Inhibitors of Protein Kinases. *ACS Chem. Biol.* **12**, 1499–1503 (2017).
 33. Backus, K. M. *et al.* Proteome-wide covalent ligand discovery in native biological systems. *Nature* **534**, 570–574 (2016).
 34. Barf, T. & Kaptein, A. Irreversible protein kinase inhibitors: Balancing the benefits and risks. *J. Med. Chem.* **55**, 6243–6262 (2012).
 35. Seeliger, M. A. *et al.* High yield bacterial expression of active c-Abl and c-Src tyrosine kinases. *Protein Sci.* **14**, 3135–3139 (2005).
 36. Dann, S. G. *et al.* P120 catenin is a key effector of a Ras-PKC ϵ oncogenic signaling axis. *Oncogene* **33**, 1385–1394 (2014).
 37. Lebraud, H. *et al.* In-gel activity-based protein profiling of a clickable covalent ERK1/2 inhibitor. *Mol. Biosyst.* **12**, 2867–2874 (2016).
 38. Cohen, M. S., Hadjivassiliou, H. & Taunton, J. A clickable inhibitor reveals context-dependent autoactivation of p90 RSK. *Nat. Chem. Biol.* **3**, 156–160 (2007).
 39. Tan, L. *et al.* Structure-guided development of covalent TAK1 inhibitors. *Bioorganic Med. Chem.* **25**, 838–846 (2017).
 40. Fabbro, D., Cowan-Jacob, S. W. & Moebitz, H. Ten things you should know about protein kinases: IUPHAR Review 14. *British Journal of Pharmacology* **172**, 2675–2700 (2015).
 41. Craig, A. W. B., Zirngibl, R. & Greer, P. Disruption of coiled-coil domains in Fer protein-tyrosine kinase abolishes trimerization but not kinase activation. *J. Biol. Chem.* **274**, 19934–19942 (1999).
 42. Islam, K. Allele-specific chemical genetics: Concept, strategies, and applications. *ACS Chem. Biol.* **10**, 343–363 (2015).
 43. Bishop, A. C. *et al.* A chemical switch for inhibitor-sensitive alleles of any protein kinase. *Nature* **407**, 395–401 (2000).
 44. Moyer, T. C., Clutario, K. M., Lambrus, B. G., Daggubati, V. & Holland, A. J. Binding of STIL to Plk4 activates kinase activity to promote centriole assembly. *J. Cell Biol.* **209**, 863–878 (2015).
 45. Zhang, C. *et al.* A second-site suppressor strategy for chemical genetic analysis of diverse protein kinases. *Nat. Methods* **2**, 435–441 (2005).
 46. Au-Yeung, B. B. *et al.* A genetically selective inhibitor demonstrates a function for the kinase Zap70 in regulatory T cells independent of its catalytic activity. *Nat. Immunol.* **11**, 1085–1092 (2010).
 47. Weerapana, E., Simon, G. M. & Cravatt, B. F. Disparate proteome reactivity profiles of carbon electrophiles. *Nat. Chem. Biol.* **4**, 405–407 (2008).
 48. Ogasawara, D. *et al.* Rapid and profound rewiring of brain lipid signaling networks by acute diacylglycerol lipase inhibition. *Proc. Natl. Acad. Sci.* **113**, 26–33 (2016).
 49. Rosenberger, A. F. N. *et al.* Protein kinase activity decreases with higher braak stages of Alzheimer’s disease pathology. *J. Alzheimer’s Dis.* **49**, 927–943 (2015).
 50. Borrelli, K. W., Benjamin, C. & Victor, G. Exploring hierarchical refinement techniques for induced fit docking with protein and ligand flexibility. *J. Comput. Chem.* **31**, 1224–1235 (2010).
 51. Baggelaar, M. P. *et al.* Highly Selective, Reversible Inhibitor Identified by Comparative Chemoproteomics Modulates Diacylglycerol Lipase Activity in Neurons. *J. Am. Chem. Soc.* **137**, 8851–8857 (2015).
 52. Florea, B. I. *et al.* Activity-based profiling reveals reactivity of the murine thymoproteasome-specific subunit $\beta 5t$. *Chem. Biol.* **17**, 795–801 (2010).
 53. Wong, J. C. *et al.* Pharmacokinetic optimization of class-selective histone deacetylase inhibitors and identification of associated candidate predictive biomarkers of hepatocellular carcinoma tumor response. *J. Med. Chem.* **55**, 8903–8925 (2012).
 54. Ménard, D. *et al.* Novel potent BRAF inhibitors: Toward 1 nM compounds through optimization of the central phenyl ring. *J. Med. Chem.* **52**, 3881–3891 (2009).

3

Precise gene editing allows visualization
of endogenous FES kinase engagement
during myeloid differentiation

Introduction

A single human cell may contain over 100 different kinases that work together in a highly regulated network with various physiological functions.^{1,2} Overexpression of a kinase to study its role may therefore disturb the intrinsic balance of the kinase signaling network, leading to compensatory changes and other artefacts in cellular processes.³ This is particularly troublesome in validation of kinases as therapeutic target, as inactivation of overexpressed (and sometimes constitutively active) kinases using small-molecule inhibitors may not match the functional effects resulting from inhibition of endogenously expressed kinases with tightly regulated activity. A prominent example was already observed in [chapter 2](#) ([Figure 2.6E](#)), where overexpression of FES kinase in U2OS cells drastically altered the global cellular phosphotyrosine profile.

Endogenous FES expression levels are highest in cells of hematopoietic origin, especially those in the myeloid lineage, but FES is also expressed in neuronal, endothelial and epithelial cells.⁴ Its initial discovery in terminally differentiated myeloid cells led to multiple studies examining its function in myeloid differentiation. For instance, stable overexpression of FES in K562 cells or transient overexpression of constitutively active FES in U937 cells induces myeloid differentiation towards macrophages.^{5,6} In addition, antisense-mediated knockdown of FES in HL-60 cells was reported to block macrophage differentiation induced by phorbol 12-myristate 13-acetate (PMA).⁷ Deletion of FES in transgenic mice (*fes*^{-/-}) resulted in decreased numbers of B lymphocytes and increased numbers of monocytes and neutrophils⁸, although these effects were not observed in a second, independently generated *fes*^{-/-} mouse strain.⁹ This latter study is in line with the observation that genetic knockout of FES in mouse embryonic stem cells (ESCs) does not impair differentiation towards macrophages, nor towards any other tested myeloid cell type.⁸ Follow-up studies employing transgenic mice expressing a kinase-dead FES variant (*fes*^{KD}) also reported no hematopoietic defects. In contrast, mice expressing an artificial, myristoylated variant (*fes*^{MF}) that harbors constitutive membrane association and thereby increased kinase activity, display increased levels of circulating myeloid cells and decreased levels of erythrocytes and platelets.¹⁰

Taken together, these observations indicate that FES activity is likely to be tightly regulated and that overexpression or constitutive activation of FES disrupts this regulatory process and thus conceals the true physiological role of FES. It remains unclear to what extent congenital, long-term disruption of FES activity in knockout animals induces compensatory mechanisms, such as upregulation of FER. Moreover, the question rises whether the observed effects are dependent on the scaffold function of FES, *e.g.* membrane localization via its F-BAR domain, or on its kinase activity. Here, the chemical genetic toolbox as described in [chapter 2](#), encompassing the use of engineered FES^{S700C} in combination with covalent, complementary probes, is applied to

pharmacologically modulate endogenous FES activity and study its role during myeloid differentiation.

Results

Gene editing allows visualization of kinases by complementary probes in human cells

To obtain a physiologically relevant model system and avoid the use of transient overexpression, CRISPR/Cas9 gene editing was employed to introduce the S700C mutation endogenously in the human HL-60 promyeloblast cell line (Figure 3.1A and 3.1B, step 1-2). Endogenous FES^{S700C} and its engagement by inhibitors can next be visualized using the mutant-specific probes WEL028 and WEL033 and covalently bound targets can be identified using quantitative label-free chemical proteomics (Figure 3.1B, step 3). Wild-type and mutant cells share potential off-targets of WEL028 with the sole exception of FES, which is exclusively targeted in mutant cells. This feature allows for a comparative experimental setup, which is instrumental to dissect on-target from off-target effects and gain insight in the role of FES activity in myeloid differentiation (Figure 3.1B, step 4).

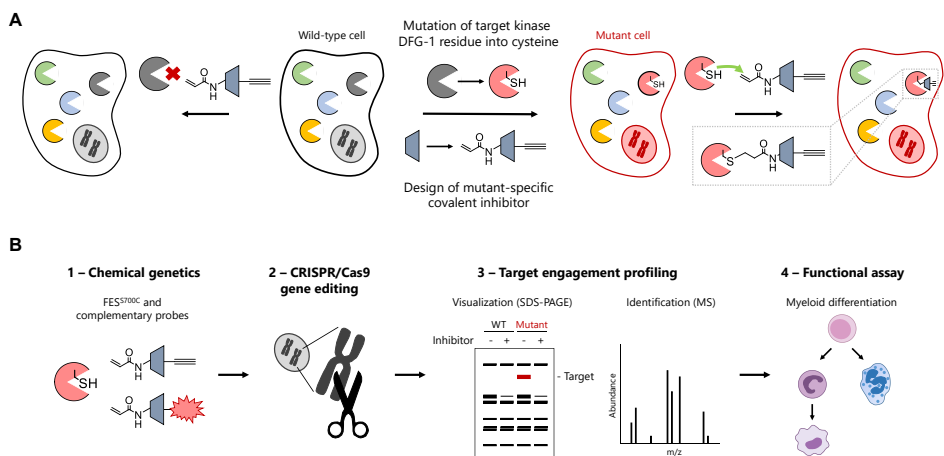


Figure 3.1 – Chemical genetic strategy and workflow to visualize endogenous kinase activity and target engagement. (A) General strategy involving mutagenesis of a kinase DFG-1 residue in a cell line using CRISPR/Cas9 gene editing. This circumvents the use of overexpression that may disturb balanced endogenous signaling networks. Wild-type cells function as control cells to account for potential off-targets of the covalent inhibitor. (B) Schematic workflow encompassing the application of chemical genetic tools described in chapter 2 in an endogenous model system, generated with the use of CRISPR/Cas9 gene editing. Endogenous mutant FES can subsequently be visualized using mutant-specific complementary probes and probe targets can be identified using quantitative label-free proteomics and mass spectrometry analysis. Using this strategy, the role of FES activity during myeloid differentiation can be studied.

HL-60 cells are a widely used model system for myeloid differentiation, since they are capable to undergo differentiation along the neutrophil as well as monocyte/macrophage lineage, depending on the differentiation agent (Figure 3.2A).^{11,12} To sensitize endogenously expressed FES in HL-60 cells to the mutant-specific probe, a single guide (sg)RNA target was selected with predicted site of cleavage in close proximity of the desired mutation in exon 16 of the human genomic *FES* locus (Figure 3.2B). In conjunction, a single-stranded oligodeoxynucleotide (ssODN) homology-directed repair (HDR) donor template was designed, aimed to introduce the target S700C mutation along with the implementation of a restriction enzyme recognition site to facilitate genotyping using a restriction fragment length polymorphism (RFLP) assay. Of note, the ssODN donor also included silent mutations to prevent cleavage of the ssODN itself or recleavage of the genomic locus after successful HDR (Figure 3.2B). HL-60 cells were nucleofected with plasmid encoding sgRNA and Cas9 nuclease along with the ssODN donor, followed by single cell dilution to obtain clonal cultures. Screening of clones using the RFLP assay led to the identification of a homozygous S700C mutant clone (Figure 3.2C). Sanger sequencing verified that the mutations had been successfully introduced without occurrence of undesired deletions or insertions (Figure 3.2D). No off-target cleavage activity was found in predicted putative off-target sites (Supplementary Figure 3.1 and Supplementary Table 3.1).

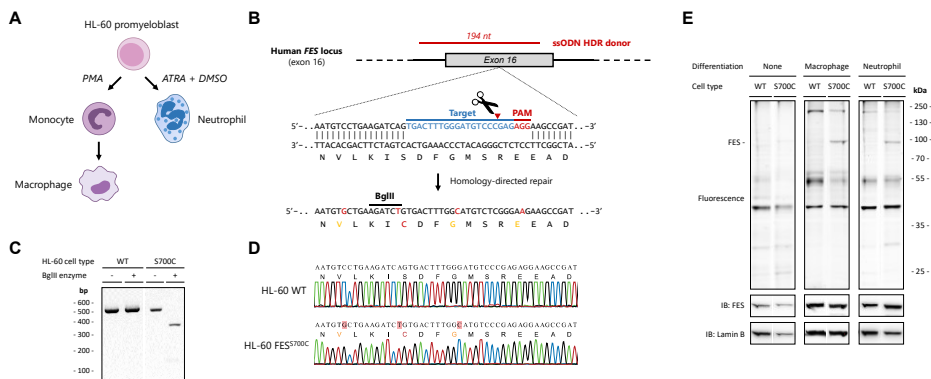


Figure 3.2 - Visualization of endogenous *FES*^{S700C} in CRISPR/Cas9-edited HL-60 cells. (A) HL-60 cells can differentiate into macrophages upon stimulation with PMA or into neutrophils with all-trans-retinoic acid (ATRA) and DMSO. (B) CRISPR/Cas9 gene editing strategy for introduction of S700C point mutation in the genomic *FES* locus. Selected sgRNA (bold blue) directs Cas9 to cleave at predicted site (red triangle). A ssODN homology-directed repair (HDR) donor template (red) flanks introduced mutations with 80 bp homology arms. The S700C mutation generates a BglIII restriction site along with three silent mutations (orange) to remove PAM sites. Of note, two of the three mutated PAM sites correspond to sgRNAs not used in this study. PAM: protospacer-adjacent motif. (C) Restriction-fragment length polymorphism (RFLP) assay for identification of HL-60 *FES*^{S700C} clone. Genomic region was amplified by PCR and amplicons were digested with BglIII. Expected fragment size after digestion: 365 + 133 bp. (D) Sequencing traces of WT HL-60 cells and homozygous *FES*^{S700C} HL-60 clone. No deletions, insertions or undesired mutations were detected. (E) Endogenous FES is visualized by WEL033 in differentiated HL-60 *FES*^{S700C} cells. Wild-type or *FES*^{S700C} HL-60 cells promyeloblasts, macrophages or neutrophils were lysed, followed by labeling with WEL033 (1 μ M, 30 min, rt). FES expression increases upon differentiation (anti-FES immunoblot).

Next, wild-type and HL-60 FES^{S700C} cells were differentiated into macrophages or neutrophils and the corresponding cell lysates were incubated with fluorescent probe WEL033 to visualize endogenous FES (Figure 3.2E). In-gel fluorescence scanning of the WEL033-labeled proteome of differentiated FES^{S700C} HL-60 cells revealed a band at the expected MW of FES (~93 kDa), which was absent in wild-type HL-60 cells. Furthermore, the fluorescent band was less prominent in non-differentiated HL-60 FES^{S700C} cells, probably due to lower FES expression levels prior to differentiation (Figure 3.2E, anti-FES immunoblot). Of note, WEL033 labeled a number of additional proteins (MW of ~200, ~55 and ~40 kDa, respectively) at the concentration used for FES detection (1 μ M). In short, these results demonstrate that endogenously expressed engineered FES can be visualized using complementary chemical probes.

Pharmacological inactivation of FES activity during myeloid differentiation

FES was previously reported as an essential component of the cellular signaling pathways involved in myeloid differentiation.^{7,13} However, most of these studies relied on the use of overexpression, constitutively active mutants, or antisense-based knockdown of FES. In addition, it remains unclear whether this role of FES is dependent on its scaffold function or kinase activity. To investigate whether acute pharmacological inactivation of endogenous FES activity affected myeloid differentiation, living wild-type and FES^{S700C} HL-60 cells were incubated with WEL028 (100 nM or 1 μ M) during PMA-induced differentiation towards monocytes/macrophages. To ensure complete FES inhibition at the moment of differentiation initiation, cells were pretreated with WEL028 2 h prior to addition of PMA. The growth medium was refreshed after 24 h to maintain FES inhibition, since recovery of active FES upon prolonged (> 48 h) exposure to WEL028 was observed, possibly due to protein resynthesis. Cells were harvested and lysed, followed by labeling of residual active FES^{S700C} by WEL033 (Figure 3.3A). This revealed full target engagement of engineered FES at a concentration of 100 nM WEL028 (Figure 3.3B), with only one identified off-target (~200 kDa). At the higher concentration of 1 μ M, WEL028 was less selective and also inhibited additional WEL033-labeled targets.

The percentage of differentiated cells after treatment with the differentiation agent was quantified by monitoring surface expression of CD11b, a receptor present on HL-60 macrophages but not on non-differentiated HL-60 cells.¹⁴ Strikingly, despite complete inhibition of FES^{S700C} at 100 nM WEL028 (Figure 3.3B), the percentage of CD11b-positive cells was unaltered (Figure 3.3C, D). Cell proliferation, an indirect hallmark of differentiation, was decreased to identical levels for FES^{S700C} HL-60 cells treated with vehicle or 100 nM WEL028 (Figure 3.3E). Accordingly, FES^{S700C} HL-60 cells treated with 100 nM WEL028 acquired macrophage morphology (*e.g.* adherence to plastic surfaces, cell clumping and cellular elongation) comparable to vehicle-treated controls (Figure

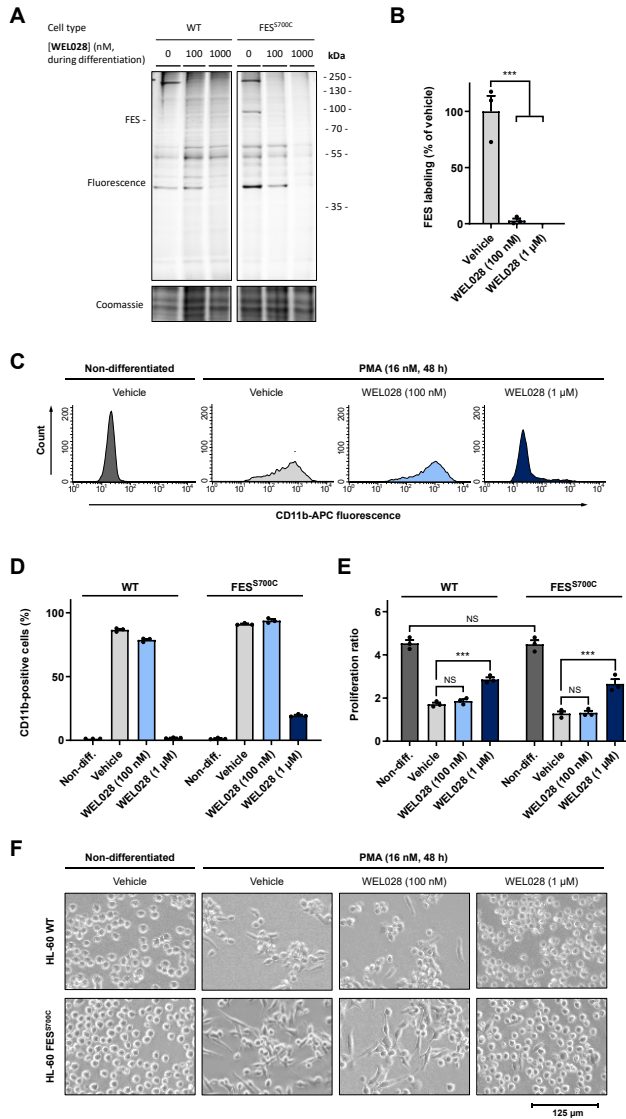


Figure 3.3 – FES activity is dispensable for differentiation of HL-60 cells into macrophages. (A, B) Target engagement profile of WEL028 on WT and FES^{S700C} HL-60 cells treated during PMA-induced differentiation. Cells were pretreated with vehicle or WEL028 (100 or 1000 nM, 1 h) prior to induction of differentiation towards monocytes/macrophages with PMA (16 nM, 48 h). Medium was refreshed with growth medium containing WEL028 and PMA after 24 h to maintain full FES inhibition. Lysates were incubated with WEL033 (1 μM, 30 min, rt). Band intensities were normalized to vehicle-treated control. (C, D) CD11b surface expression analyzed by flow cytometry. Threshold for CD11b-positive cells was determined using isotype control antibody. Histograms illustrate representative replicates of FES^{S700C} cells. (E) Proliferation of WT and FES^{S700C} HL-60 cells subjected to PMA-induced differentiation. Proliferation ratio: live cell number after differentiation divided by live cell number before differentiation. (F) Morphological inspection of WT and FES^{S700C} HL-60 cells. Shown images are representative for multiple acquired images at 20x magnification from replicates. All data represent means ± SEM (N = 3). Statistical analysis was performed using ANOVA with Holm-Sidak's multiple comparisons correction, *** $P < 0.001$; NS if $P > 0.05$.

3.3F). Together, these results show that complete FES inhibition does not affect PMA-induced differentiation of HL-60 cells into macrophages, suggesting that FES activity is dispensable for this process.

Remarkably, FES^{S700C} cells undergoing PMA-induced differentiation in presence of a higher concentration of WEL028 (1 μ M) completely failed to express CD11b, exhibited a less pronounced decrease in proliferation and displayed phenotypic characteristics similar to non-differentiated cells (Figure 3.3C-F). Competitive probe labeling experiments revealed that WEL028 targets multiple off-targets at a concentration of 1 μ M (Figure 3.3A), which suggested that the observed block in differentiation might be due to off-targets. A beneficial feature of the used chemical genetic strategy is that wild-type cells can be included to account for these off-targets. Indeed, 1 μ M WEL028 had similar effects on CD11b surface expression, proliferation and morphology of wild-type HL-60 cells subjected to differentiation (Figure 3.3D-F). This verifies that the functional effects of WEL028 at 1 μ M can indeed be attributed to off-target rather than on-target effects.

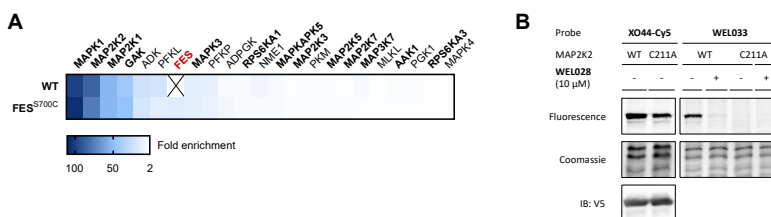


Figure 3.4 – Cellular selectivity profile of WEL028. (A) Chemical proteomic analysis of WEL028 kinase targets at 1 μ M. WEL028-labeled proteome (1 μ M, maintained for 48 h during differentiation) was conjugated to biotin-azide using click chemistry (2 eq., 1 h, 37 $^{\circ}$ C), followed by chemical proteomics workflow. Kinases with >2-fold enrichment compared to vehicle control were designated as targets. Kinases with native cysteine at DFG-1 position are shown in bold. Values represent means of fold enrichment (N = 3). Statistical analysis was performed using *t*-test with Benjamini-Hochberg multiple comparison correction, FDR = 10%. (B) Validation of MAP2K2 as off-target of WEL033 via covalent addition to DFG-1 residue Cys211. Recombinantly expressed MAP2K2 (wild-type or C221A mutant) in U2OS cell lysate was pre-incubated with WEL028 (10 μ M, 30 min, rt), followed by incubation with broad-spectrum kinase probe XO44-Cy5 or probe WEL033 (1 μ M, 30 min, rt). Protein expression was verified by immunoblot against a C-terminal V5-tag.

Quantitative label-free chemical proteomics was used to identify the off-targets of WEL028 at this concentration. The WEL028-labeled proteome was conjugated to biotin-azide post-lysis, followed by streptavidin enrichment, on-bead protein digestion and analysis of the corresponding peptides using mass spectrometry. Significantly enriched kinases in WEL028-treated samples compared to vehicle-treated samples were designated as targets (Figure 3.4A). Identified off-targets included protein kinases harboring native cysteines at the DFG-1 position (depicted in bold), as well as several metabolic kinases (ADK, PFKL, PFKP, ADPGK, NME1, PKM, PGK1), although the latter lack a DFG-motif. Notably, the off-target profile of HL-60 WT and FES^{S700C} cells was identical

with the exception of FES, which was exclusively present in mutant cells. This highlights that, despite a limited number of off-targets, WEL028 can be effectively used in comparative target validation studies between WT and FES^{S700C} HL-60 cells.

Interestingly, the identified off-targets MAPK1/3 and MAP2K1/2 are part of signaling pathways activated upon PMA treatment and are reported to be essential for HL-60 cell differentiation along the monocyte/macrophage lineage.¹⁴ Although MAPK1 and MAPK3 were no prominent targets of WEL028 in the single-dose kinome screen at 1 μ M (< 50% inhibition) (see chapter 2), both were identified as off-targets at this concentration *in situ*. This could result from different *in vitro* and *in situ* inhibitory potencies¹⁵ or high total abundance of these kinases in cells. MAP2K1 and MAP2K2 were already identified in the *in vitro* selectivity assay and although WEL028 showed only a moderate potency on these targets ($pIC_{50} = 6.6 \pm 0.06$), both are likely to be inhibited at a concentration of 1 μ M. Accordingly, recombinantly expressed MAP2K2 was effectively visualized by fluorescent probe WEL033 *in vitro* (Figure 3.4B). Labeling was abolished upon mutagenesis of the corresponding DFG-1 cysteine into an alanine (MAP2K2^{C211A}), verifying that the probe has a similar covalent mode of action as on FES^{S700C}. Notably, labeling with the active site lysine-targeting probe XO44-Cy5² (Supplementary Scheme 3.1) and protein expression levels were similar for MAP2K2^{WT} and MAP2K2^{C211A}. Altogether, these data suggest that the off-targets of WEL028 responsible for the observed block in differentiation at 1 μ M, are likely to be members of the MAP kinase family harboring native DFG-1 cysteine residues.

CRISPR/Cas9-mediated knockout of FES does not affect PMA-induced differentiation

Although FES activity was shown to be dispensable for differentiation of HL-60 cells into macrophages, it remained unclear whether FES played a role in myeloid differentiation based on its scaffold functions. To this end, a CRISPR/Cas9 gene editing strategy was designed to disrupt the *FES* gene and entirely abrogate FES expression (Figure 3.5A). A sgRNA in exon 1 was used to induce double-strand breaks in the coding sequence, which are typically repaired via error-prone non-homologous end joining (NHEJ), generating small deletions or insertions flanking the cleavage site.¹⁶ The use of a sgRNA in an early exon of the *FES* gene increases the probability of obtaining translational frameshifts that result in premature stop codons. Nucleofection of HL-60 cells with plasmid encoding sgRNA and Cas9 nuclease, single cell dilution and screening of clones using a T7 endonuclease I (T7E1) assay led to the identification of a FES^{KO} clone (Figure 3.5B). Decomposition of Sanger sequencing traces using the TIDE web tool¹⁷ revealed the individual gene editing events in the two *FES* alleles, corresponding to an indel of 1 bp and an insertion of 1 bp, respectively (Figure 3.5C). Translation of the edited alleles leads to the introduction of an early stop codon and thereby results in a truncated, dysfunctional protein. In line with this analysis, no residual FES protein was detected in

HL-60 FES^{KO} lysates by immunoblot with an anti-FES antibody (Figure 3.5D). Interestingly, FES^{KO} cells also showed all characteristics of unaffected PMA-induced differentiation compared to wild-type cells, exemplified by a similar percentage of CD11b-positive cells and an identical reduction in proliferation (Figure 3.5E, F). Moreover, FES^{KO} cells acquired macrophage morphology, although cell adhesion to the plastic surface appeared to be slightly impaired (Figure 3.5G). In conclusion, not only FES activity but also FES scaffold functions appear to not be required for differentiation of HL-60 cells in response to PMA treatment.

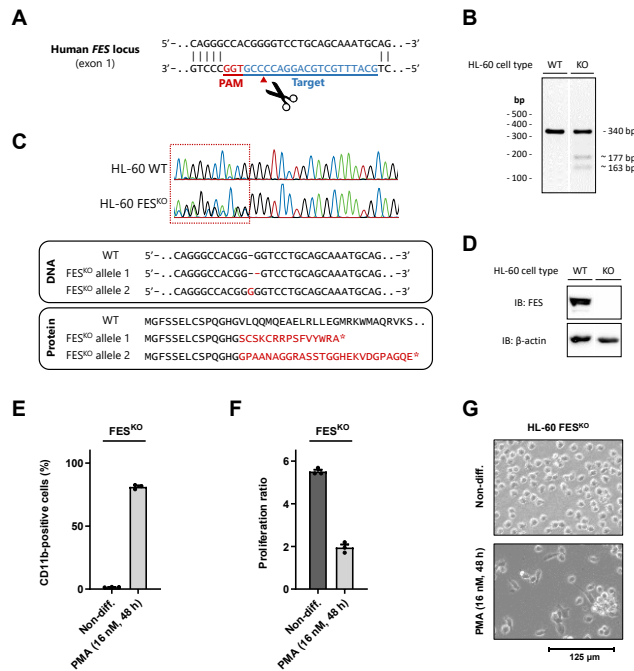


Figure 3.5 - CRISPR/Cas9-mediated knockout of FES does not affect PMA-induced differentiation.

(A) CRISPR/Cas9 gene editing strategy for FES knockout in HL-60 cells. Selected sgRNA (bold blue) directs Cas9 to cleave at predicted site (red triangle). Repair of the induced double-strand break by non-homologous end-joining (NHEJ) results in deletions or insertions that can lead to a translational frameshift and introduction of a premature stop codon. PAM: protospacer-adjacent motif. (B) T7 endonuclease I (T7E1) assay for identification of HL-60 FES^{KO} clone. Genomic region was amplified by PCR and amplicons were analyzed using T7E1 assay. Expected fragment size indicating gene editing events: ~177 and ~163 bp. (C) Sequencing traces of WT HL-60 cells and homozygous FES^{KO} HL-60 clone. Double traces indicate different gene editing events in the two independent *FES* alleles and were decomposed using TIDE analysis (<https://tide.deskgen.com>). (D) Validation of FES knockout by immunoblot analysis on WT or FES^{KO} HL-60 cell lysate using anti-FES antibody. (E) CD11b surface expression of FES^{KO} HL-60 cells incubated without or with PMA (16 nM, 48 h), analyzed by flow cytometry. (F) Proliferation of FES^{KO} HL-60 cells incubated as in E. Proliferation ratio: live cell number after differentiation divided by live cell number before differentiation. (G) Morphological inspection of FES^{KO} HL-60 cells. Shown images are representative for multiple acquired images at 20x magnification from replicates. All data represent means ± SEM (N = 3). Statistical analysis was performed using ANOVA with Holm-Sidak's multiple comparisons correction, *** *P* < 0.001; NS if *P* > 0.05.

Discussion and conclusion

Previously reported chemical genetic methods rely on overexpression systems that disturb signal transduction cascades.³ In contrast, a major benefit of the strategy described in this chapter lies in the ability to exert unprecedented control over a biological system without disturbing cellular homeostasis. One single atom out of 13.171 atoms in FES was replaced by changing only one base pair out of over 3.000.000.000 base pairs in the human genome. Arguably, this minimal change at the genome and protein level ensures that its regulation at transcriptional and (post-)translational level are minimally disturbed. In fact, it was demonstrated that wild-type and mutant cells behaved similarly in various functional assays (e.g. proliferation, differentiation, morphology and CD11b surface expression). This is in line with the comprehensive biochemical profiling of FES^{S700C} as described in chapter 2, which showed that its kinase activity, substrate preference and protein-protein interactions were similar to FES^{WT}. Yet, the conversion of an oxygen atom in a sulphur atom in the endogenously expressed protein allowed the rational design and synthesis of a chemical probe that visualizes and inhibits the engineered kinase activity in human cells.

The use of fluorescent probe WEL033 was key to visualize target engagement of FES during myeloid differentiation of HL-60 cells towards monocytes/macrophages. In contrast to previous studies relying on transient overexpression of FES or RNA knockdown approaches^{7,13}, no defects in differentiation were observed despite complete acute inhibition of FES activity. In line with these results, FES knockout mice display no defects in myeloid cell differentiation and survival, as reflected by unaltered numbers of various blood cell types, including monocytes and neutrophils, compared to wild-type mice^{9,18}. Altogether, this study suggests that FES kinase activity is dispensable for differentiation of HL-60 cells along the monocyte/macrophage lineage. In addition, CRISPR/Cas9-mediated knockout of FES did not affect PMA-induced differentiation either, although it should be taken into account that long-term genetic disruption may lead to compensatory effects.

A major advantage of the used chemical genetic method is the ability to use wild-type cells as a control to account for potential off-target effects. In this way, even a chemical probe with a limited number of defined off-targets can be effectively used for functional studies. Indeed, the off-target profile of WEL028 was identical in both wild-type and mutant HL-60 cells and the only difference in their WEL028-reactive proteome was the engineered kinase FES. The importance of distinguishing on-target from off-target effects is illustrated by the observation that WEL028 at higher concentrations disrupted differentiation of HL-60 cells. The here presented strategy was instrumental to identify that the observed effects, however, also occurred in wild-type control cells and can thus be attributed to inhibition of off-targets, rather than FES. A competitive

chemical proteomics experiment with a broad-spectrum kinase probe, such as XO44, could be employed to quantify cellular target engagement of WEL028 on off-targets.

An interesting next step would be to explore the effect of FES inactivation during differentiation of more physiologically relevant precursor cells, such as hematopoietic stem cells (HSCs). Myeloid differentiation of these cells is induced by (complex mixtures of) growth factors and cytokines and thus relies on multiple downstream signaling pathways.¹⁹ FES is currently under consideration as a therapeutic target for acute myeloid leukemia (AML)^{20,21}, a disease characterized by defective differentiation and excessive proliferation of HSCs.²² Consequently, differentiation therapy (*e.g.* with *all-trans* retinoic acid) is currently used in some AML subtypes.²³ Further investigation of the role of FES in HSCs differentiation is thus relevant, because if FES is required for this process, FES inhibitors may possibly counter-act these AML treatments. Tremendous advancements in CRISPR/Cas9 gene editing and base editing technologies will provide means to efficiently introduce the S700C mutation in the *FES* locus in HSCs²⁴ and apply this chemical genetic toolbox in a more physiologically relevant model system.

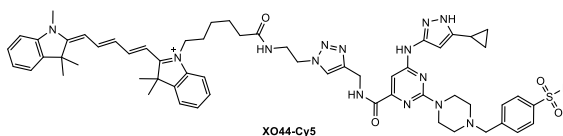
Acknowledgments

Hans den Dulk is kindly acknowledged for technical assistance with cell culture, Bogdan I. Florea for mass spectrometry analysis, Rolf Boot for useful advice and providing plasmids, and Laura de Paus for synthesis of XO44-Cy5.

Experimental procedures

General

All chemicals were purchased at Sigma Aldrich, unless stated otherwise. DNA oligos were purchased at Sigma Aldrich or Integrated DNA Technologies. Cloning reagents were obtained from Thermo Fisher. XO44-Cy5 was previously synthesized in-house based on literature procedures² and characterized by NMR and LC-MS. All cell culture disposables were purchased at Sarstedt. Mammalian protease inhibitor cocktails were obtained from Amresco.



Supplementary Scheme 3.1 – Structure of active site lysine-targeting broad-spectrum kinase probe XO44-Cy5.

Cloning

For CRISPR/Cas9 plasmids, guides were cloned into the BbsI restriction site of plasmid px330-U6-Chimeric_BB-CBh-hSpCas9 (gift from Feng Zhang, Addgene plasmid #42230) as previously described.^{25,26} pDONR223-construct with full-length human cDNA of MAP2K2 was a gift from William Hahn & David Root (Addgene Human Kinase ORF Collection). Eukaryotic expression constructs of MAP2K2 was generated using Gateway™ recombinational cloning into a pcDest40 vector, in frame with a C-terminal V5-tag, according to recommended procedures (Thermo Fisher). Point mutations were introduced by site-directed mutagenesis and all plasmids were isolated from transformed XL10-Gold competent cells (prepared using *E. coli* transformation buffer set; Zymo Research) using plasmid isolation kits following the supplier's protocol (Qiagen). All sequences were verified by Sanger sequencing (Macrogen).

Supplementary Table 3.3 – List of oligonucleotide sequences.

ID	Name	Sequence
P1	sgRNA_hFES-MUT_S700C_top	CACCTGACTTTGGGATGTCCTCCGAG
P2	sgRNA_hFES-MUT_S700C_bott	AAACCTCGGACATCCCAAAGTCA
P3	gPCR_hFES_S700C_forw	TTTTGTCTTGGCTTTCCTAGA
P4	gPCR_hFES_S700C_rev	GTGCTTACCCCTTCCACAAC
P5	HDR-template_hFES_S700C	ACTGTGGCCAAATGAGCCCTGCGCTGTCTACCCAGGGACCTGGGCTG CTCGGAATGCTGCTGTGACAGAGAAGAATGTGCTGAAGATCTGTGACTTT GGCATGTCCCGAAGAAGCCGATGGGGTCTATGCAGCCTCAGGGGGC CTCAGACAAGTCCCGTGAAGTGGACCGCACCTGAGGCCCTTAATA
P6	sgRNA_hFES-KO_exon1_top	CACCGCATTTGCTGCAGGACCCCG
P7	sgRNA_hFES-KO_exon1_bott	AAACCGGGTCTCGAGCAAATGC
P8	gPCR_hFES-KO_exon1_forw	CAGTCCATCCTGACCCTACAGT
P9	gPCR_hFES-KO_exon1_rev	AGAGTCCATAGAGACCACCT
P10	gPCR_TTC16_forw	AGAACAGACGGTGTGTAAGCAT
P11	gPCR_TTC16_rev	ATTAGACAGTTGAGTTCACCTGAGGC
P12	gPCR_TCIRG1_forw	AGAGTCTCGTAGCTGTGCTCTCT
P13	gPCR_TCIRG1_rev	CAGGTACACGGCCTTCATCT
P14	MAP2K2_C211A_forw	AGGGGAGATCAAGCTAGCTGACTCGGGGTGAG
P15	MAP2K2_C211A_rev	CTCACCCGGAAGTCAGTAGTGTGATCTCCCT

Cell culture

General cell culture

Cell lines were purchased at ATCC and were tested on regular basis for mycoplasma contamination. Cultures were discarded after 2-3 months of use. U2OS (human osteosarcoma) cells were cultured at 37 °C under 7% CO₂ in DMEM containing phenol red, stable glutamine, 10% (v/v) heat-inactivated newborn calf serum (Seradigm), penicillin and streptomycin (200 µg/mL each; Duchefa). Medium

was refreshed every 2-3 days and cells were passaged two times a week at 80-90% confluence. HL-60 (human promyeloblast) cells were cultured at 37 °C under 5% CO₂ in HEPES-supplemented RPMI containing phenol red, stable glutamine, 10% (v/v) fetal calf serum (Biowest), penicillin and streptomycin (200 µg/mL each), unless stated otherwise. Cell density was maintained between 0.2 x 10⁶ and 2.0 x 10⁶ cells/mL. Cell viability was assessed by Trypan Blue exclusion and quantification using a TC20™ Automated Cell Counter (Bio-Rad).

Transfection of U2OS cells

One day prior to transfection, U2OS cells were transferred from confluent 10 cm dishes to 15 cm dishes. Before transfection, medium was refreshed (13 mL). A 3:1 (m/m) mixture of polyethyleneimine (PEI; 60 µg/dish) and plasmid DNA (20 µg/dish) was prepared in serum-free medium and incubated for 15 min at rt. The mixture was then dropwisely added to the cells, after which the cells were grown to confluence in 72 h. Cells were then harvested by suspension in PBS, followed by centrifugation for 5 min at 200 g. Cell pellets were flash-frozen in liquid nitrogen and stored at -80 °C until sample preparation.

Transfection of HL-60 cells

Transfection of CRISPR plasmid DNA and ssODN repair template into HL-60 cells was performed using Amaxa nucleofector kit V and nucleofector I device (Lonza). One day prior to transfection, HL-60 cells were diluted to a density of 0.4 x 10⁶ cells/mL. The next day, 2 x 10⁶ cells per condition were centrifuged (200 g, 5 min) and resuspended in 100 µL nucleofection solution. Plasmid DNA (2 µg) and if applicable ssODN repair template (400 pmol) were added and cells were nucleofected using program T-019. Cells were allowed to recover (10 min, rt) before transfer to 12-well plates in antibiotics-free medium at 37 °C.

Differentiation of HL-60 cells towards monocytes/macrophages

One day prior to induction of differentiation, cells were diluted to 0.4 x 10⁶ cells/mL. The next day, monocytic/macrophage differentiation was induced by addition of phorbol 12-myristate 13-acetate (PMA) to a final concentration of 16 nM. Cells were grown for 48 h unless indicated otherwise, during which cells attached to the plastic surface and acquired macrophage characteristics. For morphological inspection, images were taken on an EVOS FL Auto 2 Imaging System (Thermo Fisher) at 20x magnification.

Inhibitor treatment in live cells

The term *in situ* is used to designate experiments in which live cell cultures are treated with inhibitor, whereas the term *in vitro* refers to experiments in which the inhibitor is incubated with cell lysates. Compounds were diluted in growth medium from a 1000x concentrated stock solution in DMSO.

For *in situ* treatment of HL-60 cells during differentiation, HL-60 cells were prepared for differentiation as described above. Cells were pre-incubated with compound for 1 h before differentiation was induced by addition of differentiation agents as described above. Medium was refreshed every 24 h with medium containing equal inhibitor and differentiation agent concentrations.

For *in situ* treatment post-differentiation, HL-60 cells were differentiated as described above, after which cells were incubated with compound for 1 h. Cells were collected by suspension for non-adherent cells and trypsinization for adherent cells. After collection, cells were centrifuged (200 g, 5 min, rt) and washed in equal volume of PBS (1000 g, 5 min, rt). Cell pellets were flash-frozen in liquid nitrogen and stored at -80 °C until use.

CRISPR/Cas9 gene editing

sgRNA selection and ssODN homology-directed repair (HDR) donor design

Selection of sgRNA was based on proximity to desired site of cleavage or mutagenesis as well as efficiency and specificity as predicted by CHOPCHOP v2 online web tool (<http://chopchop.cbu.uib.no>)²⁷. sgRNA sequences can be found in Supplementary Table 3.3. For FES knockout, a sgRNA targeting exon 1 was selected. For FES mutagenesis, a sgRNA targeting exon 16 was selected and an ssODN HDR donor was designed that after successful HDR incorporates the desired S700C mutation along with a BglII restriction site to facilitate analysis by RFLP. Furthermore, silent mutations are incorporated to remove “NGG” protospacer adjacent motifs (PAMs), preventing recleavage of the genomic sequence after successful HDR or cleavage of the ssODN donor itself.

Single cell isolation and expansion

For preparation of conditioned RPMI medium, HL-60 cells were diluted to 0.2×10^6 cells/mL and grown for 48 h at 37 °C. Cell suspension was then centrifuged (1,000 *g*, 5 min) and medium was transferred to a sterile tube, followed by a second centrifugation step (3,500 *g*, 10 min). The medium was subsequently filtered through a 0.2 µm sterile filter and stored at -80 °C until use, for no longer than 3 months.

Single cell cultures were obtained approximately 7 days post-nucleofection by dilution in 1:1 conditioned and fresh RPMI medium and expanded in 96-well plates (100 µL per well). After 14 days, plates were inspected for cell growth, clones were collected in new plates and half of the volume was transferred to 96-well PCR-plates, followed by centrifugation (1,000 *g*, 10 min). Medium was removed and cell pellets were suspended in 25 µL QuickExtract™ (Epicentre). The samples were incubated at 65 °C for 6 min, mixed by vortexing and then incubated at 98 °C for 2 min. Genomic DNA extracts were diluted in sterile water and directly used in PCR reactions. Genomic PCR reactions were performed on 5 µL isolated genomic DNA extract using Phusion High-Fidelity DNA Polymerase (Thermo Fisher) in Phusion HF buffer in a final volume of 20 µL.

Genotyping assays

For T7E1 assays, genomic PCR products were mixed in a 1:1 ratio with wild-type amplicons and denatured and reannealed in a thermocycler using the following program: 5 min at 95 °C, 95 to 85 °C using a ramp rate of -2 °C/s, 85 to 25 °C using a ramp rate of -0.2 °C/s. To annealed PCR product (8.5 µL), NEB2 buffer (1 µL) and T7 endonuclease I (5 U, 0.5 µL; New England Biolabs) were added, followed by incubation at 37 °C for 30 min. Restriction Fragment Length Polymorphism (RFLP) assays were performed by directly combining genomic PCR product (8.5 µL) with FastDigest buffer (1 µL) and FastDigest BglII (0.5 µL), followed by incubation at 37 °C for 30 min. Digested PCR products were analyzed using agarose gel electrophoresis with ethidium bromide staining.

Sanger sequencing for gene editing and off-target analysis

Genomic PCR products were purified using NucleoSpin® Gel and PCR Clean-up kit (Macherey-Nagel) prior to Sanger sequencing. For knockouts, sequence traces were decomposed using the TIDE web tool (<https://deskgen.com>).¹⁷ Potential off-target cleavage sites of the used sgRNA were predicted using DESKGEN™ online web tool (<https://deskgen.com>). Top-ranked potential coding off-target sequences containing 3 or less mismatches to the employed sgRNA sequence were selected for validation. The genomic region surrounding the potential off-target site was amplified by PCR and analyzed by Sanger sequencing.

Preparation of cell lysates

Pellets were thawed on ice and suspended in lysis buffer (50 mM HEPES pH 7.2, 150 mM NaCl, 1 mM MgCl₂, 0.1% (w/v) Triton X-100, 2 mM Na₃VO₄, 20 mM NaF, 1 x mammalian protease inhibitor cocktail, 25 U/mL benzonase). Cells were lysed by sonication on ice (15 cycles of 4" on, 9.9" off at 25% maximum amplitude). Alternatively (Figure S2-4), pellets were thawed on ice and suspended in

M-PER buffer supplemented with 1x Halt™ phosphatase and protease inhibitor cocktail (Thermo Fisher), followed by centrifugation (14,000 *g*, 10 min, 4 °C). Protein concentration was determined using Quick Start™ Bradford Protein Assay (Bio-Rad) and lysates were aliquoted, flash-frozen and stored at -80 °C until use.

Probe labeling experiments

For *in vitro* inhibition experiments, cell lysate (14 μ L) was pre-incubated with inhibitor (0.5 μ L, 29 x concentrated stock in DMSO, 30 min, rt), followed by incubation with probe WEL033 or XO44-Cy5 (0.5 μ L, 30 x concentrated stock in DMSO, 30 min, rt). For *in situ* inhibition experiments, treated cell lysate (14.5 μ L) was directly incubated with probe (0.5 μ L, 30 x concentrated stock in DMSO, 30 min, rt). Final concentrations of inhibitors and/or probe are indicated in figure legends. Reactions were quenched with 4x Laemmli buffer (5 μ L, final concentrations 60 mM Tris pH 6.8, 2% (w/v) SDS, 10% (v/v) glycerol, 5% (v/v) β -mercaptoethanol, 0.01% (v/v) bromophenol blue) and boiled for 5 min at 95 °C. Samples were resolved by SDS-PAGE on a 10% polyacrylamide gel (180 V, 75 min). Gels were scanned using Cy3 and Cy5 multichannel settings (605/50 and 695/55 filters, respectively; ChemiDoc™ MP System, Bio-Rad). Fluorescence intensity was corrected for protein loading determined by Coomassie Brilliant Blue R-250 staining and quantified with Image Lab (Bio-Rad). IC₅₀ curves were fitted with Graphpad Prism® 7 (Graphpad Software Inc.).

Proteomics

Proteomics was performed based on previously described procedures.²⁸ In summary, full cell lysates of FES^{WT} and FES^{S700C} HL-60 cells incubated *in situ* with vehicle, 100 nM or 1 μ M WEL028 during PMA-induced differentiation were prepared as aforementioned. Click mix was freshly prepared by combining CuSO₄ (1 μ L of 15 mM stock), sodium ascorbate (0.6 μ L of 150 mM stock), THPTA (0.2 μ L of 15 mM stock) and biotin-azide (0.2 μ L of 4 mM stock in DMSO). Lysates (250 μ L of 2 mg/mL) were conjugated to biotin-azide using click chemistry (25 μ L click mix, 1 h, 37 °C). The reaction was quenched and excess biotin-azide was removed by chloroform/methanol precipitation. Precipitated proteome was suspended in 6 M urea in 25 mM ammonium bicarbonate, reduced (10 mM DTT, 15 min, 65 °C) and alkylated (40 mM iodoacetamide, 30 min, rt, in the dark). SDS was added (2% final concentration, 5 min, 65 °C), samples were diluted in PBS and incubated with avidin beads (from 50% slurry, 3 h, rt, in overhead rotator). Beads were washed with 0.5% SDS in PBS, followed by 3 washes with PBS, and then transferred to low-binding Eppendorf tubes. Proteins were digested with trypsin overnight at 37 °C and resulting peptides were desalted using stage tips with C₁₈ material. Samples were analyzed on an LC-IMS-MS system with a Synapt G2-Si instrument (Waters) as previously described²⁸. Data processing was performed with ISOQuant software as previously described.^{29,30} The following cut-offs were used for target identification: unique peptides \geq 1, identified peptides \geq 2, ratio WEL028-treated over vehicle-treated \geq 2 with q-value < 0.05 based on *t*-test with Benjamini-Hochberg multiple comparison correction (FDR = 10%), kinase annotation in Uniprot database.

Immunoblot

Samples were resolved by SDS-PAGE as described above, but transferred to 0.2 μ m polyvinylidene difluoride membranes by Trans-Blot Turbo™ Transfer system (Bio-Rad) directly after fluorescence scanning. Membranes were washed with TBS (50 mM Tris pH 7.5, 150 mM NaCl) and blocked with 5% milk in TBS-T (50 mM Tris pH 7.5, 150 mM NaCl, 0.05% Tween-20) for 1 h at rt. Membranes were then either incubated with primary antibody in 5% milk in TBS-T (V5; o/n at 4 °C) or washed three times with TBS-T, followed by incubation with primary antibody in 5% BSA in TBS-T (FES, Lamin B, β -actin, o/n at 4 °C). Membranes were washed three times with TBS-T, incubated with matching secondary antibody in 5% milk in TBS-T (1 h at rt) and then washed three times with TBS-T and once with TBS. Luminol development solution (10 mL of 1.4 mM luminol in 100 mM Tris pH 8.8 + 100 μ L of 6.7 mM *p*-coumaric acid in DMSO + 3 μ L of 30% (v/v) H₂O₂) was added and chemiluminescence was detected on ChemiDoc™ MP System.

Primary antibodies: monoclonal rabbit anti-FES (1:1000, Cell Signaling Technology (CST), #85704), polyclonal rabbit anti-Lamin B1 (1:5000, Thermo Fisher, PA5-19468), monoclonal mouse anti- β -actin (1:1000, Abcam, ab8227), monoclonal mouse anti-V5 (1:5000, Thermo Fisher, R960-25). Secondary antibodies: goat anti-mouse-HRP (1:5000, Santa Cruz, sc-2005), goat anti-rabbit-HRP (1:5000, Santa Cruz, sc-2030).

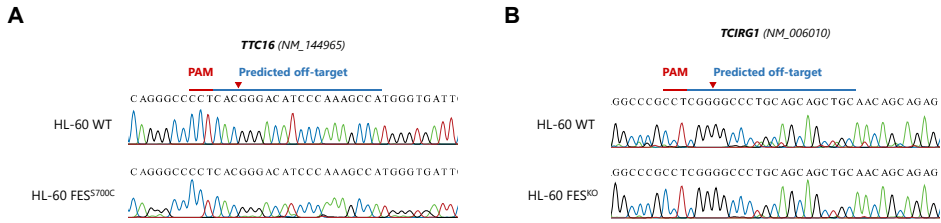
CD11b expression analysis by flow cytometry

Cells (1×10^6 per sample) were centrifuged (500 *g*, 3 min) and suspended in human FcR blocking solution (Miltenyi Biotec, 25x diluted in FACS buffer (1% BSA, 1% FCS, 0.1% NaN_3 , 2 mM EDTA in PBS)), transferred to a V-bottom 96-well plate and incubated for 10 min at 4 °C. Next, monoclonal rat CD11b-APC antibody (1:100, Miltenyi Biotec, 130-113-231) or rat anti-IgG2b-APC isotype control antibody (1:100, Miltenyi Biotec, 130-106-728) was added along with 7-AAD (7-aminoactinomycin D; 1 $\mu\text{g}/\text{mL}$) and samples were incubated for 30 min 4 °C in the dark. Samples were washed once in PBS and fixed in 1% PFA in PBS for 15 min at 4 °C in the dark, followed by two washing steps in PBS and resuspension in FACS buffer to a density of approximately 500 cells/ μL . Cell suspensions were measured on a Guava easyCyte HT and data was processed using GuavaSoft InCyte 3.3 (Merck Millipore). Events (generally 10,000 per condition) were gated by forward and side scatter (cells), side scatter area (singlets) and viability (live cells) and the percentage of CD11b-positive cells was determined based on background fluorescence for isotype control antibody and non-differentiated cells. The RED-R channel (661/15 filter) and RED-B channel (695/50 filter) were used to detect CD11b-APC and 7-AAD, respectively.

Statistical analysis

All statistical measures and methods are included in the respective Figure or Table captions. In brief, all replicates represent biological replicates and all data represent means \pm SEM, unless indicated otherwise. Statistical significance was determined using Student's *t*-tests (two-tailed, unpaired) or ANOVA with Holm-Sidak's multiple comparisons correction. *** $P < 0.001$; ** $P < 0.01$; * $P < 0.05$; NS if $P > 0.05$. All statistical analyses were conducted using GraphPad Prism® 7 or Microsoft Excel.

Supplementary Data



Supplementary Figure 3.1 - Analysis of putative sgRNA off-target sites. (A, B) Analysis of the only predicted coding off-targets of the sgRNA target sequence employed for FES^{S700C} mutagenesis, located in the *TTC16* gene (A), or for FES knockout, located in the *TCIRG1* gene (B). Genomic region surrounding putative off-target site was amplified by PCR, followed by Sanger sequencing analysis. No off-target gene editing events were observed.

Supplementary Table 3.1 - List of putative off-target cleavage sites for sgRNA employed in CRISPR/Cas9-mediated mutagenesis of FES. Specificity of sgRNA was assessed using DESKGEN™ online web tool (www.deskgen.com). Sites with 3 or less mismatches compared to the sgRNA target were included. Only 1 putative off-target is located in the coding region of a gene.

S700C	Mismatches	0	1	2	3
	Coding		0	0	1
Non-coding		0	0	1	12

Potential off-target sequence	PAM	Similarity	Mismatches	Gene	Locus
TGGCTTTGGGATGCCCGTG	AGG	5	3,19	Yes	chr9@ 127716868-127716891
TGACTTTGGCATGCCTGAG	AGG	3	10,17	No	chr16@ 50371486-50371509
TTAGTTTGGGATGCCAGAG	GGG	1	2,4,17	No	chr2@ 147874374-147874397
TGCCITTTGGTATGCCAGAG	TAG	1	3,10,17	No	chr13@ 25630797-25630820
AGACTTTGGGAGGTCCCCTG	CAG	1	1,12,19	No	chr12@ 11447626-11447649
TGGCTGTGGGATGCCCCAG	GAG	0	3,6,18	No	chr3@ 13295903-13295926
TGAGTCTGGGATGCCCTAG	AGG	0	4,6,18	No	chr5@ 137202156-137202179
TGGCTTTGGGATGCCGGAG	AAG	0	3,16,17	No	chr20@ 61773235-61773258
TGAATTTGGGATGCCCATG	TAG	0	4,18,19	No	chr5@ 135589616-135589639
TGAATTTGGGATGCCCTGAG	AGG	0	4,14,17	No	chr5@ 61639561-61639584
TGACGTTGGGATGCCAGAG	CAG	0	5,14,17	No	chr19@ 35077359-35077382
TGACTTTGGGTTGCCCCAT	GAG	0	11,18,20	No	chrX@ 112142232-112142255
TGACTTTGGGGTCTCCCAAG	AGG	0	11,13,18	No	chr2@ 95278649-95278672

Supplementary Table 3.2 - List of putative off-target cleavage sites for sgRNA employed in CRISPR/Cas9-mediated knockout of FES. Specificity of sgRNA was assessed using DESKGEN™ online web tool (www.deskgen.com). Sites with 3 or less mismatches compared to the sgRNA target were included. Only 1 putative off-target is located in the coding region of a gene.

KO	Mismatches	0	1	2	3
	Coding		0	0	0
Non-coding		0	0	1	23

Potential off-target sequence	PAM	Similarity	Mismatches	Gene	Locus
GCAGCTGCTGCAGGGCCCCG	AGG	1	4,5,15	Yes	chr11@ 68043858-68043881
GCATTTGATGCAGGACCCCT	CAG	4	8,20	No	chr10@ 123647319-123647342
GGCTTGCTCCAGGACCCCG	AGG	2	2,3,10	No	chr15@ 73308252-73308275
GCAGTTACTCCAGGACCCCG	AAG	2	4,7,10	No	chr11@ 124673324-124673347
GCCCTTGCTGCAGGACCCCG	AAG	1	3,4,20	No	chr17@ 40461935-40461958
GCAGCTGCTGCAGGACCCCT	GAG	1	4,5,20	No	chr15@ 88681640-88681663
AGATTGCTGCAGGACCCCTG	AAG	1	1,2,19	No	chr10@ 127843251-127843274
GCATTTACTTCTGGACCCCG	GGG	1	7,10,12	No	chr10@ 119366165-119366188
CCATTTGCTGCTGGACCCCA	GAG	1	1,12,20	No	chr17@ 49938799-49938822
GCACTTCTGCAGGACCCCTG	GGG	1	4,7,19	No	chr11@ 1161797-1161820
GCAATTACTGCAGGACCCAG	CAG	1	4,7,19	No	chr3@ 14607567-14607590
GCAGTTGCTGCTGGACCCAG	GGG	1	4,12,19	No	chr10@ 117925154-117925177
GGATTTGCTGCAGGACTCTG	GAG	0	2,17,19	No	chr19@ 58096538-58096561
GCACTTCTGCAGGACTCTG	CAG	0	4,17,19	No	chr4@ 173717653-173717676
ACATTTGCTGCAGGCCCCAG	AGG	0	1,15,19	No	chr5@ 144567565-144567588
GGATTTGCTGCAGGTCCCTG	CAG	0	2,15,19	No	chr18@ 46311931-46311954
TCATTTGCTGCAGGAACCCCT	GAG	0	1,16,20	No	chr2@ 240787656-240787679
GCATTTACTGCATGACCCCTG	GGG	0	7,13,19	No	chr16@ 59837242-59837265
GCATTTACTGCAGGACTCAG	GGG	0	7,17,19	No	chr14@ 98430008-98430031
GCATTTGCTGGAGGACTCCA	GAG	0	11,17,20	No	chr14@ 64605317-64605340
GCATTCGCTGCAGGACTCTG	CAG	0	6,17,19	No	chr6@ 32495339-32495362
GCATTTGAGCAGGTCCAG	GAG	0	9,15,19	No	chr20@ 63162513-63162536
GCATTTGCTGCCGGAGCCCC	AAG	0	12,16,20	No	chr16@ 1264116-1264139

References

- Jordan, J. D., Landau, E. M. & Iyengar, R. Signaling Networks. *Cell* **103**, 193–200 (2000).
- Zhao, Q. *et al.* Broad-spectrum kinase profiling in live cells with lysine-targeted sulfonyl fluoride probes. *J. Am. Chem. Soc.* **139**, 680–685 (2017).
- Prelich, G. Gene overexpression: Uses, mechanisms, and interpretation. *Genetics* **190**, 841–854 (2012).
- Haigh, J., McVeigh, J. & Greer, P. The *fps/fes* tyrosine kinase is expressed in myeloid, vascular endothelial, epithelial, and neuronal cells and is localized in the trans-golgi network. *Cell growth Differ.* **7**, 931–44 (1996).
- Yu, G., Smithgall, T. E. & Glazer, R. I. K562 leukemia cells transfected with the human *c-fes* gene acquire the ability to undergo myeloid differentiation. *J. Biol. Chem.* **264**, 10276–10281 (1989).
- Kim, J. & Feldman, R. A. Activated Fes protein tyrosine kinase induces terminal macrophage differentiation of myeloid progenitors (U937 cells) and activation of the transcription factor PU.1. *Mol. Cell. Biol.* **22**, 1903–18 (2002).
- Manfredini, R. *et al.* Antisense inhibition of *c-fes* proto-oncogene blocks PMA-induced macrophage differentiation in HL60 and in FDC-P1/MAC-11 cells. *Blood* **89**, 135–145 (1997).
- Hackenmiller, R., Kim, J., Feldman, R. A. & Simon, M. C. Abnormal stat activation, hematopoietic homeostasis, and innate immunity in *c-fes(-/-)* mice. *Immunity* **13**, 397–407 (2000).
- Senis, Y. *et al.* Targeted disruption of the murine *fps/fes* proto-oncogene reveals that Fps/Fes kinase activity is dispensable for hematopoiesis. *Mol. Cell. Biol.* **19**, 7436–7446 (1999).
- Greer, P. Closing in on the biological functions of Fps/Fes and Fer. *Nat. Rev. Mol. Cell Biol.* **3**, 278–89 (2002).
- Birnie, G. D. The HL60 cell line: a model system for studying human myeloid cell differentiation. *Br. J. Cancer* **9**, 41–45 (1988).
- Hauert, A. B., Martinelli, S., Marone, C. & Niggli, V. Differentiated HL-60 cells are a valid model system for the analysis of human neutrophil migration and chemotaxis. *Int. J. Biochem. Cell Biol.* **34**, 838–854 (2002).
- Kim, J., Ogata, Y., Ali, H. & Feldman, R. a. The Fes tyrosine kinase: a signal transducer that regulates myeloid-specific gene expression through transcriptional activation. *Blood Cells. Mol. Dis.* **32**, 302–308 (2004).
- Miranda, M. B., McGuire, T. F. & Johnson, D. E. Importance of MEK-1/-2 signaling in monocytic and granulocytic differentiation of myeloid cell lines. *Leukemia* **16**, 683–92 (2002).
- van Esbroeck, A. C. M. *et al.* Activity-based protein profiling reveals off-target proteins of the FAAH inhibitor BIA 10-2474. *Science* **356**, 1084–1087 (2017).
- Maruyama, T. *et al.* Increasing the efficiency of precise genome editing with CRISPR-Cas9 by inhibition of nonhomologous end joining. *Nat. Biotechnol.* **33**, 538–42 (2015).
- Brinkman, E. K., Chen, T., Amendola, M. & Van Steensel, B. Easy quantitative assessment of genome editing by sequence trace decomposition. *Nucleic Acids Res.* **42**, e168–e168 (2014).
- Zirngibl, R. A., Senis, Y. & Greer, P. A. Enhanced Endotoxin Sensitivity in Fps/Fes-Null Mice with Minimal Defects in Hematopoietic Homeostasis. *Mol. Cell. Biol.* **22**, 2472–2486 (2002).
- Wahlster, L. & Daley, G. Q. Progress towards generation of human haematopoietic stem cells. *Nature Cell Biology* **18**, 1111–1117 (2016).
- Voisset, E. *et al.* FES kinases are required for oncogenic FLT3 signaling. *Leukemia* **24**, 721–728 (2010).
- Weir, M. C. *et al.* Dual inhibition of Fes and Flt3 tyrosine kinases potently inhibits Flt3-ITD+ AML cell growth. *PLoS One* **12**, e0181178 (2017).
- Arber, D. A. Acute Myeloid Leukemia. *N. Engl. J. Med.* **373**, 1136–1152 (2015).
- Degos, L. & Wang, Z. Y. All trans retinoic acid in acute promyelocytic leukemia. *Oncogene* **17**, 7140–7145 (2001).
- Bak, R. O., Dever, D. P. & Porteus, M. H. CRISPR/Cas9 genome editing in human hematopoietic stem cells. *Nat. Protoc.* **13**, 358–376 (2018).
- Cong, L. *et al.* Multiplex Genome Engineering Using CRISPR/Cas System. *Science (80-.)*. **339**, 819–824 (2013).
- Ran, F. A. *et al.* Genome engineering using the CRISPR-Cas9 system. *Nat. Protoc.* **8**, 2281–2308 (2013).
- Labun, K., Montague, T. G., Gagnon, J. A., Thyme, S. B. & Valen, E. CHOPCHOP v2: a web tool for the next generation of CRISPR genome engineering. *Nucleic Acids Res.* **44**, 272–276 (2016).
- Van Rooden, E. J. *et al.* Mapping in vivo target interaction profiles of covalent inhibitors using chemical proteomics with label-free quantification. *Nat. Protoc.* **13**, 752–767 (2018).
- Kuharev, J., Navarro, P., Distler, U., Jahn, O. & Tenzer, S. In-depth evaluation of software tools for data-independent acquisition based label-free quantification. *Proteomics* **15**, 3140–3151 (2015).
- Distler, U., Kuharev, J., Navarro, P. & Tenzer, S. Label-free quantification in ion mobility-enhanced data-independent acquisition proteomics. *Nat. Protoc.* **11**, 795–812 (2016).

4

Covalent complementary probes
reveal the role of FES tyrosine kinase
in neutrophil phagocytosis
via SYK activation

Introduction

Neutrophils are the most abundant members of the innate immune system, which serve as the first line of host defense against invading pathogens and respond immediately upon infection.¹ They are recruited to the site of infection and their primary function is to internalize and eliminate the pathogen via a process named phagocytosis. The first step in phagocytosis is recognition of the pathogen, which can occur via (a cross-talk of) various immunoreceptors, including pathogen-associated molecular pattern (PAMP) receptors, Fc-gamma receptors (FcγRs) and complement receptors (CRs).² Each immunoreceptor subsequently activates an internalization machinery, ultimately leading to phagosome formation, maturation, and killing of the pathogen. Neutrophils possess a wide range of mechanisms to kill pathogens, including the production of reaction oxygen species (ROS), release of cytotoxic granule components and antimicrobial peptides, and formation of neutrophil extracellular traps (NETs).³ Elucidation of the molecular components of the phagocytic pathway is of importance to design novel anti-infective agents and molecular therapies for autoimmune disorders.

The non-receptor tyrosine kinase FES is highly expressed in phagocytes, where it is activated upon stimulation of various pathogen-recognizing receptors, including Toll-like receptor 4 (TLR4) by lipopolysaccharide (LPS) in macrophages^{4,5} and high-affinity immunoglobulin E receptor I (FcεRI) by IgE in mast cells.⁶ FES is located in signaling pathways linked to regulation of the actin cytoskeleton, cell migration and the release of inflammatory mediators. However, the role of FES and its downstream substrates in neutrophils has not been investigated so far.

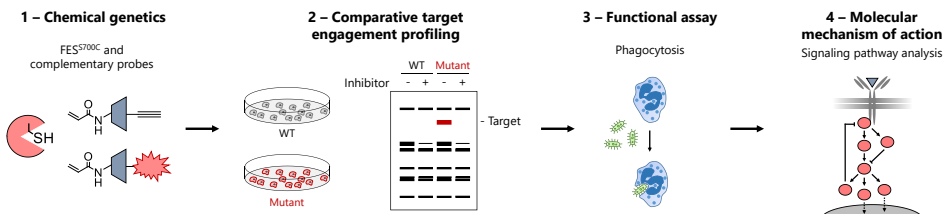


Figure 4.1 – Chemical genetics workflow to study the role of FES in neutrophil phagocytosis. Schematic workflow encompassing the application of chemical genetic tools and endogenous model system described in chapters 2 and 3. Comparative profiling using wild-type and FES^{S700C} HL-60 cells can be used to visualize target engagement of FES upon *in situ* treatment with WEL028. Phagocytosis can subsequently be measured in a flow cytometry-based assay using fluorescent bacteria. Analysis of associated signaling pathways, e.g. by phospho-specific immunoblot analysis, provides insight in the molecular mechanism of action of the target kinase.

Here, the role of FES in phagocytosis of live bacteria by neutrophils was studied. The chemical genetic toolbox described in chapter 2 (Figure 4.1, step 1) is suited to selectively inactivate endogenous FES^{S700C} in the generated mutant HL-60 cell line (Figure 4.1, step 2). Comparative target engagement profiling led to the discovery that FES is

involved in the phagocytic uptake of bacteria by neutrophils (Figure 4.1, step 3). In addition, analysis of signaling pathways downstream of FES (Figure 4.1, step 4) provides insight in the molecular mechanism via which FES regulates reorganization of the actin cytoskeleton required for receptor internalization.

Results

WEL028 reduces phagocytic uptake of bacteria by FES^{S700C} HL-60 neutrophils

HL-60 cells have been widely used to study neutrophil biology as an experimentally tractable alternative for primary neutrophils, which have a short life-span and cannot be grown in culture.⁷ It was first confirmed that FES^{S700C} HL-60 cells could be differentiated into functional neutrophils. After stimulation with all-*trans*-retinoic acid (ATRA; 1 μ M) and dimethylsulfoxide (DMSO; 1.25%) for 72 h, cells displayed a reduction in cell proliferation and an increase in surface expression of the neutrophil marker CD11b (Supplementary Figure 4.1A, B). Moreover, cells acquired the ability to induce an oxidative burst upon stimulation with phorbol 12-myristate 13-acetate (PMA), which is indicative for functional neutrophils (Supplementary Figure 4.1C, D).

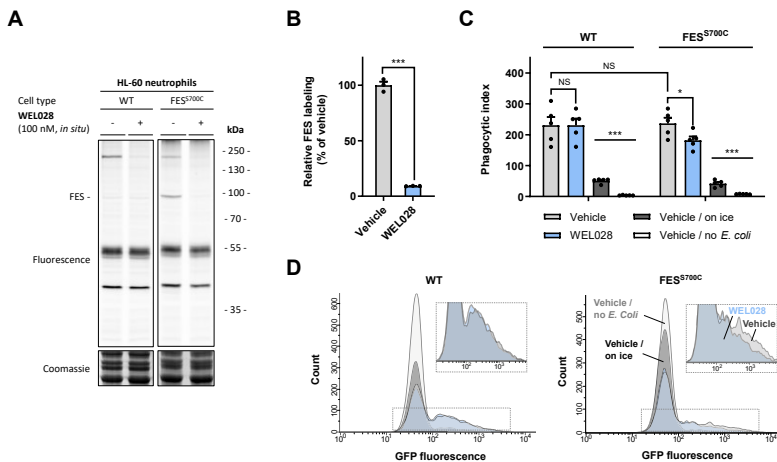


Figure 4.2 - FES inhibition reduces phagocytic uptake of *E. coli* by HL-60 neutrophils. (A, B) Complete FES inhibition at 100 nM WEL028 in FES^{S700C} HL-60 neutrophils *in situ*. Neutrophils were treated with WEL028 (100 nM, 1 h, 37 °C) and lysates were post-labeled (1 μ M WEL033, 30 min, rt). Band intensities were normalized to vehicle-treated control (N = 3). (C, D) WEL028 reduces phagocytic uptake in FES^{S700C} but not WT neutrophils. HL-60 neutrophils were incubated with vehicle or WEL028 (100 nM, 1 h, 37 °C), after which GFP-expressing *E. coli* B834 were added (MOI = 30, 1 h, 37 °C). Cells were analyzed by flow cytometry (N = 5). Phagocytic index was calculated as fraction of GFP-positive cells (number of phagocytic cells) multiplied by GFP mean fluorescence intensity (number of phagocytized bacteria). All data represent means \pm SEM. Statistical analysis was performed using ANOVA with Holm-Sidak's multiple comparisons correction, *** $P < 0.001$; * $P < 0.05$; NS if $P > 0.05$.

To measure the phagocytic uptake by HL-60 neutrophils, a flow cytometry-based assay with live GFP-expressing *E. coli* was set up.⁸ Control cells incubated on ice were included to account for surface binding without internalization. Both wild-type (WT) and FES^{S700C} neutrophils effectively internalized bacteria with identical phagocytic indices (Figure 4.2C), which is in line with the results from chapter 3 that indicated that wild-type and FES^{S700C} HL-60 cells behave identically. Phagocytic uptake showed a time-dependent increase up to 60 min and maximum uptake was observed at a multiplicity of infection (MOI) of 30 (Supplementary Figure 4.2). Interestingly, WEL028 (100 nM), at a concentration sufficient for complete and selective FES inactivation (Figure 4.2A, B), reduced the phagocytic index by 30-50% in FES^{S700C} expressing cells, but not in WT HL-60 neutrophils (Figure 4.2C, D). Reduced phagocytosis upon FES inhibition was consistently observed at various MOIs and infection times (Supplementary Figure 4.2). This indicates that FES activity plays an important role in phagocytosis of *E. coli* by neutrophils.

SYK kinase is a substrate of FES

The previously obtained substrate profile of FES (chapter 2) was examined in more detail to gain insight in the molecular mechanism of FES-mediated phagocytosis. A peptide of the non-receptor tyrosine kinase ZAP70 was identified as a prominent FES substrate with high signal intensity. Incubation with WEL028 abolished peptide phosphorylation by FES^{S700C}, but not FES^{WT} (Figure 4.3A). Although ZAP70 is predominantly linked to immune signaling in T-cells, its close homolog SYK is ubiquitously expressed in various immune cells, including neutrophils.⁹ Moreover, SYK is part of signaling pathways linked to

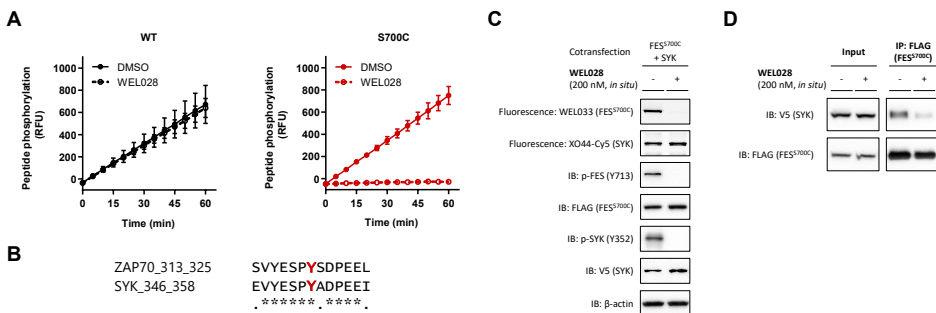


Figure 4.3 – Identification of SYK tyrosine kinase as a substrate of FES. (A) SYK Y352 as proposed phosphorylation site of FES, based on phosphorylation of homologous ZAP70 peptide by recombinant FES^{WT} (left) and FES^{S700C} (right). WEL028 selectively abolishes peptide phosphorylation by FES^{S700C} (PamChip® microarray, N = 3). (B) ZAP70 peptide sequence used in microarray and its homology to corresponding SYK peptide. Putative target tyrosine phosphorylation site is indicated in red. (C) FES phosphorylates SYK Y352 in co-transfected U2OS cells. U2OS cells co-expressing FLAG-tagged FES^{S700C} and V5-tagged SYK were incubated with vehicle or WEL028 (200 nM, 1 h, 37 °C) and lysed. Lysates were labeled (250 nM WEL033, 30 min, rt) and analyzed by in-gel fluorescence and immunoblot (N = 3). (D) SYK interacts with FES and this interaction is dependent on FES activity. Co-transfected U2OS cells were incubated as in C, followed by immunoprecipitation using anti-FLAG antibody and immunoblot analysis (N = 3). All data represent means ± SEM.

pathogen recognition and involved in bacterial uptake by neutrophils.¹⁰ The identified ZAP70 peptide substrate shows high sequence similarity to its SYK counterpart surrounding Y352 (Figure 4.3B).

To validate that SYK is a downstream target of FES, SYK-V5 and FES^{S700C}-FLAG were co-transfected in U2OS cells. First, it was confirmed that overexpression of FES^{S700C} led to autophosphorylation of FES at Y713, which was sensitive to WEL028 (Figure 4.3C). Subsequent immunoblot analysis using a SYK Y352 phospho-specific antibody showed that SYK was phosphorylated in a WEL028-dependent manner. Labeling of SYK by active site lysine-targeting probe XO44-Cy5¹¹ was unaffected by pre-incubation with WEL028, indicating that WEL028 does not inhibit SYK directly. In addition, WEL028 did not inhibit SYK in the kinome selectivity screen (chapter 2) and did not affect SYK pY352 levels when FES^{S700C} was omitted (Supplementary Figure 4.3). Immunoprecipitation against FES^{S700C} using an anti-FLAG antibody revealed a physical interaction between FES and SYK as witnessed by immunoblot against the V5-tag of SYK (Figure 4.3D). Interestingly, this interaction was dependent on the activation status of FES, because WEL028 inhibited the co-precipitation of SYK with FES. Taken together, these results suggest that SYK Y352 is a direct substrate of FES.

FES transiently phosphorylates SYK Y352 in HL-60 neutrophils exposed to *E. coli*

Next, HL-60 neutrophils were incubated with the potent SYK inhibitor R406 to verify that endogenous SYK is also involved in phagocytic uptake of *E. coli* by neutrophils. SYK inhibition reduced phagocytosis to similar levels as observed for WEL028 (Figure 4.4A).

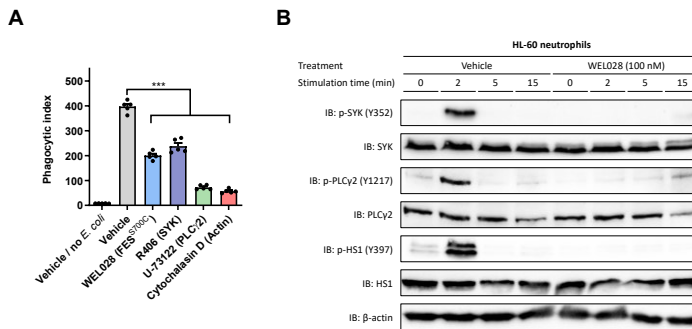


Figure 4.4 – FES phosphorylates SYK Y352 and downstream targets HSI and PLCγ2 in HL-60 neutrophils infected with *E. coli*. (A) Phagocytic uptake of *E. coli* by HL-60 neutrophils is dependent on FES, SYK and PLCγ2 activity and requires actin polymerization. HL-60 neutrophils were incubated with vehicle or indicated compounds (100 nM WEL028, 1 μM R406, 5 μM U-73122 or 10 μM Cytochalasin D, 1 h, 37 °C), after which GFP-expressing *E. coli* B834 were added (MOI = 30, 1 h, 37°C). Cells were analyzed by flow cytometry (N = 5). (B) FES rapidly phosphorylates endogenous SYK Y352 and downstream substrates HSI Y397 and PLCγ2 Y1217 in HL-60 neutrophils infected with *E. coli*. Inhibitor incubation as in A, followed by addition of GFP-expressing *E. coli* B834 (MOI = 30, 0-2-5-15 min, 37 °C) and immunoblot analysis (N = 3). All data represent means ± SEM. Statistical analysis was performed using ANOVA with Holm-Sidak’s multiple comparisons correction, *** P <0.001.

Of note, phospholipase C gamma 2 (PLC γ 2) inhibitor U-73122 and actin polymerization inhibitor Cytochalasin D were taken along as positive controls to verify that the phagocytosis was mediated via PLC γ 2 and was actin polymerization-dependent.² Finally, it was investigated whether the signaling pathway downstream of SYK was modulated in a FES-dependent manner by using immunoblot analysis with phospho-specific antibodies for SYK Y352, hematopoietic cell-specific protein-1 (HS1) Y397 (an actin-binding protein) and PLC γ 2 Y1217 (Figure 4.4B). Indeed, a transient phosphorylation of SYK, HS1 and PLC γ 2 was observed, which peaked at 2 min after incubation with bacteria. Inhibition of FES^{S700C} completely blocked the phosphorylation of these proteins, thereby demonstrating FES activation is an early event in the phagocytosis of *E. coli* in HL-60 neutrophils.

Discussion and conclusion

In this chapter, chemical genetic tools were used to uncover a novel biological role for FES in phagocytosis by neutrophils. It was demonstrated that FES plays a key role in the phagocytic uptake of bacteria in neutrophils by activating SYK and downstream substrates HS1 and PLC γ 2. In combination with previous data reported in the literature (reviewed in reference 12), these new insights led to a proposed mechanistic model for the role of FES in neutrophil phagocytosis (Figure 4.5). One of the first events in response to bacterial recognition by neutrophil surface receptors is the formation of the lipid phosphatidylinositol 4,5-bisphosphate (PIP₂) in the membrane (Figure 4.5, panel 1). FES normally resides in the cytosol in an inactive conformation. Its N-terminal F-BAR domain, a unique structural feature of FES, exclusively binds to phosphoinositide-rich lipids, such as PIP₂⁶, and drives FES translocation to the membrane. This triggers the formation of oligomers and auto-activation of FES by phosphorylation on Y713 and induces membrane curvature^{13,14} required for particle internalization.⁶ (Figure 4.5, panel 2).

FES subsequently activates SYK by phosphorylation of Y352, which poses an alternative activation mechanism of SYK compared to the traditional activation via binding to ITAM domains of immunoreceptors.¹⁵ Y352 is located in a linker region of SYK, which separates its two N-terminal SH2 domains from its C-terminal catalytic domain. Phosphorylation of this linker residue was previously shown to perturb auto-inhibitory interactions, resulting in SYK activation.¹⁵ SYK is known to phosphorylate HS1, an actin-binding protein involved in reorganization of the actin cytoskeleton. HS1 can be phosphorylated on multiple tyrosine residues that all contribute to its actin remodeling function.¹⁶ Of note, its Y378 and Y397 residues are phosphorylated by FES in mast cells, but both sites have also been identified as substrate sites for other kinases, including SYK.⁶ Phosphorylation of HS1 by FES and/or SYK drives reorganization of the actin cytoskeleton required for internalization of the bacterium-receptor complex (Figure 4.5, panel 3). Concomitantly, the phosphorylated Y352 residue in SYK can serve as binding site for the SH2 domain of PLC γ 2, followed by SYK-mediated PLC γ 2 activation. In turn, this allows

degradation of PIP₂ into diacylglycerol (DAG) and inositoltriphosphate (IP₃), which alters the membrane composition and returns it to the non-activated state: FES dissociates from the membrane and the signaling process is terminated (Figure 4.5, panel 4).

This model thus proposes a feedback mechanism in which FES indirectly regulates its own localization and activation by modulating PLC γ 2 activity via SYK. Based on the rapid, transient phosphorylation of SYK Y352 and downstream substrates (Figure 4.5B), FES seems to be rapidly deactivated, possibly via the action of phosphatases. Examination of the SH2 binding profile of FES (chapter 2) identified the phosphatases PTN6 and PTN11 as potential interaction partners of FES, but further studies are required to gain insight in the deactivation of signaling pathways underlying FES-mediated phagocytosis.

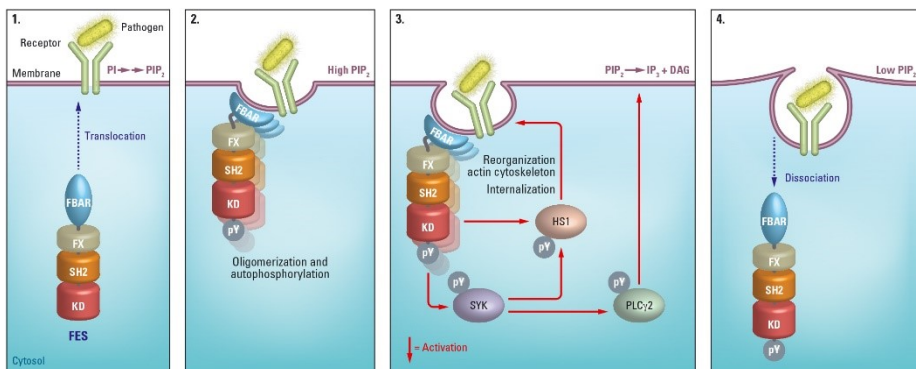


Figure 4.5 – Proposed simplified model for the role of FES in neutrophil phagocytosis. Phosphorylation sites Y378 and Y397 on HSI are shown as a single site for visualization purposes. For detailed explanation of the model, see main text. PI: phosphatidylinositol, PIP₂: phosphatidylinositol 4,5-bisphosphate, IP₃: inositol 1,4,5-trisphosphate, DAG: diacylglycerol, FX: F-BAR extension, SH2: Src Homology 2, KD: kinase domain, pY: phosphotyrosine.

It should be noted that FES possesses an F-BAR extension (FX) domain that binds phosphatidic acid (PA) and activates its kinase activity.¹⁷ PA is synthesized by phospholipase D (PLD) in response to activation of various immune receptors. PLD activation also leads to elevated intracellular Ca²⁺ levels, but the exact mechanistic pathways underlying this event remain poorly understood.¹⁸ FES could possibly be a molecular link that activates PLC γ 2 to increase Ca²⁺ in response to PA production by PLD. Further studies are required to investigate the activation mechanism of FES by PA and the role of FES in the complex cross-talk between PLD and PLC γ 2.

Since FES is also linked to other cellular processes driven by actin reorganization, such as cell migration^{19,20}, it will be interesting to investigate whether FES also mediates this function in a SYK-dependent manner. Moreover, identification of FES as a potential activator of SYK may provide new insights in previous studies reporting on FES and/or SYK function. For example, FES is involved in the development and function of osteoclasts, multinucleated cells responsible for bone resorption.²¹ Accordingly, SYK-deficient osteoclasts exhibit major defects in the actin cytoskeleton, resulting in reduced bone

resorption.²² It remains to be determined whether FES inhibition disrupts the osteoclast cytoskeleton in a similar manner, which would make FES a potential target to treat osteoporosis and cancer-associated bone disease. Furthermore, FES inhibition was shown to suppress growth of acute myeloid leukemia (AML) cells that harbor an internal tandem duplication in the *FLT3* gene (*FLT3*-ITD), but not AML cells expressing wild-type *FLT3*.^{23,24} Similarly, *FLT3*-ITD AML is more vulnerable to SYK suppression than *FLT3*-WT AML.²⁵ It would be interesting to investigate whether FES activates SYK in these AML cells and whether altered internalization of *FLT3*-ITD compared to *FLT3*-WT perhaps explains the increased susceptibility to FES and SYK inhibition.

Two SYK inhibitors have recently been approved by the FDA and several more are currently in clinical trials for the treatment of various malignancies and inflammatory diseases.²⁶ The question thus rises in what other cell types and cellular processes SYK activation is dependent on FES. Notably, FES is expressed in many cell types that contribute to the pathogenesis of inflammatory diseases, such as macrophages, mast cells, neutrophils and B-cells, but future studies will prove whether FES inhibitors may be of therapeutic value in these disorders. The chemical genetic strategy presented here may provide valuable tools to investigate FES-associated physiological processes and aid in its validation as drug target.

Acknowledgments

Riet Hilhorst, Tim van den Hooven and Rob Ruijtenbeek are kindly acknowledged for microarray measurements and helpful discussions, Daphne van Elsland for generation of the fluorescent *E. coli* strain, Laura de Paus for synthesis of XO44-Cy5, and Robert van Sluis for graphic illustrations.

Experimental procedures

General

All chemicals were purchased at Sigma Aldrich, unless stated otherwise. Cloning reagents were from Thermo Fisher. Cytochalasin D and U-73122 were purchased at Focus Biomolecules and R406 at Selleckchem. XO44-Cy5 was previously synthesized in-house according to literature procedures¹¹ and characterized by NMR and LC-MS. All cell culture disposables were obtained from Sarstedt.

Cloning

Full-length human cDNA encoding FES was obtained from Source Bioscience. pDONR223-construct with full-length human cDNA of SYK was a gift from William Hahn & David Root (Addgene Human Kinase ORF Collection). Eukaryotic expression construct of FES was generated by PCR amplification and restriction/ligation cloning into a pcDNA3.1 vector, in frame with a C-terminal FLAG-tag. Eukaryotic expression construct of SYK was generated using Gateway™ recombinational cloning into a pcDest40 vector, in frame with a C-terminal V5-tag, according to recommended procedures (Thermo Fisher). All plasmids were isolated from transformed XL10-Gold competent cells (prepared using *E. coli* transformation buffer set; Zymo Research) using plasmid isolation kits following the supplier's protocol (Qiagen). All sequences were verified by Sanger sequencing (Macrogen).

PamChip® microarray assay

Kinase activity assay

Kinase activity profiles were determined using the PamChip® 12 protein tyrosine (PTK) peptide microarray system (PamGene International B.V.) according to the instructions of the manufacturer, essentially as described²⁷ with the exception that arrays were blocked with 2% BSA and the assay buffer contained EDTA instead of EGTA. Sample input was 0.25 ng purified FES (wild-type or S700C) per array and [ATP] = 400 μM. For arrays with inhibitor, recombinant FES was pre-incubated in assay mix without ATP with vehicle or WEL028 (100 nM, 30 min, on ice, 2% final DMSO concentration).

Data analysis and quality control

Data quantification of the images at all exposure times and reaction times and visualization of the data were performed using BioNavigator software (PamGene International B.V.). Post-wash signals (local background subtracted) were used. After signal quantification and integration of exposure times, signals were log₂-transformed for visualization. Peptides without ATP-dependent signal were excluded from analysis. Identification of peptides that were significantly different between conditions was performed using a Mixed Model statistical analysis.

Cell culture

General cell culture

Cell lines were purchased at ATCC and were tested on regular basis for mycoplasma contamination. Cultures were discarded after 2-3 months of use. U2OS (human osteosarcoma) cells were cultured at 37 °C under 7% CO₂ in DMEM containing phenol red, stable glutamine, 10% (v/v) high iron newborn calf serum (Seradigm), penicillin and streptomycin (200 μg/mL each; Duchefa). Medium was refreshed every 2-3 days and cells were passaged two times a week at 80-90% confluence. HL-60 (human promyeloblast) cells were cultured at 37 °C under 5% CO₂ in HEPES-supplemented RPMI containing phenol red, stable glutamine, 10% (v/v) fetal calf serum (Biowest), penicillin and streptomycin (200 μg/mL each), unless stated otherwise. Cell density was maintained between 0.2 x 10⁶ and 2.0 x 10⁶ cells/mL. Cell viability was assessed by Trypan Blue exclusion and quantification using a TC20™ Automated Cell Counter (Bio-Rad).

Transfection

One day prior to transfection, U2OS cells were transferred from confluent 10 cm dishes to 15 cm dishes. Before transfection, medium was refreshed (13 mL). A 3:1 (m/m) mixture of polyethyleneimine (PEI; 60 µg/dish) and plasmid DNA (20 µg/dish; for co-transfections 10 µg each) was prepared in serum-free medium and incubated for 15 min at rt. The mixture was then added dropwisely to the cells, after which the cells were grown to confluence in 48 h. Cells were then harvested by scraping in lysis buffer and lysates were prepared as described.

Differentiation of HL-60 cells

One day prior to induction of differentiation, cells were diluted to 0.4×10^6 cells/mL. Neutrophil differentiation was induced by addition of all-*trans*-retinoic acid (ATRA; 1 µM) and dimethylsulfoxide (DMSO; 1.25%) for 72 – 96 h.

Inhibitor treatment in live cells

The term *in situ* is used to designate experiments in which live cell cultures are treated with inhibitor, whereas the term *in vitro* refers to experiments in which the inhibitor is incubated with cell lysates. Compounds were diluted in growth medium from a 1000x concentrated stock solution in DMSO.

For *in situ* assays on live transfected cells, cells were transfected prior to treatment as described above. After 48 h, cells were treated with compound for 1 h. Cells were then harvested by scraping in lysis buffer and lysates were prepared as described.

For *in situ* treatment post-differentiation, HL-60 cells were differentiated as described above and incubated with compound for 1 h unless specified otherwise. Cells were centrifuged (200 *g*, 5 min, rt) and washed in equal volume of PBS (1000 *g*, 5 min, rt). Cell pellets were flash-frozen in liquid nitrogen and stored at -80 °C until use.

CD11b expression analysis by flow cytometry

Cells (1×10^6 per sample) were centrifuged (500 *g*, 3 min) and suspended in human FcR blocking solution (Miltenyi Biotec, 25x diluted in FACS buffer (1% BSA, 1% FCS, 0.1% NaN₃, 2 mM EDTA in PBS)), transferred to a V-bottom 96-well plate and incubated for 10 min at 4°C. Next, monoclonal rat CD11b-APC antibody (1:100, Miltenyi Biotec, 130-113-231) or rat anti-IgG2b-APC isotype control antibody (1:100, Miltenyi Biotec, 130-106-728) was added along with 7-aminoactinomycin D (7-AAD) (1 µg/mL) and samples were incubated for 30 min 4°C in the dark. Samples were washed once in PBS and fixed in 1% paraformaldehyde (PFA) in PBS for 15 min at 4°C in the dark, followed by two washing steps in PBS and resuspension in FACS buffer to a density of approximately 500 cells/µL. Cell suspensions were measured on a Guava easyCyte HT and data was processed using GuavaSoft InCyte 3.3 (Merck Millipore). Events (10,000 per condition) were gated by forward and side scatter (cells), side scatter area (singlets) and viability (live cells) and the percentage of CD11b-positive cells was determined based on background fluorescence for isotype control antibody and non-differentiated cells. The RED-R channel (661/15 filter) and RED-B channel (695/50 filter) were used to detect CD11b-APC and 7-AAD, respectively.

Neutrophil oxidative burst assay

Cells were centrifuged (500 *g*, 3 min), suspended in PBS and seeded in triplicate per condition in 96-well plates (100,000 cells per well in 100 µL). To each well, 100 µL of PBS containing nitroblue tetrazolium (NBT) with vehicle or phorbol 12-myristate 13-acetate (PMA) was added, bringing final concentrations to 0.1% and 1.6 µM, respectively. Cells were incubated (1 h, 37 °C) and plates were imaged by phase contrast microscopy (20x magnification, EVOS FL Auto 2). Cells positive for formazan deposits were counted (3 different fields per replicate).

Preparation of cell lysates for gel and immunoblot analysis

HL-60 cells were suspended in M-PER lysis buffer supplemented with 1x Halt™ phosphatase and protease inhibitor cocktail (Thermo Fisher). U2OS cells were directly scraped in lysis buffer and collected in tubes. Lysates were centrifuged (14,000 *g*, 10 min, 4 °C) to yield the clear lysate as supernatant. Protein concentration was determined using Quick Start™ Bradford Protein Assay (Bio-Rad) and diluted to appropriate concentration in M-PER. Lysates were aliquoted, flash-frozen and stored at -80 °C until use.

Probe labeling experiments

In situ treated cell lysate (14.5 μL) was incubated with WEL033 or XO44-Cy5 (0.5 μL, 30 x concentrated stock in DMSO, 30 min, rt). Final concentrations of inhibitors and/or probe are indicated in the main text and figure legends. Reactions were quenched with 4x Laemmli buffer (5 μL, final concentrations 60 mM Tris pH 6.8, 2% (w/v) SDS, 10% (v/v) glycerol, 5% (v/v) β-mercaptoethanol, 0.01% (v/v) bromophenol blue) and boiled for 5 min at 95°C. Samples were resolved by SDS-PAGE on a 10% polyacrylamide gel (180 V, 75 min). Gels were scanned using Cy3 and Cy5 multichannel settings (605/50 and 695/55 filters, respectively; ChemiDoc™ MP System, Bio-Rad). Fluorescence intensity was corrected for protein loading determined by Coomassie Brilliant Blue R-250 staining and quantified with Image Lab (Bio-Rad). IC₅₀ curves were fitted with Graphpad Prism® 7 (Graphpad Software Inc.).

Immunoblot

Samples were resolved by SDS-PAGE as described above, but transferred to 0.2 μm polyvinylidene difluoride membranes by Trans-Blot Turbo™ Transfer system (Bio-Rad) directly after fluorescence scanning. Membranes were washed with TBS (50 mM Tris pH 7.5, 150 mM NaCl) and blocked with 5% milk in TBS-T (50 mM Tris pH 7.5, 150 mM NaCl, 0.05% Tween-20) for 1 h at rt.

Membranes were then either incubated with primary antibody in 5% milk in TBS-T (FLAG, V5, β-actin; o/n at 4 °C) or washed three times with TBS-T, followed by incubation with primary antibody in 5% BSA in TBS-T (other antibodies, o/n at 4 °C). Membranes were washed three times with TBS-T, incubated with matching secondary antibody in 5% milk in TBS-T (1:5000, 1 h at rt) and then washed three times with TBS-T and once with TBS. Luminol development solution (10 mL of 1.4 mM luminol in 100 mM Tris pH 8.8 + 100 μL of 6.7 mM *p*-coumaric acid in DMSO + 3 μL of 30% (v/v) H₂O₂) or Clarity Max™ ECL Substrate (Bio-Rad) was added and chemiluminescence was detected on ChemiDoc™ MP System.

Following detection of phospho-proteins, membranes were stripped (Restore™ Plus Stripping Buffer, Thermo Fisher) for 20 min, washed three times with TBS, and blocked and incubated with the control antibodies as described above.

Primary antibodies: monoclonal mouse anti-FLAG M2 (1:5000, Sigma Aldrich, F3156), monoclonal anti-V5 (1:5000, Thermo Fisher, R960-25), monoclonal mouse anti-β-actin (1:1000, Abcam, ab8227), polyclonal rabbit anti-phospho-FES Y713 (1:1000, Thermo Fisher, PA5-64504), polyclonal rabbit anti-phospho-SYK Y352 (1:1000, Cell Signaling Technology (CST), #2701), monoclonal rabbit anti-SYK (1:1000, CST, #13198), polyclonal rabbit anti-phospho-HS1 Y397 (1:1000, CST, #4507), polyclonal rabbit anti-HS1 (1:1000, CST, #4503), polyclonal rabbit anti-phospho-PLCγ2 Y1217 (1:1000, CST, #3871), polyclonal rabbit anti-PLCγ2 (1:1000, CST, #3872). Secondary antibodies: goat anti-mouse-HRP (1:5000, Santa Cruz, sc-2005), goat anti-rabbit-HRP (1:5000, Santa Cruz, sc-2030).

Co-immunoprecipitation

U2OS cells were co-transfected with FLAG-tagged FES and V5-tagged SYK and grown for 48 h as described above, followed by incubation with vehicle or WEL028 (200 nM) for 1 h. Cells were then washed with PBS and collected by scraping in IP-buffer (20 mM Tris-HCl pH 7.5, 150 mM NaCl, 1% Triton X-100 supplemented with 1x Halt™ phosphatase and protease inhibitor cocktail (Thermo

Fisher)). Cells were lysed by sonication on ice (3 cycles of 10 s on, 10 s off at 25% maximum amplitude), centrifuged (14,000 *g*, 10 min, 4 °C). The clear lysate was diluted to 1 mg/mL in IP-buffer and subjected to immunoprecipitation using Dynabeads™ Protein G Immunoprecipitation kit (Thermo Fisher) following manufacturer's protocol. Briefly, anti-FLAG M2 antibody (1:100, Sigma Aldrich, F3156) was incubated with beads with gentle rotation (10 min, rt), after which lysate (500 µL of 1 mg/mL) was added and incubated (1 h, 4 °C). Beads were washed three times, transferred to clean tubes and eluted by suspension in 2x Laemmli buffer (50 µL, 10 min, 70 °C). Samples (10 µL per lane) were resolved by SDS-PAGE and immunoblotted using anti-V5 or anti-FLAG antibodies. Immunoprecipitations were performed in three independent replicates.

Phagocytosis assays

Flow cytometry

HL-60 cells were differentiated to neutrophils as described. Cells were counted and centrifuged (200 *g*, 5 min), followed by resuspension in growth medium without antibiotics. Cells were incubated with vehicle or inhibitor (from 1000x concentrated stocks in DMSO) for 1 h at 37°C prior to infection (1 x 10⁶ cells in 900 µL in 12-well plate). Meanwhile, *E. coli* B834(DE3) constitutively expressing GFP^{A206K} were grown in LB medium to an OD600 of 0.4-1.0, after which bacteria were centrifuged (2,000 *g*, 5 min), washed and resuspended in PBS to appropriate density.⁸ Neutrophils were infected by addition of bacteria at multiplicity of infection (MOI) of 30 unless stated otherwise. Cells were then incubated for 1 h at 37°C unless stated otherwise, after which cells were resuspended and transferred to Eppendorf tubes, washed in FACS buffer (1% BSA, 1% FCS, 0.1% NaN₃, 2 mM EDTA in PBS; 1 mL, 500 *g*, 3 min) and fixed in 1% paraformaldehyde (PFA) in PBS (15 min, 4 °C, in the dark). Fixed cells were washed twice in PBS and resuspended in FACS buffer to a density of approximately 500 cells/µL.

Cell suspensions were measured on a Guava easyCyte HT and data was processed using GuavaSoft InCyte 3.3 (Merck Millipore). Events (20,000 per condition) were gated by forward and side scatter (cells), side scatter area (singlets) and the percentage of GFP-positive cells and GFP mean fluorescence intensity (MFI) were determined based on background fluorescence for non-infected cells. The GREEN-B channel (525/30 filter) was used to detect GFP. Phagocytic index was calculated as fraction of GFP-positive cells (number of phagocytic cells) multiplied by GFP MFI (number of phagocytized bacteria).

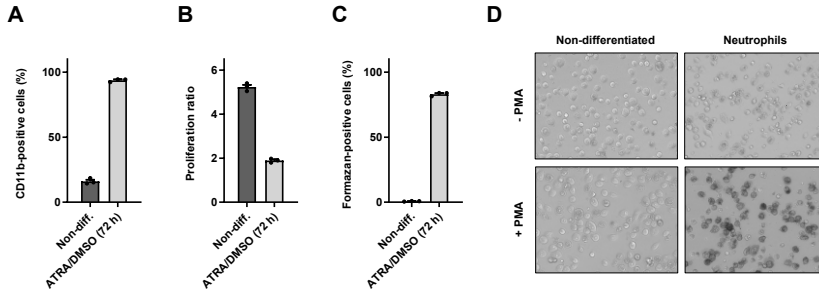
Stimulation for detection of phosphoproteins

HL-60 neutrophils were infected as described above, but in 15 mL tubes (5 x 10⁶ cells in 4 mL per sample). After indicated infection times, ice-cold PBS was added (10 mL) and suspensions were immediately centrifuged (3,500 *g*, 2 min). Supernatant was completely aspirated and cells were thoroughly resuspended in 2x Laemmli sample buffer (100 µL), followed by incubation at 95 °C for 10 min and brief sonication to reduce sample viscosity. Samples were stored at -20 °C or immediately resolved by SDS-PAGE (20 µL per lane).

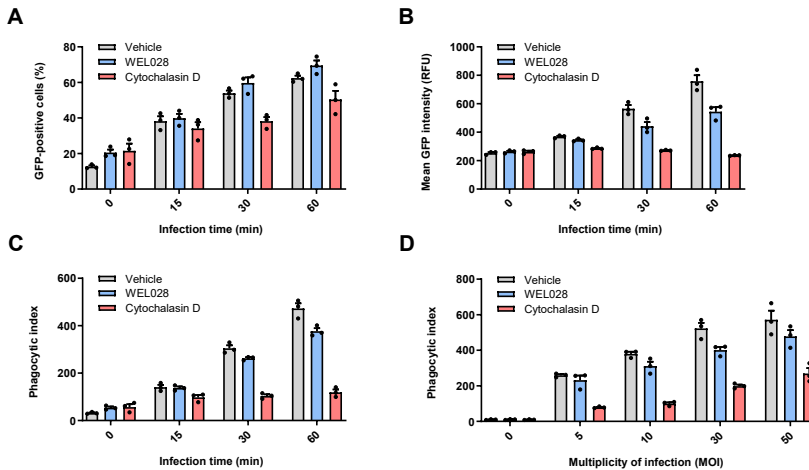
Statistical analysis

All statistical measures and methods are included in the respective Figure or Table captions. In brief: all replicates represent biological replicates and all data represent means ± SEM, unless indicated otherwise. Statistical significance was determined using Student's *t*-tests (two-tailed, unpaired) or ANOVA with Holm-Sidak's multiple comparisons correction. *** *P* < 0.001; ** *P* < 0.01; * *P* < 0.05; NS if *P* > 0.05. All statistical analyses were conducted using GraphPad Prism® 7 or Microsoft Excel.

Supplementary Data

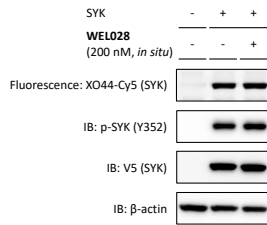


Supplementary Figure 4.1 – FES^{S700C} HL-60 cells differentiate into functional neutrophils. (A) CD11b surface expression analyzed by flow cytometry. Differentiation was induced by addition of ATRA (1 μ M) and DMSO (1.25%) for 72 h. Threshold for CD11b-positive cells was determined using isotype control antibody. (B) Proliferation of FES^{S700C} HL-60 cells subjected to neutrophil differentiation. Proliferation ratio: live cell number after differentiation divided by live cell number before differentiation. (C, D) Ability of FES^{S700C} HL-60 neutrophils to induce oxidative burst upon PMA stimulation. Cells were incubated with 0.1% NBT with or without PMA (1.6 μ M, 1 h, 37 $^{\circ}$ C), imaged by phase contrast microscopy (20x magnification) and cells positive for formazan deposits were counted. Data represent means \pm SEM (N = 3, with 9 different fields per replicate for C, D).



Supplementary Figure 4.2 - Phagocytic uptake of *E. coli* by HL-60 FES^{S700C} neutrophils at variable multiplicity of infection (MOI) and infection time. (A-C) HL-60 FES^{S700C} neutrophils were incubated with vehicle, WEL028 (100 nM) or Cytochalasin D (10 μ M) for 1 h, after which GFP-expressing *E. coli* were added at MOI of 30. After indicated times, cells were washed and fixed (1% PFA, 15 min, 4 $^{\circ}$ C), followed by flow cytometry analysis. Phagocytic index (C) was calculated as fraction of GFP-positive cells (number of phagocytic cells, A) multiplied by GFP MFI (number of phagocytized bacteria, B). (D) Neutrophils were treated as in panel A-C, but with a variable MOI for 1 h. Data represent means \pm SEM (N = 3).

Chapter 4



Supplementary Figure 4.3 - WEL028 does not affect SYK Y352 phosphorylation in U2OS cells in absence of FES^{S700C}. U2OS cells were transfected with only V5-tagged SYK. After 48 h, cells were incubated with vehicle or WEL028 (200 nM, 1 h) and lysed. Lysates were incubated with WEL033 (250 nM, 30 min, rt) and analyzed by in-gel fluorescence and immunoblot (N = 3).

References

1. Kumar, H., Kawai, T. & Akira, S. Pathogen recognition by the innate immune system. *Int. Rev. Immunol.* **30**, 16–34 (2011).
2. Rosales, C. & Uribe-Querol, E. Phagocytosis: A Fundamental Process in Immunity. *BioMed Research International* **2017**, 1–18 (2017).
3. Teng, T. S., Ji, A. L., Ji, X. Y. & Li, Y. Z. Neutrophils and immunity: From bactericidal action to being conquered. *Journal of Immunology Research* **2017**, 1–14 (2017).
4. Zirngibl, R. A., Senis, Y. & Greer, P. A. Enhanced Endotoxin Sensitivity in Fps/Fes-Null Mice with Minimal Defects in Hematopoietic Homeostasis. *Mol. Cell. Biol.* **22**, 2472–2486 (2002).
5. Kim, J. & Feldman, R. A. Activated Fes protein tyrosine kinase induces terminal macrophage differentiation of myeloid progenitors (U937 cells) and activation of the transcription factor PU.1. *Mol. Cell. Biol.* **22**, 1903–18 (2002).
6. McPherson, V. A. *et al.* Contributions of F-BAR and SH2 Domains of Fes Protein Tyrosine Kinase for Coupling to the Fc RI Pathway in Mast Cells. *Mol. Cell. Biol.* **29**, 389–401 (2009).
7. Hauert, A. B., Martinelli, S., Marone, C. & Niggli, V. Differentiated HL-60 cells are a valid model system for the analysis of human neutrophil migration and chemotaxis. *Int. J. Biochem. Cell Biol.* **34**, 838–854 (2002).
8. Van Elsland, D. M. *et al.* Detection of bioorthogonal groups by correlative light and electron microscopy allows imaging of degraded bacteria in phagocytes. *Chem. Sci.* **7**, 752–758 (2016).
9. Amulic, B., Cazalet, C., Hayes, G. L., Metzler, K. D. & Zychlinsky, A. Neutrophil Function: From Mechanisms to Disease. *Annu. Rev. Immunol.* **30**, 459–489 (2012).
10. Tohyama, Y. & Yamamura, H. Protein tyrosine kinase, Syk: A key player in phagocytic cells. *Journal of Biochemistry* **145**, 267–273 (2009).
11. Zhao, Q. *et al.* Broad-spectrum kinase profiling in live cells with lysine-targeted sulfonyl fluoride probes. *J. Am. Chem. Soc.* **139**, 680–685 (2017).
12. Craig, Andrew, W. B. FES/ FER kinase signaling in hematopoietic cells and leukemias. *Front. Biosci.* **17**, 861 (2012).
13. Shimada, A. *et al.* Curved EFC/F-BAR-Domain Dimers Are Joined End to End into a Filament for Membrane Invagination in Endocytosis. *Cell* **129**, 761–772 (2007).
14. Carman, P. J. & Dominguez, R. BAR domain proteins—a linkage between cellular membranes, signaling pathways, and the actin cytoskeleton. *Biophysical Reviews* **10**, 1587–1604 (2018).
15. Bradshaw, J. M. The Src, Syk, and Tec family kinases: Distinct types of molecular switches. *Cellular Signalling* **22**, 1175–1184 (2010).
16. Castro-Ochoa, K. F., Guerrero-Fonseca, I. M. & Schnoor, M. Hematopoietic cell-specific lyn substrate (HCLS1 or HS1): A versatile actin-binding protein in leukocytes. *Journal of Leukocyte Biology* **105**, 881–890 (2019).
17. Di Fulvio, M. *et al.* Phospholipase D2 (PLD2) shortens the time required for myeloid leukemic cell differentiation: Mechanism of action. *J. Biol. Chem.* **287**, 393–407 (2012).
18. Nunes, P. & Demareux, N. The role of calcium signaling in phagocytosis. *J. Leukoc. Biol.* **88**, 57–68 (2010).
19. Smith, J. A., Samayawardhena, L. A. & Craig, A. W. B. Fps/Fes protein-tyrosine kinase regulates mast cell adhesion and migration downstream of Kit and $\beta 1$ integrin receptors. *Cell. Signal.* **22**, 427–436 (2010).
20. Voisset, E. *et al.* FES kinase participates in KIT-ligand induced chemotaxis. *Biochem. Biophys. Res. Commun.* **393**, 174–178 (2010).
21. Hellwig, S. *et al.* Small-molecule inhibitors of the c-Fes protein-tyrosine kinase. *Chem. Biol.* **19**, 529–540 (2012).
22. Zou, W. *et al.* Syk, c-Src, the $\alpha\beta 3$ integrin, and ITAM immunoreceptors, in concert, regulate osteoclastic bone resorption. *J. Cell Biol.* **176**, 877–888 (2007).
23. Voisset, E. *et al.* FES kinases are required for oncogenic FLT3 signaling. *Leukemia* **24**, 721–728 (2010).
24. Weir, M. C. *et al.* Dual inhibition of Fes and Flt3 tyrosine kinases potently inhibits Flt3-ITD+ AML cell growth. *PLoS One* **12**, e0181178 (2017).
25. Puissant, A. *et al.* SYK Is a Critical Regulator of FLT3 in Acute Myeloid Leukemia. *Cancer Cell* **25**, 226–242 (2014).
26. Roskoski, R. Properties of FDA-approved small molecule protein kinase inhibitors. *Pharmacological Research* **144**, 19–50 (2019).
27. Rosenberger, A. F. N. *et al.* Protein kinase activity decreases with higher braak stages of Alzheimer’s disease pathology. *J. Alzheimer’s Dis.* **49**, 927–943 (2015).

5

Towards a chemical genetic strategy
for subtype-selective inhibition
of diacylglycerol lipase alpha

Introduction

Endocannabinoids are essential signaling lipids in the brain and are involved in regulation of various physiological processes, ranging from learning and memory to appetite and emotion.^{1–3} Unlike polar neurotransmitters, which are typically released from vesicles, signaling lipids such as endocannabinoids appear to be synthesized on demand.^{4,5} This implies that the cellular machinery involved in endocannabinoid homeostasis plays an essential role in signaling processes. Spatiotemporal endocannabinoid action is therefore likely controlled by a dynamic network including the enzymes for their biosynthesis and degradation.

The diacylglycerol lipases alpha and beta (DAGL α and β) are serine hydrolases responsible for the biosynthesis of the signaling lipid 2-arachidonoylglycerol (2-AG), the most abundant endogenous ligand for the cannabinoid (CB) type 1 receptor in the brain.⁶ Despite relatively low overall homology (34% identical amino acids), both enzymes share a multi-pass integral membrane domain as well as a catalytic domain with a typical α/β hydrolase fold and Ser-His-Asp catalytic triad^{6,7} (Figure 5.1A). Interestingly, DAGL α possesses an additional domain at the carboxy-terminal tail with multiple (putative) phosphorylation sites⁸ as well as a Homer protein-binding PPxxF motif.^{9,10} DAGL α and DAGL β both catalyze the hydrolysis of diacylglycerols (DAGs) at the *sn*-1 position to generate monoacylglycerols (MAGs), implying that the active sites of these two DAGL enzymes likely have high structural similarity (Figure 5.1B).

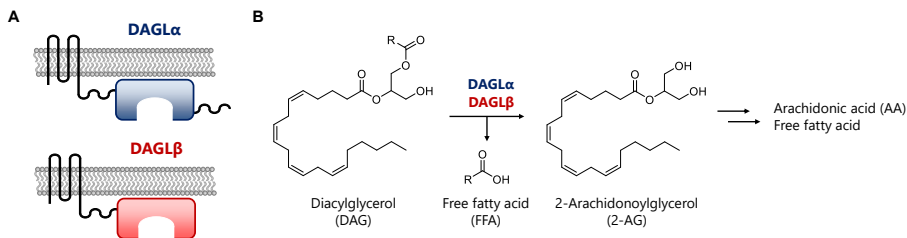


Figure 5.1 – Diacylglycerol lipase alpha and beta synthesize 2-arachidonoylglycerol from diacylglycerols. (A) DAGL α and DAGL β share a multi-pass integral membrane domain as well as a catalytic domain with a typical α/β hydrolase fold and Ser-His-Asp catalytic triad. In addition, DAGL α possesses a unique carboxyl-terminal tail. (B) Both subtypes catalyze the hydrolysis of diacylglycerols (DAGs) at the *sn*-1 position to generate monoacylglycerols such as 2-arachidonoylglycerol (2-AG).

Despite this resemblance in substrate catalysis, both DAGL subtypes appear to have distinct physiological functions. Animal models with genetic deletion of either DAGL have provided valuable insight in the relative contribution of each subtype in 2-AG biosynthesis. For example, DAGL α knockout (KO) mice have 80% lower 2-AG levels in the brain, whereas these levels were decreased by 50% in DAGL β ^{KO} counterparts. On the other hand, liver 2-AG levels were more drastically altered in DAGL β ^{KO} than DAGL α ^{KO} mice (90%

versus 60% reduction, respectively).¹¹ Although this indicates that both subtypes cannot completely compensate for each other's loss, it cannot be ruled out that long-term congenital deletion of one DAGL subtype might be partially compensated by the other variant on the transcriptome or proteome level. In addition, DAGL expression is dynamically controlled during neuronal development. DAGL α , for example, is highly expressed in neurons, whereas DAGL β is more abundant in microglia.¹² Although advanced genetic techniques allow for cell type-specific gene knockouts, these models lack the temporal control required to investigate the individual roles of the DAGL subtypes in this dynamic process.¹³

Long-term compensation effects can be avoided using acute inactivation of DAGL activity via pharmacological tools. Indeed, blockade of DAGL activity by small-molecule inhibitors with an α -keto heterocycle (LEI-105) or triazole urea scaffold (DH376 and DO34) rapidly reduced 2-AG levels in cells and the central nervous system, respectively.^{14,15} However, currently available DAGL inhibitors target both DAGL α and DAGL β . Subtype selectivity by medicinal chemistry efforts has proven to be exceptionally challenging to achieve, in part due to a lack of a crystal structure of the active site of DAGL α and DAGL β , which impedes structure-based inhibitor design. Moreover, achieving cellular specificity, *i.e.* targeting one specific cell type in the brain, such as neurons or microglia, remains a major challenge with pharmacological tools. This hampers the validation of both enzyme subtypes as a therapeutic target for various diseases, such as metabolic disorders and neurodegenerative diseases.^{16–18}

The field of chemical genetics combines the specificity of genetics with acute modulation of enzyme activity by small-molecule inhibitors. Garske *et al.* previously introduced the concept of covalent complementarity for protein kinases. Chapters 2, 3 and 4 of this thesis demonstrated that mutagenesis of active site residues into a reactive cysteine allows the development of covalent, mutant-specific inhibitors. A similar chemical genetic approach comprised of a DAGL α cysteine mutant and complementary inhibitor would be ideally suited to achieve subtype-selective inhibition of DAGL α . In addition, cell type-specific incorporation of mutant DAGL α using mouse genetics techniques would allow for acute modulation of DAGL α exclusively in a specific cell type, without affecting wild-type DAGL α expressed in other cell types.

This chapter describes the first steps towards the development of a chemical genetic strategy to identify a DAGL α cysteine mutant that can be selectively targeted by a complementary inhibitor. Leu651, directly following catalytic His650 of the catalytic triad, was identified as a position in the DAGL α active site that can be mutated into a cysteine with limited effects on catalytic activity and enzyme kinetics. Next, a complementary inhibitor was synthesized that covalently and irreversibly reacted with this cysteine, is selective for DAGL α ^{L651C} and does not target wild-type DAGL α nor DAGL β . However, a

biphasic binding behavior was observed, which indicated that only ~50% of the enzyme population was available for covalent addition to the complementary inhibitor. Further optimization is thus required to obtain a chemical genetic toolbox suitable to dissect subtype-specific roles of DAGL α and DAGL β or modulate DAGL α activity with cellular specificity.

Results

Design and biochemical characterization of DAGL α cysteine mutants

The active site of DAGL α and DAGL β recognizes similar substrates and performs similar chemical reactions. Available inhibitors generally cross-react with the other subtype and are non-selective, dual DAGL α / β inhibitors (Figure 5.2A). To achieve subtype-specific inhibition of DAGL α using chemical genetics, active site residues were mutated into a cysteine: a nucleophilic amino acid with a thiol moiety that can be covalently targeted by electrophilic inhibitors (Figure 5.2B). Since DAGL β (as well as wild-type DAGL α) lacks native cysteine residues in its active site, it is envisioned that covalent chemistry to this engineered cysteine can be exploited to improve subtype selectivity. Key to this strategy is that the catalytic activity, enzyme kinetics and substrate recognition are not abolished by the introduced mutation. This ensures minimal disturbance to normal cellular physiology when applied in living model systems, and allows for acute perturbation of the enzyme function

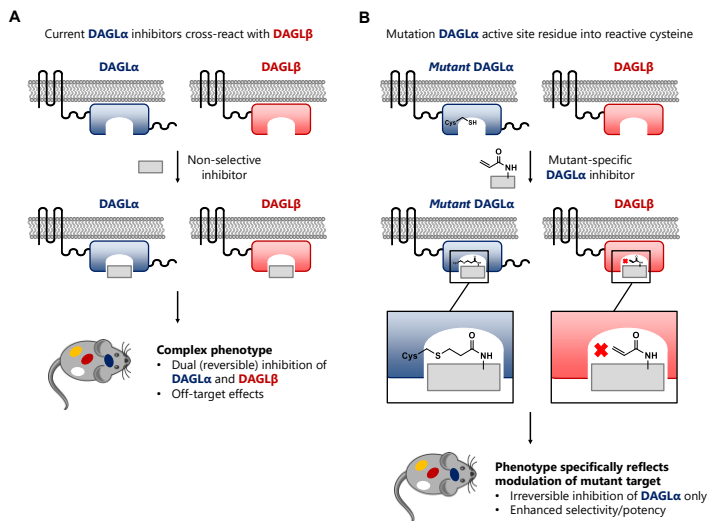


Figure 5.2 - Chemical genetic strategy for subtype-selective inhibition of DAGL α . (A) Current DAGL α inhibitors cross-react with DAGL β , resulting in dual inhibition of both subtypes. (B) The presented strategy involves mutagenesis of an active site residue in DAGL α into a cysteine, accompanied by the design of a mutant-specific, complementary inhibitor that covalently and irreversibly reacts with the introduced cysteine. This covalent, irreversible binding mode enhances inhibitor potency on DAGL α and selectivity against DAGL β , which lacks native cysteine residues in its active site.

only upon administration of the complementary, mutant-selective inhibitor. To identify an amino acid in the DAGL α active site that can be substituted for a cysteine without affecting protein function, a previously reported DAGL α homology model with docked reversible inhibitor **1** was examined.¹⁹ Twelve amino acid residues were selected for mutagenesis, based on their location, appropriate positioning and distance to the ligand (Figure 5.3A). The corresponding DAGL α cysteine mutants were subsequently generated using site-directed mutagenesis and cloned into a mammalian expression vector in frame with a C-terminal FLAG-tag. The mutant proteins were expressed in HEK293T cells (transfections performed in triplicate), followed by cell lysis and preparation of membrane fractions which were used for further biochemical profiling.

Activity-based protein profiling (ABPP) is used to visualize active pools of enzyme in complex proteomes by reacting to specific fluorescent activity-based probes (ABPs). The set of 12 mutants was profiled using MB064, a structural analog of tetrahydrolipstatin, which targets a variety of serine hydrolases including many endocannabinoid hydrolases¹⁹, and DH379, a more selective ABP that targets DAGL α/β and ABHD6¹⁵ (Figure 5.3B). Quantification of labeling intensities (Figure 5.3C) revealed that three mutants (T408C, H429C and G431C) showed greatly reduced labeling intensities by both ABPs. Interestingly, these three mutants were all located in the same binding pocket in the DAGL α active site. Other mutants (M432C, G538C, L659C) exhibited a labeling intensity of approximately 50% compared to wild-type. However, various mutants (I529C, L531C, L647C, L651C and G658C) showed only minimally reduced or, in some cases, enhanced labeling intensities. Of note, MB064 and DH379 labeling intensities showed a moderate correlation ($R^2 = 0.38$, Figure 5.3D), with preferential labeling of some mutants by one particular probe (e.g. G502C by DH379 and I529C by MB064). These results highlight the benefit of using two probes with distinct chemotypes for biochemical characterization of the enzymes.

Because ABPs only label the pool of active enzymes, reductions in labeling intensity can originate from lower probe binding affinity, altered protein folding or lower mutant expression levels compared to wild-type protein. The latter was examined using immunoblot analysis against the C-terminal FLAG-tag (Figure 5.3B, E), which revealed that some mutants (G431C, M432C, G538C, L651C) indeed had lower expression levels than wild-type DAGL α , possibly due to protein misfolding and reduced stability. However, other mutants (T408C and H429C) matched wild-type expression levels, whereas no probe labeling was observed, indicating that these substitutions may directly prevent probe binding, for example by steric clash or changes in protein folding that prohibit entry of the probe into the DAGL α active site.

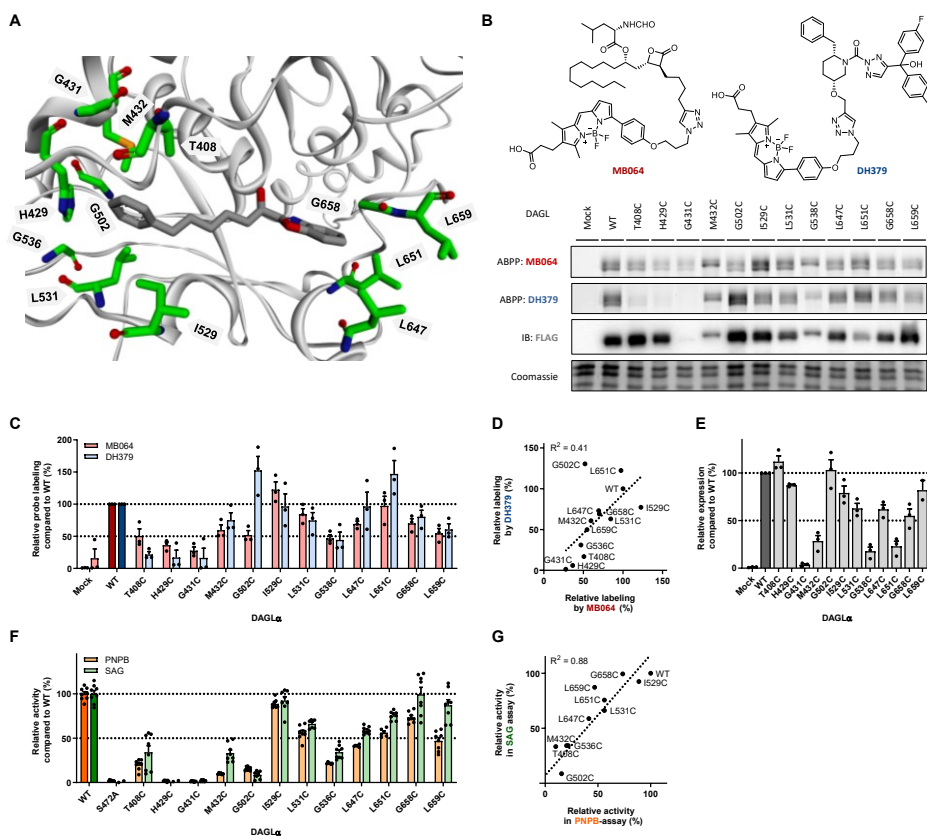


Figure 5.3 – Design of DAGL α cysteine point mutants and characterization by activity-based protein profiling and substrate assays. (A) Location of mutated active site residues in DAGL α homology model with docked reversible inhibitor 1. (B, C) Recombinantly expressed DAGL α mutants analyzed by activity-based protein profiling using probes MB064 (250 nM, 15 min, rt) and DH379 (1 μ M, 15 min, rt). Protein expression levels were determined by anti-FLAG immunoblot. Band intensities were normalized to wild-type control (N = 3, individual transfections). (D) Correlation between MB064 and DH379 labeling intensities. (E) Relative expression of DAGL α mutants compared to wild-type. Band intensities were corrected for protein loading and normalized to wild-type control (N = 3, individual transfections). (F) Biochemical activity of DAGL α mutants analyzed by surrogate (PNP-butyrate) and natural (SAG) substrate assays. Activity was determined using slope of reaction progress curve in linear range and normalized to wild-type control (N = 2, n = 4). (G) Correlation between relative activities determined using PNPB and SAG as substrates. Data represent means \pm SEM.

Next, mutant enzyme activity was measured using two substrate-based assays employing the surrogate substrate *para*-nitrophenyl butyrate (PNPB) and the natural substrate 1-stearoyl-2-arachidonoyl-*sn*-glycerol (SAG), respectively (Figure 5.3F). Membrane preparations overexpressing DAGL α variants were incubated with the chromogenic substrate PNPB, resulting in hydrolysis of the ester bond and release of *para*-nitrophenol that can be monitored by absorbance measurements.²⁰ In a similar fashion, hydrolysis of the physiological substrate SAG by DAGL α results in release of 2-AG, which is indirectly converted into a fluorescent signal via a multi-enzyme cascade reaction.²¹ The slopes of the corresponding reaction progress curves were determined in the linear range

and normalized to wild-type DAGL α activity. Multiple mutants (T408C, H429C, G431C, M432C, G502C and G536C) showed a more than 50% reduction of hydrolytic activity in both substrate assays (Figure 5.3F). This reduction in hydrolase activity can for some mutants (e.g. G431C and M432C) be ascribed to reduced expression levels. However, other inactive mutants (e.g. H429C) had no hydrolytic activity despite expression levels similar to wild-type, suggesting that His429 is essential for substrate binding or conversion. Activities determined in the substrate assays showed a good correlation ($R^2 = 0.78$) with a general trend of slightly higher activity using SAG opposed to PNPB as substrate (Figure 5.3G). Moreover, the substrate hydrolysis activity profile was relatively similar to the ABPP labeling profile, with the most prominent exception being mutant G502C, which showed completely abolished substrate hydrolysis activity, even though labeling by DH379 and MB064 was (partially) preserved.

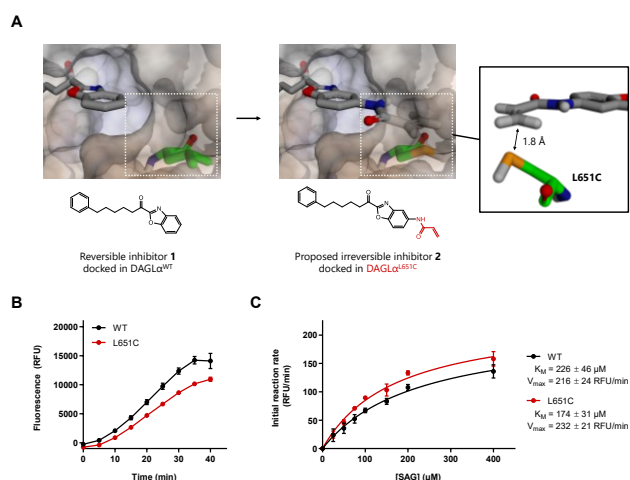


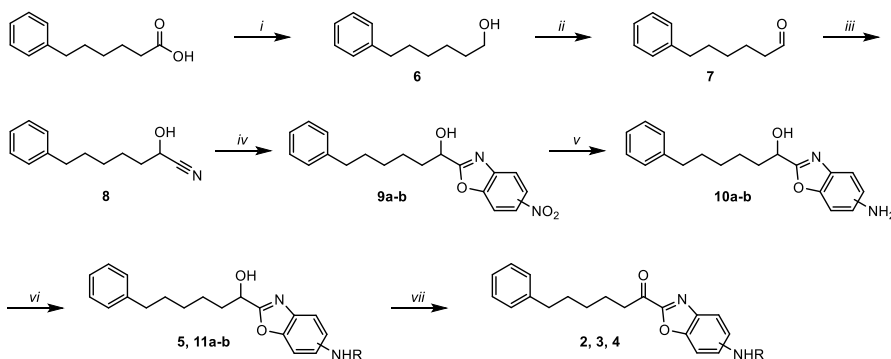
Figure 5.4 – Selection of DAGL α^{L651C} as catalytically active mutant for the design of complementary, irreversible inhibitors. (A) Design of a proposed irreversible inhibitor **2** to covalently target DAGL α^{L651C} . Installation of an acrylamide warhead on reversible inhibitor **1** positions this Michael acceptor in close proximity (1.8 Å) of the target cysteine. (B) Reaction progress curve of SAG hydrolysis by DAGL α^{WT} and DAGL α^{L651C} ($N = 2$, $n = 2$). (C) Determination of kinetic parameters K_M and V_{max} using SAG hydrolysis assay. Initial reaction rates correspond to slopes of reaction progress curves in the linear part ($N = 2$, $n = 2$). Data represent means \pm SEM.

In particular, interest was drawn to a subset of mutants, *i.e.* L647C, L651C, G658C and L659C, which all retained hydrolytic activity and could be labeled by both ABPs. Furthermore, these residues are all located in the same hydrophobic pocket and in close proximity of the benzoxazole moiety of **1**. Previous structure-activity studies verified that this pocket is not completely occupied by **1** and can accommodate an additional tolyl-group¹⁴. It was therefore reasoned that these cysteine mutants might be targetable by an appropriately positioned electrophile on compound **1**. Of these mutants, DAGL α^{L651C} was expected to be most promising, since it appeared to be in close proximity (1.8 Å) and adequately positioned to react with proposed inhibitor **2** via a Michael addition reaction to its acrylamide warhead (Figure 5.4A). For this reason, DAGL α^{L651C} was biochemically

profiled in more detail using the SAG hydrolysis assay. DAGL α ^{L651C} showed a reaction progress curve similar to DAGL α ^{WT} (Figure 5.4B). Despite slightly lower SAG hydrolysis activity (76% compared to WT), its maximal reaction rate was unaffected (WT: $V_{\max} = 216 \pm 24$ RFU/min, L651C: $V_{\max} = 232 \pm 21$ RFU/min; $P > 0.05$). In contrast, DAGL α ^{L651C} showed a minor but non-significant increase in SAG binding affinity as reflected by a lower Michaelis-Menten constant (WT: $K_M = 226 \pm 46$ μ M, L651C: $K_M = 174 \pm 31$ μ M; $P > 0.05$) (Figure 5.4C). Finally, it was confirmed that mutagenesis of Leu651 into a cysteine had no detrimental effect on the affinity of **1** (WT: $pIC_{50} = 5.8 \pm 0.04$, L651C: $pIC_{50} = 5.5 \pm 0.05$) (Table 5.1 and Supplementary figure 5.1).

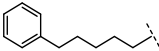
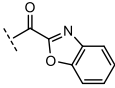
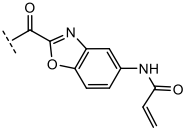
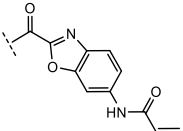
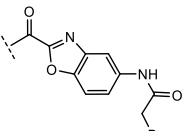
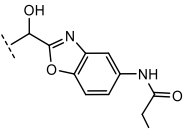
Design and synthesis of mutant-specific inhibitors

Compound **1** served as a suitable starting point for the design of mutant-specific inhibitors, since it was previously reported to have a relatively low affinity ($pIC_{50} \sim 5$) for DAGL α and DAGL β .^{19,22} Electrophilic derivatives were synthesized, possessing acrylamide warheads intended to react with the cysteine residues (Scheme 5.1). Compounds **2** and **3**, proposed as potential irreversible inhibitors by undergoing a Michael addition to nearby Cys651 (Figure 5.4A), did not show any increase in potency on DAGL α ^{L651C} or other mutants under standard assay conditions (20 min pre-incubation, rt) (Table 5.1 and Supplementary figure 5.1). Interestingly, compound **2** showed potent inhibition (> 100 -fold increase) of the engineered enzyme upon increased incubation time and elevated temperatures (60 min, 37 °C) (Figure 5.5B). This suggested that the initial lack of mutant inhibition may not be due to inappropriate positioning of the warhead on the scaffold, but is due to low reactivity of the cysteine. For this reason, compound **4** with a bromoacetamide warhead, a more reactive electrophile than the acrylamide group, was synthesized. Indeed, a marked increase in inhibitory potency was observed on DAGL α ^{L651C} but not on DAGL α ^{WT} compared to compound **2** under standard assay conditions (Figure 5.5A).



Scheme 5.1 - Synthesis towards electrophilic derivatives of compound 1. i) LiAlH₄, Et₂O, 0 °C, 97%. ii) DMSO, oxalyl chloride, DCM, -78 °C. iii) KCN, THF:H₂O (1:1), rt, 73% over 2 steps. iv) Acetyl chloride, EtOH, CHCl₃; 2-amino-4-nitrophenol (**9a**) or 2-amino-5-nitrophenol (**9b**), pyridine, EtOH, 80 °C, 30-64%. v) PtO₂, H₂, EtOAc, rt, 57%-quant. vi) Bromoacetyl bromide (**5**) or acryloyl chloride (**11a-b**), DIPEA, DCM, 0 °C, 76%-quant. vii) Dess-Martin periodinane, DCM, rt, 75-88%.

Table 5.1 – Inhibitory potency of synthesized compounds on DAGL α ^{WT} and mutants. Shown values represent pIC₅₀ ± SD determined using the PNPB hydrolysis assay with 20 min pre-incubation at rt (N = 2, n = 4 for vehicle, N = 2, n = 2 for inhibitor-treated). The two values (i, ii) for compound **2** and **4** on L651C represent both pIC₅₀ values of the biphasic dose-response curve. † Inhibitor incubation 60 min at 37 °C.

Compound	Structure	pIC ₅₀ WT	pIC ₅₀ L651C
			
1		5.8 ± 0.04	5.5 ± 0.05
2		< 5 5.0 ± 0.07 †	5.0 ± 0.10 i) 8.3 ± 0.12 † ii) < 5 †
3		< 5	5.5 ± 0.05
4		5.9 ± 0.05	i) 8.9 ± 0.39 ii) 5.8 ± 0.19
5		4.8 ± 0.08	4.8 ± 0.03

Identification and characterization of a subtype-selective inhibitor for DAGL α ^{L651C}

Notably, compound **4** (and **2** under modified conditions) displayed a biphasic IC₅₀ curve that was independent of assay buffer pH and reduction agent (Supplementary Figure 5.2). This biphasic curve can potentially be explained by two putative binding events of the compound: an irreversible binding event of the introduced cysteine with the bromoacetamide warhead (pIC₅₀ = 8.9 ± 0.39) and a reversible binding event of the catalytic serine to the α -keto group (pIC₅₀ = 5.8 ± 0.19). Three different experiments were performed to investigate this hypothesis. First, membranes overexpressing DAGL α were pre-incubated with iodoacetamide (IAA), an alkylating agent that irreversibly reacts with the thiol group of cysteine residues, to block the covalent reaction of Cys651 to the bromoacetamide group of compound **4**, while leaving the reactivity of the catalytic serine of the enzyme intact. Indeed, IAA pretreatment reverted the two-phase binding curve of compound **4** on DAGL α ^{L651C} to a one-phase dose-response curve with a low pIC₅₀ similar

to reversible control compound **1** (Figure 5.5C), whereas IAA did not affect the inhibitory effect of compound **4** on DAGL α ^{WT} (Figure 5.5E) or basal DAGL α activity (Figure 5.5D, F). Second, the pIC₅₀ of compound **4** was determined using different pre-incubation times.

This analysis revealed that the enzyme inhibition was time-dependent only for the binding event reflected by the most potent interaction, but not for lower affinity interaction (Figure 5.5G, H). Third, a displacement assay was performed using ABP MB064. Membranes overexpressing DAGL α ^{L651C} were pre-incubated with **4** or reversible control inhibitor LEI105¹⁴ at their corresponding IC₈₀-concentration, followed by addition of

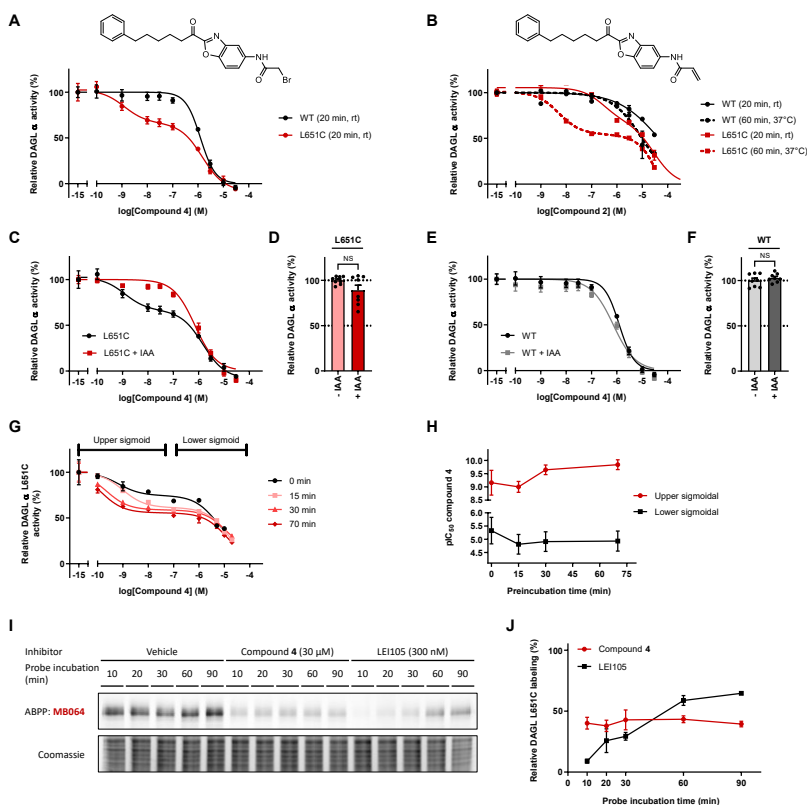


Figure 5.5 – Identification of mutant-selective, irreversible inhibitors of DAGL α ^{L651C}. (A, B) Dose-response curves of compound **4** (A) and **2** (B) on DAGL α ^{WT} and DAGL α ^{L651C}, determined using PNPB hydrolysis assay (N = 2, n = 4 for vehicle, N = 2, n = 2 for inhibitor-treated). (C, E) Pre-incubation with alkylating agent iodoacetamide (IAA, 20 mM, 30 min in the dark, rt) reverts biphasic binding curve of **4** on DAGL α ^{L651C} (C), but does not alter inhibition profile on DAGL α ^{WT} (E). (D, F) IAA pre-incubation does not affect basal DAGL α activity. (G) Two-phase binding profile of **4** on DAGL α ^{L651C} is time-dependent. Compound was pre-incubated for 0-15-30-70 min prior to addition of PNPB substrate. (H) pIC₅₀ of upper sigmoidal increases with pre-incubation time of **4**, while pIC₅₀ of lower sigmoidal remains constant. (I, J) ABP MB064 outcompetes LEI105 but not compound **4** binding over time. Compounds were pre-incubated at the respective IC₈₀-concentration (30 μ M for **4** and 300 nM for LEI105, 20 min, rt), followed by incubation with MB064 (250 nM, 10-20-30-60-90 min, rt). Band intensities were normalized to vehicle-treated control at same time point (N = 3). Data represent means \pm SEM. Statistical analysis was performed using two-tailed *t*-test: NS if *P* > 0.05.

MB064 for different incubation times. DAGL α ^{L651C} labeling did not recover after pre-incubation with **4**, whereas reversible inhibitor LEI105 showed substantial displacement (Figure 5.5I, J). Altogether, the results of these three experiments suggested that the most potent inhibitory interaction is reflecting the irreversible reaction of Cys651 with the bromoacetamide warhead, while the weaker inhibitory effect is mediated by the reversible, covalent interaction of Ser472 with the α -keto group. Strikingly, compound **5**, in which the ketone is substituted for a hydroxyl moiety, showed no inhibition of DAGL α ^{L651C} (Table 5.1), implying that initial binding of Ser472 to the α -keto group is essential prior to covalent bond formation with Cys651. Having established that compound **4** potently and covalently inhibits DAGL^{L651C}, it was investigated whether compound **4** is a subtype-selective inhibitor of DAGL α ^{L651C} in the presence of DAGL β . To this end, an ABPP experiment was performed using DH379. Membranes overexpressing DAGL β and DAGL α ^{L651C} or DAGL α ^{WT} were mixed in a various ratios, which revealed that a 1:1 ratio was most optimal to achieve efficient labeling of both DAGL subtypes (Supplementary figure 5.3). DAGL α / β mixtures were then pre-incubated with different concentrations of compound **4** or LEI105, a reversible, potent dual DAGL inhibitor with related chemical structure¹⁴ (Figure 5.6A). Quantification of the labeling intensities confirmed that LEI105 does not discriminate between DAGL α and DAGL β , with equipotent inhibition on both subtypes (Figure 5.6B). However, the chemical genetic strategy employing DAGL α ^{L651C} and compound **4** allowed for selective inhibition of DAGL α in presence of DAGL β (Figure 5.6C). Of note, a similar biphasic dose-response curve was observed in this ABPP experiment, verifying that this phenomenon was not assay-dependent.

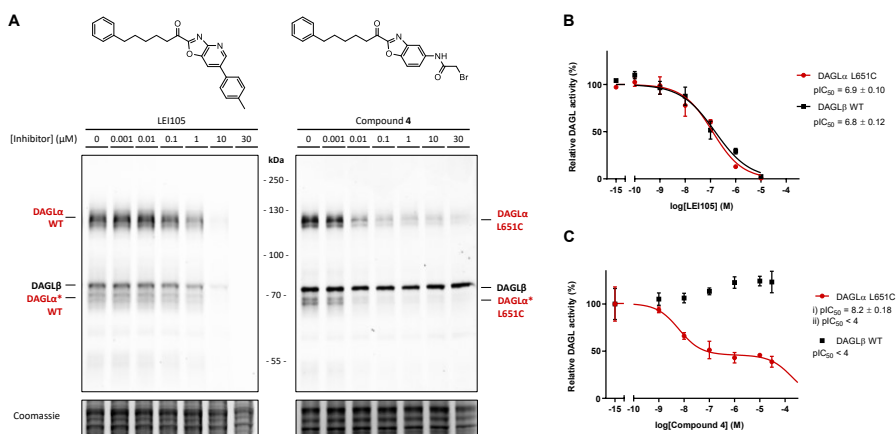


Figure 5.6 – Chemical genetic strategy allows subtype-selective inhibition of DAGL α in presence of DAGL β . (A-C) Membranes overexpressing DAGL α ^{WT} or DAGL α ^{L651C} and DAGL β (2 mg/mL) were mixed (1:1 ratio) and incubated with LEI105 or **4** (20 min, rt), followed by addition of DH379 (1 μ M, 15 min, rt). DAGL α band marked with asterisk corresponds to a previously reported degradation product.¹⁹ Band intensities were normalized to vehicle-treated control (N = 3). Data represent means \pm SEM.

Discussion and conclusion

Previously reported DAGL inhibitor chemotypes, such as the α -ketoheterocycles¹⁴, glycine sulfonamides²³ and 1,2,3-triazole ureas^{15,24}, are all dual DAGL α/β inhibitors. Exclusive targeting of one subtype has proven difficult to achieve so far. This chapter describes the first steps towards a chemical genetic strategy that allows for subtype-selective targeting of DAGL α in presence of the structurally and functionally similar DAGL β subtype. This approach employs mutagenesis of a DAGL α active site residue into a reactive cysteine that can be selectively targeted by a complementary, covalent inhibitor.

Homology model-directed mutant design and comprehensive biochemical characterization using ABPP and substrate hydrolysis assays led to the identification of Leu651 as a suitable residue for mutagenesis into a cysteine, since DAGL α ^{L651C} retained its catalytic activity and kinetic properties, ensuring minimal interference to normal cellular physiology if introduced in host systems. Follow-up experiments would involve mutagenesis of this residue in an endogenous model system such as cell lines or mice using the CRISPR/Cas9 gene editing technology.²⁵⁻²⁷ This circumvents the use of overexpression systems and allows subtype-selective targeting of DAGL α ^{L651C} under the appropriate epigenetic control. Mouse genetics techniques, such as Cre-LoxP recombination combined with brain cell-specific promoters²⁸, can be applied to introduce the engineered DAGL α protein in specific brain regions. This would enable acute pharmacological modulation of DAGL α activity exclusively in selected cell populations, for example cortical neurons or cerebellar Purkinje cells, without affecting DAGL α (and DAGL β) activity in other neuronal cell types in the brain.

Compound **4** was identified as a mutant-specific inhibitor of DAGL α ^{L651C}, which displayed biphasic binding behaviour that may reflect the presence of two warheads in the inhibitor. The most potent inhibitory interaction is likely the result of the irreversible, covalent reaction of Cys651 with the bromoacetamide electrophile, while the weaker inhibitory effect is mediated by the reversible, covalent interaction of catalytic Ser472 to the α -keto group. Currently, it is unknown why the engagement of the thiol does not result in complete inhibition of the enzyme, but levels off at approximately 50%. It may indicate that there are possibly two proteoforms of DAGL α ^{L651C}, of which one possesses a non-reactive cysteine, for example due to oxidation. The thiol group of cysteine is known to be prone to oxidation, either by formation of disulfides, sulfur oxyacids or S-nitroso-species.²⁹ None of these oxidized cysteine species possess a reactive thiol for nucleophilic chemistry, resulting in a mixture of two DAGL α ^{L651C} proteoforms of which only one is potently inhibited by compound **4**. However, the biphasic binding behavior could not be reverted by incubation with various reducing agents *in vitro*. Alternatively, it is possible that DAGL α ^{L651C} exists as a homodimer that undergoes a conformational change upon inhibitor

binding, rendering the other monomer insusceptible to inhibition by **4**. Additional studies are required to explain these results.

In summary, this study describes the first steps towards a chemical genetic strategy that potentially allows for subtype-selective or cell type-specific inhibition of DAGL α . Residue Leu651, located directly upstream of the catalytic triad His650, was identified as a suitable position to mutate into a cysteine without substantially affecting DAGL α enzymatic activity and kinetics. Structure-based design led to the discovery of compound **4** as a mutant-selective, complementary DAGL α ^{L651C} inhibitor that displays irreversible binding characteristics and can selectively target DAGL α ^{L651C} in presence of DAGL β . Further optimization of compound **4** and investigation of its biphasic binding behavior are required to obtain a chemical genetic toolbox suitable for dissecting subtype-specific roles of DAGL α and DAGL β in endogenous model systems.

Acknowledgments

Timo Wendel and Florian Mohr are kindly acknowledged for their contribution to the synthesis of compounds.

Experimental procedures - Biochemistry

General

All chemicals and other reagents were purchased from Sigma Aldrich, unless stated otherwise. Assay enzymes (glycerol kinase from *Cellulomonas sp.*, product code G6142; glycerol-3-phosphate oxidase from *Streptococcus thermophilus*, product code G4388; horse radish peroxidase from *Horseradish*, product code 77332) were purchased from Sigma Aldrich. 1-Stearoyl-2-arachidonoyl-*sn*-glycerol was purchased from Cayman Chemicals.

Cloning

Full-length wild-type human DAGL α and mouse DAGL β cDNA was obtained from Source Bioscience and cloned into pcDNA3.1 expression vectors as previously described.¹⁹ Mutations were introduced using Phusion site-directed mutagenesis kit (Thermo Fisher). Briefly, target plasmid was amplified by PCR using two phosphorylated primers that anneal back to back to the plasmid, of which one contains the desired mutation. The product was then circularized by blunt-end ligation with T4 DNA ligase and transformed to XL10-Gold competent cells (prepared using *E. coli* transformation buffer set; Zymo Research). Mutant plasmids were isolated using plasmid isolation kits following the supplier's protocol (Qiagen). All constructs were verified by Sanger sequencing (Macrogen).

Supplementary Table 1 – List of oligonucleotide sequences.

ID	Name	Sequence	ID	Name	Sequence
P1	DAGL- α _T408C_forw	CCCAAGGATGCCCTGTGTGACCTGACGGGTGAT	P13	DAGL- α _L531C_forw	GTCCCCAGGATTGGCTGCTCAGCTGGAAGGC
P2	DAGL- α _T408C_rev	GGACAGGGTCCCGGACTACTGATC	P14	DAGL- α _L531C_rev	GAGGCTCTTTGCCAGAACACAGCA
P3	DAGL- α _H429C_forw	GGCACCTGGTGGGTGCAAGGGTATGGTCTCT	P15	DAGL- α _G536C_forw	CTCTCTCAGCTGGAATGCTTCCGACAGACAGCTC
P4	DAGL- α _H429C_rev	GTGGTGGCCCTCCACGGGAGGCGC	P16	DAGL- α _G536C_rev	GCCAATCCTGGGGACGAGGCTTTG
P5	DAGL- α _G431C_forw	TGGTGGCCACACAAGTGTATGTCCTCTCAGCT	P17	DAGL- α _L647C_forw	ATCTGCCAGCCATGTGTATGAGCACCTGCC
P6	DAGL- α _G431C_rev	GGTGGCCGTGTGCCCTCCACGGGG	P18	DAGL- α _L647C_rev	GATCACCTATTGAAGGCCCTTTG
P7	DAGL- α _M432C_forw	CTGGGCCACAAGGGTTGGCTCTCTCAGCTGAG	P19	DAGL- α _L651C_forw	ATGCTGCATGAGCACGTCCCTATGTGGTCATG
P8	DAGL- α _M432C_rev	CCAGTGGCCCTGGTCCCTCCACCG	P20	DAGL- α _L651C_rev	GGCTGGCAGATGATCACCTCATTG
P9	DAGL- α _G502C_forw	TACTCCCCGCCAGGGTGCCTGTGAGTGAGGAT	P21	DAGL- α _G658C_forw	TATGTGGTCATGGAGTGTCTCAACAAGGTGCTG
P10	DAGL- α _G502C_rev	GGCAAAGCACTTGAGGTGCGGATAC	P22	DAGL- α _G658C_rev	GGGCAGGTGCTCATGAGCATGGCT
P11	DAGL- α _L529C_forw	GACCTGTCGCCAGGTGTGGCTCTCTCAGCTG	P23	DAGL- α _L659C_forw	GTGGTCATGGAGGGGTGCAACAAGGTGCTGGAG
P12	DAGL- α _L529C_rev	TTTGCCAGAACCACAGCAGTACG	P24	DAGL- α _L659C_rev	ATAGGCGAGGTGCTCATGAGCATG

Cell culture

HEK293T (human embryonic kidney) cells were obtained from ATCC and tested on regular basis for mycoplasma contamination. Cultures were discarded after 2-3 months of use. Cells were cultured at 37 °C under 7% CO₂ in DMEM containing phenol red, stable glutamine, 10% (v/v) heat-inactivated newborn calf serum (Seradigm), penicillin and streptomycin (200 μ g/mL each; Duchefa). Medium was refreshed every 2-3 days and cells were passaged two times a week at 80-90% confluence. One day prior to transfection, HEK293T cells were transferred from confluent 10 cm dishes to 15 cm dishes. Before transfection, medium was refreshed (13 mL). A 3:1 mixture of polyethylenimine (PEI; 60 μ g/dish) and plasmid DNA (20 μ g/dish) was prepared in serum-free medium (2 mL) and incubated for 15 min at rt. The mixture was then dropwisely added to the cells, after which the cells were grown to confluence in 72 h. Cells were then harvested by suspension in PBS, followed by centrifugation (200 *g*, 5 min). Cell pellets were flash-frozen in liquid nitrogen and stored at -80 °C until membrane fraction preparation.

Membrane fraction preparation

Cell pellets were thawed on ice and homogenized by polytron (20,000 rpm, 3 x 7 s; SilentCrusher S, Heidolph) in lysis buffer A (20 mM HEPES pH 7.2, 2 mM DTT, 250 mM sucrose, 1 mM MgCl₂ and 25 U/mL benzonase). Suspensions were incubated on ice for 30 min to yield total lysates. For preparation of membrane fractions, total lysates were subjected to ultracentrifugation (93,000 *g*, 30 min, 4 °C; Beckman Coulter, Ti70 or Ti70.1 rotor) and pellets were homogenized in storage buffer B (20 mM HEPES pH 7.2, 2 mM DTT) by polytron (20,000 rpm, 1 x 10 s). Protein concentrations were determined

using Quick Start™ Bradford Protein Assay (Bio-Rad). Membrane preparations were frozen in liquid nitrogen and stored at -80 °C until use.

PNP-butyrate hydrolysis assay

Assays were performed in 50 mM HEPES pH 7.0 in clear, flat-bottom 96-well plates (Greiner). Inhibitors were added from 40x concentrated stock solution in DMSO. DAGL α -overexpressing membrane preparations (10 μ g per well) were incubated with inhibitor for 20 min at rt in a total volume of 190 μ L. Next, 10 μ L substrate solution (PNP-butyrate in 1:1 mixture of DMSO/H₂O, final concentration 300 μ M) was added. Absorbance at 420 nm was measured at 37 °C in 1 min intervals for 20 min on a GENios plate reader (Tecan). Final assay concentrations: 50 ng/ μ L DAGL α -overexpressing membranes, 300 μ M PNP-butyrate, 5% DMSO in a total volume of 200 μ L. All measurements were performed in N = 2 (individual plates), n = 2 (technical replicates on same plate) or N = 2, n = 4 for controls, with Z' \geq 0.6.

SAG hydrolysis assay

Assays were performed in HEMNB buffer (50 mM HEPES pH 7.4, 1 mM EDTA, 5 mM MgCl₂, 100 mM NaCl, 0.5% (w/w) BSA) in black, flat-bottom 96-well plates (Greiner). Inhibitors were added from 40x concentrated stock solution in DMSO. A substrate solution of 1-stearoyl-2-arachidonoyl-*sn*-glycerol was prepared just prior to use. The SAG stock solution (10 mg/mL in methyl acetate) was dried under argon and subsequently taken up in 50 mM HEPES buffer (pH 7.0) + 0.75% (w/w) Triton X-100. The substrate solution was mixed to form an emulsion and stored on ice until use. DAGL α -overexpressing membrane preparations (10 μ g per well) were incubated with inhibitor for 20 min at rt in a total volume of 100 μ L. Next, 100 μ L assay mix containing monoacylglycerol lipase (MAGL), glycerol kinase (GK), glycerol-3-phosphate oxidase (GPO), horse radish peroxidase (HRP), adenosine triphosphate (ATP), Amplifu™Red and 1-stearoyl-2-arachidonoyl-*sn*-glycerol (SAG) was added. Fluorescence (λ_{ex} = 535 nm, λ_{em} = 595 nm) was measured at rt in 5 min intervals for 60 min on a GENios plate reader (Tecan). Final assay concentrations: 5 ng/ μ L MAGL-overexpressing membranes, 0.2 U/mL GK, GPO and HRP, 125 μ M ATP, 10 μ M Amplifu™Red, 150 μ M SAG, 5% DMSO, 0.0075% (w/w) Triton X-100 in a total volume of 200 μ L. For IC₅₀ determinations, assays were performed with variable inhibitor concentrations. For K_M determinations, assays were performed with variable SAG concentrations and fluorescence was measured at rt in 2 min intervals for 60 min on a CLARIOstar plate reader (BMG Labtech). All measurements were performed in N = 2 (individual plates), n = 2 (technical replicates on same plate) or N = 2, n = 4 for controls, with Z' \geq 0.6.

Activity-based protein profiling

Total lysates or membrane fractions (14 μ L, 1.38 mg/mL) were incubated with inhibitor (0.5 μ L in DMSO, 29x concentrated stock, 20 min, rt), followed by incubation with probe MB064 or DH379 (0.5 μ L in DMSO, 30x concentrated stock, 15 min, rt). Reactions were quenched with 4x Laemmli buffer (5 μ L, final concentrations 60 mM Tris pH 6.8, 2% (w/v) SDS, 10% (v/v) glycerol, 5% (v/v) β -mercaptoethanol, 0.01% (v/v) bromophenol blue) for 15 min at rt. Samples were resolved by SDS-PAGE on a 10% polyacrylamide gel (180 V, 75 min or 200 V, 120 min in case of DAGL α and DAGL β mixtures). Gels were scanned using Cy3 channel settings (605/50 filter; ChemiDoc™ MP System, Bio-Rad). Fluorescence intensity was corrected for protein loading determined by Coomassie Brilliant Blue R-250 staining and quantified with Image Lab (Bio-Rad).

Immunoblot

Samples were resolved by SDS-PAGE and transferred to 0.2 μ m polyvinylidene difluoride membranes by Trans-Blot Turbo™ Transfer system (Bio-Rad) directly after fluorescence scanning. Membranes were washed with TBS (50 mM Tris pH 7.5, 150 mM NaCl) and blocked with 5% milk in TBS-T (50 mM Tris pH 7.5, 150 mM NaCl, 0.05% Tween-20) for 1 h at rt. Membranes were then incubated with primary antibody in 5% milk in TBS-T (o/n at 4 °C). Membranes were washed three times with TBS-T, incubated with matching secondary antibody in 5% milk in TBS-T (1 h at rt) and then washed three times with

TBS-T and once with TBS. Imaging solution (10 mL luminol in 100 mM Tris pH 8.8, 100 μ L ECL enhancer, 3 μ L H₂O₂) was added and chemiluminescence was detected on ChemiDoc™ MP System. Primary antibody: monoclonal mouse anti-FLAG M2 (1:5000, Sigma Aldrich, F3156), secondary antibody: goat anti-mouse-HRP (1:5000, Santa Cruz, sc-2005).

Data analysis, statistics and software

All shown data represent means \pm SEM, unless indicated otherwise. Replicates are indicated in figure legends with N for biological and n for technical replicates, respectively. For substrate hydrolysis assays, absorbance or fluorescence values were corrected for the average of the negative control (mock-membranes + vehicle; or DAGL-membranes with no SAG for Michaelis-Menten experiment). DAGL α -overexpressing (wild-type or mutant) membranes incubated with vehicle served as a positive control. Slopes of the corrected data were determined in the linear interval. The Z'-factor for each assay plate was calculated using the formula $Z' = 1 - 3(\sigma_{pc} + \sigma_{nc})/(\mu_{pc} - \mu_{nc})$ with σ = standard deviation, μ = mean, pc = positive control and nc = negative control. Plates with $Z' \geq 0.6$ were accepted for further analysis. For IC₅₀ determination, slopes were normalized to the positive control and analyzed using 'Non-linear dose-response analysis with variable slope' (GraphPad Prism 7.0). For curves with clear two-phase binding behavior, data were analyzed using 'Two sites - Fit logIC50'. For K_M and V_{max} determination, data were subjected to 'Michaelis-Menten' fit (GraphPad Prism 7.0).

All modeling figures were rendered using Discovery Studio 2016 (BIOVIA). The design of compounds was based on the homology model of DAGL α with compound **1**, with the Leu651 residue manually changed into a cysteine.¹⁹

Experimental procedures - Chemistry

General information

All reactions were performed using oven- or flame-dried glassware and dry solvents. Reagents were purchased from Sigma-Aldrich, Acros, and Merck and used without further purification unless noted otherwise. All moisture sensitive reactions were performed under an argon atmosphere. ^1H and ^{13}C NMR spectra were recorded on a Bruker AV 400 MHz spectrometer at 400.2 (^1H) and 100.6 (^{13}C) MHz using CDCl_3 , MeOD or CD_3CN as solvent. Chemical shift values are reported in ppm with tetramethylsilane or solvent resonance as the internal standard (CDCl_3 : δ 7.26 for ^1H , δ 77.16 for ^{13}C ; MeOD: δ 3.31 for ^1H , δ 49.00 for ^{13}C ; CD_3CN : δ 1.94 for ^1H , δ 118.26 for ^{13}C). Data are reported as follows: chemical shifts (δ), multiplicity (s = singlet, d = doublet, dd = double doublet, td = triple doublet, t = triplet, q = quartet, m = multiplet), coupling constants J (Hz), and integration. HPLC purification was performed on a preparative LC-MS system (Agilent 1200 series) with an Agilent 6130 Quadrupole MS detector. High-resolution mass spectra were recorded on a Thermo Scientific LTQ Orbitrap XL. Compound purity (> 95% unless stated otherwise) was determined by liquid chromatography on a Finnigan Surveyor LC-MS system, equipped with a C18 column. Flash chromatography was performed using SiliCycle silica gel type SiliaFlash P60 (230–400 mesh). TLC analysis was performed on Merck silica gel 60/Kieselguhr F254, 0.25 mm. Compounds were visualized using KMnO_4 stain (K_2CO_3 (40 g), KMnO_4 (6 g) in water (600 mL)) or ninhydrin stain (ninhydrin (1.5 g) in *n*-butanol (100 mL) and 3 mL acetic acid).

Synthesis of 6-phenylhexan-1-ol (**6**)

LiAlH_4 (13.1 mL, 26 mmol) was added to dry Et_2O (80 mL) at 0 °C, followed by dropwise addition of 6-phenyl hexanoic acid (1.27 g, 6.6 mmol) in dry Et_2O (10 mL). The mixture was allowed to warm to rt and stirred for 16 h. The reaction was quenched by sequential addition of H_2O (60 mL) and 1 M HCl (60 mL) and filtered over celite. The organic layer was washed with 1 M HCl (1 x 100 mL), sat. NaHCO_3 (1 x 100 mL) and brine (1 x 100 mL), dried over Na_2SO_4 and concentrated to obtain title compound (1.13 g, 6.3 mmol, 97%). ^1H NMR (400 MHz, CDCl_3): δ 7.32 – 7.23 (m, 2H), 7.23 – 7.12 (m, J = 7.0, 4.4, 2.7 Hz, 3H), 3.62 (t, J = 6.6 Hz, 2H), 2.61 (t, 2H), 1.69 – 1.59 (m, J = 8.9, 7.7 Hz, 2H), 1.59 – 1.51 (m, 2H), 1.48 (s, 1H), 1.44 – 1.30 (m, 4H). ^{13}C NMR (101 MHz, CDCl_3): δ 142.84, 128.50, 128.36, 125.73, 63.10, 36.00, 32.81, 31.56, 29.18, 25.73.

Synthesis of 6-phenylhexanal (**7**)

Oxalyl chloride (2.4 g, 19 mmol) was added to dry DCM (60 mL) at -78 °C, followed by dropwise addition of a solution of DMSO (2.9 g, 38 mmol) in dry DCM (20 mL). The mixture was stirred for 1 h, after which compound **6** (1.1 g, 6.2 mmol) in dry DCM (20 mL) was added dropwisely. The reaction mixture was stirred for 1 h, followed by dropwise addition of triethylamine (8.7 mL, 62 mmol). The mixture was allowed to warm to rt and stirred for 16 h, after which it was diluted with 1 M HCl (100 mL). Layers were separated and the aqueous layer was extracted with DCM (2 x 100 mL). Combined organic layers were washed with brine (200 mL), dried over Na_2SO_4 and concentrated, yielding title compound (1.1 g, 6.2 mmol, quant.). ^1H NMR (400 MHz, CDCl_3): δ 9.62 (t, J = 1.6 Hz, 1H), 7.05 – 7.17 (m, 5H), 2.51 (t, J = 7.6 Hz, 2H), 2.29 (dt, J = 1.6, 7.6 Hz, 2H), 1.50 – 1.56 (m, 4H), 1.24 – 1.28 (m, 2H). ^{13}C NMR (101 MHz, CDCl_3) δ 202.66, 142.38, 128.37, 128.23, 125.60, 43.79, 35.69, 31.21, 28.73, 21.89.

Synthesis of 2-hydroxy-7-phenylheptanenitrile (**8**)

Compound **7** (600 mg, 3.4 mmol) was dissolved in THF/ H_2O (1:1 ratio, 100 mL) at rt, followed by addition of KCN (2.4 g, 37 mmol). The mixture was stirred for 72 h, after which H_2O (100 mL) and Et_2O (200 mL) were added and layers were separated. The aqueous layer was extracted with Et_2O (2 x 100 mL). Combined organic layers were washed with sat. NaHCO_3 , H_2O and brine (200 mL each), dried over Na_2SO_4 and subsequently concentrated. The crude residue was purified by flash column chromatography (5% \rightarrow 20% EtOAc in pentane), yielding title compound (497 mg, 2.4 mmol, 72%). ^1H NMR (400 MHz, CDCl_3): δ 7.32 – 7.23 (m, 2H), 7.21 – 7.09 (m, 3H), 4.40 (t, J = 6.8 Hz, 1H), 3.15 (s, 1H),

2.60 (t, 2H), 1.86 – 1.72 (m, $J = 11.4$, 7.0 Hz, 2H), 1.70 – 1.57 (m, $J = 15.4$, 7.6 Hz, 2H), 1.57 – 1.44 (m, 2H), 1.44 – 1.30 (m, $J = 11.1$, 8.9, 4.8 Hz, 2H). ^{13}C NMR (101 MHz, CDCl_3): δ 142.44, 128.47, 128.39, 125.82, 120.19, 61.23, 35.76, 35.06, 31.18, 28.55, 24.47.

Synthesis of 1-(6-nitrobenzo[d]oxazol-2-yl)-6-phenylhexan-1-ol (9a)

Acetyl chloride (2.8 mL, 40 mmol) was dissolved in dry EtOH/ CHCl_3 (1:1 ratio, 4 mL) at 0 °C and stirred for 45 min, followed by dropwise addition of compound **8** (250 mg, 1.2 mmol) dissolved in dry CHCl_3 (2 mL). The mixture was stirred until completion monitored by TLC, after which it was allowed to warm to rt and subsequently concentrated *in vacuo* at 25 °C. The crude imidate intermediate was coevaporated with toluene (3 x 5 mL) and dissolved in dry EtOH (2 mL). Meanwhile, 2-amino-5-nitrophenol (208 mg, 1.4 mmol) and pyridine (107 μL , 1.3 mmol) were dissolved in dry EtOH (5 mL) and the mixture was stirred at 80 °C for 30 min, followed by dropwise addition of the imidate solution. The mixture was stirred at 80 °C for 16 h and concentrated. The crude residue was purified by flash column chromatography (10% \rightarrow 20% EtOAc in pentane), yielding title compound as a mixture with 2-amino-5-nitrophenol, which was used as such in the next step (approximately 30% yield based on NMR).

Synthesis of 1-(6-aminobenzo[d]oxazol-2-yl)-6-phenylhexan-1-ol (10a)

The mixture containing compound **9a** was dissolved in degassed EtOAc (50 mL), followed by addition of PtO_2 (13 mg, 0.06 mmol). The mixture was stirred under H_2 atmosphere for 16 h at rt, after which it was filtered over celite and concentrated to obtain title compound (62 mg, 0.20 mmol, 17% over 2 steps). ^1H NMR (400 MHz, CDCl_3): δ 7.38 (d, $J = 8.5$ Hz, 1H), 7.30 – 7.19 (m, 3H), 7.19 – 7.06 (m, $J = 8.9$ Hz, 3H), 6.74 (d, $J = 1.7$ Hz, 1H), 6.62 (dd, $J = 8.4$, 1.9 Hz, 1H), 4.86 (t, $J = 7.1$, 5.9 Hz, 1H), 2.57 (t, $J = 15.3$, 7.7 Hz, 2H), 2.00 – 1.85 (m, 2H), 1.59 (quint, $J = 15.1$, 7.5 Hz, 2H), 1.53 – 1.40 (m, 2H), 1.40 – 1.31 (m, 2H).

Synthesis of N-(2-(1-hydroxy-6-phenylhexyl)benzo[d]oxazol-6-yl)acrylamide (11a)

Compound **10a** (60 mg, 0.19 mmol) was dissolved in dry DCM (10 mL) and cooled to 0 °C, followed by addition of DIPEA (33 μL , 0.19 mmol). Next, acryloyl chloride (17 mg, 0.19 mmol) in dry DCM (2 mL) was dropwisely added and the mixture was stirred until completion monitored by TLC. The reaction was quenched by addition of H_2O (10 mL) and layers were separated. The aqueous layer was extracted with DCM (3 x 10 mL), combined organic layers were dried over Na_2SO_4 and subsequently concentrated at 25 °C, yielding title compound (69 mg, 0.19 mmol, quant.). ^1H NMR (400 MHz, MeOD): δ 8.32 (d, $J = 1.2$ Hz, 1H), 7.94 (d, $J = 13.2$ Hz, 1H), 7.64 (d, 1H), 7.45 (dd, $J = 8.6$, 1.7 Hz, 1H), 7.28 – 7.21 (m, 2H), 7.20 – 7.10 (m, 3H), 6.48 (qd, $J = 16.9$, 5.9 Hz, 4H), 5.83 (dd, $J = 9.4$, 2.3 Hz, 1H), 4.89 (t, $J = 6.8$ Hz, 1H), 2.60 (t, $J = 7.6$ Hz, 1H), 2.05 – 1.92 (m, 1H), 1.69 – 1.60 (m, $J = 14.8$, 7.5 Hz, 2H), 1.59 – 1.50 (m, 2H), 1.40 (ddd, $J = 20.9$, 10.3, 6.2 Hz, 2H).

Synthesis of N-(2-(6-phenylhexanoyl)benzo[d]oxazol-6-yl)acrylamide (3)

Compound **11a** (81 mg, 0.24 mmol) was dissolved in DCM (8 mL), followed by addition of Dess-Martin periodinane (164 mg, 0.39 mmol). The mixture was stirred for 16 h at rt, after which sat. NaHCO_3 (5 mL) and 1 M $\text{Na}_2\text{S}_2\text{O}_3$ (5 mL) were added, followed by stirring for 1 h. The aqueous layer was extracted with DCM (3 x 10 mL) and the combined organic layers were washed with sat. NaHCO_3 and brine (both 30 mL). The organic layers were dried over Na_2SO_4 and concentrated at 25 °C. The crude residue was purified by flash column chromatography (10% \rightarrow 50% EtOAc in pentane), yielding title compound (69 mg, 0.19 mmol, 79%). HRMS (ESI+) m/z calculated for $\text{C}_{22}\text{H}_{22}\text{N}_2\text{O}_3$ ($[\text{M}+\text{H}]^+$): 363.17032, found: 363.17039. ^1H NMR (400 MHz, CDCl_3): δ 8.33 (s, 1H), 7.92 (s, 1H), 7.79 (d, $J = 8.7$ Hz, 1H), 7.48 (dd, $J = 8.7$, 1.9 Hz, 1H), 7.33 – 7.22 (m, 3H), 7.21 – 7.07 (m, 3H), 6.50 (dd, $J = 16.8$, 1.1 Hz, 1H), 6.34 (dd, $J = 16.8$, 10.2 Hz, 1H), 5.83 (dd, $J = 10.2$, 1.1 Hz, 1H), 3.20 (t, $J = 7.4$ Hz, 2H), 2.63 (t, 2H), 1.92 – 1.76 (m, $J = 15.2$, 7.5 Hz, 2H), 1.76 – 1.64 (m, $J = 15.5$, 7.6 Hz, 2H), 1.52 – 1.43 (m, 2H). ^{13}C NMR (101 MHz, CDCl_3): δ 190.12, 163.84, 157.63, 151.44, 142.57, 138.67, 137.05, 130.85, 128.96, 128.54, 128.41, 125.82, 122.38, 118.58, 103.32, 39.51, 35.85, 31.32, 28.86, 23.86.

Synthesis of 1-(5-nitrobenzo[d]oxazol-2-yl)-6-phenylhexan-1-ol (9b)

The title compound was synthesized from *2-hydroxy-7-phenylheptanenitrile* (**8**, 200 mg, 0.98 mmol) according to the procedure described for compound **9a**. The crude residue was purified by flash column chromatography (0% \rightarrow 40% EtOAc in pentane), yielding title compound (214 mg, 0.63 mmol, 64%). $^1\text{H NMR}$ (400 MHz, CDCl_3): δ 8.54 (d, J = 2.2 Hz, 1H), 8.26 (dd, J = 9.0, 2.3 Hz, 1H), 7.60 (d, J = 9.0 Hz, 1H), 7.29 – 7.18 (m, 2H), 7.18 – 7.09 (m, 3H), 5.03 (t, J = 7.6, 5.4 Hz, 1H), 2.58 (t, 2H), 2.10 – 1.94 (m, 2H), 1.67 – 1.58 (m, J = 15.3, 7.5 Hz, 2H), 1.58 – 1.45 (m, 2H), 1.45 – 1.33 (m, 2H). $^{13}\text{C NMR}$ (101 MHz, CDCl_3): δ 171.29, 154.16, 145.26, 142.43, 140.88, 128.34, 128.25, 125.66, 121.32, 116.29, 111.13, 67.89, 35.78, 35.31, 31.25, 28.88, 24.92.

Synthesis of 1-(5-aminobenzo[d]oxazol-2-yl)-6-phenylhexan-1-ol (10b)

The title compound was synthesized from *1-(5-nitrobenzo[d]oxazol-2-yl)-6-phenylhexan-1-ol* (**9b**, 214 mg, 0.63 mmol) according to the procedure described for compound **10a**, yielding title compound (195 mg, 0.63 mmol, quant.). $^1\text{H NMR}$ (400 MHz, CDCl_3): δ 7.30 – 7.18 (m, 3H), 7.18 – 7.07 (m, 3H), 6.90 (d, J = 2.2 Hz, 1H), 6.62 (dd, J = 8.6, 2.3 Hz, 1H), 4.86 (t, J = 7.4, 5.6 Hz, 1H), 3.83 (s, 1H), 2.56 (t, 2H), 2.20 – 1.70 (m, 2H), 1.64 – 1.53 (m, J = 15.8, 7.9 Hz, 2H), 1.52 – 1.40 (m, J = 15.4, 9.2, 3.8 Hz, 2H), 1.40 – 1.30 (m, 2H). $^{13}\text{C NMR}$ (101 MHz, CDCl_3): δ 168.54, 144.71, 143.74, 142.70, 141.40, 128.46, 128.32, 125.69, 113.79, 110.89, 105.15, 67.98, 35.87, 35.47, 31.34, 29.01, 24.97.

Synthesis of N-(2-(1-hydroxy-6-phenylhexyl)benzo[d]oxazol-5-yl)acrylamide (11b)

The title compound was synthesized from *1-(5-aminobenzo[d]oxazol-2-yl)-6-phenylhexan-1-ol* (**10b**, 43 mg, 0.14 mmol) according to the procedure described for compound **11a**, yielding title compound (50 mg, 0.14 mmol, quant.). $^1\text{H NMR}$ (400 MHz, CDCl_3): δ 8.24 (s, 1H), 7.77 (s, 1H), 7.59 (d, J = 8.1 Hz, 1H), 7.35 (d, J = 8.8 Hz, 1H), 7.30 – 7.20 (m, 2H), 7.20 – 7.09 (m, 3H), 6.43 (dd, J = 16.9, 1.0 Hz, 1H), 6.27 (dd, J = 16.9, 10.2 Hz, 1H), 5.72 (dd, J = 10.2, 1.2 Hz, 1H), 4.91 (dd, J = 7.4, 5.5 Hz, 1H), 3.31 (s, 1H), 2.07 – 1.85 (m, 1H), 1.66 – 1.55 (m, 2H), 1.52 – 1.43 (m, 2H), 1.41 – 1.33 (m, J = 16.7, 10.2, 3.2 Hz, 2H). $^{13}\text{C NMR}$ (101 MHz, CDCl_3): δ 169.04, 164.09, 147.72, 142.67, 140.50, 134.86, 128.19, 77.48, 77.16, 76.84, 35.91, 35.48, 31.37, 29.02, 24.98.

Synthesis of N-(2-(6-phenylhexanoyl)benzo[d]oxazol-5-yl)acrylamide (2)

The title compound was synthesized from *N-(2-(1-hydroxy-6-phenylhexyl)benzo[d]oxazol-5-yl)acrylamide* (**11b**, 32 mg, 0.09 mmol) according to the procedure described for compound **3**. The crude residue was purified by flash column chromatography (0% \rightarrow 100% EtOAc in pentane), yielding title compound (24 mg, 0.07 mmol, 75%). HRMS (ESI+) m/z : calculated for $\text{C}_{22}\text{H}_{22}\text{N}_2\text{O}_3$ ($[\text{M}+\text{H}]^+$): 363.17032, found: 363.17039. $^1\text{H NMR}$ (400 MHz, $\text{CDCl}_3/\text{MeOD}$): δ 8.37 (d, J = 1.8 Hz, 1H), 7.76 (dd, J = 8.9, 2.1 Hz, 1H), 7.63 (d, J = 8.9 Hz, 1H), 7.51 (s, 1H), 7.26 (dd, J = 10.1, 4.6 Hz, 2H), 7.21 – 7.10 (m, 3H), 6.45 (s, 1H), 6.43 (d, J = 1.8 Hz, 1H), 5.80 (dd, J = 6.7, 5.0 Hz, 1H), 3.22 (t, J = 7.4 Hz, 2H), 2.65 (t, J = 7.7 Hz, 2H), 1.94 – 1.77 (m, 2H), 1.71 (dt, J = 15.4, 7.6 Hz, 2H), 1.58 – 1.42 (m, 2H).

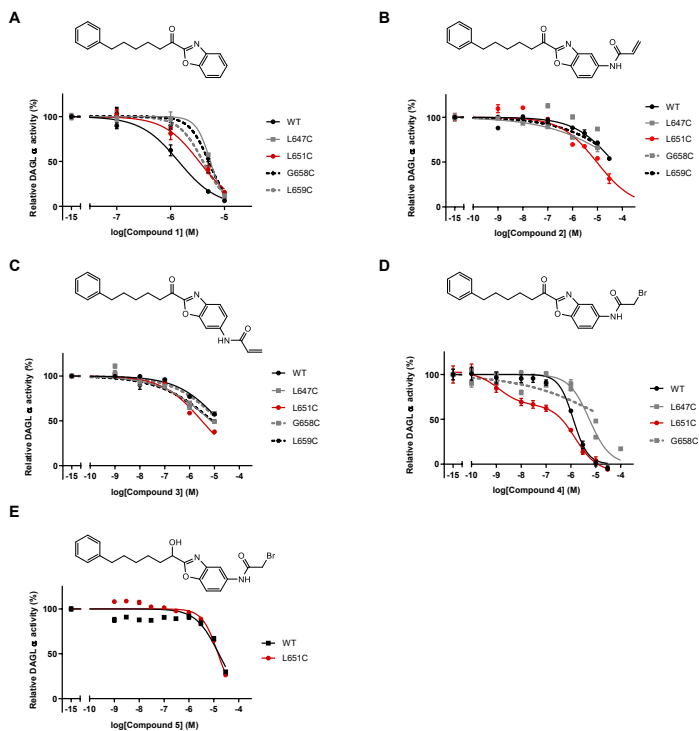
Synthesis of 2-bromo-N-(2-(1-hydroxy-6-phenylhexyl)benzo[d]oxazol-5-yl)acetamide (5)

Compound **10b** (50 mg, 0.16 mmol) was dissolved in dry DCM (5 mL) and cooled to 0 °C, followed by addition of DIPEA (28 μL , 0.16 mmol). Next, bromoacetyl bromide (32.5 mg, 0.16 mmol) in dry DCM (1 mL) was dropwisely added and the mixture was stirred until completion monitored by TLC. The reaction was quenched by addition of H_2O (10 mL) and layers were separated. The aqueous layer was extracted with DCM (3 x 10 mL), combined organic layers were dried over Na_2SO_4 and subsequently concentrated at 25 °C, yielding title compound (53 mg, 0.12 mmol, 76%). $^1\text{H NMR}$ (400 MHz, CDCl_3): δ 8.53 (s, 1H), 7.85 (s, 1H), 7.46 – 7.37 (m, 2H), 7.31 – 7.20 (m, J = 9.8, 6.9 Hz, 2H), 7.20 – 7.10 (m, 3H), 4.93 (dd, J = 7.4, 5.4 Hz, 1H), 4.02 (s, 2H), 2.58 (t, J = 14.3, 6.8 Hz, 2H), 2.12 – 1.88 (m, 2H), 1.74 – 1.54 (m, J = 11.3, 5.6 Hz, 2H), 1.54 – 1.43 (m, 2H), 1.44 – 1.32 (m, 2H). $^{13}\text{C NMR}$ (101 MHz, CDCl_3): δ 169.22, 164.27, 148.09, 142.63, 140.75, 133.95, 128.47, 128.34, 125.73, 118.74, 112.31, 110.96, 68.08, 35.89, 35.48, 31.34, 29.58, 28.99, 24.93.

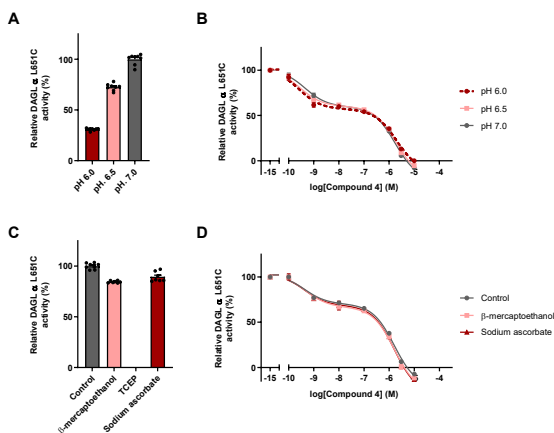
Synthesis of 2-bromo-N-(2-(6-phenylhexanoyl)benzo[d]oxazol-5-yl)acetamide (4)

The title compound was synthesized from 2-bromo-N-(2-(1-hydroxy-6-phenylhexyl)benzo[d]oxazol-5-yl)acetamide (**5**, 30 mg, 0.07 mmol) according to the procedure described for compound **3**. The crude residue was purified by flash column chromatography (0% → 50% EtOAc in pentane), yielding title compound (22 mg, 0.05 mmol, 88%). HRMS (ESI+) *m/z*: calculated for C₂₁H₂₁BrN₂O₃ ([M+H]): 429.08083, found: 429.08082. ¹H NMR (400 MHz, CD₃CN): δ 8.98 (s, 1H), 8.25 (d, *J* = 1.9 Hz, 1H), 7.68 (dt, *J* = 8.9, 5.5 Hz, 2H), 7.35 – 7.13 (m, 5H), 4.03 (s, 2H), 3.20 (t, *J* = 7.3 Hz, 2H), 2.70 – 2.61 (m, 2H), 1.87 – 1.74 (m, 2H), 1.69 (dt, *J* = 15.5, 7.6 Hz, 2H), 1.54 – 1.39 (m, 2H). ¹³C NMR (101 MHz, CD₃CN): δ 190.06, 165.07, 158.33, 147.36, 142.78, 140.80, 136.21, 128.38, 128.25, 125.61, 121.34, 112.49, 111.94, 39.03, 35.25, 31.14, 29.56, 28.34, 23.18.

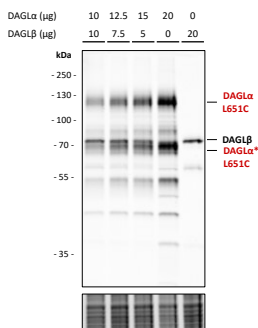
Supplementary Data



Supplementary Figure 5.1 – Dose-response curves of synthesized compounds on DAGL α ^{WT} and mutants. All data were obtained using the PNPB hydrolysis assay (N = 2, n = 4 for vehicle, N = 2, n = 2 for inhibitor-treated). Corresponding pIC₅₀-values can be found in Table 5.1. Data represent means \pm SEM.



Supplementary Figure 5.2 – Biphasic binding behavior of compound 4 on DAGL α ^{L651C} is not pH-dependent nor affected by reducing agents. (A) Relative DAGL α ^{L651C} activity in buffer of different pH-values. (B) Dose-response curve of **4** at different pH-values. (C) Relative DAGL α ^{L651C} activity upon treatment with various reducing agents (20 mM, 30 min, 37 °C). (D) Dose-response curve of compound **4** after pre-incubation with reducing agents as in panel B. All data was obtained using PNPB hydrolysis assay (N = 2, n = 4 for vehicle, N = 2, n = 2 for inhibitor-treated) and represent means \pm SEM.



Supplementary Figure 5.3 – Optimization of ABPP on DAGL α /DAGL β mixtures. Membranes overexpressing DAGL α or DAGL β (2 mg/mL) were mixed in various ratios and incubated with DH379 (1 μ M, 15 min, rt). DAGL α band marked with asterisk corresponds to a previously reported degradation product.¹⁹

References

1. Mechoulam, R. & Parker, L. a. The Endocannabinoid System and the Brain. *Annu. Rev. Psychol.* **64**, 21-47 (2011).
2. Lutz, B. Endocannabinoid signals in the control of emotion. *Current Opinion in Pharmacology* **9**, 46-52 (2009).
3. Silvestri, C. & Di Marzo, V. The endocannabinoid system in energy homeostasis and the etiopathology of metabolic disorders. *Cell Metabolism* **17**, 475-490 (2013).
4. Alger, B. E. & Kim, J. Supply and demand for endocannabinoids. *Trends in Neurosciences* **34**, 304-315 (2011).
5. Min, R., Di Marzo, V. & Mansvelde, H. D. DAG lipase involvement in depolarization-induced suppression of inhibition: Does endocannabinoid biosynthesis always meet the demand? *Neuroscientist* **16**, 608-613 (2010).
6. Bisogno, T. *et al.* Cloning of the first sn1-DAG lipases points to the spatial and temporal regulation of endocannabinoid signaling in the brain. *J. Cell Biol.* **163**, 463-468 (2003).
7. Reisenberg, M., Singh, P. K., Williams, G. & Doherty, P. The diacylglycerol lipases: Structure, regulation and roles in and beyond endocannabinoid signalling. *Philosophical Transactions of the Royal Society B: Biological Sciences* **367**, 3264-3275 (2012).
8. Shonesy, B. C. *et al.* CaMKII regulates diacylglycerol lipase- α and striatal endocannabinoid signaling. *Nat. Neurosci.* **16**, 456-463 (2013).
9. Jung, K.-M. *et al.* A Key Role for Diacylglycerol Lipase- in Metabotropic Glutamate Receptor-Dependent Endocannabinoid Mobilization. *Mol. Pharmacol.* **72**, 612-621 (2007).
10. Murataeva, N., Straiker, A. & MacKie, K. Parsing the players: 2-arachidonoylglycerol synthesis and degradation in the CNS. *British Journal of Pharmacology* **171**, 1379-1391 (2014).
11. Gao, Y. *et al.* Loss of retrograde endocannabinoid signaling and reduced adult neurogenesis in diacylglycerol lipase knock-out mice. *J. Neurosci.* **30**, 2017-2024 (2010).
12. Viader, A. *et al.* A chemical proteomic atlas of brain serine hydrolases identifies cell type-specific pathways regulating neuroinflammation. *Elife* **5**, (2016).
13. Oudin, M. J., Hobbs, C. & Doherty, P. DAGL-dependent endocannabinoid signalling: Roles in axonal pathfinding, synaptic plasticity and adult neurogenesis. *European Journal of Neuroscience* **34**, 1634-1646 (2011).
14. Baggelaar, M. P. *et al.* Highly Selective, Reversible Inhibitor Identified by Comparative Chemoproteomics Modulates Diacylglycerol Lipase Activity in Neurons. *J. Am. Chem. Soc.* **137**, 8851-8857 (2015).
15. Ogasawara, D. *et al.* Rapid and profound rewiring of brain lipid signaling networks by acute diacylglycerol lipase inhibition. *Proc. Natl. Acad. Sci.* **113**, 26-33 (2016).
16. Di Marzo, V. Targeting the endocannabinoid system: to enhance or reduce? *Nat. Rev. Drug Discov.* **7**, 438-455 (2008).
17. Janssen, F. J. & van der Stelt, M. Inhibitors of diacylglycerol lipases in neurodegenerative and metabolic disorders. *Bioorganic Med. Chem. Lett.* **26**, 3831-3837 (2016).
18. Di Marzo, V. New approaches and challenges to targeting the endocannabinoid system. *Nature Reviews Drug Discovery* **17**, 623-639 (2018).
19. Baggelaar, M. P. *et al.* Development of an activity-based probe and in silico design reveal highly selective inhibitors for diacylglycerol lipase- α in brain. *Angew. Chemie - Int. Ed.* **52**, 12081-12085 (2013).
20. Pedicord, D. L. *et al.* Molecular characterization and identification of surrogate substrates for diacylglycerol lipase α . *Biochem. Biophys. Res. Commun.* **411**, 809-814 (2011).
21. van der Wel, T. *et al.* A natural substrate-based fluorescence assay for inhibitor screening on diacylglycerol lipase α . *J. Lipid Res.* **56**, 927-935 (2015).
22. Janssen, F. J. *et al.* Comprehensive Analysis of Structure-Activity Relationships of α -Ketoheterocycles as sn-1-Diacylglycerol Lipase α Inhibitors. *J. Med. Chem.* **58**, 9742-9753 (2015).
23. Janssen, F. J. *et al.* Discovery of glycine sulfonamides as dual inhibitors of sn-1-diacylglycerol lipase α and α/β -hydrolase domain 6. *J. Med. Chem.* **57**, 6610-6622 (2014).
24. Deng, H. *et al.* Triazole Ureas Act as Diacylglycerol Lipase Inhibitors and Prevent Fasting-Induced Refeeding. *J. Med. Chem.* **60**, 428-440 (2017).
25. Ran, F. A. *et al.* Genome engineering using the CRISPR-Cas9 system. *Nat. Protoc.* **8**, 2281-2308 (2013).
26. Cho, S. W. and Chang, H. Y. CRISPR engineering turns on genes. *Nature* **517**, 560-562 (2015).
27. Yang, H., Wu, J. J., Tang, T., Liu, K. De & Dai, C. CRISPR/Cas9-mediated genome editing efficiently creates specific mutations at multiple loci using one sgRNA in *Brassica napus*. *Sci. Rep.* **7**, (2017).
28. Alvarez-Castelao, B. *et al.* Cell-type-specific metabolic labeling of nascent proteomes in vivo. *Nat. Biotechnol.* **35**, 1196-1201 (2017).
29. Poole, L. B. The basics of thiols and cysteines in redox biology and chemistry. *Free Radical Biology and Medicine* **80**, 148-157 (2015).

6

A natural substrate activity assay
for high-throughput screening
on monoacylglycerol lipase

Introduction

Lipid metabolism is a tightly regulated cellular process involving enzymes responsible for spatiotemporal lipid biosynthesis and degradation. Homeostasis of lipids is often dysregulated in disease, for example in (auto-)immune disorders and cancer.¹⁻³ Monoacylglycerol lipase (MAGL) is a membrane-associated serine hydrolase responsible for breakdown of monoacylglycerols into free fatty acids (FFAs) and glycerol. The enzyme employs a serine-histidine-aspartate catalytic triad to cleave the ester bond of monoacylglycerols, whereas it is unable to hydrolyze di- or triacylglycerols.^{4,5} Structurally, MAGL possesses a typical α/β hydrolase fold, composed of a central β -sheet flanked on both sides by eight α -helices.⁶ Access to the active site is probably regulated by a hydrophobic lid domain that allows the enzyme to adopt either an open or closed conformational state.⁷ The open conformation presumably allows association to the membrane and recruitment of its substrate, after which the lid domain closes and MAGL dissociates.⁸

MAGL was initially discovered as the main enzyme responsible for degradation of the endocannabinoid 2-arachidonoylglycerol (2-AG) in the brain (Figure 6.1).⁹ The signaling lipid 2-AG is an endogenous ligand of the cannabinoid (CB) 1 and 2 receptors, which are involved in various physiological processes, such as appetite, pain, emotion and energy homeostasis.¹⁰ Hydrolysis of 2-AG by MAGL terminates CB receptor activation and

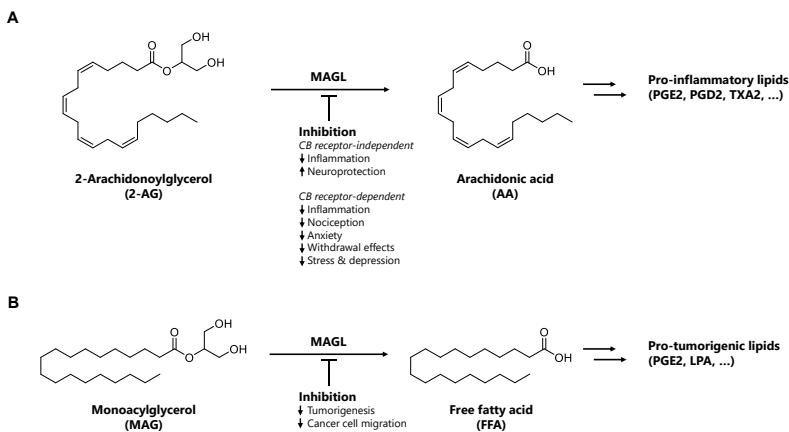


Figure 6.1 – Monoacylglycerol lipase is a central player in biosynthesis of free fatty acids from monoacylglycerols.

(A) MAGL is the main enzyme responsible for degradation of 2-arachidonoylglycerol (2-AG) into arachidonic acid (AA) in the brain. Inhibition of MAGL results in neuroprotection and reduced inflammation due to lowered cellular pools of AA, which is a precursor for pro-inflammatory lipids such as prostaglandins E2/D2 (PGE2/PGD2) and thromboxane A2 (TXA2). In addition, MAGL inhibition prolongs 2-AG-mediated CB receptor signaling, resulting in various CB receptor-dependent physiological effects. **(B)** Free fatty acids (FFAs) produced by hydrolysis of monoacylglycerols (MAGs) by MAGL are precursors for pro-tumorigenic lipids such as PGE2 and lysophosphatidic acid (LPA). Inhibition of MAGL results in lower cellular FFA pools and reduces tumorigenesis and cancer cell migration.

liberates free arachidonic acid (AA). In turn, AA is a precursor of pro-inflammatory eicosanoids such as prostaglandins.^{3,11}

More recently, MAGL was found to also be highly expressed in various aggressive human cancer cells and primary tumors in comparison with nonaggressive counterparts.¹² MAGL probably contributes to the cancer pathogenesis via multiple mechanisms by directly increasing *de novo* synthesis of FFAs, making tumor cells less dependent on lipid uptake from the extracellular environment.^{2,13} FFAs are required for the biosynthesis of cell membranes and pro-tumorigenic signaling molecules, such as lysophosphatidic acid (LPA) and prostaglandin E2 (PGE2).^{12,14} In addition, FFAs can be used as a direct energy source, for example by beta-oxidation in the mitochondrial matrix to generate ATP.¹⁵

The central role of MAGL in lipid metabolism makes it a potential therapeutic target for a variety of disorders. Recently, the irreversible MAGL inhibitor ABX-1431, developed by Abide Therapeutics, has shown promising data in Phase 1 clinical studies in patients with Tourette syndrome.^{16,17} In addition, pharmacological inhibition of MAGL showed beneficial effects in various inflammation-related disease models, such as amyotrophic lateral sclerosis (ALS)¹⁸, multiple sclerosis (MS)¹⁹ and Parkinson's and Alzheimer's disease.²⁰ MAGL inactivation also exerts CB1R-dependent anti-nociceptive effects²¹, reduces anxiety²², attenuates withdrawal symptoms in drug addiction²³ and ameliorates stress and depression in mouse models.²⁴ Finally, inhibition of MAGL reduced cancer cell migration, invasion and survival²⁵, and slowed tumor growth.^{12,26}

Most reported MAGL inhibitors have an irreversible mode of action, forming a covalent complex after nucleophilic attack by the catalytic serine. As therapeutics, irreversible inhibitors can have several benefits, such as increased potency and a long residence time that can drive pharmacological efficacy. Furthermore, irreversible binders may have an advantageous pharmacodynamics profile, since no excessive circulating levels of inhibitor are required to maintain target engagement.²⁷ On the other hand, the irreversible mode of action may also have several drawbacks. Idiosyncratic drug-related toxicity remains a point of concern, either by formation of reactive drug metabolites with poorly predictable effects or by haptization of covalent inhibitor-enzyme adducts that may trigger an immune response.^{28,29} In case of MAGL inhibition specifically, chronic exposure to irreversible inhibitor JZL184 resulted in pharmacological tolerance, development of physical dependence, impaired synaptic plasticity and receptor desensitization in the nervous system.^{30,31}

The question thus rises whether inhibition of MAGL by reversible binders may avoid these undesirable side-effects. However, most described MAGL inhibitors have an irreversible mode of action and compounds that target MAGL in a reversible manner are currently underrepresented.^{19,32} In addition, most compounds lack potency, selectivity or

the right physicochemical properties for use in *in vivo* studies. Therefore, it is of great relevance to identify novel chemotypes to reversibly inhibit MAGL.

Here, the optimization and miniaturization of a biochemical activity assay for MAGL is described, which was subsequently applied in a high-throughput screen on 233,820 unique compounds within the Cancer Drug Discovery Initiative (CDDI). Hit validation was performed using an orthogonal gel-based activity-based protein profiling assay, ultimately resulting in qualified hits that constitute starting points for the development of novel, reversible MAGL inhibitors.

Results

Assay setup and optimization

Although widely used in high-throughput screening assays for their ease of detection, surrogate substrates generally have an attenuated binding affinity for the enzyme active site compared to physiologically relevant natural substrates. This may lead to distorted results when determining inhibitor potency. For this reason, a MAGL activity assay was set up and optimized employing its natural substrate 2-AG.³³ Glycerol production from 2-AG by MAGL is coupled to the generation of a fluorescent signal using an enzymatic cascade reaction (Figure 6.2A).⁵ The continuous assay setup and fluorescence readout in multi-well plates ensures HTS compatibility.

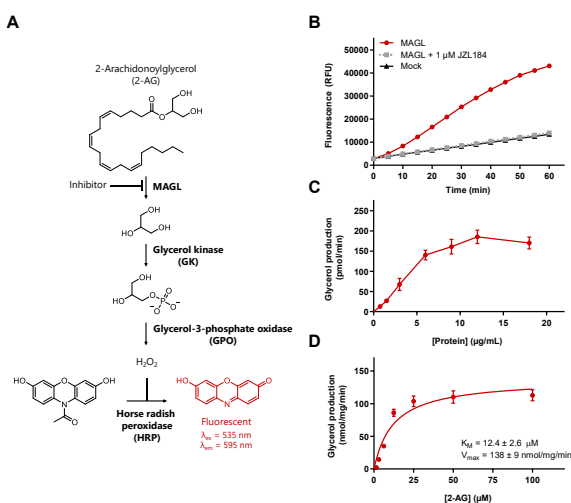


Figure 6.2 – MAGL activity assay setup and optimization in 96-well plate format. (A) Hydrolysis of 2-AG by MAGL is linked to the production of a fluorescent signal via an enzymatic cascade reaction. Liberated glycerol is phosphorylated by glycerol kinase (GK), followed by oxidation to dihydroxyacetone phosphate and hydrogen peroxide using glycerol-3-phosphate oxidase (GPO). The produced hydrogen peroxide is used by horse radish peroxidase (HRP) to oxidize Ampliflu™Red to fluorescent resorufin. (B) Time course of 2-AG hydrolysis by MAGL, as measured by resorufin fluorescence. (C, D) Glycerol production by MAGL as function of protein (C) or substrate (D) concentration. Data shown are means \pm SEM (N = 2, n = 2).

First, full-length human MAGL was transiently overexpressed in HEK293T cells, after which membrane fractions were isolated. Cells transfected with empty vector (mock) served as a control for background fluorescence from 2-AG hydrolysis by endogenous hydrolases in these cells. Membranes were incubated with assay mix containing 2-AG and components required for the enzymatic cascade reaction. Assays were initially performed in 96-well plates in a total volume of 200 μ L. A time-dependent increase in fluorescence was observed, which was reduced to mock-levels upon pre-incubation with MAGL inhibitor JZL184 (Figure 6.2B). The measured glycerol production rates were dependent on the used protein concentration, with a linear range up to 10 μ g/mL (Figure 6.2C). In a similar fashion, reaction rates were measured at various concentrations of 2-AG (Figure 6.2D), resulting in a V_{max} of 138 ± 9 nmol/mg/min and an apparent K_M of 12 ± 3 μ M, which is in line with a previous report using the same assay setup.³⁴

Next, the assay was miniaturized to 384-well format in a reaction volume of 30 μ L. Using a two-fold increase in protein concentration (from 1.5 to 3 ng/ μ L in 96- to 384-well format, respectively), similar reaction progression curves were observed as in 96-well format (Figure 6.3A). Under these assay conditions, MAGL activity is dose-dependently inhibited by MAGL inhibitor JZL184 with a pIC_{50} of 7.6 ± 0.05 (Figure 6.3B), which is in the same nanomolar range as previously reported.³⁵ Assay conditions were sufficiently robust for further miniaturization, as reflected by decent Z' -factors (> 0.6) and S/B ratios (> 5). Intra-assay variability was assessed by measuring the reaction rates of 64 individual positive and negative control samples in a single plate, resulting in a coefficient of variation of 6.6% and 7.5% respectively.

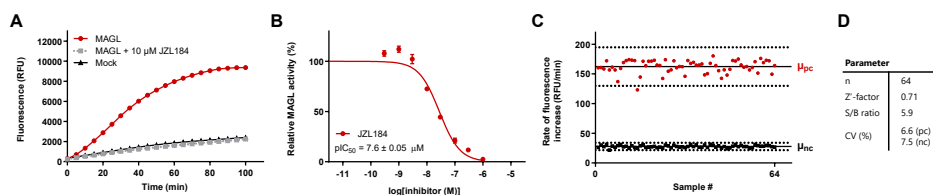


Figure 6.3 – Miniaturization of MAGL activity assay to 384-well plate format. (A) Time course of 2-AG hydrolysis by MAGL, as measured by resorufin fluorescence. (B) Dose-response curve of MAGL inhibitor JZL184. (C) Intra-assay variability plot. Solid lines represent the mean of individual data points (μ_{pc}/μ_{nc}); dashed lines represent $\mu \pm 3\sigma$. (D) Assay performance parameters. S/B: signal to background; CV: coefficient of variation. Data shown are means \pm SEM (n = 64 for A-C; N = 2, n = 2 for B).

Within the Cancer Drug Discovery Initiative, the assay was then further miniaturized to 1536-well format. The assay reaction volume was further reduced to 4 μ L and protein concentrations were increased to 9 ng/ μ L to improve the S/B ratio. In addition, the assay buffer was supplemented with 0.03% (w/w) Tween-20 to improve assay performance. End point instead of kinetic measurements were performed to simplify the data analysis process. Validation runs demonstrated that the assay was sufficiently reproducible and robust for use in a HTS campaign.

High-throughput screening

In total, 233,820 compounds were screened in the optimized 1536-well assay, divided over two days. Assays were performed at a single dose of 10 μM inhibitor with 30 min pre-incubation. Screening quality was assessed by calculating the Z'-factor (Figure 6.4A) and S/B ratio (Figure 6.4B) for each of the 188 individual plates. Plates measured on day 2 showed better overall performance than those measured on day 1, but all plates met the requirement of Z'-factor >0.6 . All screened compounds were categorized by percentage MAGL inhibition (Figure 6.4C) and the 1,555 compounds showing $\geq 50\%$ inhibition at 10 μM were designated as primary assay hits, corresponding to a hit rate of 0.67% (Table 6.1). Using a nearest neighbor clustering model, potential false negatives were added to the hit list, resulting in a number of 4,389 compounds. Active confirmation was then performed on these compounds using the exact same assay conditions, resulting in a list of confirmed actives of 1,142 compounds. Subsequently, a deselection assay was performed using glycerol instead of 2-AG as the substrate. This deselection assay aims to exclude false positives, for example compounds that interfere with the assay setup. This is particularly relevant in case of an enzymatic cascade assay, since inhibition of either of the enzymes downstream of MAGL will result in a reduced fluorescent signal. After deselection, the remaining 334 compounds were further reduced to 146 compounds by applying a more stringent criterion of $>60\%$ inhibition at 10 μM in the primary assay. Subsequently, structures were examined and compounds with an apparent irreversible mode of action were excluded at this stage, as well as those with poor physicochemical properties or protection by intellectual property. This triage process resulted in a qualified hit list of 50 compounds of which chemical structures were disclosed.

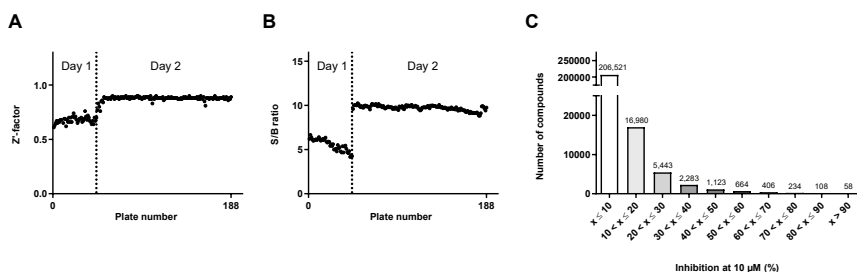


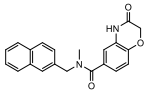
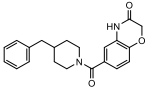
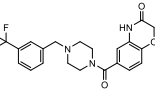
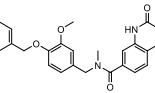
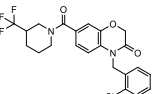
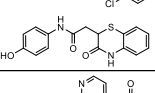
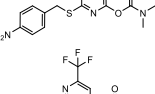
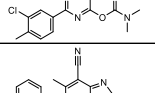
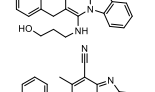
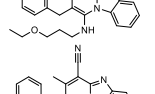
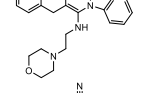
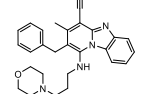
Figure 6.4 – High throughput screen overview of assay quality and hits. (A, B) Screen quality assessed by Z'-factor (A) and S/B ratio (B) for each individual 1536-well plate. Plates 1-46 were measured on day 1, plates 47-188 on day 2. (C) Overview of screened compounds categorized by percentage MAGL inhibition at 10 μM .

Table 6.1 – High-throughput screen triage process. Criteria and cut-offs used at each step are indicated. DRC: dose-response curve, ABPP: activity-based protein profiling.

	Remaining compounds	Criterion	% of total
Complete screen	233,820	-	100%
Primary assay hits	1,555	≥ 50% inhibition at 10 μM	0.67%
Nearest neighbors	4,389	Clustering algorithm; < 50% inhibition at 10 μM	1.88%
Active confirmation	1,142	≥ 50% inhibition at 10 μM in confirmation assay	0.49%
Deselection	334	< 10% inhibition on glycerol conversion at 10 μM	0.14%
Stringency	146	> 60% inhibition at 10 μM	0.06%
Triage	111	Chemical eye, mode of action, intellectual property	0.05%
DRC	50	IC ₅₀ , no time dependence	0.02%
Orthogonal assay	7	> 25% inhibition at 10 μM in ABPP assay	0.003%

Within the qualified hit list, 9 clusters of different chemotypes could be distinguished (Table 6.2), many of which contained piperidine or piperazine structural motifs. Of note, the clusters of benzoxazine derivatives **1-6** and piperazine amide **34** were already previously reported as MAGL inhibitors.³⁶ Many identified clusters, such as benzoxazine derivatives **1-6**, imidazopyridines **13-16**, naphthyl amides **20-28**, phenyl thiazoles **29-30** and piperidine amides **31-33**, all possess favorable physicochemical properties (MW <500 g/mol, cLogP <5).³⁷ Other clusters, however, such as the (fused) imidazopyridines **9-12** and **17-19** have higher cLogP values and therefore overall lower LipEs. The tPSA of nearly all compounds is <90 Å², which is the generally accepted upper limit for molecules to cross the blood-brain barrier, except for carbamate **7**, singletons **35** and **40** and sulfonamides **47** and **48**. All qualified hits were measured in dose-response experiments and pIC₅₀ values were determined at various time points. No clear time-dependent inhibition, indicative of an irreversible mode of action, was observed for any of the compounds. The hit pIC₅₀ values ranged from 4.7 to 6.9 (Table 6.2).

Table 6.2 – Qualified hit list. Hits are clustered by chemotype. Purity (> 90%) and mass were confirmed by LC-MS. Deviations from expected mass are shown as Δ MW. pIC_{50} values were determined in end point measurement after 45 min. Percentages inhibition in orthogonal ABPP assay are relative to vehicle-treated controls. Physicochemical properties (cLogP, tPSA, HBD, HBA) were calculated using ChemDraw Professional 16.0. MW: molecular weight; tPSA: topological polar surface area; HBD: number of hydrogen bond donors; HBA: number of hydrogen bond acceptors; LipE: lipophilic efficiency (LipE = pIC_{50} primary assay – cLogP); LE: ligand efficiency (LE = $1.4 \times pIC_{50}/N$ where N = number of non-hydrogen atoms). † A mass discrepancy of 16 Da that may indicate an under-oxidized analog of the intended compound.

Cluster	Entry	Structure	MW (Da)	Confirmed purity	Confirmed mass	Δ MW (Da)	pIC_{50} primary assay	Inhibition ABPP assay (%)	cLogP	tPSA (\AA^2)	HBD	HBA	LipE	LE
Benzoxazine derivative	1		346	Yes	Yes	-	5.5	-3	3.16	58.6	1	3	2.3	0.29
Benzoxazine derivative	2		350	No	Yes	-	6.8	-2	2.92	58.6	1	3	3.8	0.36
Benzoxazine derivative	3		419	Yes	Yes	-	6.5	17	3.13	61.9	1	7	3.3	0.30
Benzoxazine derivative	4		449	Yes	Yes	-	6.1	13	3.86	67.9	1	4	2.2	0.27
Benzoxazine derivative	5		453	Yes	Yes	-	6.0	-6	3.56	49.9	0	6	2.4	0.27
Benzoxazine derivative	6		314	Yes	Yes	-	5.6	2	1.58	78.4	3	3	4.0	0.36
Carbamate	7		334	Yes	Yes	-	5.4	-4	2.12	106.1	0	4	3.3	0.33
Carbamate	8		360	Yes	Yes	-	5.8	2	3.83	54.3	0	6	2.0	0.34
Fused imidazopyridine	9		370	No	Yes	-	6.0	-13	5.16	71.7	2	5	0.9	0.30
Fused imidazopyridine	10		399	Yes	Yes	-	6.2	2	6.30	60.7	1	5	-0.1	0.30
Fused imidazopyridine	11		426	Yes	Yes	-	6.3	-11	5.77	63.9	1	6	0.6	0.28
Fused imidazopyridine	12		440	Yes	Yes	-	6.0	-12	6.04	63.9	1	6	0.0	0.26

A natural substrate activity assay for high-throughput screening on MAGL

Table 6.2 – Qualified hit list (continued).

Cluster	Entry	Structure	MW (Da)	Confirmed purity	Confirmed mass	Δ MW (Da)	IC ₅₀ primary assay	Inhibition ABPP assay (%)	cLogP	tPSA (Å ²)	HBD	HBA	LipE	LE
Imidazopiperidine	13		370	Yes	No†	+371	5.5	10	3.56	56.7	2	4	2.0	0.29
Imidazopiperidine	14		428	Yes	Yes	-	5.7	17	3.88	66.3	1	6	1.8	0.25
Imidazopiperidine	15		377	Yes	Yes	-	5.8	9	4.00	57.1	2	5	1.8	0.29
Imidazopiperidine	16		390	Yes	Yes	-	6.3	6	3.87	66.3	1	5	2.4	0.30
Imidazopyridines	17		243	Yes	Yes	-	5.4	-10	4.72	15.6	0	2	0.7	0.45
Imidazopyridines	18		257	Yes	Yes	-	5.4	4	5.26	15.6	0	2	0.1	0.42
Imidazopyridines	19		263	Yes	Yes	-	5.6	10	4.94	15.6	0	2	0.7	0.46
Naphtyl amide	20		359	No	No	+113	5.7	-9	3.14	61.8	1	3	2.5	0.29
Naphtyl amide	21		346	Yes	No	+28	5.8	51	3.96	32.8	0	3	1.8	0.31
Naphtyl amide	22		336	No	Yes	-	6.2	16	4.97	23.6	0	2	1.3	0.35
Naphtyl amide	23		344	No	No	+45	4.9	-4	4.73	23.6	0	2	0.2	0.26
Naphtyl amide	24		308	No	Yes	-	5.5	-11	3.77	23.6	0	2	1.7	0.35
Naphtyl amide	25		334	Yes	Yes	-	5.3	-7	4.55	23.6	0	2	0.7	0.30
Naphtyl amide	26		365	Yes	Yes	-	5.4	24	4.94	23.6	0	2	0.5	0.29
Naphtyl amide	27		439	Yes	Yes	-	6.2	-17	4.92	32.8	0	3	1.3	0.31
Naphtyl amide	28		356	Yes	Yes	-	5.7	69	3.42	41.9	0	3	2.3	0.30

Chapter 6

Table 6.2 – Qualified hit list (continued).

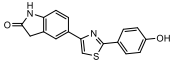
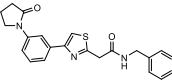
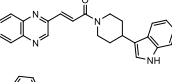
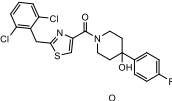
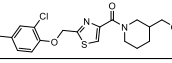
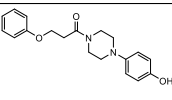
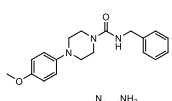
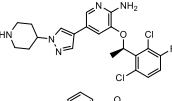
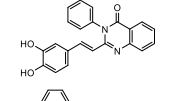
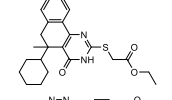
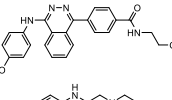
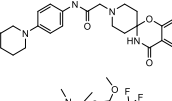
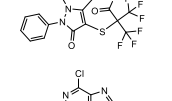
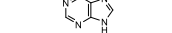
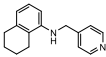
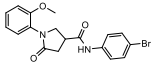
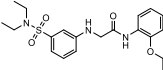
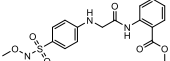
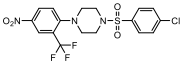
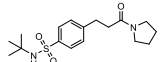
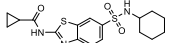
Cluster	Entry	Structure	MW (Da)	Confirmed purity	Confirmed mass	Δ MW (Da)	pIC ₅₀ primary assay	Inhibition ABPP assay (%)	cLogP	tPSA (Å ²)	HBD	HBA	LipE	LE
Phenyl thiazole	29		308	Yes	Yes	-	5.8	1	2.96	61.7	2	3	2.9	0.37
Phenyl thiazole	30		391	Yes	No	+15	5.9	11	3.12	61.8	1	3	2.8	0.30
Piperidine amide	31		382	No	Yes	-	5.6	49	3.43	57.1	1	4	2.2	0.27
Piperidine amide	32		465	Yes	Yes	-	5.6	16	3.93	52.9	1	4	1.7	0.26
Piperidine amide	33		401	Yes	Yes	-	5.8	5	2.13	62.1	1	4	3.7	0.33
Singleton	34		326	No	Yes	-	5.6	-1	2.97	53.0	1	4	2.6	0.33
Singleton	35	To be disclosed	490	Yes	No	-16†	6.2	86	3.09	135.8	0	6	3.1	0.26
Singleton	36		325	Yes	Yes	-	5.5	-6	3.39	44.8	1	3	2.1	0.32
Singleton	37		450	Yes	Yes	-	5.5	18	4.29	75.2	2	7	1.2	0.26
Singleton	38		356	Yes	Yes	-	5.5	12	4.08	73.1	2	4	1.5	0.29
Singleton	39		413	Yes	Yes	-	4.7	-3	5.59	67.8	1	3	-0.9	0.23
Singleton	40		400	No	Yes	-	5.7	2	3.18	106.3	4	6	2.5	0.26
Singleton	41		449	Yes	Yes	-	6.0	6	3.29	73.9	2	5	2.7	0.25
Singleton	42		428	No	Yes	-	5.5	7	2.94	49.9	0	9	2.6	0.28
Singleton	43		155	Yes	No	+205	5.7	0	-1.12	51.2	0	4	6.8	0.80

Table 6.2 – Qualified hit list (continued).

Cluster	Entry	Structure	MW (Da)	Confirmed purity	Confirmed mass	Δ MW (Da)	pIC ₅₀ primary assay	Inhibition ABPP assay (%)	cLogP	TPSA (Å ²)	HBD	HBA	LipE	LE
Singleton	44		238	Yes	Yes	-	6.0	62	3.16	24.4	1	2	2.9	0.47
Singleton	45		389	Yes	Yes	-	5.9	46	4.32	58.6	1	3	1.6	0.34
Sulfonamide	46		406	Yes	Yes	-	5.5	18	3.20	87.7	2	5	2.3	0.27
Sulfonamide	47		407	No	Yes	-	6.1	-7	1.94	114.0	2	6	4.2	0.31
Sulfonamide	48		450	No	No	+22	6.3	13	5.08	92.4	0	7	1.2	0.30
Sulfonamide	49		338	Yes	Yes	-	6.9	32	1.54	66.5	1	3	5.3	0.42
Sulfonamide	50		379	No	No	+328	5.5	0	4.20	87.6	2	4	1.3	0.31

Hit validation by orthogonal ABPP assay

Next, the qualified hits were tested in an orthogonal gel-based competitive activity-based protein profiling (ABPP) assay on mouse brain membrane proteome. The used probe, FP-TAMRA, is a broad-spectrum probe that targets a wide range of serine hydrolases including the endocannabinoid hydrolases MAGL, fatty acid amide hydrolase (FAAH) and alpha/beta hydrolase domain-containing protein 6 (ABHD6). Remarkably, in an initial competitive ABPP assay using standard labeling conditions (500 nM FP-TAMRA, 15 min incubation), no significant inhibition was observed for any of the compounds (data not shown). This is probably due to the irreversible mode of action of probe FP-TAMRA, resulting in rapid outcompetition of reversible inhibitors. This was addressed by reducing probe concentration and incubation time (100 nM FP-TAMRA, 10 min incubation), resulting in 7 compounds showing >25% inhibition at 10 μ M under these conditions (Figure 6.5A, 6.5C, Table 6.2, Supplementary Figure 6.1). Interestingly, some chemotypes (benzoxazine derivatives **1-6** and naphthyl amides **20-28**) showed decent inhibition in the primary assay but were ineffective in the ABPP assay. A correlation between inhibitor potency in the primary substrate-based assay and orthogonal ABPP assay was observed for all compounds except **49**, which was the most potent hit in the primary assay but showed poorest inhibition in the ABPP assay (Figure 6.5B). At this point, compound purity and mass were analyzed by LC-MS, which revealed that 14 of the 50 qualified hits were <90% pure and 9 compounds differed in mass. Of note, the most potent inhibitor identified by ABPP

(compound **35**) showed a mass discrepancy of 16 Da, which might indicate that this may be an under-oxidized analog of the intended compound.

Competitive ABPP is a powerful technique to obtain an initial selectivity profile of the qualified hits. Most tested compounds showed good selectivity profiles on the mouse brain membrane proteome at 10 μM (Figure 6.5A). However, 7 compounds showed >25% inhibition of FAAH, the endocannabinoid hydrolase responsible for degradation of the endocannabinoid anandamide (Figure 6.5D). Direct comparison of MAGL versus FAAH labeling profiles (Figure 6.5E) revealed that compound **35** is the most potent MAGL inhibitor and selective over FAAH at 10 μM , making it an interesting candidate for further hit optimization.

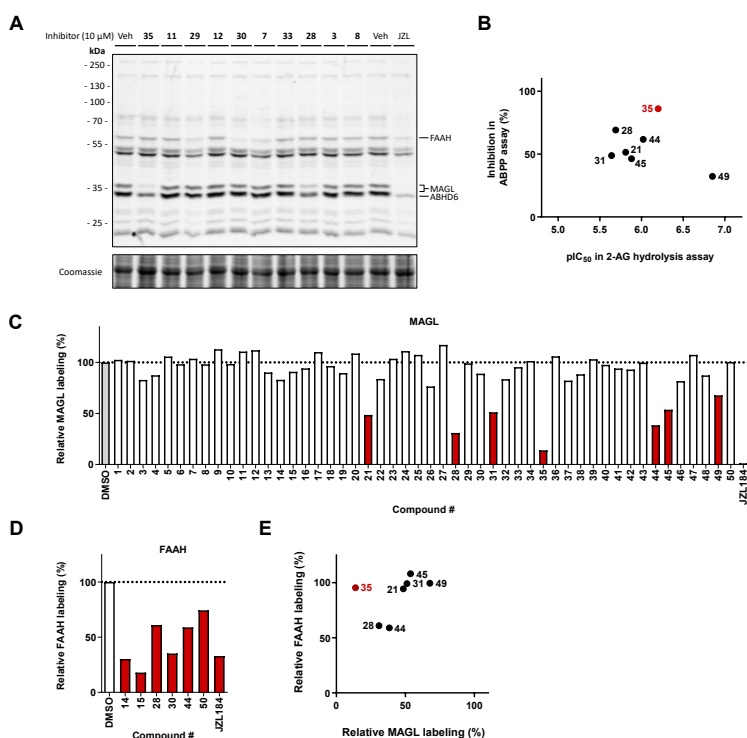


Figure 6.5 – Hit validation and selectivity assessment in orthogonal activity-based protein profiling (ABPP) assay. (A) Competitive ABPP assay on mouse brain membrane proteome using FP-TAMRA. Proteome was pre-incubated with inhibitor (10 μM , 30 min), followed by incubation with FP-TAMRA (100 nM, 10 min). JZL184 was included as positive control. (B) Correlation between primary 2-AG hydrolysis activity assay and orthogonal competitive ABPP assay. (C, D) Quantification of MAGL (C) and FAAH (D) band intensity as described in A, corrected for relative protein loading determined by Coomassie staining (N = 1). (E) Correlation between MAGL and FAAH inhibition determined by competitive ABPP.

Conclusion

A 2-AG hydrolysis assay for MAGL was successfully optimized and miniaturized to 1536-well format. Subsequently, this assay was applied in a high-throughput screen on 233,820 compounds. This resulted in a total of 1,142 confirmed hits, which after deselection and hit triage resulted in a qualified hit list of 50 compounds that were measured in dose-response assays. In total 10 clusters of different chemotypes could be identified, among which two were previously reported as MAGL inhibitors. Many of these clusters have favorable physicochemical properties, such as low MW, cLogP and tPSA. The 50 qualified hits were analyzed in an orthogonal gel-based competitive ABPP assay. Although reversible inhibition was challenging to detect using the irreversibly binding probe FP-TAMRA, 7 compounds showed >25% inhibition of MAGL. Comparison of labeling profiles in the mouse brain proteome revealed the qualified hit selectivity profiles, with FAAH being a prominent off-target of several compounds. Altogether, given its inhibitory potency, favorable selectivity profile and good physicochemical properties, compound **35** may be an especially interesting candidate for further hit optimization efforts.

Acknowledgments

Tsang-Wai Lam and Helma Rutjes are kindly acknowledged for their contributions to the miniaturization and optimization of the assay for the high-throughput screen, Hui Deng for collaboration with hit validation experiments and Constant A.A. van Boeckel for the hit triage process.

Experimental procedures

General

All chemicals, oligonucleotides and other reagents were purchased from Sigma Aldrich, unless stated otherwise. Oligo sequences can be found in Supplementary Table 6.1. Cloning reagents and FP-TAMRA probe were purchased at Thermo Fisher Scientific. Assay enzymes (glycerol kinase from *Cellulomonas sp.*, product code G6142; glycerol-3-phosphate oxidase from *Streptococcus thermophilus*, product code G4388; horse radish peroxidase from *Horseradish*, product code 77332) were purchased from Sigma Aldrich. 2-Arachidonoylglycerol was purchased from Cayman Chemicals. High-throughput screen was performed at Pivot Park Screening Centre (Oss, The Netherlands) and executed within the Cancer Drug Discovery Initiative.

Cloning

Full-length cDNA encoding human MAGL (Source Bioscience) was amplified by PCR and cloned into expression vector pcDNA3.1 in frame with a C-terminal FLAG-tag. All plasmids were isolated from transformed XL10-Gold competent cells (prepared using *E. coli* transformation buffer set; Zymo Research) using plasmid isolation kits following the supplier's protocol (Qiagen). Constructs were verified by Sanger sequencing (Macrogen).

Supplementary Table 6.1 – List of oligonucleotide sequences.

ID	Name	Sequence
P1	MAGL_forw	CTTAAGCTTTGGTACCGCCGCCACCATGGAACAGGACCTGAAG
P2	MAGL_rev	CATTCTAGATCACTCGAGACCGGTGGGTGGGACGCAGTTC

Cell culture

HEK293T (human embryonic kidney) cells were obtained from ATCC and tested on regular basis for mycoplasma contamination. Cultures were discarded after 2-3 months of use. Cells were cultured at 37 °C under 7% CO₂ in DMEM containing phenol red, stable glutamine, 10% (v/v) high iron newborn calf serum (Seradigm), penicillin and streptomycin (200 µg/mL each; Duchefa). Medium was refreshed every 2-3 days and cells were passaged two times a week at 80-90% confluence. One day prior to transfection, HEK293T cells were transferred from confluent 10 cm dishes to 15 cm dishes (16 dishes for HTS). Before transfection, medium was refreshed (13 mL). A 3:1 mixture of polyethylenimine (PEI; 60 µg/dish) and plasmid DNA (20 µg/dish) was prepared in serum-free medium (2 mL) and incubated for 15 min at rt. The mixture was then dropwisely added to the cells, after which the cells were grown to confluence in 72 h. Cells were then harvested by suspension in PBS, followed by centrifugation (200 g, 5 min). Cell pellets were flash-frozen in liquid nitrogen and stored at -80 °C until membrane fraction preparation.

Membrane fraction preparation

Mouse brains were isolated according to guidelines approved by the ethical committee of Leiden University (DEC#13191), frozen in liquid nitrogen and stored at -80 °C until use. Cell pellets or mouse brains were thawed on ice and homogenized by polytron (20,000 rpm, 3 x 7 s; SilentCrusher S, Heidolph) in lysis buffer A (20 mM HEPES pH 7.2, 2 mM DTT, 250 mM sucrose, 1 mM MgCl₂ and 25 U/mL benzonase). Suspensions were incubated on ice for 30 min, followed by low speed centrifugation (2500 g, 3 min, 4 °C) to remove debris. Supernatants were then subjected to ultracentrifugation (93,000 g, 30 min, 4 °C; Beckman Coulter, Ti70 or Ti70.1 rotor). Pellets were homogenized in storage buffer B (20 mM HEPES pH 7.2, 2 mM DTT) by polytron (20,000 rpm, 1 x 10 s). Protein concentrations were determined using Quick Start™ Bradford Protein Assay (Bio-Rad). Membrane preparations were frozen in liquid nitrogen and stored at -80 °C until use.

Biochemical MAGL activity assays and deselection assay

96-well format

Assays were performed in HEMNB buffer (50 mM HEPES pH 7.4, 1 mM EDTA, 5 mM MgCl₂, 100 mM NaCl, 0.5% (w/w) BSA) in black, flat-bottom 96-well plates (Greiner). Inhibitors were added from 40x concentrated stock solution in DMSO. MAGL-overexpressing membrane preparations (0.3 µg per well) were incubated with inhibitor for 20 min at rt in a total volume of 100 µL. Next, 100 µL assay mix containing glycerol kinase (GK), glycerol-3-phosphate oxidase (GPO), horse radish peroxidase (HRP), adenosine triphosphate (ATP), Amplifu™Red and 2-arachidonoylglycerol (2-AG) was added. Fluorescence ($\lambda_{\text{ex}} = 535 \text{ nm}$, $\lambda_{\text{em}} = 595 \text{ nm}$) was measured at rt in 5 min intervals for 60 min on a GENios plate reader (Tecan). Final assay concentrations: 1.5 ng/µL MAGL-overexpressing membranes, 0.2 U/mL GK, GPO and HRP, 125 µM ATP, 10 µM Amplifu™Red, 25 µM 2-AG, 5% DMSO, 0.5% ACN in a total volume of 200 µL. All measurements were performed in N = 2 (individual plates), n = 2 (technical replicates on same plate) or N = 2, n = 4 for controls, with Z' \geq 0.6. For K_M and IC₅₀ determinations, the assay was performed as described above, but with variable 2-AG and inhibitor concentrations, respectively.

384-well format

Assays were performed as described for the 96-well format, unless stated otherwise. Assays were performed in black, flat-bottom 384-well plates (Greiner). Inhibitors (40x concentrated stock solution in DMSO) and MAGL-overexpressing membranes were diluted in HEMNB buffer to 2x concentrated solutions. Membranes (10 µL) were incubated with inhibitor (10 µL) for 20 min at rt, after which assay mix (10 µL of 3x concentrated solution) was added. Final assay concentrations were same as in 96-well format, but with 3 ng/µL MAGL-overexpressing membranes in a total volume of 30 µL. Fluorescence ($\lambda_{\text{ex}} = 535 \text{ nm}$, $\lambda_{\text{em}} = 595 \text{ nm}$) was measured at rt in 5 min intervals for 100 min on an Infinite M1000 Pro plate reader (Tecan).

1536-well format

Assays were performed as described for the 96-well format, unless stated otherwise. Assays were performed in black, flat-bottom non-treated 1536-well plates (Corning 3724). HEMNB buffer was supplemented with 0.03% (w/w) Tween-20. Inhibitors (200x concentrated stock solution in DMSO, 20 nL per well) were added using acoustic dispensing (Labcyte 555 Echo Liquid Handler) and diluted in assay buffer (1 µL). Membranes (2 µL) were added and mixtures were incubated for 30 min at rt, after which assay mix (1 µL) was added. Final assay concentrations were same as in 96-well format, but with 9 ng/µL MAGL-overexpressing membranes in a total volume of 4 µL. Fluorescence ($\lambda_{\text{ex}} = 531 \text{ nm}$, $\lambda_{\text{em}} = 595 \text{ nm}$) end point measurement was performed after 45 min incubation at rt on an EnVision Multimode plate reader (Perkin Elmer). Deselection assays were performed as described for the 1536-well format MAGL assay, but with glycerol (12.5 µM) instead of 2-AG as substrate.

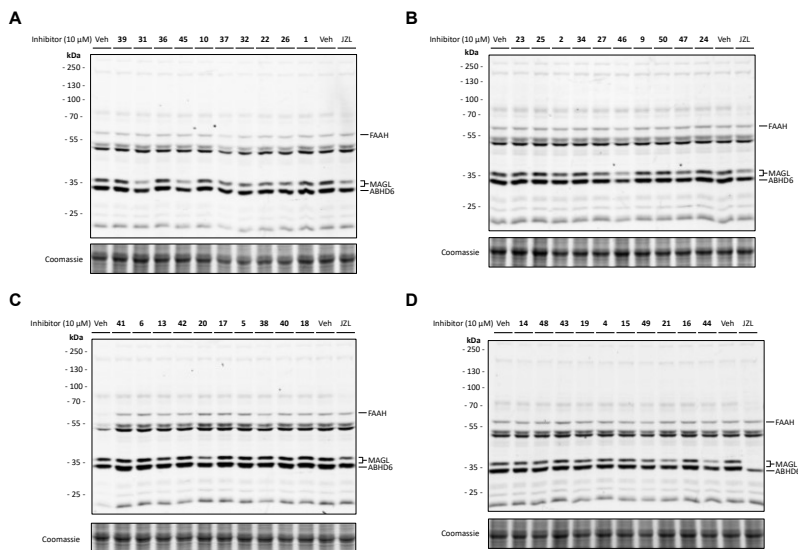
Activity-based protein profiling

Inhibitor solutions (50 nL in DMSO, final concentration 10 µM) were added to 384-well plates using acoustic dispensing (Labcyte 555 Echo Liquid Handler), after which mouse brain membrane preparation (10 µL, 2 mg/mL) was added. The mixture was incubated for 30 min at rt, followed by incubation with FP-TAMRA (0.5 µL in DMSO, final concentration 100 nM, 10 min, rt). Reactions were quenched with 4x Laemmli buffer (3.5 µL, final concentrations 60 mM Tris pH 6.8, 2% (w/v) SDS, 10% (v/v) glycerol, 5% (v/v) β-mercaptoethanol, 0.01% (v/v) bromophenol blue) for 30 min at rt. Samples (18 µg protein) were resolved by SDS-PAGE on a 10% polyacrylamide gel (180 V, 75 min). Gels were scanned using Cy3 channel settings (605/50 filter; ChemiDoc™ MP System, Bio-Rad). Fluorescence intensity was corrected for protein loading determined by Coomassie Brilliant Blue R-250 staining and quantified with Image Lab (Bio-Rad).

Data analysis and statistics

Fluorescence values were corrected for the average fluorescence of the negative control (mock-membranes + vehicle for 96- and 384-well format, MAGL-overexpressing membranes + 10 μ M JZL184 for 1536-well format). MAGL-overexpressing membranes incubated with vehicle served as a positive control. Slopes of the corrected data were determined in the linear interval. If relevant, the slopes in RFU/min were converted into slopes in nmol converted glycerol per milligram protein per minute via a glycerol standard curve with the rate of fluorescence increase as a function of converted glycerol. The Z'-factor for each assay plate was calculated using the formula $Z' = 1 - 3(\sigma_{pc} + \sigma_{nc})/(\mu_{pc} - \mu_{nc})$ with σ = standard deviation, μ = mean, pc = positive control and nc = negative control. Plates with $Z' \geq 0.6$ were accepted for further analysis. For K_M and V_{max} determination, data were subjected to Michaelis-Menten analysis (GraphPad Prism 5.0). For IC_{50} determination, slopes were normalized to the positive control and analyzed in a non-linear dose-response analysis with variable slope (GraphPad Prism 5.0). All shown data represent means \pm SEM, unless stated otherwise.

Supplementary Data



Supplementary Figure 6.1 – Complete set of activity-based protein profiling (ABPP) assays. Competitive ABPP assay on mouse brain membrane proteome using FP-TAMRA. Proteome was pre-incubated with inhibitor (10 μ M, 30 min), followed by incubation with FP-TAMRA (100 nM, 10 min). JZL184 was included as positive control on all gels. Quantification of MAGL and FAAH labeling intensity can be found in Figure 6.5.

References

- Buckley, M. L. & Ramji, D. P. The influence of dysfunctional signaling and lipid homeostasis in mediating the inflammatory responses during atherosclerosis. *Biochimica et Biophysica Acta - Molecular Basis of Disease* **1852**, 1498–1510 (2015).
- Currie, E., Schulze, A., Zechner, R., Walther, T. C. & Farese, R. V. Cellular fatty acid metabolism and cancer. *Cell Metabolism* **18**, 153–161 (2013).
- Serhan, C. N., Chiang, N. & Van Dyke, T. E. Resolving inflammation: Dual anti-inflammatory and pro-resolution lipid mediators. *Nature Reviews Immunology* **8**, 349–361 (2008).
- Bertrand, T. *et al.* Structural Basis for Human Monoglyceride Lipase Inhibition. *J. Mol. Biol.* **396**, 663–673 (2010).
- Navia-Paldanius, D., Savinainen, J. R. & Laitinen, J. T. Biochemical and pharmacological characterization of human α/β -hydrolase domain containing 6 (ABHD6) and 12 (ABHD12). *J. Lipid Res.* **53**, 2413–2424 (2012).
- Schalk-Hihi, C. *et al.* Crystal structure of a soluble form of human monoglyceride lipase in complex with an inhibitor at 1.35 Å resolution. *Protein Sci.* **20**, 670–683 (2011).
- Labar, G. *et al.* Crystal structure of the human monoacylglycerol lipase, a key actor in endocannabinoid signaling. *ChemBioChem* **11**, 218–227 (2010).
- Riccardi, L. *et al.* Lid domain plasticity and lipid flexibility modulate enzyme specificity in human monoacylglycerol lipase. *Biochim. Biophys. Acta - Mol. Cell Biol. Lipids* **1862**, 441–451 (2017).
- Blankman, J. L., Simon, G. M. & Cravatt, B. F. A Comprehensive Profile of Brain Enzymes that Hydrolyze the Endocannabinoid 2-Arachidonoylglycerol. *Chem. Biol.* **14**, 1347–1356 (2007).
- Blankman, J. L. & Cravatt, B. F. Chemical probes of endocannabinoid metabolism. *Pharmacol. Rev.* **65**, 849–71 (2013).
- Mulvihill, M. M. & Nomura, D. K. Therapeutic potential of monoacylglycerol lipase inhibitors. *Life Sci.* **92**, 492–497 (2013).
- Nomura, D. K. *et al.* Monoacylglycerol Lipase Regulates a Fatty Acid Network that Promotes Cancer Pathogenesis. *Cell* **140**, 49–61 (2010).
- Omabe, M., Ezeani, M. & Omabe, K. N. Lipid metabolism and cancer progression: The missing target in metastatic cancer treatment. *Journal of Applied Biomedicine* **13**, 47–59 (2015).
- Zaidi, N. *et al.* Lipogenesis and lipolysis: The pathways exploited by the cancer cells to acquire fatty acids. *Progress in Lipid Research* **52**, 585–589 (2013).
- DeBerardinis, R. J., Lum, J. J., Hatzivassiliou, G. & Thompson, C. B. The Biology of Cancer: Metabolic Reprogramming Fuels Cell Growth and Proliferation. *Cell Metabolism* **7**, 11–20 (2008).
- Cisar, J. S. *et al.* Identification of ABX-1431, a Selective Inhibitor of Monoacylglycerol Lipase and Clinical Candidate for Treatment of Neurological Disorders. *J. Med. Chem.* **61**, 9062–9084 (2018).
- Jiang, M. & Van Der Stelt, M. Activity-Based Protein Profiling Delivers Selective Drug Candidate ABX-1431, a Monoacylglycerol Lipase Inhibitor, to Control Lipid Metabolism in Neurological Disorders. *Journal of Medicinal Chemistry* **61**, 9059–9061 (2018).
- Pasquarelli, N. *et al.* Evaluation of monoacylglycerol lipase as a therapeutic target in a transgenic mouse model of ALS. *Neuropharmacology* **124**, 157–169 (2017).
- Hernández-Torres, G. *et al.* A reversible and selective inhibitor of monoacylglycerol lipase ameliorates multiple sclerosis. *Angew. Chemie - Int. Ed.* **53**, 13765–13770 (2014).
- Chen, R. *et al.* Monoacylglycerol Lipase Is a Therapeutic Target for Alzheimer's Disease. *Cell Rep.* **2**, 1329–1339 (2012).
- Griebel, G. *et al.* Selective blockade of the hydrolysis of the endocannabinoid 2-arachidonoylglycerol impairs learning and memory performance while producing antinociceptive activity in rodents. *Sci. Rep.* **5**, 7642 (2015).
- Kinsey, S. G., O'Neal, S. T., Long, J. Z., Cravatt, B. F. & Lichtman, A. H. Inhibition of endocannabinoid catabolic enzymes elicits anxiolytic-like effects in the marble burying assay. *Pharmacol. Biochem. Behav.* **98**, 21–27 (2011).
- Ramesh, D. *et al.* Dual inhibition of endocannabinoid catabolic enzymes produces enhanced antiwithdrawal effects in morphine-dependent mice. *Neuropsychopharmacology* **38**, 1039–1049 (2013).
- Zhong, P. *et al.* Monoacylglycerol lipase inhibition blocks chronic stress-induced depressive-like behaviors via activation of mTOR signaling. *Neuropsychopharmacology* **39**, 1763–1776 (2014).
- Nomura, D. K. *et al.* Monoacylglycerol lipase exerts dual control over endocannabinoid and fatty acid pathways to support prostate cancer. *Chem. Biol.* **18**, 846–856 (2011).
- Pagano, E. *et al.* Pharmacological inhibition of MAGL attenuates experimental colon carcinogenesis. *Pharmacol. Res.* **119**, 227–236 (2017).
- Barf, T. & Kaptein, A. Irreversible protein kinase inhibitors: Balancing the benefits and risks. *J. Med. Chem.* **55**, 6243–6262 (2012).
- Singh, J., Petter, R. C., Baillie, T. A. & Whitty, A. The resurgence of covalent drugs. *Nature Reviews Drug*

- Discovery* **10**, 307–317 (2011).
29. King, A. R. *et al.* Discovery of Potent and Reversible Monoacylglycerol Lipase Inhibitors. *Chem. Biol.* **16**, 1045–1052 (2009).
 30. Schlosburg, J. E. *et al.* Chronic monoacylglycerol lipase blockade causes functional antagonism of the endocannabinoid system. *Nat. Neurosci.* **13**, 1113–1119 (2010).
 31. Chanda, P. K. *et al.* Monoacylglycerol Lipase Activity Is a Critical Modulator of the Tone and Integrity of the Endocannabinoid System. *Mol. Pharmacol.* **78**, 996–1003 (2010).
 32. Tuccinardi, T. *et al.* Identification and characterization of a new reversible MAGL inhibitor. *Bioorganic Med. Chem.* **22**, 3285–3291 (2014).
 33. van der Wel, T. *et al.* A natural substrate-based fluorescence assay for inhibitor screening on diacylglycerol lipase α . *J. Lipid Res.* **56**, 927–935 (2015).
 34. Savinainen, J. R. *et al.* Robust Hydrolysis of Prostaglandin Glycerol Esters by Human Monoacylglycerol Lipase (MAGL). *Mol. Pharmacol.* **86**, 522–535 (2014).
 35. Long, J. Z. *et al.* Selective blockade of 2-arachidonoylglycerol hydrolysis produces cannabinoid behavioral effects. *Nat. Chem. Biol.* **5**, 37–44 (2009).
 36. Granchi, C., Caligiuri, I., Minutolo, F., Rizzolio, F. & Tuccinardi, T. A patent review of Monoacylglycerol Lipase (MAGL) inhibitors (2013-2017). *Expert Opinion on Therapeutic Patents* **27**, 1341–1351 (2017).
 37. Hitchcock, S. A. & Pennington, L. D. Structure-brain exposure relationships. *Journal of Medicinal Chemistry* **49**, 7559–7583 (2006).

7

Summary & Future prospects

The aim of the research described in this thesis was to develop a chemical genetic strategy that can be used for target engagement and target validation studies.

Target engagement and target validation in drug discovery

Chapter 1 provided an overview of the current multi-stage drug discovery and development process. The initial stage of target validation remains a major challenge and relies on the availability of chemical tools to study the engagement of drugs to their intended target. Chemical probes with a covalent, irreversible mode of action can serve as powerful tools to visualize target engagement. However, these probes have to meet strict requirements in terms of potency, selectivity and cell permeability and the development of such probes can be a challenge on its own. The field of chemical genetics provides means to improve the potency and selectivity of small molecules by not only modifying the ligand, but also by engineering the protein target. Although different approaches have been reported, not all are applicable for target engagement studies. The engineered, mutant proteins often suffer from distorted protein folding, reduced catalytic activity or other functional defects. Moreover, current chemical genetic strategies all rely on the overexpression of a mutant protein, which may induce artefacts and disturbs cellular physiology. Novel strategies and probes are thus required to address these issues.

Chemical genetics to visualize engineered kinases and their target engagement

Chapter 2 introduced a chemical genetic strategy that allows visualization of engineered kinases and their target engagement. The non-receptor tyrosine kinase feline sarcoma oncogene (FES) was selected as exemplary target in this study. Currently, there are no suitable chemical tools available for target validation of FES. Furthermore, FES does not possess targetable cysteine residues in its catalytic pocket, rendering it difficult to develop chemical probes that can report on its target engagement.

In silico mutant design based on a previously reported crystal structure of FES revealed residues suitable for mutagenesis into a cysteine. Expression, purification and biochemical profiling of these mutants revealed that the DFG-1 residue Ser700 is an excellent position to mutate into a cysteine without affecting kinase activity, substrate recognition or SH2 domain binding profile. Subsequent design and synthesis of electrophilic derivatives of the reversible, broad-spectrum kinase inhibitor TAE684 resulted in the identification of WEL028 as a mutant-specific inhibitor of FES^{S700C} with low-nanomolar *in vitro* and *in situ* potencies (Figure 7.1A).

Kinome-wide selectivity screening revealed that WEL028 has a greatly improved selectivity profile compared to the starting point TAE684, with only a limited number of prominent off-targets.¹ Regardless, these few off-targets may limit applicability in functional studies, for example when these kinases are involved in the same signaling

pathway or associated with similar physiological processes as the kinase of interest. Further improvement of the selectivity of WEL028 may therefore be beneficial. Previous studies have shown that the *ortho*-methoxy substituent on the aniline moiety of TAE684 is positioned in a pocket formed by the kinase hinge region.² Incorporation of more bulky groups may therefore improve compound selectivity. FES, for example, has a relatively large pocket that can accommodate ethoxy- or isopropoxy-substituents, which could prove useful to eliminate some of the off-targets of WEL028 (Figure 7.1B).³ In reverse,

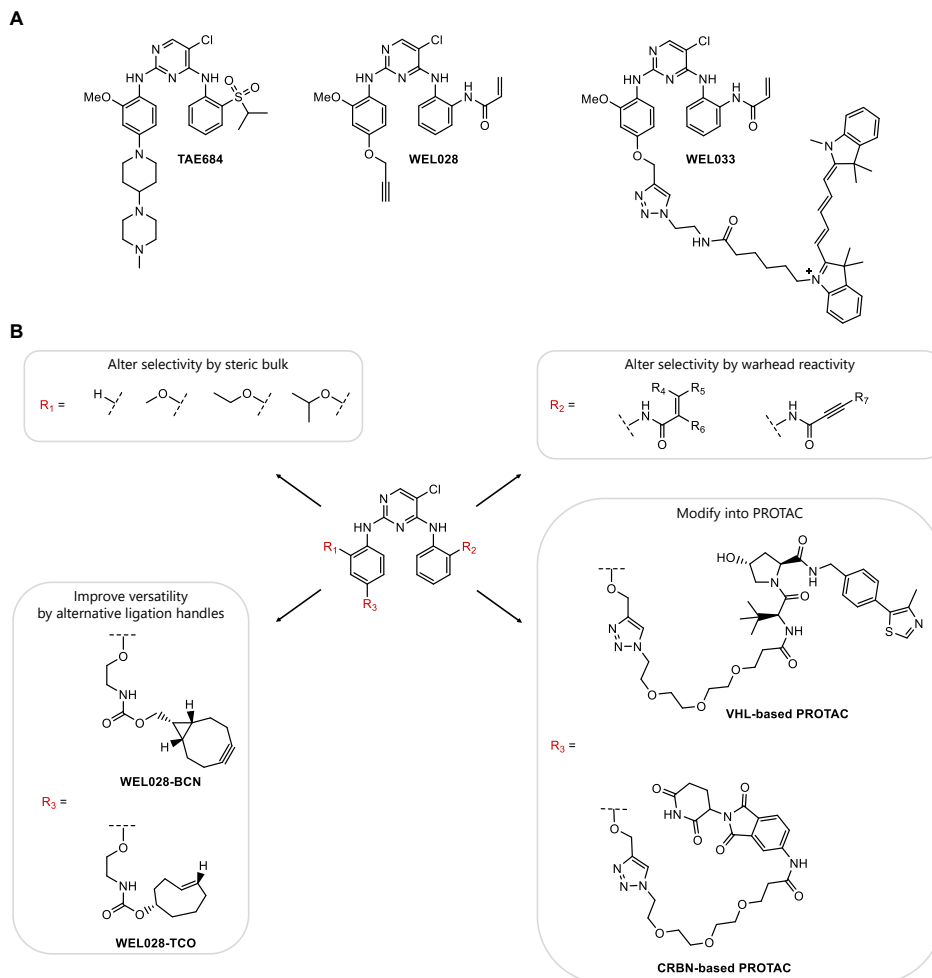


Figure 7.1 – Developed and proposed chemical genetic tools for kinase target validation. (A) Chemical structures of starting compound TAE684, mutant-specific FES^{S700C} inhibitor WEL028 and fluorescent probe WEL033. (B) Proposed WEL028 derivatives for improving selectivity, versatility in bioorthogonal conjugation or modification into PROTACs. BCN: bicyclononyne. TCO: trans-cyclooctene. VHL: Von Hippel-Lindau tumor suppressor. CRBN: protein cereblon.

removal of the *ortho*-methoxy moiety of WEL028 may allow for its use on a wider range of kinases that have larger amino acid residues in the hinge region. Undoubtedly, this structural change will also affect the compound's selectivity profile and kinome-wide selectivity screening should be performed on these WEL028 derivatives.

Another factor that affects covalent inhibitor selectivity is the reactivity of the nucleophilic (cysteine) residue and corresponding electrophile. Studies have shown that the pK_a of the cysteine sulfhydryl group is greatly affected by proximal amino acids^{4,5}, and that cysteines at the DFG-1 position are sufficiently reactive to undergo covalent addition to acrylamide warheads.⁶⁻⁸ Since the nucleophilicity of the cysteine is inherent to its surrounding microenvironment and cannot readily be manipulated, tuning electrophile reactivity is increasingly considered as a means to improve covalent inhibitor selectivity.⁹ Sufficiently reactive cysteines will also form covalent adducts with less reactive electrophiles, such as substituted acrylamides or butynamides (Figure 7.1B).⁵ More detailed examination of the structure-reactivity relationship of WEL028 for engineered cysteine mutant kinases may therefore prove useful to further improve its kinome-wide selectivity, although the nucleophilicity of this engineered cysteine is likely to be different for each individual mutant kinase and should therefore be experimentally examined for each individual case.

Expanding the toolbox of complementary probes

Chapter 2 also provided evidence for a covalent, irreversible binding mode of WEL028, using a combination of LC-MS/MS and biochemical assays. Conjugation of a fluorescent Cy5 group to the alkyne moiety of WEL028 using click chemistry yielded the one-step probe WEL033 (Figure 7.1A), which enabled direct target engagement studies by fluorescently labeling recombinantly expressed FES^{S700C} but not FES^{WT} in cell lysate. One-step fluorescent probes such as WEL033 are useful tools to visualize target engagement *in vitro*, but usually have limited applicability for applications in living cells due to limited cell permeability. Two-step probes are therefore often better alternatives due to their lower molecular weight and improved cellular target engagement.¹⁰ In chapter 2, WEL028 was used as a two-step probe to visualize target engagement on FES, but its alkyne handle requires copper-catalyzed click chemistry to conjugate reporter tags and the toxicity of the associated Cu^I species prohibits live cell imaging. In recent years, various alternative bioorthogonal groups have been reported that can allow conjugation without the use of copper, such as bicyclononyne (BCN) and trans-cyclooctene (TCO).¹¹ Incorporation of these handles onto the WEL028 scaffold (Figure 7.1B) would therefore allow for visualization of bound WEL028 targets in live cells, which may prove useful to investigate cellular localization of a kinase of interest during signaling processes.

Broader applicability of the developed chemical genetic toolbox was illustrated by gel-based labeling experiments on the DFG-1 cysteine mutant of four other kinases. It is unlikely, however, that a single chemical scaffold is able to target the entire kinome. Although TAE684 is a promiscuous kinase inhibitor that inhibits 98 out of 296 tested kinases with an $IC_{50} < 100$ nM¹², it targets kinases mainly in the tyrosine kinase (TK) and calcium/calmodulin-dependent protein kinase (CAMK) families (Figure 7.2A). Therefore, different chemotypes may be required to enable a more complete coverage of the kinome.

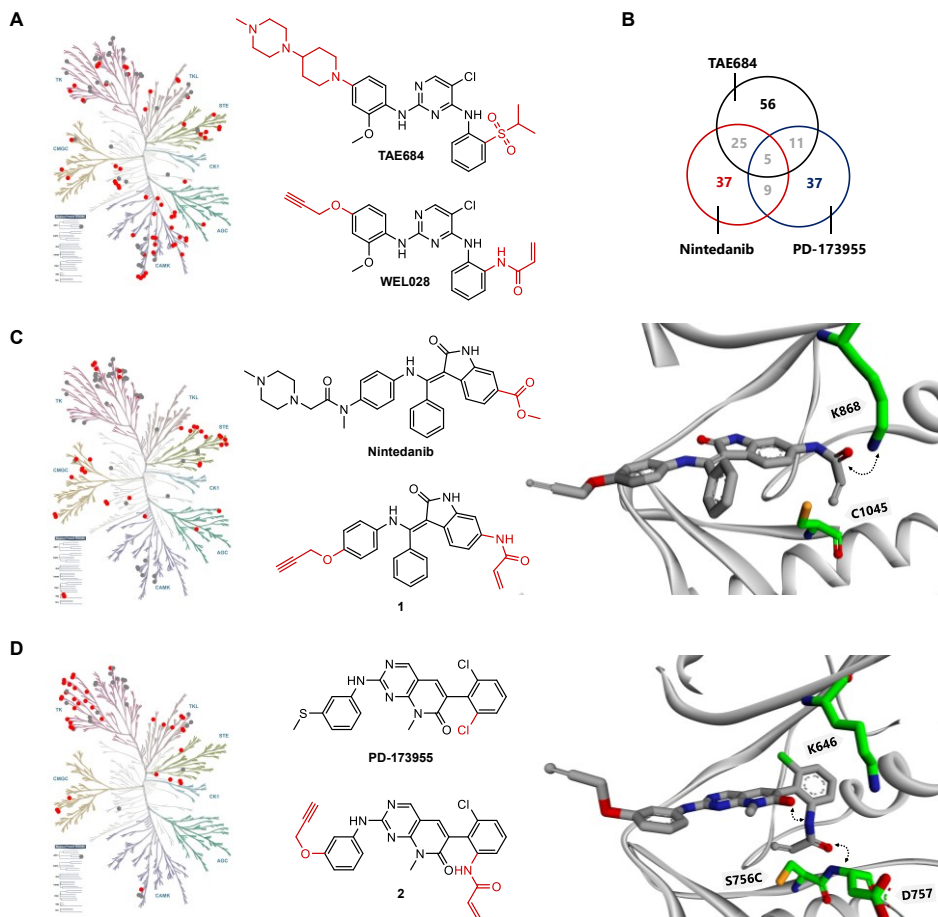


Figure 7.2 – Proposed chemotypes to expand the toolbox of complementary probes and improve kinome coverage. (A-D) Kinase target profile of the inhibitors TAE684, nintedanib and PD-173955 and proposed design of chemical probes **1** and **2** based on these inhibitors. Kinases with $IC_{50} < 100$ nM as reported by Davis *et al.* were designated as targets.¹ Unique targets of TAE684 (A), nintedanib (C) and PD-173955 (D) are indicated as red dots, shared targets as grey dots. (B) Venn diagram visualizing unique and shared targets of the inhibitors. (C, D) Proposed binding mode of **1** and **2** in crystal structure (C: VEGFR2 kinase domain, PDB: 3c7q; D: EphA2 kinase domain, PDB: 5ia3).^{13,14} Structures were manually modified. Dotted arrows indicate potential interactions that may aid in positioning of the acrylamide warhead to undergo covalent addition to the DFG-1 cysteine. Kinome illustrations were rendered using KinMap (www.kinhub.org/kinmap), reproduced courtesy of Cell Signaling Technology, Inc. (www.cellsignal.com).

Davis *et al.* previously reported on the comprehensive target profile of 38 kinase inhibitors¹ and examination of these profiles revealed that the inhibitors nintedanib (VEGFR/FGFR/PDGFR inhibitor) and PD-173955 (BCR-ABL/SRC inhibitor) have a complementary profile to TAE684 with few overlapping targets (Figure 7.2B). For example, nintedanib has a good coverage of the STE subfamily (Figure 7.2C) and PD-173955 covers members of the tyrosine kinase-like (TKL) subfamily along with several non-receptor TKs (Figure 7.2D). Inspection of crystal structures of nintedanib (in VEGFR2 kinase domain, PDB: 3c7q) and PD-173955 (in EPHA2 kinase domain, PDB: 5ia3) revealed that minor structural modifications of these compounds may provide chemical probes with electrophilic warheads in close proximity of the respective DFG-1 residues (Figure 7.2C, D, compound **1** and **2**). Interestingly, interactions between the acrylamide carbonyl of **1** with a catalytic lysine may position its warhead in the appropriate conformation to undergo a Michael addition to the DFG-1 cysteine (Figure 7.2C), in a similar way as predicted in docking studies with WEL028 in the crystal structure of FES. Compound **2** probably does not reach far enough into this pocket to interact with Lys646, but hydrogen bonding between the acrylamide carbonyl and protein backbone amide might adequately position its warhead for covalent addition in a similar fashion (Figure 7.2D). Both chemical scaffolds could thus provide useful additions to the chemical genetic toolbox to improve kinome coverage.

Precise gene editing and complementary probes for target validation of FES kinase

Chapter 3 applied the combination of FES^{S700C} and its mutant-specific probes to study the role of FES activity during differentiation of myeloid cells. CRISPR/Cas9 gene editing was employed for mutagenesis of the genomic *FES* locus, which resulted in a homozygous HL-60 FES^{S700C} mutant cell line. Endogenous FES^{S700C} could be visualized in lysates of differentiated HL-60 cells using fluorescent probe WEL033. The ability to study target engagement by WEL028 in living HL-60 cells undergoing differentiation was instrumental to reveal that FES activity was not required for myeloid differentiation of HL-60 cells along the monocyte/macrophage lineage. This contradicted previous studies relying on transient overexpression or RNA knockdown of FES and demonstrates the benefit of acute, pharmacological modulation of endogenous kinase activity. Chapter 3 also illustrates the importance of being able to discern on-target from off-target effects. WEL028 disrupted differentiation of HL-60 cells at a higher concentration than required for complete FES inhibition. However, this effect also occurred in wild-type control cells and could thus be attributed to off-targets, which most likely are members of the MAP kinase family.

Chapter 3 concludes with a differentiation study in FES knockout cells, generated using CRISPR/Cas9. HL-60 FES^{KO} cells differentiated towards macrophages in a similar fashion as wild-type cells, suggesting that FES has no essential scaffold functions required for myeloid differentiation. It should be noted, however, that long-term ablation of FES expression may induce compensatory effects, *e.g.* by upregulation of other kinases. Kinase

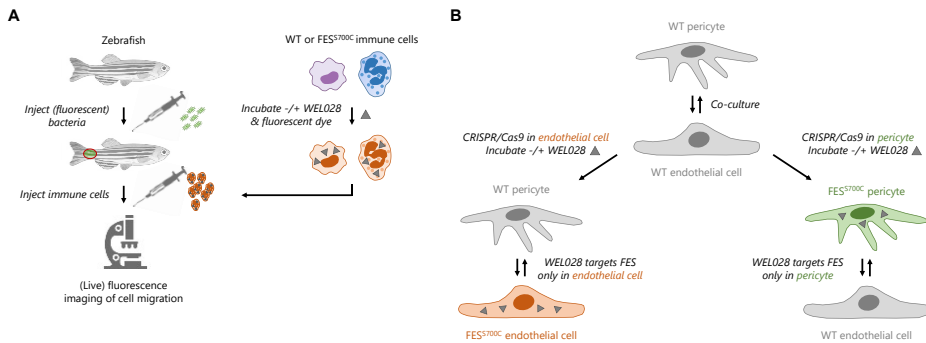
inhibitors coupled to a ligand for VHL and CRBN ubiquitin ligases can function as proteolysis targeting chimeras (PROTACs), inducing acute proteolytic degradation of the targeted kinase by hijacking E3 ligases.¹⁵⁻¹⁸ Active degradation of FES using a PROTAC might prove a valuable alternative for congenital knockout models. In addition to non-selective PROTACs that were previously reported to induce FES degradation¹⁹, conjugation of WEL028 to a VHL or CRBN ligand (Figure 7.1B) could be considered as a more selective alternative.

It remains to be investigated whether FES is involved in the differentiation of other cell types, or downstream of other growth factor receptors. To this end, it would be interesting to use gene editing to mutate FES in inducible pluripotent stem cells (iPSCs) or hematopoietic stem cells (HSCs), since these can differentiate into a wide range of specialized cell types. A major advantage of using such a chemical genetic approach is the temporal control that allows acute modulation of FES activity at every stage of cell differentiation, opposed to permanent congenital knockout models where FES expression is absent already at the stem cell stage.

Chapter 4 showcased how the chemical genetic toolbox of chapter 2 and mutant cell line of chapter 3 can be used to study the role of kinases in cellular processes. Using a flow cytometry-based assay with GFP-expressing *E. coli*, it was shown that FES inhibition reduced the phagocytic uptake of HL-60 neutrophils. Examination of the FES substrate profile of chapter 2 led to the hypothesis that the tyrosine kinase SYK could be a potential FES substrate in this process. Transient co-expression experiments showed that FES phosphorylates SYK Y352 *in situ* and that FES interacts with SYK in a WEL028-dependent manner. Immunoblot analysis with phospho-specific antibodies revealed that blocking SYK Y352 phosphorylation abolished activation of the downstream proteins HS-1 and PLC γ 2, two key players in phagocytosis.^{20,21} These results suggest that FES mediates the activation of a signaling pathway involved in reorganization of the actin cytoskeleton required for bacterium internalization. Chapter 4 concludes with a model, proposing that FES may indirectly activate PLC γ 2 to alter the membrane composition, resulting in its own dissociation from the membrane and thereby terminating the signaling input.

SYK is a central regulator of immune function and SYK inhibitors have therapeutic potential for cancer as well as autoimmune diseases, such as rheumatoid arthritis and lupus.^{22,23} It would be interesting to explore, therefore, in what cell types and downstream of which receptors FES activates SYK, and whether FES inhibition may have similar therapeutic potential. In addition, great opportunities lay in the use of more advanced model systems, such as zebrafish. Zebrafish are increasingly appreciated as a valuable model to study host-pathogen interactions due to their genetic and physiological similarity to vertebrates and transparency that facilitates *in vivo* imaging.²⁴ Injection of vehicle- or WEL028-treated FES^{S700C} immune cells into the circulation of live fish suffering from

(bacterial) infection would be a suitable experimental setup to investigate the role of FES in migration of immune cells to the site of infection (Figure 7.3A). In combination with high-resolution (fluorescence) imaging techniques, this may provide valuable insights in FES immunobiology.



7.3 – Future applications of the chemical genetic toolbox to study FES biology. (A) Experimental setup that allows *in vivo* evaluation of acute FES inhibition by complementary probe WEL028. Zebrafish are injected with fluorescent bacteria to generate an infection. Next, wild-type or CRISPR/Cas9-modified FES^{S700C} immune cells are incubated with WEL028 and fluorescently labeled with a live-cell dye, followed by injection into the zebrafish. High-resolution fluorescence microscopy can be used to visualize immune cell migration *in vivo*, and study the effects of FES inhibition in this process. (B) Exemplary application to modulate FES activity with cellular specificity during blood vessel formation. The generation of new blood vessels is directed by complex cross-talk between endothelial cells and pericytes. CRISPR/Cas9 gene editing can be used to introduce the S700C mutation in the FES locus of one of these cell types, which enables cell type-specific inhibition of FES exclusively in either endothelial cells or pericytes.

Phagocytosis is not only important for elimination of pathogens, but also essential for the elimination of apoptotic cells and tissue homeostasis.²⁰ In the brain, for example, microglia survey the microenvironment and phagocytose dying neurons to prevent tissue damage.²⁵ However, microglia can also phagocytose protein aggregates that occur in neurodegenerative diseases (*e.g.* amyloid- β in Alzheimer's disease and α -synuclein in Parkinson's).^{26–28} Very recently, studies have shown that a naturally occurring, rare genetic variant of PLC γ 2 in microglia results in a P522R mutation that moderately increases its phospholipase activity.²⁹ This variant is protective against neurodegenerative diseases, such as Alzheimer's, Lewy body dementia and frontotemporal dementia, and increases the likelihood of longevity.^{30,31} It would be interesting to investigate whether FES also indirectly activates PLC γ 2 in microglia and whether FES activation has neuroprotective effects in models for these diseases.

Internalization of immunoreceptors is the fundamental process of phagocytosis. It remains to be seen whether FES plays a more general role in the internalization of other receptors. FES is not exclusively expressed in immune cells, but also in endothelial, epithelial and neuronal cell types.³² Substrate and SH2 domain binding profiling revealed many cell surface receptors (*e.g.* VEGFR1/2, PDGFRB, CD79A, EPHA1/2) as potential FES substrates or binding partners. FES has been implicated in physiological processes

associated to some of these receptors, such as blood vessel formation and angiogenesis downstream of VEGFR in vascular endothelial cells.^{33–35} The role of kinase activity in this process is particularly challenging to study, since the formation of blood vessels involves multiple cell types, including endothelial cells and pericytes.³⁶ Moreover, it remains a major challenge to achieve cellular specificity using pharmacological agents. The here presented chemical genetic approach would be ideally suited to investigate the cell type-specific function of FES in such complex biological processes, since it allows mutagenesis of FES in one specific cell type, whereas wild-type FES in other surrounding cell types is not affected (Figure 7.3B). Angiogenesis is essential for tumor growth, invasion and the development of metastasis, and a role for FES in this process would thus render it a potential therapeutic target for various types of cancer.³⁷

Chemical genetics to achieve subtype-selective inhibition of DAGLs

Chapter 5 describes the first steps towards a chemical genetic strategy to achieve subtype-selective inhibition of the serine hydrolase DAGL α . Various positions in the DAGL α active site were mutated into a cysteine and the corresponding mutants were recombinantly expressed. Activity-based protein profiling with the two activity-based probes (ABPs) MB064 and DH379 and two substrate hydrolysis assays with PNPB and SAG were used for biochemical characterization of the DAGL α mutants. This revealed a general trend that mutation of residues in one pocket exhibited greatly reduced ABP labeling intensity and hydrolase activity, whereas mutations in another pocket were mostly tolerated. Design and synthesis of mutant-specific inhibitors based on a homology model³⁸ led to the identification of compound **4** (Figure 7.4F) as an inhibitor of DAGL α ^{L651C} but not DAGL α ^{WT} or other DAGL α mutants. In addition, it showed selective inhibition of DAGL α over DAGL β using competitive ABPP on mixed lysates of both DAGL subtypes. Compound **4**, however, showed a biphasic dose-response curve in all employed assays, suggesting two distinct binding events. The most potent interaction corresponded to a covalent, irreversible binding event of Cys651 to the bromoacetamide warhead of **4**, whereas the other interaction likely resembled a reversible binding event of catalytic Ser472 to the α -keto group. Further optimization of **4** is required prior to application of this chemical genetic strategy in cellular model systems.

The question arises whether the same chemical genetic approach could also be applied to generate subtype-selective inhibitors of DAGL β . Mutagenesis of the homologous residue Met639 into a cysteine resulted in partially preserved labeling intensities by probes MB064 and DH379 (~50% compared to WT, Figure 7.4A–C), similar protein expression levels (Figure 7.4D) and slightly reduced hydrolase activity based on the PNPB substrate assay (~75% activity compared to WT, Figure 7.4E). Although compound **3** and **4** showed a 10-fold higher potency on DAGL β ^{M639C} compared to DAGL β ^{WT} (Figure 7.4G, H), this mutant-specific effect is more moderate than observed for DAGL α . It remains to

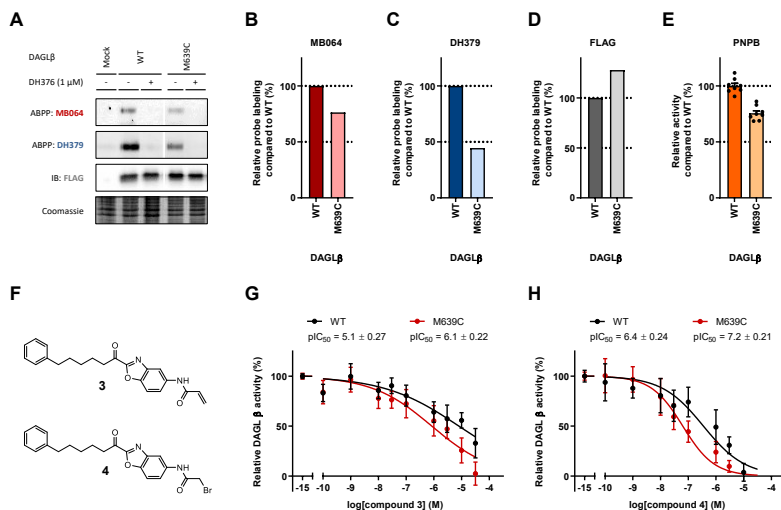


Figure 7.4 – DAGL β mutant homolog M639C is expressed and active but less sensitive towards inhibition by complementary inhibitors than DAGL α ^{L651C}. (A–D) Recombinantly expressed DAGL β ^{WT} and DAGL β ^{M639C} analyzed by activity-based protein profiling using probes MB064 (500 nM, 15 min, rt) and DH379 (1 μM, 15 min, rt). Protein expression was verified by anti-FLAG immunoblot. Band intensities were corrected for protein loading and normalized to wild-type control (N = 1). (E) Biochemical activity of DAGL β ^{WT} and DAGL β ^{M639C} analyzed by PNP-butyrates hydrolysis assay. Activity was determined using slope of reaction progress curve in linear range and normalized to wild-type control (N = 2, n = 4). (F) Chemical structures of compounds 3 and 4. (G, H) Dose-response curves of 3 (G) and 4 (H) on DAGL β ^{WT} and DAGL β ^{M639C}, determined using PNPB hydrolysis assay (N = 2, n = 4 for vehicle, N = 2, n = 2 for inhibitor-treated). Data represent means \pm SEM.

be investigated, therefore, whether this potency increase results from irreversible, covalent addition of Cys639 to the electrophilic warheads of **3** and **4**.

A particularly interesting future application of a chemical genetic approach for DAGL α would involve the generation of genetically engineered mice that express the corresponding mutant exclusively in specific (brain) cell types. This allows one to modulate DAGL α activity in an acute and dynamic fashion with a cellular specificity that is very challenging to achieve by conventional medicinal chemistry efforts. Consequently, this will contribute to our understanding of DAGL α -dependent lipid signaling in different brain cell types and aid in the validation of DAGL α as a therapeutic target for various diseases related to the central nervous system, such as metabolic disorders and neurodegenerative diseases.³⁹

Identification of reversible MAGL inhibitors: towards future drugs and chemical genetic tools

The serine hydrolase MAGL is responsible for degradation of the lipid 2-AG in the brain, which is synthesized by DAGL α .⁴⁰ To generate tools to modulate both the synthesis of 2-AG (by DAGL α , chapter 5) and its degradation, it was explored whether a chemical genetic

strategy could be applied to MAGL. In contrast to DAGL α , information about the MAGL protein structure is available. A structure of MAGL co-crystallized with Johnson & Johnson's inhibitor ZYX304 (PDB: 3pe6)⁴¹ was used to select active site residues for mutagenesis into a cysteine (Figure 7.5A). The corresponding mutants were recombinantly expressed and biochemically characterized. ABPP analysis with broad-spectrum probe FP-TAMRA and tailored MAGL probe LEI463 (Figure 7.5B) showed that some mutants were more effectively labeled by one of these ABPs than by the other ($R^2 = 0.66$, Figure 7.5C, D). This phenomenon was also observed for DAGL α mutants in chapter 5. Immunoblot analysis

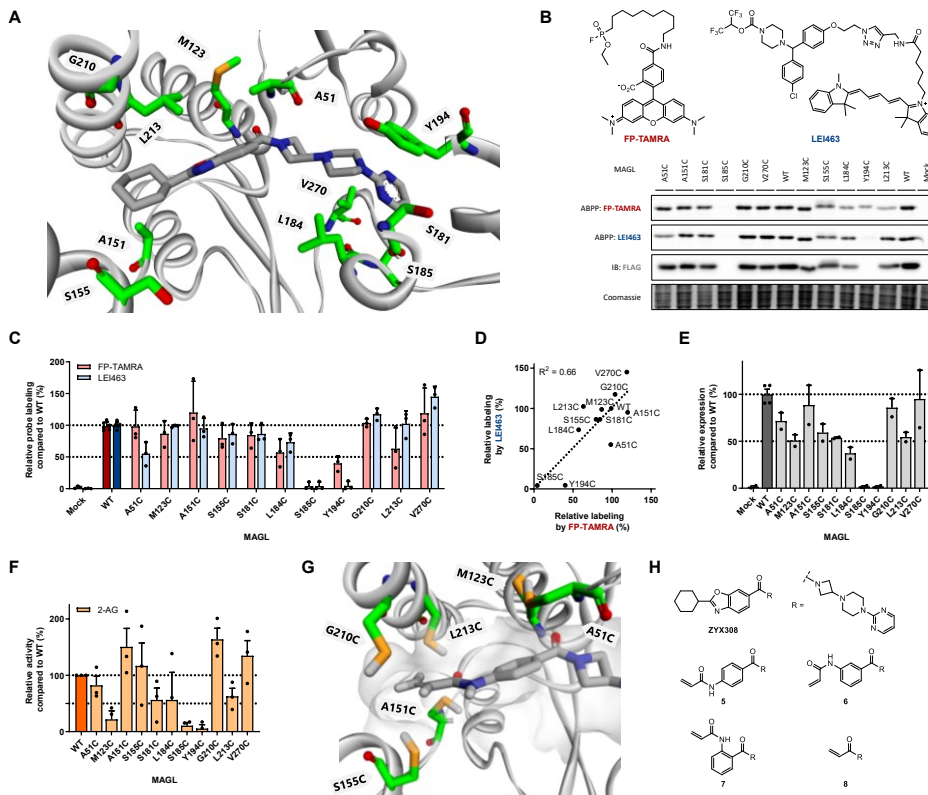


Figure 7.5 – Design of MAGL cysteine point mutants and characterization by activity-based protein profiling and substrate assays. (A) Location of mutated active site residues in MAGL crystal structure with inhibitor ZYX304 (PDB: 3pe6).⁴¹ (B, C) Recombinantly expressed MAGL mutants analyzed by activity-based protein profiling using probes FP-TAMRA (500 nM, 20 min, rt) and LEI463 (100 nM, 20 min, rt). Protein expression levels were determined by anti-FLAG immunoblot. Band intensities were normalized to wild-type control (N = 3, individual transfections). (D) Correlation between FP-TAMRA and LEI463 labeling intensities. (E) Relative expression of MAGL mutants compared to wild-type. Band intensities were corrected for protein loading and normalized to wild-type control (N = 3, individual transfections). (F) Biochemical activity of DAGL α mutants analyzed by 2-AG hydrolysis assay. Activity was determined using slope of reaction progress curve in linear range and normalized to wild-type control (N = 3, individual transfections measured in n = 4 technical replicates). (G) Design of proposed irreversible inhibitor **5** to covalently target indicated cysteines in this pocket. (H) Structures of designed and synthesized ZYX304 analogs to covalently target MAGL cysteine mutants. Compounds **5-8** did not inhibit wild-type MAGL nor any of the tested mutants A151C, S155C and G210C ($pIC_{50} < 5$ in 2-AG hydrolysis assay). Data represent means \pm SEM.

revealed that mutants S185C and Y194C were not expressed (Figure 7.5E), suggesting that these mutations result in a unstable protein fold that is prone to degradation. Three mutants (M123C, S185C and Y194C) showed a major reduction (> 80%) in 2-AG hydrolysis activity, whereas the activity of S181C, L184C and L213C was reduced by approximately 50% (Figure 7.5F). In most cases, these reductions can be ascribed to lower expression levels. Other mutants showed 2-AG hydrolysis activity comparable to or even higher than wild-type (A51C, A151C, S155C, G210C and V270C). Interestingly, most of these active mutants were located in the cyclohexyl-benzoxazole binding pocket (Figure 7.5A and G). Acrylamide-derivatized ZYX304 analogs **5-8** were designed and synthesized to target (one of) these cysteine mutants (Figure 7.5H). Compounds were tested in dose-response experiments, which revealed that all derivatives had greatly diminished inhibitory potency on both wild-type MAGL and tested mutants A151C, S155C and G210C ($pIC_{50} < 5$ in 2-AG hydrolysis assay). This suggests that the cyclohexyl-benzoxazole group may be required for initial binding in the active site, or that the cysteine residues cannot be targeted by the acrylamide warhead of these compounds. Another possibility is that the acrylamide is not sufficiently reactive to undergo Michael addition to the cysteines under the employed assay conditions, as was also observed in chapter 5 for DAGL α . It may be useful to explore whether compounds bearing more reactive warheads do show a mutant-specific inhibition profile. Alternatively, other MAGL mutants could be selected for structure-based design of new derivatives, such as V270C, the MAGL homolog of DAGL α ^{L651C}, directly adjacent to the catalytic His269 residue.

Chapter 6 reports on the optimization and miniaturization of a natural substrate-based activity assay for MAGL. This assay was then used for a high-throughput screening campaign on 233,820 compounds, which resulted in 1,142 confirmed actives. Deselection assays and hit triaging reduced this number to a list of 50 compounds that were profiled in dose-response experiments. Validation of these hits in an orthogonal competitive ABPP experiment led to a selection of 7 compounds that constitute starting points for the development of novel, reversible MAGL inhibitors. Blockage of 2-AG hydrolysis with MAGL inhibitors may prove beneficial for a wide variety of disorders, including Tourette syndrome, neuroinflammation, anxiety, pain and cancer.⁴²⁻⁴⁷ In addition to their use as potential future therapeutics, these reversible hit compounds may be used for the design of chemical genetic tools as alternative for the ZYX304 scaffold.

Integration of chemical genetics in drug discovery

The development of new therapeutics depends on our understanding of the protein targets that are targeted by these drugs. The potential compensatory effects and lack of temporal control using genetic techniques as well as the lack of selective pharmacological modulators to acutely perturb protein function contribute to the fact that target validation remains a major challenge in current drug discovery.

As demonstrated in this thesis, the use of chemical genetic approaches may provide novel opportunities to aid in the validation of putative therapeutic targets. The specificity achieved by the use of an engineered, mutant protein allows one to apply the same chemical probe on a variety of different targets within a larger protein family, such as kinases or serine hydrolases. In addition, mutagenesis of amino acid residues into a reactive cysteine also allows one to target protein classes that completely lack nucleophilic residues in their binding site and are thus challenging to target with conventional chemical probes.

The generation of a homozygous mutant cell line as an endogenous model system is one of the key steps in the developed chemical genetic approach. Tremendous advances in gene and base editing technologies are expected to improve the efficiency and throughput of site-directed mutagenesis in cells. It would be interesting to explore whether fluorescent chemical probes that covalently bind to the engineered cysteine, such as WEL033, can be used to select and enrich for mutant cells in a fluorescence-activated cell sorting (FACS) setup. On the long term, it may be possible to generate site-directed mutagenesis libraries that can be universally applied to any (human) cell line of choice.^{48,49} Broad applicability of the corresponding chemical probes is another prerequisite for effective integration in the drug discovery process, since it circumvents laborious optimization of the probes prior to application in target validation studies. It would be particularly powerful to couple target engagement and target validation studies to techniques that allow unbiased, global identification and quantification of target-specific downstream cellular processes, *e.g.* phosphoproteomics for kinases and lipidomics for lipases.

Concluding remarks

In this thesis, it was demonstrated that the field of chemical genetics can provide powerful tools to aid in target validation. Chemical genetics combines the specificity of genetic techniques with the acute and dynamic nature of pharmacology using small-molecule inhibitors. Compounds that bind in a covalent, irreversible fashion to mutant proteins harboring engineered cysteine residues are particularly useful by acting as chemical probes that can visualize target engagement. Chapter 2 showed the development of such a chemical genetic strategy that can be used for visualization of mutant kinases and their engagement by inhibitors. Potential applications in the target validation process were illustrated in chapter 3 and 4. The ability to perform comparative target engagement studies in wild-type and mutant cells was instrumental to refute the role of FES in myeloid differentiation of HL-60 cells. Chemical genetics can also be a valuable method to discover new enzyme substrates and functions, such as the identification of SYK as a substrate of FES and the discovery that FES plays a role in neutrophil phagocytosis. Chapter 5 demonstrated that a similar chemical genetic approach can be applied to other enzyme

classes, such as serine hydrolases. This also highlighted that successful design of mutant-specific inhibitors with a covalent binding mode greatly depends on structural information of the protein target, the reactivity of the introduced cysteine and the available (reversible) inhibitors. Chapter 6 reported on the use of high-throughput screening to identify novel chemical scaffolds with reversible binding modes that can be used for further optimization towards covalent probes or future therapeutics.

In conclusion, chemical genetics provides versatile pharmacological tools to modulate protein function with high specificity and can aid in the validation of proteins as therapeutic targets.

Acknowledgments

Bart Verschuren is kindly acknowledged for cloning and expression of DAGL β variants, Rick Meijer for expression and characterization of MAGL mutants and Enrico Verpalen for synthesis of MAGL inhibitors.

Experimental procedures

General

All chemicals were purchased at Sigma Aldrich, unless stated otherwise. DNA oligos were purchased at Sigma Aldrich or Integrated DNA Technologies and sequences can be found in Supplementary Table 1. Cloning reagents were from Thermo Fisher. FP-TAMRA⁵⁰ and LE1463 were previously synthesized in-house and characterized by NMR and LC-MS. All cell culture disposables were from Sarstedt. Bacterial and mammalian protease inhibitor cocktails were obtained from Amresco. Assay enzymes (glycerol kinase from *Cellulomonas sp.*, product code G6142; glycerol-3-phosphate oxidase from *Streptococcus thermophilus*, product code G4388; horse radish peroxidase from *Horseradish*, product code 77332) were purchased from Sigma Aldrich. 2-Arachidonoylglycerol was purchased from Cayman Chemicals.

Cloning

Full-length wild-type mouse DAGL β and human MAGL cDNA was obtained from Source Bioscience and cloned into pcDNA3.1 expression vectors as previously described.³⁸ Point mutations were introduced by site-directed mutagenesis and all plasmids were isolated from transformed XL10-Gold competent cells (prepared using *E. coli* transformation buffer set; Zymo Research) using plasmid isolation kits following the supplier's protocol (Qiagen). All sequences were verified by Sanger sequencing (Macrogen).

Supplementary Table 1 – List of oligonucleotide sequences.

ID	Name	Sequence	ID	Name	Sequence
P1	MAGL_forw	CTTAAGCTTTGGTACCCGCCACCACCTGGAACAGGACCTGAAG	P15	MAGL_S185C_forw	CGGGCCATCGACTCGAGCGTCTCTGCGAATAAGACAGA
P2	MAGL_rev	CATTCTAGACTACTCGAGACCCGGTGGTGGGACGACGATTC	P16	MAGL_S185C_rev	TCTGTCTTATTCGACAGAGCAGCTCGAGCTGATGGGCCCC
P3	MAGL_A51C_forw	TTTGTGTCCTCCATGATGTGGAGAGCACAGTGGC	P17	MAGL_Y194C_forw	TAAGACAGAGGTGACATATGTAACTACAGCCCTT
P4	MAGL_A51C_rev	GCCACTGTGCTCTCCACATCCATGGGACACAAA	P18	MAGL_Y194C_rev	AGGGGGTCTGAGTTACATATGTGACCTCTGTCTTA
P5	MAGL_M123C_forw	CTTCTGGGCACTCTCTGTGGAGGGCCATCGCC	P19	MAGL_G210C_forw	CTGAAGGTGTGCTTCTGCACTCAGCTGTAATCGCGTC
P6	MAGL_M123C_rev	GGCGATGGCCCTCCACAGAGGTGGCCAGAAAG	P20	MAGL_G210C_rev	GACGGCATTGACAGCTGGATCGAAGACACACTCTCA
P7	MAGL_A151C_forw	ACTCATTGGCTCTGAAAGTCTTGAATCCTGAATCTGCG	P21	MAGL_L213C_forw	GAAGGTGTGCTTGGGAATCAATGCGTGAATCGCTCTCA
P8	MAGL_A151C_rev	GCAGATCAGGATGCAAAAGTACTAGAGCGCAATGAGT	P22	MAGL_L213C_rev	TGAGAGCGCATTGAGCGATTGAAATCCGAAGACACCTTC
P9	MAGL_S155C_forw	GGTCTTCCGCAATCCGGAATGTGACAGCACTTTCAA	P23	MAGL_V270C_forw	CAAGATTTATGAGGGCGTCCACATGCGCTCCACAGGAGCTT
P10	MAGL_S155C_rev	TTGAAAGTGTGACATCTCGGATTTGGCAAGAACC	P24	MAGL_V270C_rev	AAGTCTCTGTGAGGGCAATGTAAGCGCTTCAATAATCTTG
P11	MAGL_S181C_forw	TCGGGCCATCGACTCGACGCTGCTCTCTCG	P25	mDAGLb_forw	CTTAAGCTTTGATCCCGCCGACACATCGCGGGATGTGCTGTT
P12	MAGL_S181C_rev	CGAGAGAGACGCTCGAGTGCATGGGCCCCGA	P26	mDAGLb_rev	GAGCGGCCCGACTCGCATACCCGTCGGTAGACTGAGCGCGCTT
P13	MAGL_L184C_forw	CGGGCCCATCGACTCGAGCGTGTCTCTCGGAATAAGAC	P27	mDAGLb_M639C_forw	ATGCTGATGACCTGCGCTGACGCTCATGATT
P14	MAGL_L184C_rev	GTCTTATCCGAGAGCACGCTCGAGTGCATGGGCCCCG	P28	mDAGLb_M639C_rev	AATCATGACGTGAGGGCGATGTGCTCAATCAGCAT

Cell culture

HEK293T (human embryonic kidney) cells were obtained from ATCC and tested on regular basis for mycoplasma contamination. Cultures were discarded after 2-3 months of use. Cells were cultured at 37 °C under 7% CO₂ in DMEM containing phenol red, stable glutamine, 10% (v/v) heat-inactivated newborn calf serum (Seradigm), penicillin and streptomycin (200 µg/mL each; Duchefa). Medium was refreshed every 2-3 days and cells were passaged two times a week at 80-90% confluence. One day prior to transfection, HEK293T cells were transferred from confluent 10 cm dishes to 15 cm dishes. Before transfection, medium was refreshed (13 mL). A 3:1 mixture of polyethyleneimine (PEI; 60 µg/dish) and plasmid DNA (20 µg/dish) was prepared in serum-free medium (2 mL) and incubated for 15 min at rt. The mixture was then dropwisely added to the cells, after which the cells were grown to confluence in 72 h. Cells were then harvested by suspension in PBS, followed by centrifugation (200 g, 5 min). Cell pellets were flash-frozen in liquid nitrogen and stored at -80 °C until membrane fraction preparation.

Membrane fraction preparation

Cell pellets were thawed on ice and homogenized by polytron (20,000 rpm, 3 x 7 s; SilentCrusher S, Heidolph) in lysis buffer A (20 mM HEPES pH 7.2, 2 mM DTT or 0.5 mM TCEP, 250 mM sucrose, 1 mM MgCl₂ and 25 U/mL benzonase). Suspensions were incubated on ice for 30 min to yield cell lysates. For preparation of membrane fractions, lysates were subjected to ultracentrifugation (93,000 g, 30

min, 4 °C; Beckman Coulter, Ti70 or Ti70.1 rotor) and pellets were homogenized in storage buffer B (20 mM HEPES pH 7.2, 2 mM DTT or 0.5 mM TCEP) by polytron (20,000 rpm, 1 x 10 s). Protein concentrations were determined using Quick Start™ Bradford Protein Assay (Bio-Rad). Membrane preparations were frozen in liquid nitrogen and stored at -80 °C until use.

Activity-based protein profiling (DAGLβ)

Membrane fractions (14 μL, 1.38 mg/mL) were incubated with inhibitor (0.5 μL in DMSO, 29x concentrated stock, 20 min, rt), followed by incubation with probe MB064 or DH379 (0.5 μL in DMSO, 30x concentrated stock, 15 min, rt). Reactions were quenched with 4x Laemmli buffer (5 μL, final concentrations 60 mM Tris pH 6.8, 2% (w/v) SDS, 10% (v/v) glycerol, 5% (v/v) β-mercaptoethanol, 0.01% (v/v) bromophenol blue) for 15 min at rt. Samples were resolved by SDS-PAGE on a 10% polyacrylamide gel (180 V, 75 min). Gels were scanned using Cy3 channel settings (605/50 filter; ChemiDoc™ MP System, Bio-Rad). Fluorescence intensity was corrected for protein loading determined by Coomassie Brilliant Blue R-250 staining and quantified with Image Lab (Bio-Rad).

Activity-based protein profiling (MAGL)

Cell lysate (14 μL, 1.38 mg/mL) was incubated with inhibitor (0.5 μL in DMSO, 29x concentrated stock, 20 min, rt), followed by incubation with probe FP-TAMRA or LEI463 (0.5 μL in DMSO, 30x concentrated stock, 20 min, rt). Reactions were quenched with 4x Laemmli buffer (5 μL, final concentrations 60 mM Tris pH 6.8, 2% (w/v) SDS, 10% (v/v) glycerol, 5% (v/v) β-mercaptoethanol, 0.01% (v/v) bromophenol blue) for 5 min at 95 °C. Samples were resolved by SDS-PAGE on a 10% polyacrylamide gel (180 V, 75 min). Gels were scanned using Cy3 and Cy5 multichannel settings (605/50 and 695/55 filters, respectively; ChemiDoc™ MP System, Bio-Rad). Fluorescence intensity was corrected for protein loading determined by Coomassie Brilliant Blue R-250 staining and quantified with Image Lab (Bio-Rad).

Immunoblot

Samples were resolved by SDS-PAGE and transferred to 0.2 μm polyvinylidene difluoride membranes by Trans-Blot Turbo™ Transfer system (Bio-Rad) directly after fluorescence scanning. Membranes were washed with TBS (50 mM Tris pH 7.5, 150 mM NaCl) and blocked with 5% milk in TBS-T (50 mM Tris pH 7.5, 150 mM NaCl, 0.05% Tween-20) for 1 h at rt. Membranes were then incubated with primary antibody in 5% milk in TBS-T (FLAG: 1:5000, 1 h at rt or o/n at 4 °C). Membranes were washed three times with TBS-T, incubated with matching secondary antibody in 5% milk in TBS-T (1:5000, 1 h at rt) and then washed three times with TBS-T and once with TBS. Imaging solution (10 mL luminol in 100 mM Tris pH 8.8, 100 μL ECL enhancer, 3 μL H₂O₂) was added and chemiluminescence was detected on ChemiDoc™ MP System. Primary antibody: monoclonal mouse anti-FLAG M2 (1:5000, Sigma Aldrich, F3156), secondary antibody: goat anti-mouse-HRP (1:5000, Santa Cruz, sc-2005).

PNP-butyrates hydrolysis assay (DAGLβ)

Assays were performed in 50 mM HEPES pH 7.0, 10 mM CaCl₂ in clear, flat-bottom 96-well plates (Greiner). Inhibitors were added from 40x concentrated stock solution in DMSO. DAGLβ-overexpressing membrane preparations (20 μg per well) were incubated with inhibitor for 20 min at rt in a total volume of 190 μL. Next, 10 μL substrate solution (PNP-butyrates in 1:1 mixture of DMSO/H₂O, final concentration 600 μM) was added. Absorbance at 420 nm was measured at 37 °C in 1 min intervals for 20 min on a GENios plate reader (Tecan). Final assay concentrations: 100 ng/μL DAGLβ-overexpressing membranes, 600 μM PNP-butyrates, 5% DMSO in a total volume of 200 μL. All measurements were performed in N = 2 (individual plates), n = 2 (technical replicates on same plate) or N = 2, n = 4 for controls, with Z' ≥ 0.6.

2-AG hydrolysis assay (MAGL)

Assays were performed in HEMNB buffer (50 mM HEPES pH 7.4, 1 mM EDTA, 5 mM MgCl₂, 100 mM NaCl, 0.5% (w/w) BSA) in black, flat-bottom 96-well plates (Greiner). Inhibitors were added from 40x

concentrated stock solution in DMSO. MAGL-overexpressing membrane preparations (0.3 µg per well) were incubated with inhibitor for 20 min at rt in a total volume of 100 µL. Next, 100 µL assay mix containing glycerol kinase (GK), glycerol-3-phosphate oxidase (GPO), horse radish peroxidase (HRP), adenosine triphosphate (ATP), Amplifu™Red and 2-arachidonoylglycerol (2-AG) was added. Fluorescence ($\lambda_{\text{ex}} = 535 \text{ nm}$, $\lambda_{\text{em}} = 595 \text{ nm}$) was measured at rt in 5 min intervals for 60 min on a GENios plate reader (Tecan). Final assay concentrations: 1.5 ng/µL MAGL-overexpressing membranes, 0.2 U/mL GK, GPO and HRP, 125 µM ATP, 10 µM Amplifu™Red, 25 µM 2-AG, 5% DMSO, 0.5% ACN in a total volume of 200 µL. All measurements were performed in N = 2 (individual plates), n = 2 (technical replicates on same plate) or N = 2, n = 4 for controls, with $Z' \geq 0.6$.

Data analysis, statistics and software

All shown data represent means \pm SEM, unless indicated otherwise. Replicates are indicated in figure legends with N for biological and n for technical replicates, respectively. All modeling figures were rendered using Discovery Studio 2016 (BIOVIA).

For substrate hydrolysis assays, absorbance or fluorescence values were corrected for the average of the negative control (mock-membranes + vehicle). DAGL β - or MAGL-overexpressing (wild-type or mutant) membranes incubated with vehicle served as a positive control. Slopes of the corrected data were determined in the linear interval. The Z' -factor for each assay plate was calculated using the formula $Z' = 1 - 3(\sigma_{\text{pc}} + \sigma_{\text{nc}})/(\mu_{\text{pc}} - \mu_{\text{nc}})$ with σ = standard deviation, μ = mean, pc = positive control and nc = negative control. Plates with $Z' \geq 0.6$ were accepted for further analysis. For IC₅₀ determination, slopes were normalized to the positive control and analyzed using 'Non-linear dose-response analysis with variable slope'. For curves with clear two-phase binding behavior, data were analyzed using 'Two sites – Fit logIC50' (GraphPad Prism 7.0).

References

- Davis, M. I. *et al.* Comprehensive analysis of kinase inhibitor selectivity. *Nat. Biotechnol.* **29**, 1046–1051 (2011).
- Hellwig, S. *et al.* Small-molecule inhibitors of the c-Fes protein-tyrosine kinase. *Chem. Biol.* **19**, 529–540 (2012).
- Marsilje, T. H. *et al.* Synthesis, Structure–Activity Relationships, and in Vivo Efficacy of the Novel Potent and Selective Anaplastic Lymphoma Kinase (ALK) Inhibitor 5-Chloro-N2-(2-isopropoxy-5-methyl-4-(piperidin-4-yl)phenyl)-N4-(2-(isopropylsulfonyl)phenyl)pyrimidine-2,4-diam. *J. Med. Chem.* **56**, 5675–5690 (2013).
- Garske, A. L., Peters, U., Cortesi, A. T., Perez, J. L. & Shokat, K. M. Chemical genetic strategy for targeting protein kinases based on covalent complementarity. *Proc. Natl. Acad. Sci. U. S. A.* **108**, 15046–15052 (2011).
- Demont, D. *et al.* Acalabrutinib (ACP-196): A Covalent Bruton Tyrosine Kinase Inhibitor with a Differentiated Selectivity and In Vivo Potency Profile. *J. Pharmacol. Exp. Ther.* **363**, 240–252 (2017).
- Lebraud, H. *et al.* In-gel activity-based protein profiling of a clickable covalent ERK1/2 inhibitor. *Mol. BioSyst.* **12**, 2867–2874 (2016).
- Cohen, M. S., Hadjivassiliou, H. & Taunton, J. A clickable inhibitor reveals context-dependent autoactivation of p90 RSK. *Nat. Chem. Biol.* **3**, 156–160 (2007).
- Tan, L. *et al.* Structure-guided development of covalent TAK1 inhibitors. *Bioorganic Med. Chem.* **25**, 838–846 (2017).
- Flanagan, M. E. *et al.* Chemical and computational methods for the characterization of covalent reactive groups for the prospective design of irreversible inhibitors. *J. Med. Chem.* **57**, 10072–10079 (2014).
- Sipthorp, J. *et al.* Visualization of Endogenous ERK1/2 in Cells with a Bioorthogonal Covalent Probe. *Bioconjug. Chem.* **28**, 1677–1683 (2017).
- Devaraj, N. K. The Future of Bioorthogonal Chemistry. *ACS Cent. Sci.* **4**, 952–959 (2018).
- Karaman, M. W. *et al.* A quantitative analysis of kinase inhibitor selectivity. *Nat. Biotechnol.* **26**, 127–132 (2008).
- Hilberg, F. *et al.* BIBF 1120: Triple angiokinase inhibitor with sustained receptor blockade and good antitumor efficacy. *Cancer Res.* **68**, 4774–4782 (2008).
- Heinzlmeir, S. *et al.* Chemical Proteomics and Structural Biology Define EPHA2 Inhibition by Clinical Kinase Drugs. *ACS Chem. Biol.* **11**, 3400–3411 (2016).
- Crews, C. M. *et al.* Protacs: Chimeric molecules that target proteins to the Skp1-Cullin-F box complex for ubiquitination and degradation. *Proc. Natl. Acad. Sci.* **98**, 8554–8559 (2002).
- Lai, A. C. & Crews, C. M. Induced protein degradation: An emerging drug discovery paradigm. *Nature Reviews Drug Discovery* **16**, 101–114 (2017).
- Ottis, P. & Crews, C. M. Proteolysis-Targeting Chimeras: Induced Protein Degradation as a Therapeutic Strategy. *ACS Chemical Biology* **12**, 892–898 (2017).
- Collins, I., Wang, H., Caldwell, J. J. & Chopra, R. Chemical approaches to targeted protein degradation through modulation of the ubiquitin–proteasome pathway. *Biochem. J.* **474**, 1127–1147 (2017).
- Huang, H. T. *et al.* A Chemoproteomic Approach to Query the Degradable Kinome Using a Multi-kinase Degradator. *Cell Chem. Biol.* **25**, 88–99.e6 (2018).
- Rosales, C. & Uribe-Querol, E. Phagocytosis: A Fundamental Process in Immunity. *BioMed Research International* **2017**, 1–18 (2017).
- Castro-Ochoa, K. F., Guerrero-Fonseca, I. M. & Schnoor, M. Hematopoietic cell-specific lyn substrate (HCLS1 or HS1): A versatile actin-binding protein in leukocytes. *Journal of Leukocyte Biology* **105**, 881–890 (2019).
- Ruzza, P., Biondi, B. & Calderan, A. Therapeutic prospect of Syk inhibitors. *Expert Opin. Ther. Pat.* **19**, 1361–1376 (2009).
- Liu, D. & Mamorska-Dyga, A. Syk inhibitors in clinical development for hematological malignancies. *Journal of Hematology and Oncology* **10**, 145 (2017).
- Torraca, V. & Mostowy, S. Zebrafish Infection: From Pathogenesis to Cell Biology. *Trends in Cell Biology* **28**, 143–156 (2018).
- Aguzzi, A., Barres, B. A. & Bennett, M. L. Microglia: Scapegoat, Saboteur, or Something Else? *Science (80-.)*. **339**, 156–161 (2013).
- Glass, C. K., Saijo, K., Winner, B., Marchetto, M. C. & Gage, F. H. Mechanisms Underlying Inflammation in Neurodegeneration. *Cell* **140**, 918–934 (2010).
- Sokolowski, J. D. & Mandell, J. W. Phagocytic clearance in neurodegeneration. *American Journal of Pathology* **178**, 1416–1428 (2011).
- Brown, G. C. & Neher, J. J. Microglial phagocytosis of live neurons. *Nat. Rev. Neurosci.* **15**, 209–216 (2014).
- Magno, L. *et al.* Alzheimer’s disease phospholipase C-gamma-2 (PLCG2) protective variant is a functional hypermorph. *Alzheimer’s Res. Ther.* **11**, 16 (2019).
- Conway, O. J. *et al.* ABI3 and PLCG2 missense variants as risk factors for neurodegenerative diseases in Caucasians and African Americans 11 Medical and Health Sciences 1109 Neurosciences 06 Biological Sciences 0604 Genetics. *Mol. Neurodegener.* **13**, 53 (2018).

31. van der Lee, S. J. *et al.* A nonsynonymous mutation in PLCG2 reduces the risk of Alzheimer's disease, dementia with Lewy bodies and frontotemporal dementia, and increases the likelihood of longevity. *Acta Neuropathol.* **138**, 237–250 (2019).
32. Haigh, J., McVeigh, J. & Greer, P. The fps/fes tyrosine kinase is expressed in myeloid, vascular endothelial, epithelial, and neuronal cells and is localized in the trans-golgi network. *Cell growth Differ.* **7**, 931–44 (1996).
33. Sangrar, W., Mewburn, J. D., Vincent, S. G., Fisher, J. T. & Greer, P. A. Vascular defects in gain-of-function fps/fes transgenic mice correlate with PDGF- and VEGF-induced activation of mutant Fps/Fes kinase in endothelial cells. *J. Thromb. Haemost.* **2**, 820–832 (2004).
34. Kanda, S., Mochizuki, Y., Miyata, Y. & Kanetake, H. The role of c-Fes in vascular endothelial growth factor-A-mediated signaling by endothelial cells. *Biochem. Biophys. Res. Commun.* **306**, 1056–1063 (2003).
35. Kanda, S., Kanetake, H. & Miyata, Y. Downregulation of Fes inhibits VEGF-A-induced chemotaxis and capillary-like morphogenesis by cultured endothelial cells. *J. Cell. Mol. Med.* **11**, 495–501 (2007).
36. Sweeney, M. & Foldes, G. It Takes Two: Endothelial-Perivascular Cell Cross-Talk in Vascular Development and Disease. *Front. Cardiovasc. Med.* **5**, 154 (2018).
37. Bergers, G. & Benjamin, L. E. Tumorigenesis and the angiogenic switch. *Nature Reviews Cancer* **3**, 401–410 (2003).
38. Baggelaar, M. P. *et al.* Development of an activity-based probe and in silico design reveal highly selective inhibitors for diacylglycerol lipase- α in brain. *Angew. Chemie - Int. Ed.* **52**, 12081–12085 (2013).
39. Janssen, F. J. & van der Stelt, M. Inhibitors of diacylglycerol lipases in neurodegenerative and metabolic disorders. *Bioorganic Med. Chem. Lett.* **26**, 3831–3837 (2016).
40. Bisogno, T. *et al.* Cloning of the first sn1-DAG lipases points to the spatial and temporal regulation of endocannabinoid signaling in the brain. *J. Cell Biol.* **163**, 463–468 (2003).
41. Schalk-Hihi, C. *et al.* Crystal structure of a soluble form of human monoglyceride lipase in complex with an inhibitor at 1.35 Å resolution. *Protein Sci.* **20**, 670–683 (2011).
42. Pasquarelli, N. *et al.* Evaluation of monoacylglycerol lipase as a therapeutic target in a transgenic mouse model of ALS. *Neuropharmacology* **124**, 157–169 (2017).
43. Hernández-Torres, G. *et al.* A reversible and selective inhibitor of monoacylglycerol lipase ameliorates multiple sclerosis. *Angew. Chemie - Int. Ed.* **53**, 13765–13770 (2014).
44. Chen, R. *et al.* Monoacylglycerol Lipase Is a Therapeutic Target for Alzheimer's Disease. *Cell Rep.* **2**, 1329–1339 (2012).
45. Kinsey, S. G., O'Neal, S. T., Long, J. Z., Cravatt, B. F. & Lichtman, A. H. Inhibition of endocannabinoid catabolic enzymes elicits anxiolytic-like effects in the marble burying assay. *Pharmacol. Biochem. Behav.* **98**, 21–27 (2011).
46. Griebel, G. *et al.* Selective blockade of the hydrolysis of the endocannabinoid 2-arachidonoylglycerol impairs learning and memory performance while producing antinociceptive activity in rodents. *Sci. Rep.* **5**, 7642 (2015).
47. Nomura, D. K. *et al.* Monoacylglycerol Lipase Regulates a Fatty Acid Network that Promotes Cancer Pathogenesis. *Cell* **140**, 49–61 (2010).
48. Zhou, Y. *et al.* High-throughput screening of a CRISPR/Cas9 library for functional genomics in human cells. *Nature* **509**, 487–491 (2014).
49. Mason, D. M. *et al.* High-throughput antibody engineering in mammalian cells by CRISPR/Cas9-mediated homology-directed mutagenesis. *Nucleic Acids Res.* **46**, 7436–7449 (2018).
50. Janssen, A. P. A. *et al.* Development of a Multiplexed Activity-Based Protein Profiling Assay to Evaluate Activity of Endocannabinoid Hydrolase Inhibitors. *ACS Chemical Biology* (2018). doi:10.1021/acscchembio.8b00534

Samenvatting

Het doel van het onderzoek beschreven in dit proefschrift was het ontwikkelen van een chemisch-genetische strategie die gebruikt kan worden voor 'target engagement' en 'target validatie' studies.

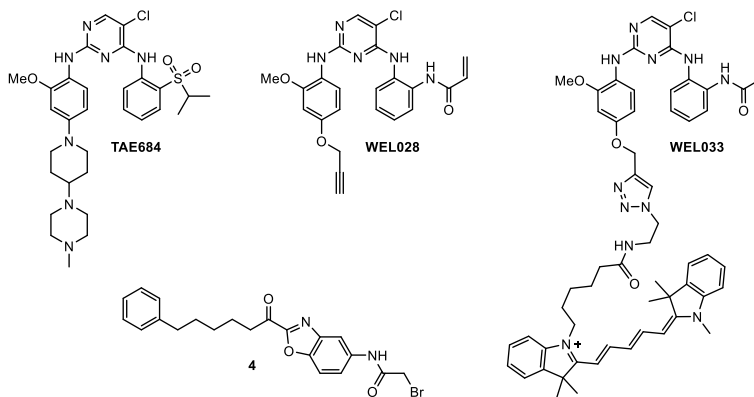
Target engagement en target validatie in medicijnontwikkeling

Hoofdstuk 1 geeft een overzicht van de verscheidene stappen van het huidige medicijnontdekking- en ontwikkelingsproces. Het eerste stadium omvat validatie van het therapeutische doel-eiwit (*target*). Dit is vooralsnog een grote uitdaging en afhankelijk van de beschikbaarheid van chemisch gereedschap (*tools*) om de interactie van medicijnen met hun beoogde doel-eiwit (*target engagement*) te bestuderen. Chemische sensoren (*probes*) met een covalente, irreversibele bindingsmodus kunnen als waardevolle tools dienen om deze interacties te visualiseren. Deze sensoren moeten echter voldoen aan strikte criteria op het gebied van potentie, selectiviteit en cel-permeabiliteit en het ontwikkelen van zulke sensoren is vaak een uitdaging op zich. Het vakgebied van de chemische genetica biedt middelen om de potentie en selectiviteit van moleculen te verbeteren door niet enkel het ligand aan te passen, maar ook het doel-eiwit te modificeren. Alhoewel er in het verleden verschillende benaderingen zijn gerapporteerd, zijn deze niet allemaal geschikt voor *target engagement* studies. In het algemeen brengt het gebruik van mutant-eiwitten vaak verstoringen in eiwitvouwing, een verlaging van katalytische activiteit of andere functionele defecten met zich mee. De huidige chemisch-genetische strategieën zijn bovendien allen afhankelijk van het tot overexpressie brengen van een mutant eiwit, wat tot artefacten kan leiden en de cellulaire fysiologie kan verstoren. Nieuwe strategieën en *probes* zijn dus vereist om deze problemen aan te pakken.

Chemische genetica voor visualisatie van gemodificeerde kinases en hun interacties

Hoofdstuk 2 introduceert een chemisch-genetische strategie die het mogelijk maakt om gemodificeerde kinases en hun interactie met remmers te visualiseren. Het doel-eiwit voor deze studie was het tyrosine-kinase FES. Tot op heden waren er geen geschikte chemische tools beschikbaar om FES te valideren als therapeutisch target. De afwezigheid van cysteïneresiduen in de katalytische regio maakt het bovendien moeilijk om chemische sensoren voor FES te ontwikkelen. Aan de hand van een eerder gerapporteerde kristalstructuur van FES werden residuen in de katalytische regio geselecteerd die mogelijk geschikt waren voor mutagenese naar een cysteïne. Deze mutant-eiwitten werden tot expressie gebracht, gezuiverd en geprofileerd in biochemische *assays*, wat tot het inzicht leidde dat serine 700, een aminozuurresidu direct voorafgaand aan het geconserveerde DFG-motief, een uitstekende positie was om in een cysteïne te muteren zonder dat dit de kinase-activiteit, substraatherkenning of eiwit-eiwit-interacties beïnvloedde. Hieropvolgend werden electrofiële derivaten van de breedspectrum kinaseremmer TAE684 ontworpen en gesynthetiseerd. Dit leidde tot de identificatie van WEL028 als een mutant-

specifieke remmer van FES^{S700C} met een laag-nanomolaire *in vitro* en *in situ* potentie (Figuur 1). Profilering van de kinoom-brede selectiviteit onthulde dat WEL028 een veel gunstiger selectiviteitsprofiel had in vergelijking met de uitgangsstof TAE684, met slechts een beperkt aantal prominente *off-targets*. Deze *off-targets* kunnen echter de toepasbaarheid voor functionele studies beperken, bijvoorbeeld wanneer deze kinases betrokken zijn bij dezelfde cellulaire signaleringsroutes of worden geassocieerd met vergelijkbare fysiologische processen als het doel-eiwit. Verdere verbetering van de selectiviteit van WEL028 zou in deze gevallen gunstig zijn. Hoofdstuk 2 leverde tevens bewijs voor een covalente, irreversibele bindingsmodus van WEL028. Conjugatie van een fluorescente groep aan de alkyn-substituent van WEL028 resulteerde in de één-stapssensor WEL033, die in staat is om FES^{S700C} maar niet wild-type FES fluorescent te labelen in cellysaten. Breder toepasbaarheid van de ontwikkelde chemisch-genetische gereedschapskist werd geïllustreerd met fluorescente labelingsexperimenten op de DFG-1 cysteinemutanten van vier andere kinases.



Figuur 1 – Chemische structuren van uitgangsstof TAE684, mutant-specifieke FES^{S700C}-remmer WEL028, fluorescente sensor WEL033 en mutant-specifieke DAGL α ^{L651C}-remmer 4.

In hoofdstuk 3 werd de combinatie van de FES^{S700C}-mutant en de mutant-specifieke sensoren gebruikt om de rol van FES kinaseactiviteit tijdens differentiatie van myeloïde cellen te bestuderen. CRISPR/Cas9-gemedieerde genmodificatie werd gebruikt voor mutagenese van de genomische *FES* locus, wat resulteerde in een homozygote HL-60 FES^{S700C} mutant-cel lijn. Met behulp van de fluorescente sensor WEL033 (Figuur 1) kon endogeen FES^{S700C} gevisualiseerd worden in lysaten van gedifferentieerde HL-60 cellen. Het inzicht in *target engagement* van WEL028 op FES^{S700C} in levende, differentiërende HL-60 cellen leidde tot de ontdekking dat FES activiteit niet vereist is voor myeloïde differentiatie van HL-60 cellen naar macrofagen. Deze resultaten zijn in tegenspraak met voorgaande studies die gebaseerd zijn op overexpressie van FES of op *knockdown* van FES op RNA-niveau en laten de voordelen zien van acute, farmacologische modulatie van endogene kinaseactiviteit. Bovendien illustreren

deze resultaten het belang om *on-target*- en *off-target*-effecten te kunnen onderscheiden. Op hogere concentraties dan vereist voor volledige FES-inactivatie verstoorde WEL028 de differentiatie van HL-60 cellen wel; deze effecten deden zich echter ook voor in de wild-type controlecellen en konden dus toegeschreven worden aan *off-targets*, hoogstwaarschijnlijk kinases uit de MAP kinase-familie. Hoofdstuk 3 besluit met een differentiatiestudie in FES *knockout*-cellen, welke ook gegenereerd werden met behulp van CRISPR/Cas9. Deze *knockout*-cellen behielden de mogelijkheid in een vergelijkbare wijze te differentiëren naar macrofagen als wild-type cellen, wat suggereerde dat FES ook geen essentiële structurele functie heeft als bindingspartner voor andere eiwitten in dit proces.

Hoofdstuk 4 demonstreert hoe de chemisch-genetische methode beschreven in hoofdstuk 2 en de mutant-celijn uit hoofdstuk 3 gebruikt kunnen worden om de rol van kinases in cellulaire processen te bestuderen. Met behulp van een flowcytometrische meetmethode en fluorescente *E. coli*-bacteriën kon worden aangetoond dat FES-activiteit een rol speelt in de het fagocytoseproces van HL-60 neutrofielen. Nadere inspectie van het substraatprofiel van FES (beschreven in hoofdstuk 2) leidde tot de hypothese dat het tyrosine-kinase SYK een potentieel substraat van FES is in dit proces. Co-expressie experimenten lieten zien dat FES inderdaad SYK Y352 fosforyleert *in situ*, dat FES bindingsinteracties kan aangaan met SYK, en dat deze interactie afhankelijk is van FES activiteit. Immunoblotanalyse met fosfo-specifieke antilichamen onthulde dat het blokkeren van SYK Y352 fosforylering met WEL028 de activatie van de eiwitten HS-1 en PLC γ 2 verhinderde, wier activatie beide belangrijk is voor het fagocytoseproces. Deze resultaten suggereren dat FES een signaleringsroute activeert die betrokken is bij de reorganisatie van het actine-cytoskelet, welke vereist is voor de internalisatie van de te doden bacterie. Hoofdstuk 4 besluit met een hypothetisch model waarin FES indirect PLC γ 2 activeert om de lipide-samenstelling van het membraan te veranderen, wat resulteert in zijn eigen dissociatie van het membraan en waarmee de signaleringsinput stopt.

Hoofdstuk 5 beschrijft de eerste stappen naar een chemisch-genetische strategie om het serine hydrolase DAGL α subtype-selectief te kunnen remmen. Verschillende posities in de katalytische regio van DAGL α werden gemuteerd naar een cysteïne en de desbetreffende mutant-eiwitten werden recombinant tot expressie gebracht. Activiteits-gebaseerde eiwitprofilering (*ABPP*) met de twee sensoren MB064 en DH379, alsmede twee substraathydrolyse-assays, werden gebruikt voor biochemische karakterisering van de DAGL α mutanten. Deze methodes toonden aan dat het aanbrengen van mutaties in één bepaalde holte in de katalytische regio desastreuze gevolgen had voor de labeling door sensoren en de hydrolase-activiteit. Daarentegen werden mutaties in een andere bindingsholte veelal getolereerd. Aan de hand van een homologiemodel werden mutant-specifieke enzymremmers ontworpen en gesynthetiseerd, wat leidde tot de identificatie van verbinding **4** (Figuur 1) als remmer van DAGL α ^{L651C} maar niet wild-type DAGL α of andere DAGL α -mutanten. Bovendien was het mogelijk om met deze verbinding

selectieve remming van DAGL α in aanwezigheid van DAGL β te bewerkstelligen in een competitief *ABPP*-experiment op gemengde cellysaten van beide DAGL subtypes. Verbinding **4** vertoonde echter een tweefasige dosis-responscurve in alle gebruikte *assays*, wat duidt op twee verschillende bindingsmodi. De meest potente interactie kwam overeen met een covalente, irreversibele bindingsmodus van Cys651 met de bromoacetamide-groep van **4**, terwijl de andere interactie vermoedelijk overeenkomt met een reversibele binding van de katalytische serine 472 met de α -keto-groep. Verdere optimalisatie van **4** is vereist voordat deze chemisch-genetische strategie toegepast kan worden in cellulaire modelsystemen.

Hoofdstuk 6 rapporteert de optimalisatie en miniaturisatie van een activiteits-*assay* voor het serine hydrolase MAGL, welke gebaseerd is op omzetting van 2-AG, het natuurlijke substraat van MAGL. Deze meetmethode werd vervolgens gebruikt in een *high-throughput screen* waarin 233,820 verbindingen werden getest en welke resulteerde in de identificatie van 1,142 actieve stoffen. Met behulp van deselectie-*assays* en triage werd dit aantal teruggebracht tot een lijst van 50 verbindingen, welke vervolgens verder geprofileerd werden in dosis-respons experimenten. Validatie van deze *hits* in een orthogonaal, competitief *ABPP*-experiment resulteerde in een selectie van 7 verbindingen die het startpunt vormden voor de ontwikkeling van nieuwe, reversibele MAGL-remmers. Het blokkeren van 2-AG hydrolyse met MAGL-remmers is vanuit therapeutisch oogpunt gunstig voor een verscheidenheid aan ziektes, waaronder het syndroom van Tourette, neuroinflammatie, angststoornissen, pijn en kanker. Naast een mogelijke toepassing als toekomstige medicijn kunnen deze reversibele verbindingen bovendien als startpunt dienen voor de ontwikkeling van chemisch-genetische sensoren voor MAGL.

Tot slot

De ontwikkeling van nieuwe medicijnen is afhankelijk van onze kennis van de doel-eiwitten die als aangrijpingspunt dienen voor deze medicijnen. Het valideren van nieuwe therapeutische aangrijpingspunten blijft een grote uitdaging in het huidige medicijnontwikkelingsproces. Validatie van *targets* met genetische methodes komt niet altijd overeen met de effecten van acute modulatie met chemische liganden en het permanente karakter van genetische modulatie kan leiden tot compensatie-effecten. Bovendien is een farmacologische aanpak niet altijd mogelijk door een gebrek aan selectieve, potente modulators.

De chemische genetica combineert de specificiteit van genetische technieken met het acute, dynamische karakter van farmacologische modulators. De specificiteit die verkregen wordt door het gebruik van een gemodificeerd eiwit, stelt men in staat om dezelfde chemische sensor toe te passen op een variëteit aan doel-eiwitten binnen een bepaalde eiwitfamilie, zoals de kinases of serine hydrolases. Bovendien biedt mutagenese van een aminozuurresidu naar een reactieve cysteine de mogelijkheid om covalente

sensoren te ontwikkelen voor eiwitten die van nature geen nucleofiele aminozuren in hun bindingsholtes bevatten, zoals werd geïllustreerd in hoofdstuk 2. Zulke chemische sensoren uitermate nuttige om *target engagement* te visualiseren. Potentiële toepassingen van chemisch-genetische methoden in het targetvalidatieproces werden geïllustreerd in hoofdstuk 3 en 4. De mogelijkheid om vergelijkingsstudies in wild-type en mutant cellen uit te voeren leidde tot het inzicht dat FES activiteit niet vereist is voor myeloïde differentiatie van HL-60 cellen. De chemische genetica kan ook bijdragen aan de ontdekking van nieuwe substraten of functies van bepaalde doel-eiwitten, zoals de identificatie van SYK als een substraat van FES, en de ontdekking dat FES een rol speelt in fagocytose door neutrofielen. Hoofdstuk 5 illustreerde dat een vergelijkbare chemisch-genetische strategie ook toepasbaar is op andere enzymklassen, zoals de serine hydrolases. Tevens werd hier benadrukt dat succesvol ontwerp van mutant-specifieke remmers met een covalente bindingsmodus in grote mate afhankelijk is van eiwitstructuurinformatie en beschikbare (reversibele) remmers die als startpunt kunnen dienen. Hoofdstuk 6 rapporteerde over het gebruik van *high-throughput screening* om nieuwe chemische entiteiten te identificeren met een reversibele bindingsmodus, welke verder ontwikkeld kunnen worden als chemisch-genetische sensoren of toekomstige medicijnen.

Tezamen laat dit proefschrift zien dat het gebruik van chemisch-genetische methoden mogelijkheden biedt om bij te dragen aan de validatie van nieuwe therapeutische aangrijpingspunten.

List of publications

Identification of α,β -hydrolase domain containing protein 6 as a diacylglycerol lipase in Neuro-2a cells

A.C.M. van Esbroeck*, V. Kantae*, X. Di, [T. van der Wel](#), H. den Dulk, A.F. Stevens, S. Singh, A.T. Bakker, B.I. Florea, N. Stella, H.S. Overkleeft, T. Hankemeier & M. van der Stelt.
Front. Mol. Neurosci. 12, 286 (2019)

Chiral disubstituted piperidiny ureas: a class of dual diacylglycerol lipase- α and ABHD6 inhibitors

H. Deng, [T. van der Wel](#), R.J.B.H.N. van den Berg, A.M.C.H. van den Nieuwendijk, F.J. Janssen, M.P. Baggelaar, H.S. Overkleeft & M. van der Stelt,
Med. Chem. Commun. 1–7 (2017).

Activity-based protein profiling reveals off-target proteins of the FAAH inhibitor BIA 10-2474

A.C.M. van Esbroeck*, A.P.A. Janssen*, A.B. Cognetta, D. Ogasawara, G. Shpak, M. van der Kroeg, V. Kantae, M.P. Baggelaar, F.M.S. de Vrij, H. Deng, M. Allarà, F. Fezza, Z. Lin, [T. van der Wel](#), M. Soethoudt, E.D. Mock, H. den Dulk, I.L. Baak, B.I. Florea, G. Hendriks, L. De Petrocellis, H.S. Overkleeft, T. Hankemeier, C.I. De Zeeuw, V. Di Marzo, M. Maccarrone, B.F. Cravatt, S.A. Kushner & M. van der Stelt.
Science 356, 1084–1087 (2017).

Triazole Ureas Act as Diacylglycerol Lipase Inhibitors and Prevent Fasting-Induced Refeeding

H. Deng, S. Kooijman, A.M.C.H. van den Nieuwendijk, D. Ogasawara, [T. van der Wel](#), F. van Dalen, M.P. Baggelaar, F.J. Janssen, R.J.B.H.N. van den Berg, H. den Dulk, B.F. Cravatt, H.S. Overkleeft, P.C.N. Rensen & M. van der Stelt.
J. Med. Chem. 60, 428–440 (2017).

Rapid and profound rewiring of brain lipid signaling networks by acute diacylglycerol lipase inhibition

D. Ogasawara*, H. Deng*, A. Viader, M.P. Baggelaar, A. Breman, H. den Dulk, A.M.C.H. van den Nieuwendijk, M. Soethoudt, [T. van der Wel](#), J. Zhou, H.S. Overkleeft, M. Sanchez-Alavez, S. Mori, W. Nguyen, B. Conti, X. Liu, Y. Chen, Q. Liu, B.F. Cravatt & M. van der Stelt.
Proc. Natl. Acad. Sci. 113, 26–33 (2016).

Triazole DAGL α inhibitors

B.F. Cravatt, D. Ogasawara, A. Viader, H. Deng, [T. van der Wel](#) & M. van der Stelt.
US Patent Application US20180344729A1. Priority date 2 December 2015. Filing date 2 December 2016.

A natural substrate-based fluorescence assay for inhibitor screening on diacylglycerol lipase α

[T. van der Wel](#), F.J. Janssen, M.P. Baggelaar, H. Deng, H. den Dulk, H.S. Overkleeft & M. van der Stelt.
J. Lipid Res. 56, 927–935 (2015).

Highly Selective, Reversible Inhibitor Identified by Comparative Chemoproteomics Modulates Diacylglycerol Lipase Activity in Neurons

M.P. Baggelaar, P.J.P. Chameau, V. Kantae, J. Hummel, K.L. Hsu, F.J. Janssen, T. van der Wel, M. Soethoudt, H. Deng, H. den Dulk, M. Allarà, B.I. Florea, V. Di Marzo, W.J. Wadman, C.G. Kruse, H.S. Overkleeft, T. Hankemeier, T.R. Werkman, B.F. Cravatt & M. van der Stelt.
J. Am. Chem. Soc. 137, 8851–8857 (2015).

Discovery of glycine sulfonamides as dual inhibitors of sn-1-diacylglycerol lipase α and α/β -hydrolase domain 6

F.J. Janssen, H. Deng, M.P. Baggelaar, M. Allarà, T. van der Wel, H. den Dulk, A. Ligresti, A.C.M. van Esbroeck, R. McGuire, V. Di Marzo, H.S. Overkleeft & M. van der Stelt.
J. Med. Chem. 57, 6610–6622 (2014).

Chemical genetics strategy to profile kinase target engagement reveals role of FES in neutrophil phagocytosis via SYK activation

T. van der Wel, R. Hilhorst, H. den Dulk, T. van den Hooven, N.M. Prins, J.A.P.M. Wijnakker, B.I. Florea, E.B. Lenselink, G.J.P. van Westen, R. Ruijtenbeek, H.S. Overkleeft, A. Kaptein, T. Barf & M. van der Stelt.
Manuscript submitted.

Towards a chemical genetic strategy for subtype-selective inhibition of diacylglycerol lipase alpha

T. van der Wel, T.J. Wendel, F. Mohr, H. den Dulk & M. van der Stelt.
Manuscript in preparation.

Discovery of an *in vivo* active NAPE-PLD inhibitor that reduces brain anandamide levels and pain behavior

E.D. Mock, M. Mustafa, R. Cinar, V. Kantae, X. Di, Z.V. Varga, J. Palocz, G. Donvito, A.C.M. van Esbroeck, A.M.F. van der Gracht, I. Kotsogianni, J.K. Park, A. Martella, T. van der Wel, M. Soethoudt, M. Jiang, T.J. Wendel, A.P.A. Janssen, A. Bakker, B.I. Florea, J. Wat, H. van den Hurk, M. Wittwer, U. Grether, M.W. Buczynski, C.A.A. van Boeckel, T. Hankemeier, P. Pacher, A.H. Lichtman & M. van der Stelt.
Manuscript submitted.

Highly Specific, Fluorescent Cannabinoid Type 2 Receptor Probes Enable Applications in Microscopy, Flow Cytometry and FRET-based Binding Assays

R. Sarott, M. Westphal, P. Pfaff, C. Korn, D. Sykes, T. Gazzi, B. Brennecke, K. Atz, M. Weise, Y. Mostinski, P. Hompluem, T. Miljus, N. Roth, H. Asmelash, M. Vong, J. Piovesan, W. Guba, A. Rufer, E. Kuszniur, S. Huber, C. Raposo, E. Zirwes, A. Osterwald, A. Pavlovic, S. Moes, J. Beck, I. Benito-Cuesta, T. Grande, A. Yeliseev, F. Drawnel, G. Widmer, D. Holzer, T. van der Wel, H. Mandhair, Y. Saroz, N. Grimsey, C. Yuan, W. Drobyski, M. Honer, J. Fingerle, K. Gawrisch, J. Romero, C. Hillard, Z. Varga, M. van der Stelt, P. Pacher, J. Gertsch, P. McCormick, C. Ullmer, S. Oddi, M. Maccarrone, D. Veprintsev, M. Nazare, U. Grether & E. Moran Carreira.
Manuscript submitted.

Drug Derived Fluorescent Probes for the Specific Visualization of Cannabinoid Type 2 Receptor - A Toolbox Approach

T. Gazzì, B. Brennecke, K. Atz, C. Korn, D. Sykes, R. Sarott, M. Westphal, P. Pfaff, M. Weise, Y. Mostinski, B. Horare, T. Miljuš, M. Mexi, W. Guba, A. Alker, A. Rufer, E. Kuszniir, S. Huber, C. Raposo, E. Zirwes, A. Osterwald, A. Pavlovic, S. Moes, J. Beck, I. Benito-Cuesta, T. Grande, F. Drawnel, G. Widmer, D. Holzer, T. van der Wel, H. Mandhair, Y. Saroz, N. Grimsey, M. Honer, J. Fingerle, K. Gawrisch, J. Romero, C. Hillard, P. McCormick, Z. Varga, M. van der Stelt, P. Pacher, J. Gertsch, C. Ullmer, S. Oddi, M. Maccarrone, D. Veprintsev, E. Carreira, U. Grether, M. Nazaré.

Manuscript submitted.

Chemical proteomics enables cellular selectivity profiling of clinical FLT3 inhibitors

S.H. Grimm, E.J. van Rooden, R. Wijdeven, L. de Paus, H. You, M. Quik, T. van der Wel, E.D. Mock, H.S. Overkleef, J. Neefjes & M. van der Stelt.

Manuscript in preparation.

Development of a fluorescent probe reveals the mitochondrial localization of monoacylglycerol lipase in breast cancer cells

H. Deng, M. Jiang, A.C.M. van Esbroeck, A.C.P. Zottola, T. van der Wel, D.M. van Elsland, H.M.N. Klaassen, S. Eshuis, H. den Dulk, Z. Varga, R.J.B.H.N. van den Berg, G. Marsicano, P. Pacher, S.I. van Kasteren, S.E. Le Dévédec & M. van der Stelt.

Manuscript in preparation.

Discovery and optimization of PLAAT2 α -ketoamide inhibitors that reduce *N*-acylethanolamine production

J. Zhou*, E.D. Mock*, K. Al Ayed, V. Kantae, X. Di, L. Burggraaff, A.F. Stevens, A. Martella, F. Mohr, M. Jiang, T. van der Wel, T.J. Wendel, T. Ofman, Y. Tran, N. de Koster, G. van Westen, T. Hankemeier & M. van der Stelt.

Manuscript in preparation.

* Authors contributed equally.

Curriculum Vitae

Tom van der Wel was born on May 6th, 1991 in Delft, The Netherlands. He obtained his high school diploma (VWO) from the Interconfessionele Scholengemeenschap Westland (ISW) in 's-Gravenzande in 2009. The same year, he started a bachelor study in Life Science and Technology, a shared program between the TU Delft and Leiden University. After a minor in organic chemistry in Leiden, he performed a research internship titled '*A tetrahedral boron catalyst for the aldol reaction*' in the Biocatalysis & Organic Chemistry group at TU Delft. The bachelor degree was obtained in 2012.

He subsequently started the master program Chemistry with specialization 'Design and Synthesis' at Leiden University later that year. In this period, Tom performed a research internship on '*Development and application of natural substrate-based assays for endocannabinoid hydrolases*' in the group of Bio-organic Synthesis at Leiden University. During this internship, he set up biochemical assays for various hydrolases of the endocannabinoid system and applied these in the process of inhibitor hit optimization. The corresponding thesis was nominated for the KNCV Golden Master Award 2014 and resulted in a first author publication. Tom obtained his master's degree *summa cum laude* in 2014.

In October 2014, he started his doctoral studies in the Bio-organic Synthesis group under supervision of prof. dr. M. van der Stelt and prof. dr. H.S. Overkleeft. A year later, part of this group transitioned into the new Molecular Physiology group, headed by prof. dr. M. van der Stelt. The research described in this thesis was performed in collaboration with dr. A. Kaptein and dr. T. Barf of Covalution Biosciences. NWO and Topsector Chemistry (TKI-project 'OncoDrugs') are kindly acknowledged for financial support.

Parts of the research described in this thesis were presented on posters at various (inter)national conferences, including CHAINS (Veldhoven 2014 and 2016), the Reedijk symposium (Leiden 2015 and 2018), International Cannabinoid Research Society's conference (Leiden 2018), ABPP conference (Leuven 2019), and EMBO Chemical Biology (Heidelberg 2018), of which the latter was awarded a poster prize. Oral presentations were held at CHAINS (Veldhoven 2017), the ABPP conference (Oxford 2018) and most recently at the FIGON Dutch Medicine Days (Leiden 2019), which was granted the best oral presentation award by the KNCV Division Medicinal Chemistry. In addition, Tom was selected to present his work as delegate for the Netherlands during the Young Medicinal Chemist Symposium (EFMC-YMCS 2020) in Basel, Switzerland.

Dankwoord

De multidisciplinariteit van chemisch-biologisch onderzoek is iets wat mij vanaf dag één al aansprak en het samenwerken met mensen uit verschillende disciplines is hier onlosmakelijk mee verbonden. Het is overduidelijk dat behalve ikzelf ook vele anderen een bijdrage aan dit proefschrift hebben geleverd.

In de eerste plaats mijn beide promotores, *Mario van der Stelt* en *Hermen Overkleef*. *Mario*, al vanaf de eerste dag dat ik in de groep binnenkwam (toen nog als masterstudent), heb ik me op mijn plek gevoeld. Bedankt voor de prettige begeleiding, het delen van kennis, de motiverende woorden en de vrijheid om eigen ideeën na te jagen. *Hermen*, tijdens jouw colleges werd mijn interesse in de chemische biologie gewekt. Bedankt voor je bijdrage tijdens het promotietraject en nadien bij het vinden van een nieuwe uitdaging.

De collega's van de groep 'moleculaire fysiologie' hebben de afgelopen jaren bijgedragen aan een aangename sfeer op de werkvloer, tijdens de koffiepauzes en bij feestjes. *Alexander, Anthe, Berend, Bing, Elliot, Floor, Hedwich, Kim, Laura, Na, Rob, Sebastiaan, Verena* en *Wouter*: thank you all for the great atmosphere, your help and useful discussions. *Mirjam, Tyrza, Thomas* en *Nina*: ook jullie bedankt voor de gezelligheid tijdens het pipetteren en met de lunch. Bepaalde delen van mijn werk bouwen verder op de fundamenteën die voorgangers hebben gelegd. I also want to acknowledge former colleagues for this: *Freek, Marc, Hui, Marjolein, Eva, Sebastian, Andrea* and *Juan. Florian, Ming, Timo*: I'm very grateful for your help with (re)synthesis of some of the compounds in this thesis. En natuurlijk *Hans den Dulk*: ik ben heel dankbaar voor je hulp, je ideeën en het delen van je jarenlange ervaring.

De afgelopen jaren heb ik een groot aantal studenten mogen begeleiden. *Sanne, Timo, Alessandro, Bart, Jessica, Nienke, Paulien, Mandy, Rick, Tim, Glenn* and *Joost*: thank you for your effort. Some of you are likely to find parts of your work back in this thesis; in many other cases your projects were continued by other group members and some of these are still ongoing.

Tijdens mijn projecten heb ik tevens mogen samenwerken met vele personen buiten de eigen onderzoeksgroep. Het werk dat het grootste gedeelte van dit proefschrift in beslag neemt, is uitgevoerd in samenwerking met (copromotor) *Tjeerd Barf* en *Allard Kaptein* van Covalution Biosciences. Bedankt voor jullie ideeën en suggesties de afgelopen jaren. Tevens wil ik de mensen van PamGene hartelijk bedanken. *Riet Hilhorst, Tim van den Hooven* en *Rob Ruijtenbeek*, jullie bijdrage heeft ervoor gezorgd dat we concrete aangrijpingspunten vonden om het kinaseproject mee te vervolgen. Bedankt voor jullie enthousiasme en de prettige en efficiënte samenwerking. *Tsang-Wai Lam, Helma Rutjes* en *Stan van Boeckel* van Pivot Park Oss: veel dank voor de optimalisatie en uitvoering van de high-throughput screen en de verdere selectie van hits. *Bobby* en *Hans van den Elst*: bedankt voor de technische ondersteuning. *Rolf, Marco, Marri, Martijn* en *Daphne*: het was

erg fijn af en toe naar beneden te kunnen lopen om gebruik te maken van jullie expertise of apparatuur. *Geri Moolenaar* en *Nora Goosen*, dank voor jullie hulp bij één van de allereerste stappen van het kinaseproject: de eiwitexpressie en –zuiveringen. *Bart Lenselink* en *Gerard van Westen*, bedankt voor jullie bijdrage op het vlak van de computationele chemie. *Mónica Varela*, I greatly appreciate your time and efforts with the zebrafish experiments. It is a pity we could not make it work in the limited amount of time we had. *Ruud Wijdeven*, onze experimenten samen hebben helaas niet veel opgeleverd, maar desondanks waardeer ik het dat je hiervoor tijd wilde vrijmaken. Graag wil ik ook mijn waardering laten blijken voor de medewerkers van ‘de keuken’. *Hellen*, *Annelies* en *Sebastiaan*, naar mijn mening wordt soms onderschat hoeveel dingen jullie voor ons uit handen nemen, bedankt hiervoor.

Natuurlijk mogen mijn twee paranimfen in dit dankwoord niet ontbreken. *Annelot*, we zijn ooit samen gestart met onze studie, en later beide op dezelfde dag begonnen aan ons PhD-avontuur. Bedankt voor het meedenken met experimenten, het betalen van vele bekertjes kantinesoep en bovenal voor je humor en steun. *Lindsey*, wij begonnen ooit samen aan onze masterstage bij toenmalig Biosyn, en sindsdien hebben we flink wat uurtjes geklaagd, gelachen en gediscussieerd (jij op alle fronten wat luider dan ik). Ik weet zeker dat ik jullie ook na onze promotieperiode blijf zien.

Tenslotte uiteraard het thuisfront. *Pa, ma, schoonfamilie*, en bovenal *Jordy*: ook jullie hebben bijgedragen aan dit proefschrift met jullie support, interesse en de nodige afleiding. Bedankt voor dit alles!

Tom

"In biology, nothing is clear, everything is too complicated, everything is a mess, and just when you think you understand something, you peel off a layer and find deeper complications beneath. Nature is anything but simple."

— Richard Preston